HAL
open science

Ultrasensitive nanowire force sensors in extreme conditions : from dilution temperature to ultra-strong coupling in cavity nano-optomechanics

Francesco Fogliano

To cite this version:

Francesco Fogliano. Ultrasensitive nanowire force sensors in extreme conditions : from dilution temperature to ultra-strong coupling in cavity nano-optomechanics. Condensed Matter [cond-mat]. Université Grenoble Alpes, 2019. English. NNT : 2019GREAY070 . tel-02634206

HAL Id: tel-02634206

https://theses.hal.science/tel-02634206v1

Submitted on 27 May 2020

HAL is a multi-disciplinary open access archive for the deposit and dissemination of scientific research documents, whether they are published or not. The documents may come from teaching and research institutions in France or abroad, or from public or private research centers.

L'archive ouverte pluridisciplinaire **HAL**, est destinée au dépôt et à la diffusion de documents scientifiques de niveau recherche, publiés ou non, émanant des établissements d'enseignement et de recherche français ou étrangers, des laboratoires publics ou privés.

Communauté UNIVERSITÉ Grenoble Alpes

THÈSE

Pour obtenir le grade de

DOCTEUR DE LA COMMUNAUTÉ UNIVERSITÉ GRENOBLE ALPES

Spécialité : **Physique**

Arrêté ministériel : 25 mai 2016

Présentée par

Francesco Fogliano

Thèse encadrée par **Olivier Arcizet** et **Benjamin Pigeau**
et dirigée par **Jean-Philippe Poizat**

préparée au sein de l'**Institut Néel, CNRS**
et de **l'École Doctorale de Physique de Grenoble**

ULTRASENSITIVE NANOWIRE FORCE SENSORS IN EXTREME CONDITIONS:
from dilution temperature to ultra-strong coupling in cavity nano-optomechanics

Thèse soutenue publiquement le **13 Décembre 2019**,
devant le jury composé de :

Antoine Heidman
Directeur de recherche, LKB, Paris (Rapporteur)

Adrian Bachtold
Professeur, ICFO, Barcelone (Rapporteur)

Fabio Pistolesi
Directeur de recherche, LOMA, Bordeaux (Président)

David Hunger
Professeur, KIT, Karlsruhe (Examinateur)

Eddy Collin
Chargé de recherche, Institut Néel, Grenoble (Examinateur)

Université Grenoble Alpes

PhD in Physics

PhD Thesis

Ultrasensitive nanowire force sensors in extreme conditions

From dilution temperature to ultra-strong coupling in cavity nano-optomechanics

Candidate
Francesco Fogliano
Institut Néel

Advisor
Dr. Olivier Arcizet
Institut Néel

Advisor
Dr. Benjamin Pigeau
Institut Néel

Academic Year 2018/2019

Francesco Fogliano
Ultrasensitive nanowire force sensors
in extreme conditions
PhD
© december 2019

This thesis work has been realized with LaTeX and edited with Kile on Chakra Linux using ArsClassica, a reworked version from Lorenzo Pantieri of the Classic Thesis style of André Miede inspired by *The Elements of Typographic Style* of Robert Bringhurst.

"La montagna più alta rimane sempre dentro di noi"
("The highest mountain is always within us")

— Walter Bonatti

To my family, my anchor in this stormy world

ACKNOWLEDGMENTS

If I have seen further it is by standing on the shoulders of Giants. It has been a few centuries since Newton wrote these words poking fun at his friend Hooke, but when taking stock at the end of a PhD, they acquire a whole new meaning.

I met several *Giants* during my studies, but here I would like to especially thank my advisors Olivier Arcizet and Benjamin Pigeau. Through their humility, their enthusiasm but most of all their deep understanding of the subject, they made my job not only far easier, but also extremely interesting and pleasant, and allowed me to learn a lot. When we first started the cryogenic experiment, we were not sure if light would have come out of it: it took a while, but now most of the (very few!) photons we send in are coming out, telling a really *sensitive* story. When we first started the cavity experiment, we didn't know if the two systems would couple properly: it turns out they did it *ultra-well*. In both cases, I was granted the freedom to follow my own ideas and interests, to make mistakes and learn from them, to lose myself in Python conundrums while learning how to automatize the measurements, to experiment with bizarre color maps and to forget all of the "-s"s and the "-ed"s in most sentences. The patience and the constant guidance of my advisors have made this a unique and invaluable experience.

Thanks a lot to Jean-Philippe Poizat, for the trust he put in me when he accepted to be my official advisor, the numerous discussions and the counsel. I am also grateful to the institute's director, Etienne Bustarret: the *Néel Institute* is a unique place that greatly enhances the interactions between students and researchers and it is for sure one the reasons this work was made possible.

A special thank to Antoine Heidman and Adrian Bachtold, who agreed to review this manuscript and whose numerous advices have been precious. Thanks to David Hunger and Eddy Collin, who have been part of my defense jury, as well as its president Fabio Pistolesi.

I will probably never finish to express my gratitude to my two big academic brothers, Benjamin Besga and Laure Mercier de Lépinay. Benjamin literally took me by the hand and guided me through the initial stages and the realization of both experiments: I owe him a lot, both personally and professionally. Laure has been a remarkable example as a student, as a physicist and as a person equally: from zero to hero, both in Python and in force measurement, she has been a constant and fundamental help. When they left the group, I have been lucky enough to have them replaced by two other extraordinary people. Antoine Reigue's deep and accurate work in simulating the NIM system prevented me from getting lost in its immense phase space; and Philip Heringlake, despite fighting against incredibly difficult and delicate measurements, always found the time to help me make my setup work, no matter if we were dealing with physics, computers or bad luck! My gratitude also goes to all the students who have been part of the group these years. I have learned a lot from them and I hope I have taught them something, too. So, from the cryostat to the fondue, from the cavity to the beers, cheers to Tobias, Kevin, Lukas, Clément and Hugo.

The low temperature experiment has been realized with an extraordinary instrument, the SIONLUDI dilution fridge: Wolfgang Wernsdorfer's and Eric Eyraud's constant help, lessons and technical expertise have been invaluable and made this experiment possible.

Together with them I would like to thank the other member of the Cryoptics group, Laetitia Marry, Nedjma Bendiab and Corinne Felix in particular. Numerous researchers at the institute contributed in different ways to this work: Olivier Bourgeois for his in depth knowledge of low-temperature thermal transport, Guillaume Bachelier for the Mie resonances simulation, all the members of the NOF group, and finally N. Roch, O. Buisson, J. Renard and E. Collin for their cryogenic and experimental assistance.

Thanks to the Atomic-Chip group of the LKB who provided the fibers for the cavity experiment, particularly J. Reichel, R. Long, J. Hare, C. Vaneph. The people of the ILM in Lyon - P. Poncharal, P. Vincent, A. Ayari - provided samples and expertise when dealing with silicon-carbide nanowires.

All the technicians who contributed in uncountable ways to the realization of both experiments deserve a special mention: J. Jarreau, L. Del Rey, D. Dufeu, R. Haettel, D.Lepoittevin, J. Minet, G. Bres, P. Charecchio, C. Hoarau, S. Triqueneaux, G. Donnier-Valentin, D. Jegouso, V. Reita and S. Le Denmat. The computer science department people, P. Belmain and J. Michel, have always been at my disposal when a computer did not want to obey. I am also grateful to all the members of the administration who make our work possible every day: F. Pois, S. Gadal, A. Laurent. M. Boyer, C. Bartoli and Y. Milin.

I would also like to thank Professor Ennio Arimondo and Professor Donatella Ciambini, who first introduced me to the field of optomechanics through my master thesis and then allowed me to take part to the Les Houches summer school, where this beautiful adventure started.

A huge hug to all the students, the friends and the extraordinary people I met at the institute and here in Grenoble: between physics and climbing, mountain and pastis, it has been an incredible journey. So thank you Hugo, Kimon, Athanasios, Roberto, Alvaro, Jorge, Tim, Stefano, Joachim, Corentin, Juliang, Everton, Thierry, Simone, Tatiana, Alessia, Maria, Chantal, Alex, David, Olivier, Luca, Juliette, Aashutosh, Kazi, Ana, Jesus and Marco. And also Jessica, for her huge help in correcting the manuscript's grammar right until the end.

Finally, my gratitude goes to my family: it is not always easy to explain to them what I study and why, but since the day I decided to study physics, their support and advice have been the foundations upon which all this has been possible.

Grenoble, december 2019 F. F.

CONTENTS

PREFACE xix

I INTRODUCTION

1 ULTRA-SENSITIVE MEASUREMENTS IN OPTOMECHANICAL SYSTEMS 3
1.1 Optomechanical systems and measurements . . . 4
1.2 Cavity Optomechanics . . . 5
1.2.1 A mechanical resonator coupled to a thermal bath . . . 6
1.2.2 Principles of optomechanical coupling . . . 11
1.2.3 Quantum limit in optical position sensing and the SQL . . . 14
1.3 SiC nanowires ultrasensitive sensors . . . 17

II NANO-OPTOMECHANICAL FORCE SENSING AT DILUTION TEMPERATURE

2 THE CRYOGENIC EXPERIMENT 25
2.1 Force sensing at cryogenic temperatures . . . 25
2.2 The cryostat . . . 27
2.2.1 Dilution fridges . . . 27
2.2.2 SIONLUDI: an inverted dilution fridge . . . 33
2.2.3 Measuring and controlling the temperature . . . 37
2.2.4 Environment acoustic isolation . . . 40
2.2.5 Cryostat control and interface . . . 42
2.3 Optical cryogenic head . . . 43
2.3.1 Interferometric objectives . . . 43
2.3.2 Nanowire support . . . 48
2.3.3 Piezo-positioners and scanners . . . 49
2.3.4 Suspended optical head . . . 51
2.4 System control and signal detection . . . 53
2.4.1 Experiment control and interface . . . 53
2.4.2 Optical scheme . . . 54
2.4.3 Vibrations measurements in the photon counting regime . . . 55

3 OPERATION OF A FORCE SENSOR AT DILUTION TEMPERATURE 63
3.1 SiC nanowires force sensors . . . 64
3.1.1 Physical Properties and their temperature dependence . . . 64
3.1.2 Mechanical properties . . . 66
3.1.3 Optical properties . . . 74
3.2 Brownian thermometry . . . 76
3.2.1 The Brownian thermal motion . . . 76
3.2.2 Dependence on the cryostat base temperature . . . 79
3.2.3 Optical heating . . . 81
3.2.4 Frequency and quality factor temperature dependence: TLS signature 82
3.3 Low temperature heat transport at the nanoscale . . . 86
3.3.1 The low temperature heat transport regimes . . . 86
3.3.2 Static heating of the nanowire at cryogenic temperatures . . . 90
3.4 Response measurement and force sensitivity . . . 92
3.5 Comparison across multiple samples . . . 95

III CAVITY-OPTOMECHANICS IN THE ULTRA-STRONG COUPLING REGIME
4 FIBER-CAVITY OPTOMECHANICS 101
4.1 Mechanical resonators in the middle of an optical cavity . . . 102
4.2 Optical cavity basics . . . 104
4.2.1 The transfer matrix formulation . . . 104
4.2.2 The Fabry-Perot cavity . . . 105
4.2.3 High-finesse fiber optical cavity . . . 107
4.3 MIM: membrane in the middle . . . 110
4.3.1 Reflection and transmission of the cavity . . . 110
4.3.2 Intra-cavity field . . . 112
4.3.3 Force on the membrane . . . 115
4.4 NIM: nanowire in the middle . . . 116
4.4.1 Nanowire in a Gaussian beam . . . 116
4.4.2 Transfer matrix of a NIM system . . . 118
4.4.3 Frequency shift of the cavity resonance . . . 118
4.4.4 Optical cavity mode imaging . . . 119
4.4.5 Intracavity field and optical force on the nanowire . . . 120
4.5 Experimental implementation . . . 122
4.5.1 General overview . . . 122
4.5.2 Functionalized fibers . . . 124
4.5.3 Fiber supports . . . 126
4.5.4 Nanowire support . . . 129
4.5.5 Vacuum chamber . . . 130
4.5.6 Vibration and thermal insolation . . . 130
4.5.7 Optical scheme . . . 131
4.5.8 Experiment control and interface . . . 135
4.6 Optomechanical coupling in a NIM . . . 136
4.6.1 Bare cavity resonances . . . 136
4.6.2 Optomechanical interaction . . . 140
4.6.3 The ultrastrong coupling regime . . . 145
4.6.4 Coupling to higher-order optical modes . . . 145
5 OPTICAL MODE IMAGING AND FORCE SENSING IN A NIM SYSTEM 149
5.1 Cavity locking . . . 150
5.2 Intracavity field characterization . . . 153
5.2.1 Cavity mode imaging . . . 153
5.2.2 Scattered light and cavity losses . . . 154
5.2.3 Correction maps . . . 158
5.2.4 Imaging higher-order optical modes . . . 160
5.3 Nano-optomechanical investigation of the intracavity force . . . 162
5.3.1 Independent optical readout and nanowires dynamics . . . 162
5.3.2 Intracavity force in a NIM . . . 166
5.3.3 Brownian motion 2D map . . . 171

CONCLUSION AND FUTURE DEVELOPMENTS 177

BIBLIOGRAPHY 185

LIST OF FIGURES

Figure 1.1 Recent impressive results in optomechanics 5
Figure 1.2 Power spectral density and autocorrelation function 10
Figure 1.3 Scheme of an ideal optomechanical system. 11
Figure 1.4 Schemes of the different OM regimes 13
Figure 1.5 The standard quantum limit 16
Figure 1.6 Silicon carbide nanowires ultrasensitive force sensor 17
Figure 1.7 Typical readout scheme to probe the NW vibrations 18
Figure 1.8 Phenomenology of the mode dressing of a nanowire in a force field 19
Figure 1.9 Scheme of a nanowire-in-the-middle system 21

Figure 2.1 Typical experiments for ultrasensitive force sensing 26
Figure 2.2 Phase diagram of ^{3}He and ^{4}He 27
Figure 2.3 Properties of liquid helium 28
Figure 2.4 Scheme of a dilution refrigerator 30
Figure 2.5 Subsequent stages and relative screens employed in the SIONLUDI. 33
Figure 2.6 Scheme of a SIONLUDI inverted dilution refrigerator 34
Figure 2.7 Pictures of the SIONLUDI dilution fridge 35
Figure 2.8 Cooling cycle of a SIONLUDI dilution fridge 36
Figure 2.9 Thermometers' resistances 38
Figure 2.10 The MMR3 and MGC3 controller 39
Figure 2.11 Picture of the gas handling system of the cryostat 40
Figure 2.12 Scheme of the gas handling system in real space 41
Figure 2.13 Graphical user interface used to control the cryostat operation . . . 42
Figure 2.14 ^{3}He reserve and main component of the gas handling group 42
Figure 2.15 Scheme of the optical cryogenic head 43
Figure 2.16 The cryogenic objective 44
Figure 2.17 Cryogenic objectives interference pattern 45
Figure 2.18 Chromatic focal shift of the cryogenic objectives 46
Figure 2.19 Collimator chromatic focal shift and beam waist dimension 47
Figure 2.20 Nanowire support 48
Figure 2.21 Baking of a nanowire 48
Figure 2.22 Attocube stepper tower mounted on the suspended optical head . 49
Figure 2.23 Cryostat optical head 52
Figure 2.24 User graphical interface of the NIL software. 54
Figure 2.25 Scheme of the optical setup. 55
Figure 2.26 Setup used to calibrate the spectrum of an APD photon-counter . . 56
Figure 2.27 Pulse and autocorrelation function of the photon-counter signal . . 58
Figure 2.28 Calibration of a noise signal measured with a photon counter . . . 61

Figure 3.1 Phase diagram of silicon carbide 64

Figure 3.2 Specific heat and thermal conductivity of silicon carbide 65
Figure 3.3 Absorption coefficient for a SiC crystal 66
Figure 3.4 Conventions for the *Euler-Bernoulli* description. 67
Figure 3.5 Graphical solution to compute the wavenumber β_n. 67
Figure 3.6 Transverse mode-shapes $u_n(y)$ of the first 5 fundamental modes . . 68
Figure 3.7 Response spectrum of the sample $NW1$ 69
Figure 3.8 Electrostatic tip used to drive the nanowire motion 69
Figure 3.9 NW properties as a function of their geometrical dimensions . . . 70
Figure 3.10 Effective mass as a function of the position along the NW 71
Figure 3.11 Estimation of the effective mass of the sample $NW2$ at 300 K 72
Figure 3.12 Imprecision noise limit to detect a NW thermalised at 20 mK 73
Figure 3.13 SiC nanowires's color chart 74
Figure 3.14 Relative optical cross section at 633 nm 74
Figure 3.15 NWs properties (including Mie scattering) vs length and diameter 75
Figure 3.16 Simulation of the Brownian thermal motion of a SiC nanowire . . . 76
Figure 3.17 Typical position noise spectral density $S_{\delta r_\beta}$ 77
Figure 3.18 SEM and optical (inset) image of the sample $NW1$. 78
Figure 3.19 Heating curves of the sample holder and of the mixing chamber . 79
Figure 3.20 Dependence of the noise temperature on the cryostat temperature 80
Figure 3.21 Noise temperature of $NW3$ as a function of the injected power . . 82
Figure 3.22 Temperature dependence of the mechanical frequency and damping rate 83
Figure 3.23 Mechanical property of amorphous material at low temperature . 84
Figure 3.24 Frequency versus optical power for different nanowires 85
Figure 3.25 Phonon spectral density distribution 87
Figure 3.26 Analysis of light induced heating of the NW 91
Figure 3.27 Response measurements at dilution temperature $NW3$ 93
Figure 3.28 Response measurements at dilution temperature $NW3$ 94
Figure 3.29 Temperature scan for $NW2$ and $NW4$ 95
Figure 3.30 Power scan for $NW4$ 96

Figure 4.1 Typical experiments in the resonator-in-the-middle configuration . 102
Figure 4.2 Reflection and transmission coefficients for a FPC 105
Figure 4.3 Properties of a high-finesse fiber optical cavity 108
Figure 4.4 M transfer matrix for a cavity made of two concave mirrors 110
Figure 4.5 Scheme of a membrane in the middle of a Fabry-Perot cavity . . . 111
Figure 4.6 Theoretical intensity transmission coefficient for a MIM system . . 112
Figure 4.7 Itracavity field and forces in a MIM 114
Figure 4.8 Scheme of the simple NIM system model 117
Figure 4.9 Simulation of the optical frequency shift in a NIM system 119
Figure 4.10 Mode imagining simulation of the resonant mode TM_{00} 120
Figure 4.11 Overview of the experimental setup 123
Figure 4.12 Laser ablation of a fiber extremity 124
Figure 4.13 Transmission property of the Bragg mirror 125
Figure 4.14 Aluminium support made to glue the fibers 127
Figure 4.15 Optical fiber support 128

FIGURE 4.16 Ensemble of the NW support. 129
FIGURE 4.17 Vacuum chamber and system isolation 130
FIGURE 4.18 Scheme of the optical setup employed in the NIM system. 132
FIGURE 4.19 Image of a nanowire in the middle of a fiber cavity 134
FIGURE 4.20 Graphical user interface developed to control the NIM system. . . 135
FIGURE 4.21 Cavity scan over two free-spectral-range 136
FIGURE 4.22 Typical reflection and transmission signals of the fiber micro-cavity 137
FIGURE 4.23 Cavity properties as a function of the pump wavelength 139
FIGURE 4.24 Split of the TM_{00} mode due to birefringence effect 139
FIGURE 4.25 Optical frequency shift vs transverse NW position 140
FIGURE 4.26 Resonance cavity shit for three different NWs diameter 141
FIGURE 4.27 Resonant cavity shift for the orthogonal and parallel polarization . 142
FIGURE 4.28 Resonant cavity shift measured through different channels 142
FIGURE 4.29 Optical frequency shift vs axial NW position 143
FIGURE 4.30 Resonant cavity shift in the vertical plane 144
FIGURE 4.31 Resonant cavity shift of the transverse mode TM_{12} 146
FIGURE 4.32 Optical transverse modes cross-coupling 147

FIGURE 5.1 Typical experimental error signal of the locking system 150
FIGURE 5.2 Scheme of the cavity locking system. 151
FIGURE 5.3 The PyRPL software used to control the Red-Pitaya FPGA card . . 152
FIGURE 5.4 Imaging of the TM_{00} mode in the horizontal XZ plane 154
FIGURE 5.5 Imaging of the TM_{00} mode for different insertion depth 155
FIGURE 5.6 Imaging of the fundamental TM_{00} mode in the vertical YZ plane . 156
FIGURE 5.7 Filtering of the correction signal map 158
FIGURE 5.8 Imaging of the TM_{00} mode for different light polarization 159
FIGURE 5.9 Imaging of higher transversal modes in the XZ plane 160
FIGURE 5.10 Imaging of the TM_{00} mode in the transversal XY plane 161
FIGURE 5.11 Interference patterns of the pump and probe lasers 163
FIGURE 5.12 Estimation of the mechanical parameters of the cavity samples . . 164
FIGURE 5.13 Nanomechanical measurement of the intracavity optical force . . . 165
FIGURE 5.14 Intracavity force along the optical axis 167
FIGURE 5.15 Simulations of the optical force profile 167
FIGURE 5.16 Principle of multi-frequency response 168
FIGURE 5.17 Maps of the measurement vectors 169
FIGURE 5.18 Correction for blind measurement in multi-frequency responses . . 170
FIGURE 5.19 Nano-optomechanical mapping of the intracavity force field 171
FIGURE 5.20 Transmission, scatter and correction signals of the TM_{12} mode . . . 172
FIGURE 5.21 Spectra of the transmission signal in the mode TM_{12} 173
FIGURE 5.22 Transmission $2D$ map of BW motion inside the mode TM_{12} 174
FIGURE 5.23 Scatter $2D$ map of BW motion inside the mode TM_{12} 175
FIGURE 5.24 Map of the intracavity force field for the mode TM_{12} 175

FIGURE 5.25 Pump-probe measurements on a nanowire at 300 K 178
FIGURE 5.26 Unexplained frequency signature 179
FIGURE 5.27 A photonic crystal on a SiC nanowire 180

Figure 5.28 Simulation of the frequency shift including Mie resonances 182
Figure 5.29 Simulation of the maximum frequency shift vs NW diameter . . . 182
Figure 5.30 (a) single-photon recoil. (b) single-photon bistability. 183

LIST OF TABLES

Table 1.1 The OM regimes for different values of g_0, Ω_m and κ. 13

Table 2.1 Coupling and transmission efficiency o the cryostat optics 55

Table 3.1 Physical properties of silicon carbide 66
Table 3.2 Wavenumber $\beta_n L$ for the first 10 modes. 67
Table 3.3 Frequency of the first 10 fundamental modes of the sample $NW1$. 69
Table 3.4 Main NW samples employed in the cryogenic setup 79

Table 4.1 Parameters of the fiber mirrors employed for the cavity setup . . . 126
Table 4.2 Main NW samples employed in the cavity setup 129

LIST OF SYMBOLS

T	Noise or sample temperature
Φ	Average photon flux
Ω_{m}	Mechanical frequency
Γ	Mechanical damping rate
M_{eff}	Effective mass of the mechanical oscillator
x_{zpf}	Mechanical zero-point fluctuations
δF_{th}	Langevin force
Q	Mechanical quality factor, $Q = \Omega_{\mathrm{m}}/\Gamma$
ω_{cav}	Resonant cavity frequency of the considered optical mode
κ	Cavity decay rate
$\tau^{(1)}$	Lifetime of a photon in the cavity, $\tau^{(1)} = 2/\kappa$
Δ	Optical cavity detuning
L	Optical cavity length
ω_{FSR}	Free spectral range, $\omega_{\mathrm{FSR}} = \frac{\pi c}{L}$
$\mathcal{F}$	Finesse, $\mathcal{F} = \frac{\omega_{\mathrm{FSR}}}{\kappa}$
$\bar{n}_{\mathrm{cav}}$	Photon number circulating inside the cavity
λ	Laser wavelength
k	Wave vector in vacuum, $k = 2\pi/\lambda$
n	Refractive index of the material
g_0	Optomechanical single-photon coupling strength
G	Optical frequency shift per displacement, $g_0 = G x_{\mathrm{zpf}}$
g	Light-enhanced optomechanical coupling for the linearized regime, $g = g_0\sqrt{\bar{n}_{\mathrm{cav}}}$
κ_{ph}	Thermal conductivity
C_{ph}	Specific heat
v_s	Speed of sound in the material
K	Thermal conductance, $K = k_{ph}\frac{S}{L}$
λ_{dom}	Phonons' dominant wavelength, $\lambda_{\mathrm{dom}} = \frac{h v_s}{2.82 k_{\mathrm{B}} T}$
Λ_{ph}	Phonons' mean free path, $k_{ph} = \frac{1}{3} C_{ph} v_s \Lambda_{ph}$
Λ_{cas}	Phonons' mean free path in the Casimir regime
Λ_{zim}	Phonons' mean free path in the Ziman regime
G_q	Quantum of thermal conductance, $G_q = \frac{\pi^2 k_{\mathrm{B}}^2}{3h} T$
η	Average surface roughness

PREFACE

In recent years nano-optomechanical systems have proven to be a powerful resource to detect ultra-weak forces, thus providing new insights on fundamental interactions. In this work we extend the experimental range of ultrasensitive force measurements based on the optically readout vibrations of suspended silicon carbide nanowires to novel experimental regimes: first through operations at dilution temperatures, second in the ultrastrong coupling regime of cavity nano-optomechanics.

AUTHOR'S CONTRIBUTION At the arrival of the author in the group, silicon-carbide nanowires had already been thoroughly studied as vectorial ultrasensitive force sensors at ambient temperature [232, 233, 234]. In order to extend the range of possible applications and to further increase their sensitivity, a new dilution fridge had just terminated the test phase and it was ready to host a new experiment at dilution temperature, which was developed from scratch.

Most of the first year and a half of the work was dedicated, in collaboration with B. Besga (postdoc in the group), to the development of a novel optical readout scheme, capable of working reliably and continuously from 300 K to 20 mK. Several challenges had to be overcome, including the realization of new cryogenic objectives, the identification and suppression of several noise sources (of both acoustic and electric origin) and the development of new signal analysis technique which allows to employ optical sensors operating in the photon-counting regime. After an extended period of time spent in the testing room, where we were able to probe the NWs thermal noise at cryogenic temperature as well as to keep the system cold for several months, the whole setup was moved to its final location in the Z building (a low noise building opened in 2017) and the whole experimental apparatus was rebuilt. After a phase of optimization of the cryostat and the gas handling system, we prolonged the experimental developments: the optical head was suspended above the cryostat cold plate, to further decouple it from external noise, and new record force sensitivity where achieved for a scanning probe system, together with some preliminary studies on the thermal properties of silicon-carbide at dilution temperature.

In parallel to the low-temperature setup, a first implementation of the room-temperature cavity optomechanical experiment was started together with B. Besga and T. Heldt (master internship), allowing for a preliminary evaluation of the experimental requirements ($D304$). The second year and a half of the PhD was dedicated to a deeper investigation of this system: the setup was unmounted, optimized and rebuilt in a new and more suitable experimental room (D302) and the original couple of fiber-mirrors were replaced with a new set, allowing for smaller optical mode volumes. The vast parameter space allowed by this new configuration was vastly explored and it was possible to further explore this novel regime of the nano-optomechanical interaction. Also, we implemented the novel force measurement techniques developed by P. Heringlake, PhD in the group, to realize the first maps of the optomechanical force field within the cavity mode volume. A systematic theoretical investigation of the nanowire-cavity system was developed by A. Reigue, a postdoc in the group.

New interesting possibilities, resulting from the combined results of the two experiments studied by the author in this work, are currently under investigation in the group.

The compact fiber objectives developed in this work were subsequently used to produce a movable optical waist, that served to produce a tunable rotational force field. This allowed to investigate the nanowire thermal noise reduction and squeezing mechanism enabled by a circulating force field. These results are not described in this work, but will soon appear [55].

The presentation will be divided as follows:

THE FIRST CHAPTER introduces the context and the motivations that lead to this work, together with some of the basic concepts of cavity optomechanics and noise measurements which will be extensively used across the manuscript. A brief description of the previous works in the group and in others using suspended nanowires as ultrasensitive force probes are described.

THE SECOND CHAPTER presents a complete description of the cryostat employed in this work, as well as a description of the optical techniques developed to probe the nanowires motion at low temperature. The new signal analysis techniques developed to operate at ultra-low optical powers are also fully discussed.

THE THIRD CHAPTER exposes all the main results of the dilution temperature experiment. After a brief description of the NWs physical, mechanical and thermal properties, the dependence of the Brownian noise on the cryostat temperature and on the probe laser power is exposed, leading to extreme force sensitivities for a scanning probe force sensor. An introductory discussion of the measured thermal properties of the nanowire is also presented, and motivates future measurements to fully understand the peculiar heat propagation within the nanowires.

THE FOURTH CHAPTER describes the principle of a *resonator-in-the-middle* cavity-nano-optomechanical experiment. A modelisation that qualitatively permits to understand the most important features in the system is discussed, knowing that a more involved one that take into-account the light-nanowire interaction (currently under study) permits to reach a quasi quantitative agreement with the experimental observations. The experimental setup is also described and we evaluate the optomechanical coupling strength achieved, in the ultrastrong coupling regime.

THE FIFTH CHAPTER investigates the optomechanical interaction between the intracavity light field and the nano-mechanical oscillator in the 2 directions. We first present how the nanowire can be used to investigate the intracavity field using optical cavity signals. This allows to evaluate and spatially map the $2D$ optomechanical coupling vector, as well as to identify the locations in the optical mode where the ultrastrong coupling regime arises. Then we investigate the interaction in the opposite direction and explore the optical force field applied on the nanowire by the intracavity field. Those measurements are based on a pump-probe technique realized with 2 separate lasers. The nanowire is then used to realize a fully three dimensional cartography of the optomechanical interaction, which is complementary to the above mentioned investigation.

THE SUMMARY presents possible future applications and developments arising from this work. Several questions have emerged for both experiments and will constitute the focus of future investigations, together with their joint integration in a single setup to explore the novel regime of single-photon cavity optomechanics.

Part I

INTRODUCTION

... I would like to relate briefly a supposedly true story, which may help support the argument. About 400 years ago, there lived a count in a small town in Germany. He was one of the benign counts, and he gave a large part of his income to the poor in his town. This was much appreciated, because poverty was abundant during medieval times, and there were epidemics of the plague which ravaged the country frequently. One day, the count met a strange man. He had a workbench and little laboratory in his house, and he labored hard during the daytime so that he could afford a few hours every evening to work in his laboratory. He ground small lenses from pieces of glass; he mounted the lenses in tubes, and he used these gadgets to look at very small objects. The count was particularly fascinated by the tiny creatures that could be observed with the strong magnification, and which he had never seen before. He invited the man to move with his laboratory to the castle, to become a member of the count's household, and to devote henceforth all his time to the development and perfection of his optical gadgets as a special employee of the count.

The townspeople, however, became angry when they realized that the count was wasting his money, as they thought, on a stunt without purpose. "We are suffering from this plague," they said, "while he is paying that man for a useless hobby!" But the count remained firm. "I give you as much as I can afford," he said, "but I will also support this man and his work, because I know that someday something will come out of it!"

Indeed, something very good came out of this work, and also out of similar work done by others at other places: the microscope. It is well known that the microscope has contributed more than any other invention to the progress of medicine, and that the elimination of the plague and many other contagious diseases from most parts of the world is largely a result of studies which the microscope made possible.

The count, by retaining some of his spending money for research and discovery, contributed far more to the relief of human suffering than he could have contributed by giving all he could possibly spare to his plague-ridden community...

— Ernst Stuhlinger, **"Why explore space?"**

1 ULTRA-SENSITIVE MEASUREMENTS IN OPTOMECHANICAL SYSTEMS

In this chapter we introduce the context and the state of the art of optomechanical experiments and force sensing. The basic concepts of cavity optomechanics and noise measurements, which will be extensively used across the manuscript, are explained. A brief description of the previous investigations in the group and some common notation that will repeatedly encounter in this work are also given.

CONTENTS

1.1 Optomechanical systems and measurements 4
1.2 Cavity Optomechanics 5
1.2.1 A mechanical resonator coupled to a thermal bath 6
The quantum harmonic oscillator 6
Coupling to the environment 7
The power spectral density 8
Position fluctuations 9
1.2.2 Principles of optomechanical coupling 11
Hamiltonian formulation 11
Optomechanical parameters and coupling regimes 12
1.2.3 Quantum limit in optical position sensing and the SQL 14
1.3 SiC nanowires ultrasensitive sensors 17
A 2*D* vectorial force sensor 18
Towards low-temperature experiments 20
Dispersive optomechanics with a nanowire 21

1.1 OPTOMECHANICAL SYSTEMS AND MEASUREMENTS

On May 20, 2019, four of the seven base units of the International System (SI), namely the kilogram, the ampere, the kelvin and the mole, were redefined by setting exact numerical values for the Planck constant (h), the elementary electric charge (e), the Boltzmann constant (k_B), and the Avogadro constant (N_A), respectively. The base units are the building block that we use to quantify our measurements, and measuring permits to explore and quantify novel physical observations. Starting from the Egyptian and the Roman sundial, going through the telescope of Galileo to arrive to the modern gravitational wave detectors, improving our measuring instruments has historically proven to be one of the best way to increase our knowledge of nature and to develop new technologies.

In recent years optomechanical systems have demonstrated to be a robust and versatile resource to push these limits further away [18, 221, 139, 41, 136, 240]. The origins and the essence of optomechanics can be found at the interface between the macro and the microscopic world, trying to fill the gap between classical and quantum mechanics. On one side, the pioneering work from Braginsky and Caves [28, 29, 30, 38, 36, 37] on interferometers paved the way to modern cavity optomechanics as well as to the recent experiment on gravitational waves detection. On the other, the innovative ideas of Arthur Ashkin [17] on the use of focused laser beam to trap and control dielectric particle, lead to the realization of optical tweezers (fundamental in nowadays biological science) which followed the development in laser cooling of ions and neutral atoms [252], culminating with the experimental realization of atomic Bose-Einstein condensates [10, 52] and lead to the development of experimental techniques which presents some analogy with the more recently developed optomechanical cooling. In between, recent advancements in fabrication technologies have allowed the flourishing of countless micro- and nano-mechanical devices, which have become the natural candidates for the realization of macroscopic quantum systems.

The motivations for developing the optomechanical research are multiple, but can be separated in two main families. On one hand, the need for precision measurements and the detection of weak signals, trying to overcome the limits imposed by thermal and quantum noises. The advances realized in the field of (continuous) quantum measurement [224, 241, 51, 263, 250, 46] lead to remarkable achievements, such as displacement sensing with an imprecision level at and beyond the standard quantum limit (SQL) [14, 194, 1, 133], as well as new sensitive record in the detection of forces [142], masses [213, 40, 180] or accelerations [107, 88]. On the other hand, a lot of efforts have been made in order to manipulate and detect mechanical motion in the quantum regime, trying to create non-classical states of light, mechanics, or both. For states with Gaussian statistics, the realization of both squeezed [178, 32, 166] and entangled [210, 160, 114] states has already been proven. In the case of non-Gaussian statistics, this has proven to be much more challenging. The generation of non-classical states usually requires a strong coupling condition, which motivates in particular the developments of systems that exhibit larger and larger single photon coupling strength (g_0) [145, 31, 116, 132, 42, 152].

Several impressive results related to the principle of optomechanics were achieved in the field over the last decade, such as the first detection of gravitational waves produced by two merging black holes [122] (see fig. 1.1a), the ground state cooling of a macroscopic mechanical object [39, 196] (see fig. 1.1b) or the observation of a quantum superposition of surface acoustic wave phonons [181] (see fig. 1.1c), which underline the continuing stimulating new efforts and ideas that can be expected when developing extreme sensors.

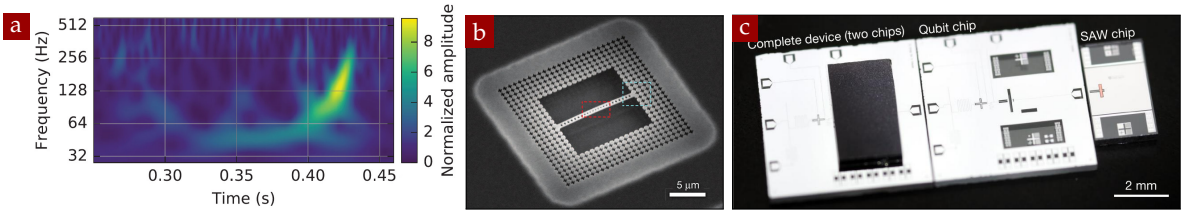

FIGURE 1.1 – Recent impressive results based on the principles of optomechanics: (a) the first detection of a gravitational wave [122]; (b) ground state cooling of a macroscopic mechanical object [39]; (c) quantum superposition of surface acoustic wave phonons [181].

In this work, by making use of ultrasensitive SiC nanowires, we will aim at improving the capacities of nanomechanical scanning force sensors, in particular by operating them in a cryogenic environment. We will also explore a novel optomechanical system in a configuration termed *"nanowire in the middle"* (of a small-volume fiber micro-cavity), where the interaction strength is so large that the single photon regime of cavity optomechanics becomes accessible.

1.2 CAVITY OPTOMECHANICS

Across the whole landscape of optomechanical approaches, cavity optomechanical systems are by far the most used and versatile, allowing to engineer their resonant properties to obtain very large interaction across a wide range of wavelengths, from the microwave to the optical regime.

The first experiments in cavity optomechanics date back to the '70s and the '80s [28, 29], both in the microwave and in the optical domain, with, among others, the first demonstrations of optomechanical bistability due to the radiation pressure force acting on a macroscopic end-mirror [63, 138, 87]. In the '90s, exploiting the intrinsic nonlinearity of the OM interaction, several works explored the possibility to generate squeezed state of light [72, 130], as well as to perform quantum non-demolition (QND) detection [157, 97, 90] or to allow the realization of nonclassical and entangled states [26, 129].

Optomechanical cooling was then proposed as a mean to approach the quantum ground state [131], subsequently realized experimentally in different ways (feedback cooling [48], photothermal cooling [137], radiation pressure cooling [15, 85, 182]). Since then, the domain expanded considerably and the OM coupling has been studied in a large variety of novel systems. Among these, we could find Fabry-Pérot cavities with suspended mirrors of kilogram-scale [2], whispering gallery microdisks, microtoroids or microspheres [209, 149, 201], membrane and nanorods inside optical cavities [197, 74], photonic crystals [67, 39, 179] and superconducting resonators [170, 195]. Also, the recently developed hybrid systems [16, 177, 214] present some analogies with optomechanical systems since they investigate the interaction between a mechanical degree of freedom and a two level system.

In the following pages we present the basic theoretical description of an optomechanical system, as well as the main regimes of interest.

1.2.1 A mechanical resonator coupled to a thermal bath

Here we introduce some of the concepts and notations used in the manuscript to describe the thermal noise of an harmonic oscillator coupled to a thermal bath, both in the classical and in the quantum framework. For the interested reader more on this subject can be found in [46, 18, 241, 257, 245, 173, 225, 263, 250, 51, 47, 269].

THE QUANTUM HARMONIC OSCILLATOR The precursor of most physical systems is the simple harmonic oscillator with position and impulsion operators x and p, a given mass M and a resonance frequency $\Omega_\mathrm{m}/2\pi$. It can be described by the Hamiltonian

$$H = \frac{p^2}{2M} + \frac{M\Omega_\mathrm{m}^2}{2}x^2. \tag{1.2.1}$$

Classic harmonic oscillator

The canonical equations read $\dot{x} = p/M$ and $\dot{p} = -M\Omega_\mathrm{m}^2 x$ and given the initial condition $x(0)$ and $p(0)$, the solutions can be expressed as

$$x(t) = x(0)\cos(\Omega_\mathrm{m}t) + p(0)\frac{1}{M\Omega_\mathrm{m}}\sin(\Omega_\mathrm{m}t) \tag{1.2.2a}$$

$$p(t) = p(0)\cos(\Omega_\mathrm{m}t) - x(0)M\Omega_\mathrm{m}\sin(\Omega_\mathrm{m}t). \tag{1.2.2b}$$

To obtain the equivalent quantum system, the canonical procedure consists in replacing in eq. (1.2.1) the classical variables with the equivalent operators $\hat{x}$ and $\hat{p}$, which satisfy the commutation relation

$$[\,\hat{x}\,,\hat{p}\,] = i\hbar. \tag{1.2.3}$$

For a given operator $\hat{A}$, we introduce its **expectation** value and its **uncertainty**, which are given by

$$\langle\hat{A}\rangle = \mathrm{tr}\{\hat{\rho}\hat{A}\} \qquad \text{and} \qquad \Delta A = \sqrt{\mathrm{tr}\{\hat{\rho}(\delta\hat{A})^2\}} = \sqrt{\langle\hat{A}^2\rangle - \langle\hat{A}\rangle^2}, \tag{1.2.4}$$

where $\hat{\rho}$ is the **density operator** and $\delta\hat{A} = \hat{A} - \langle\hat{A}\rangle$ is the **fluctuation operator**. For two non-commuting observables A and B it can be proven that

$$\Delta A \Delta B \geq \frac{1}{2}\left|\langle\,[\,\hat{A}\,,\hat{B}\,]\,\rangle\right|. \tag{1.2.5}$$

This is the mathematical expression of the well known Heisenberg's uncertainty principle [91]. If we now introduce the normalized position and momentum operators

$$\hat{X} = \hat{x}/x_\mathrm{zpf} \qquad \hat{P} = \hat{p}/p_\mathrm{zpf} \tag{1.2.6}$$

for which the commutation and uncertainty relations satisfy

$$[\,\hat{X}\,,\hat{P}\,] = 2i \qquad \text{and} \qquad \Delta X \Delta P \geq 1 \tag{1.2.7}$$

and where we have defined the **zero-point-fluctuations**

$$x_\mathrm{zpf} = \sqrt{\frac{\hbar}{2M\Omega_\mathrm{m}}} \qquad \text{and} \qquad p_\mathrm{zpf} = \sqrt{\frac{\hbar M\Omega_\mathrm{m}}{2}}, \tag{1.2.8}$$

the Hamiltonian can be written as

Quantum harmonic oscillator

$$\hat{H} = \frac{\hbar\Omega_{\mathrm{m}}}{4}\left(\hat{X}^2 + \hat{P}^2\right) \tag{1.2.9}$$

The minimum of its expectation value

$$\langle\hat{H}\rangle = \frac{\hbar\Omega_{\mathrm{m}}}{4}\left(\Delta X^2 + \Delta P^2 + \langle\hat{X}\rangle^2 + \langle\hat{P}\rangle^2\right) \tag{1.2.10}$$

is obtain for $\Delta X = \Delta P = 1$ and $\langle\hat{X}\rangle = \langle\hat{P}\rangle = 0$. While in the classical case the harmonic oscillator is allowed to have zero energy at rest, from the previous expression we can see that the minimum energy of the quantum oscillator is given by $E_0 = \hbar\Omega_{\mathrm{m}}/2$. This conveys the fact that position and momentum can not be exactly zero: even in the vacuum state they present some residual quantum fluctuations which contribute to the ground state energy of the oscillator. These are called vacuum or **zero-point fluctuations** whose spreading is given by eq. (1.2.8).

The previous Hamiltonian can also be expressed in term of the creation and annihilation operators $\hat{b}$ and $\hat{b}^\dagger$, making use of the relations

$$\hat{X} = \hat{b}^\dagger + \hat{b} \qquad \hat{P} = i(\hat{b}^\dagger - \hat{b}) \qquad [\hat{b}, \hat{b}^\dagger] = 1 \tag{1.2.11}$$

so that we obtain

$$\hat{H} = \hbar\Omega_{\mathrm{m}}(\hat{b}^\dagger\hat{b} + \frac{1}{2}). \tag{1.2.12}$$

The number operator $\hat{N} = \hat{b}^\dagger\hat{b}$ presents a discrete spectrum made of positive integers, n, which represent the number of energy *quanta* associated to each eigenmode $|n\rangle$. These eigenvectors are commonly referred to as Fock states, they present a discrete energy spectrum and verify $\hat{H}\,|n\rangle = E_n\,|n\rangle$ with $E_n = \hbar\Omega_{\mathrm{m}}\left(n + \frac{1}{2}\right)$. The energy spacing between the levels of the harmonic ladder is constant and given by $\hbar\Omega_{\mathrm{m}}$. Noted $\Psi_n(x)$ the wave function of the n state, the expectation value of the position operator is $\langle\hat{x}\rangle_n = \int x|\Psi_n(x)|^2 dx = 0$, while then uncertainty is $\Delta\hat{x}_n^2 = \hbar/M\Omega_{\mathrm{m}}(n + 1/2)$. For the ground state we thus see that this is equal to the zero-point-fluctuations: $\Delta\hat{x}_0 = x_{\mathrm{zpf}}$.

COUPLING TO THE ENVIRONMENT Any real system can never be considered completely isolated from the surrounding environment. If we model the latter as an infinite ensemble of harmonic oscillators coupled to our system by an interacting term $\bar{H}_c$, the result is that the proper states of the system are not the ones of the free harmonic oscillator anymore. In other words, it is not possible to factorize the system states between an environment and an oscillator counterparts. Additionally, in most situations the proper state of the environment is not known or not accessible, resulting in missing information to describe the system and its evolution. Nonetheless, if we describe it as a statistic mixture of its different proper states, thus as a system in a thermodynamic equilibrium state at temperature T, we can characterize it by means of the density operator

$$\hat{\rho} = \frac{1}{Z}e^{-\hat{H}/k_{\mathrm{B}}T}, \tag{1.2.13}$$

where k_{B} is the Boltzmann constant and Z the partition function to ensure the normalization:

$$Z = \sum_0^\infty e^{-(n+1/2)\hbar\Omega_{\mathrm{m}}/k_{\mathrm{B}}T} = \frac{e^{-\hbar\Omega_{\mathrm{m}}/2k_{\mathrm{B}}T}}{1 - e^{-\hbar\Omega_{\mathrm{m}}/k_{\mathrm{B}}T}} \tag{1.2.14}$$

The average energy of the oscillator will thus be given by

$$\langle \hat{H} \rangle = \mathrm{tr}\{\hat{\rho}\hat{H}\} = \hbar\Omega_\mathrm{m}(n_T + 1/2) \qquad \text{with} \qquad n_T = \frac{1}{e^{\hbar\Omega_\mathrm{m}/k_\mathrm{B}T} - 1}. \tag{1.2.15}$$

n_T is the Bose-Einstein occupation factor: it is linked to the average energy of the oscillator at equilibrium and depicts the average number of thermal phonons.

It is important to compare this result to the classical case for which, as a consequence of the equipartition theorem, the energy of the oscillator is given by $\langle H \rangle_\mathrm{class} = k_\mathrm{B}T$. If we define the quantum temperature T_Q as

$$k_\mathrm{B}T_Q = \hbar\Omega_\mathrm{m}, \tag{1.2.16}$$

we see that for $T \gg T_Q$, the quantum expression converges towards the classical one. On the contrary, for temperatures $T \leq T_Q$ the energy tends to $\langle \hat{H} \rangle \simeq \hbar\Omega_\mathrm{m}/2 = E_0$, meaning that the oscillator is in its quantum ground state and that in this temperature range the system is dominated by its quantum properties.

THE POWER SPECTRAL DENSITY We saw that noise is something that naturally emerges in the quantum case. Furthermore, it can arise from the interaction of the oscillator with the environment (a thermal bath or the measurement setup), but can also simply represent a technical noise. Let us define a random signal $V(t)$ characterized by a zero mean value, $\langle V(t) \rangle = 0$. We can define its temporal **autocorrelation** function, which describes whether its fluctuations are statistically correlated or independent:

$$C_\mathrm{VV}(t - t') = \langle V(t)V(t') \rangle. \tag{1.2.17}$$

If the process is stationary (i.e. the statistical properties are time translation invariant), C_VV only depends on the time differences ($t - t' = \tau$), so the previous expression can be rewritten as

$$C_\mathrm{VV}(\tau) = \langle V(t)V(t+\tau) \rangle \tag{1.2.18}$$

Furthermore if the above process is Gaussian distributed and its characteristic correlation time τ_c is small compared to the measurement time T [108], this is a reasonable approximation for the case of a Brownian noise or that of a system subjected to a Langevin force, which are the cases we are interested in. Given the windowed Fourier transform[1] of our signal $V_T[\Omega]$, if we define the **power spectral density (PSD)** as the ensemble average quantity $S_\mathrm{VV}[\Omega] \equiv \lim_{T\to\infty}\langle |V_T[\Omega]|^2 \rangle$ and we make use of the Wiener-Khinchin theorem[2], we obtain the important result that the spectral density and the autocorrelation function are the Fourier transform of one another, namely

The power spectral density

$$S_\mathrm{VV}[\Omega] = \int_{-\infty}^{\infty} d\tau\, e^{i\Omega\tau}\, C_\mathrm{VV}(\tau) \qquad \text{and} \qquad C_\mathrm{VV}(\tau) = \int_{-\infty}^{\infty} \frac{d\Omega}{2\pi}\, e^{-i\Omega\tau}\, S_\mathrm{VV}[\Omega] \tag{1.2.19}$$

A simple example of the application of this equations is that of "white noise", characterized be a flat spectrum and auto-correlation time which tends to 0:

$$S_\mathrm{VV}[\Omega] = \kappa^2 \qquad \text{and} \qquad C_\mathrm{VV}(\tau) = \kappa^2\delta(\tau) \tag{1.2.20}$$

[1] The windowed Fourier transform is defined as $V_T[\Omega] = \frac{1}{\sqrt{T}}\int_{-T/2}^{T/2} dt\, e^{i\Omega t}\, V(t)$.

[2] A derivation of the theorem can be find in the appendix of [46].

where κ is a constant.

For the case of the simple harmonic oscillator, if we compute the autocorrelation function of eq. (1.2.2a) we obtain:

$$C_{xx}(\tau) = \langle x(\tau)x(0)\rangle = \langle x(0)x(0)\rangle \cos(\Omega_m t) + \langle p(0)x(0)\rangle \frac{1}{M\Omega_m} \sin(\Omega_m t); \tag{1.2.21}$$

because classically there are no correlations between position and momentum and, making use of the equipartition theorem $\frac{1}{2}M\Omega_m^2\langle x^2\rangle = \frac{1}{2}k_B T$, we get

$$C_{xx}(\tau) = \frac{k_B T}{M\Omega_m^2} \cos(\Omega_m \tau) \tag{1.2.22}$$

and for the spectral density

$$S_{xx}[\Omega] = \pi \frac{k_B T}{M\Omega_m^2} \left[\delta(\Omega - \Omega_m) + \delta(\Omega + \Omega_m)\right]. \tag{1.2.23}$$

Notice that this last expression is **symmetric in frequency**, as a consequence of the fact that being $x(t)$ a classical real-value signal, $C_{xx}(t)$ is always real and it is symmetric in time ($x(t)$ commutes with itself at other times: $\langle x(t)x(t')\rangle = \langle x(t')x(t)\rangle$).

POSITION FLUCTUATIONS To completely describe a real system, it is thus necessary to describe its coupling to the environment. Usually this interaction is decribed by the Langevin formalism. It consists in two aspects: first it opens an energy loss channel, which will be modelled by a viscous damping term, Γ, then this new channel can also reinject fluctuations in the system, which will be modelled by a random Langevin force δF_{th}. The magnitude of both effects will be coupled by the fluctuation dissipation theorem. The equation of motion of the nanowire thus follows a Langevin equation, where its position fluctuations δx is given by:

$$\delta\ddot{x}(t) + \Omega_m^2 \delta x(t) + \Gamma \delta\dot{x}(t) = \frac{\delta F_{th}(t)}{M}. \tag{1.2.24}$$

Here the random Langevin force has a zero average value and a white noise character traducing the absence of memory in the bath over the mechanical time scales. Taking the Fourier transform of this equation permits to introduce the **mechanical susceptibility** of the oscillator:

$$\delta x[\Omega] = \chi[\Omega]\delta F_{th}[\Omega] \qquad \chi[\Omega] = \frac{1}{M(\Omega_m^2 - \Omega^2 - i\Omega\Gamma)}. \tag{1.2.25}$$

The Langevin force thus drives the oscillator into motion. In the framework of the linear response theory, the fluctuation-dissipation theorem permits to connect the mechanical susceptibility of the oscillator and the noise spectral density of the Langevin Force according to[3]:

$$S_{F_{th}}[\Omega] = -\frac{2k_B T}{\Omega} \operatorname{Im}\left[\frac{1}{\chi[\Omega]}\right] \qquad S_{\delta x}[\Omega] = \frac{2k_B T}{\Omega} \operatorname{Im}\chi[\Omega]. \tag{1.2.26}$$

[3] for a temporal variable $x(t)$ we employ the convention for the Fourier components : $x[\Omega] \equiv \int dt x(t) e^{i\Omega t}$ and $x(t) \equiv 1/2\pi \int d\Omega x[\Omega] e^{-i\Omega t}$, then the noise spectral density is defined as : $\langle \delta x[\Omega]\delta x[\Omega']\rangle = 2\pi\delta(\Omega + \Omega')S_{\delta x}[\Omega]$ where the average is taken on multiple realisations of the noise process or assuming the ergodic theorem holds, on sufficiently long time scales.

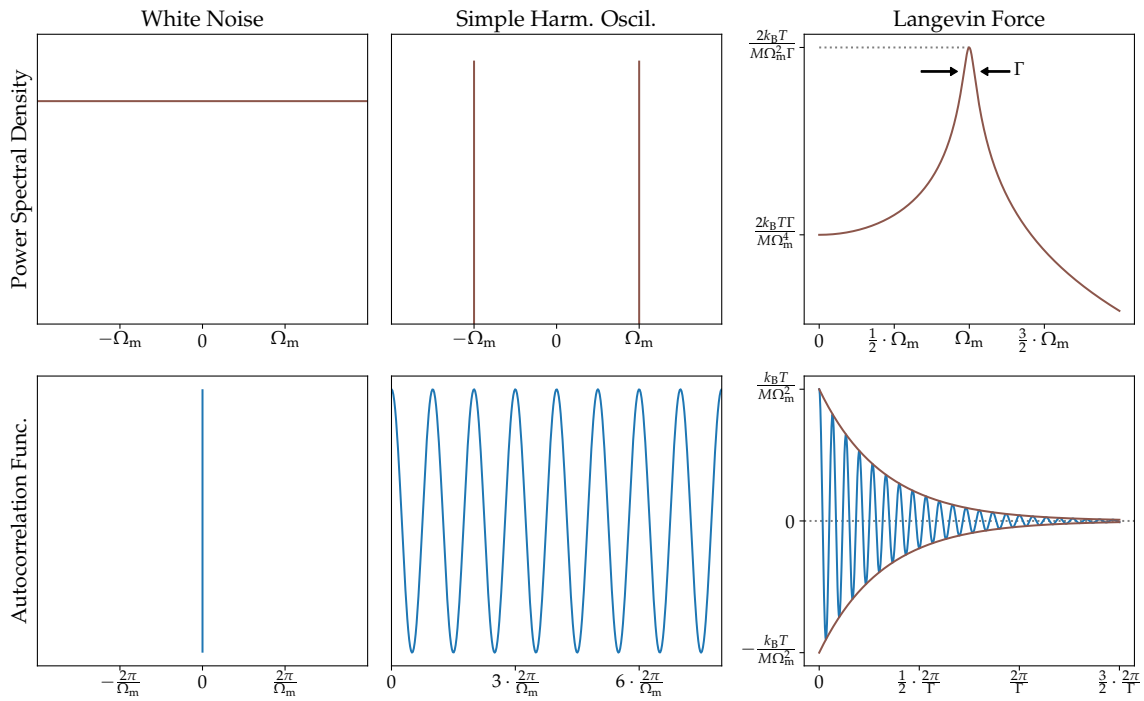

FIGURE 1.2 – Power spectral density and autocorrelation function for a white noise, for a simple uncoupled harmonic oscillator and for an harmonic oscillator coupled to a thermal bath.

Making use of the previous expressions, the PSD of the Langevin force will be given by

$$S_{F_{\text{th}}}[\Omega] = 2M\Gamma k_B T, \tag{1.2.27}$$

while we can express the power spectral density of the position fluctuations in a way that we will extensively use in the following:

$$S_{\delta x}[\Omega] = \frac{2\Gamma k_B T}{M\big((\Omega_m^2 - \Omega^2)^2 + \Gamma^2\Omega^2\big)}. \tag{1.2.28}$$

Notice how this equation depends directly on the T/M ratio and can be used to extract the temperature of the resonator if its effective mass is known, and vice-versa. Using eq. (1.2.19), it is also possible to compute the autocorrelation function:

$$C_{\delta x}(\tau) \equiv \langle \delta x(t)\delta x(t+\tau)\rangle = \frac{k_B T}{M\Omega_m^2} e^{-\frac{\Gamma\tau}{2}} \left(\cos\Omega_c\tau + \frac{\Gamma}{2\Omega_c}\sin\Omega_c\tau\right) \tag{1.2.29}$$

where $\Omega_c^2 \equiv \Omega_m^2 - \Gamma^2/4$, see fig. 1.2.

From the above expression, we can also compute the variance of the oscillator position fluctuations, which is connected to the area of the noise spectral density and verifies the equipartition theorem:

$$\Delta x_{\text{th}}^2 \equiv \int_{-\infty}^{+\infty} \frac{d\Omega}{2\pi} S_{\delta x}[\Omega] = \frac{k_B T}{M\Omega_m^2}; \tag{1.2.30}$$

this spatial spreading of the thermal noise has a direct impact on the spatial resolution of scanning force sensors. Also, if one wants to detect a monochromatic force, the thermal noise will represent a practical limit to the oscillator force sensitity, and one will have to average a sufficient amount of time in order to reveal weak forces. The smallest mea-

surable force depends on the resolution bandwidth employed (RBW), and amounts to :

$$\delta F_{\min} = \sqrt{\mathrm{RBW} \times S_{F_{\mathrm{th}}}[\Omega]} = \sqrt{\mathrm{RBW} \times 2M\Gamma k_{\mathrm{B}} T} \tag{1.2.31}$$

from which we clearly see that the lower the temperature, the higher is the force sensitivity we can attain.

We note that it is possible to extrapolate this classical description to mechanical systems approaching their quantum ground state at the condition to replace the force noise spectral density by its quantum counterpart:

$$S_{\mathrm{FF}} = \hbar \left| \mathrm{Im} \frac{1}{\chi[\Omega]} \right| \coth\left(\frac{\hbar|\Omega|}{2k_{\mathrm{B}}T}\right). \tag{1.2.32}$$

1.2.2 Principles of optomechanical coupling

In its most simple and ideal formulation, an optomechanical system investigates the interaction between a single optical mode of an optical cavity with frequency ω_{cav} and one mechanical normal mode with frequency Ω_{m}. Those two subsystems are evolving at very different frequencies, and the coupling mechanism is a parametric interaction where the cavity frequency depends on the position x of the mechanical resonator $\omega_{\mathrm{cav}} = \omega_{\mathrm{cav}}(x)$ and reciprocally, the light field applies a force on the oscillator, proportional to the intracavity intensity. In this sense the optomechanical coupling is a "dispersive" mechanism. It can take different forms, such as direct momentum transfer upon reflection in Fabry-Pérot with one movable mirror and associated approaches, or by making use of near-fields effects when nano-resonators are approached in the evanescent field of an optical micro-resonator, or by inserting the nano-resonator in a high finesse (micro-)cavity (membrane in the middle). Both the mechanical and the cavity modes are considered as harmonic oscillators, with loss rates Γ and κ respectively, as shown in fig. 1.3. We will not discuss it here, but we note that if the latter also arises with the resonator position ($\kappa = \kappa(x)$), this is usually referred to as "dissipative" coupling.

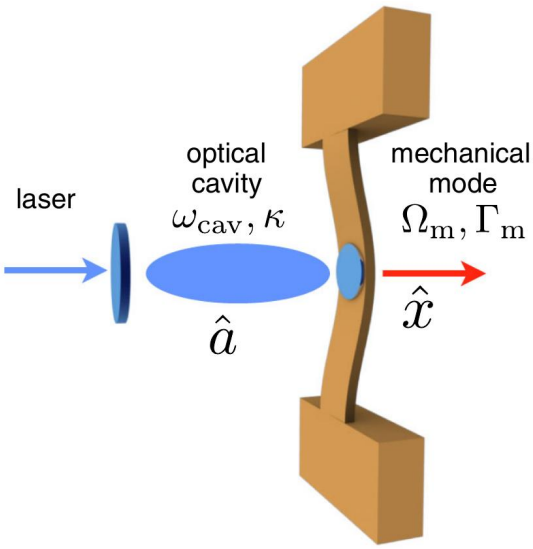

FIGURE 1.3 – Scheme of a simple ideal optomechanical system. Image from [18].

HAMILTONIAN FORMULATION The system can be described by the Hamiltonian

$$\hat{H}_{\mathrm{OM}} = \hbar\omega_{\mathrm{cav}}(\hat{x})\hat{a}^{\dagger}\hat{a} + \hbar\Omega_{\mathrm{m}}\hat{b}^{\dagger}\hat{b}, \tag{1.2.33}$$

where $\hat{a}$ and $\hat{b}$ are the annihilation operators of the cavity and mechanical modes. Because we are usually interested only in small mechanical displacements, it is possible to Taylor expand the above expression, and if we only retain the first order terms and introduce $\hat{x} = x_{\mathrm{zpf}}(\hat{b} + \hat{b}^{\dagger})$, we can recast the Hamiltonian into

$$\hat{H}_{\mathrm{OM}} = \hbar\omega_{\mathrm{cav}}\hat{a}^{\dagger}\hat{a} + \hbar\Omega_{\mathrm{m}}\hat{b}^{\dagger}\hat{b} + \hbar g_0 \hat{a}^{\dagger}\hat{a}(\hat{b} + \hat{b}^{\dagger}) \equiv \hat{H}_0 + \hat{H}_{\mathrm{int}}, \tag{1.2.34}$$

where we have introduced the *single-photon optomechanical coupling strength* g_0,

$$g_0 = Gx_{\text{zpf}} = \frac{\partial \omega_{\text{cav}}}{\partial x} x_{\text{zpf}} = \frac{\partial \omega_{\text{cav}}}{\partial x} \sqrt{\frac{\hbar}{2M\Omega_{\text{m}}}}, \tag{1.2.35}$$

G being the optical frequency shift per displacement. A more detailed derivation can be found in [113]. Through this formulation, it is clear that at a fundamental level the interaction between a movable mirror and the radiation field is a **nonlinear** process, involving three operators; in other words, the optomechanical interaction mediates an optical Kerr-type nonlinearity.

Because most of the systems that have been studied up to now present a relatively small coupling strength g_0, it is necessary to operate with many photons in order to enhance the interaction strength. Thus it is common to introduce a linearized approximation of this Hamiltonian. By splitting the cavity field into the average coherent amplitude ($\langle \hat{a} \rangle = \bar{\alpha} = \sqrt{\bar{n}_{\text{cav}}}$) and a fluctuating term, $\hat{a} = \bar{\alpha} + \delta\hat{a}$, and keeping only the first order terms, the interaction Hamiltonian now becomes

$$\hat{H}_{\text{int}}^{(\text{lin})} = -\hbar g_0 \sqrt{\bar{n}_{\text{cav}}} (\delta\hat{a}^\dagger + \delta\hat{a})(\hat{b} + \hat{b}^\dagger) \tag{1.2.36}$$

Here we can see that the interaction is now mediated by an effective coupling strength $g = g_0\sqrt{\bar{n}_{\text{cav}}}$, where the single-photon coupling is enhanced by the mean field in the cavity. In this description, the OM system can be seen as a linear element mixing mechanical and optical signals.

The linearized approach has the advantage that the equations of motion can be solved analytically and has proven to be capable of describing most of the aspects of the OM interaction, from the optomechanical cooling to the strong-coupling regime, from the optomechanically induced transparency to the displacement detection down to the SQL, etc. However, this linearized approximation will find its limits when operating with largely coupled mechanical oscillators, in which the strength of the fluctuations of the EM field become comparable to the mean field.

OPTOMECHANICAL PARAMETERS AND COUPLING REGIMES The magnitude of the different parameters that characterize an OM system allow a generic classification, leading to different sets of possible experimental outcomes. The starting point for almost all cases is the assumption of working with a high-quality mechanical oscillator, meaning $\Omega_{\text{m}} \gg \Gamma$. In case the mechanical frequency is also larger than the optical linewidth κ, the system enters in the *resolved sideband regime*, meaning that the mechanical modulation of the cavity generates sidebands that are spectrally resolved with respect to cavity linewidth. This is one of the usual requirement to obtain a pure optomechanical cooling capable of reaching the ground state, when the Doppler temperature is smaller than a single excitation energy: $\hbar\kappa < \hbar\Omega_{\text{m}}$. The opposite case ($\kappa \gg \Omega_{\text{m}}$) is the *adiabatic cavity regime*, which is also the one characterizing this work. In this regime the response of the cavity to the mechanical motion or to any external perturbation is much faster than the mechanical frequency and thus of the mechanical decay time, so that it can be assumed to instantaneously reach its steady state value. In such a configuration, most of the second order optomechanical interaction mechanisms occur when a parameter becomes dependent on the oscillator's position. In that case the oscillator will evolve in a spatially modulated force field, leading to a dynamical back-action having a different origin than the original scheme.

Considering the magnitude of the dressed coupling strength g, we can introduce the (resolved) strong-coupling regime that verifies $g \gg \kappa$. In this case, for sufficiently high driving power it is possible to assist to an hybridisation between the optical and the mechanical modes, which give rise to two new modes splitted by $2g$. This can also be viewed as a result of a loss of efficiency of the optomechanical interaction for mechanical frequencies located outside of the cavity linewidth window centered on the mechanical frequency. The phenomenon of optomechanically-induced transparency can also be obtained in similar conditions. This regime has been extensively explored experimentally and is represented by the zone 6 in fig. 1.4.

If we now consider larger values of the more fundamental single-photon-coupling strength g_0, interesting regimes appear, but not yet experimentally achieved, leading to non-linearities at the single photon level. g_0 is considered "large" when the steady-state displacement produced by a single photon in the cavity is larger than the zero-point-fluctuation of the mechanical oscillator. A single photonic excitation ($\langle \hat{a}^\dagger \hat{a} \rangle$) generates an optical force of $F^{(1)} = -\hbar g_0 / x_{\mathrm{zpf}}$ which causes a static displacement of $\delta x^{(1)} = F^{(1)}/M\Omega_{\mathrm{m}}^2 = 2g_0/\Omega_{\mathrm{m}} x_{\mathrm{zpf}}$. Requiring to have $\delta x^{(1)} > x_{\mathrm{zpf}}$ is then equivalent to require $g_0 > \Omega_{\mathrm{m}}/2$: this is defined as the *ultra-strong coupling* (USC) regime of the optomechanical parametric interaction. We note that this criteria is defined for a parametric interaction, and has nothing to do with the ultrastrong coupling regime of a transverse interaction in the Jaynes-Cummings picture, achieved when the Rabi frequency approaches the qubit transition frequency.

The single-photon coupling can also be compared to the cavity decay rate κ: the ratio g_0/κ is know as the "granularity parameter", meaning that for value greater than one it allows to discriminate the granularity of the photon streams. An alternative way to explain this inequality is that the coupling strength is so strong that the presence of one single phonon would be enough to shift the optical frequency by more than one cavity linewidth.

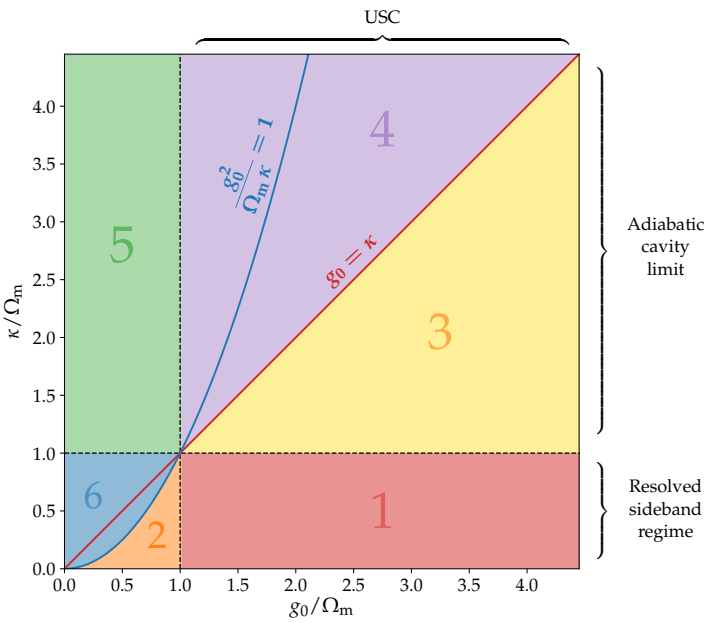

FIGURE 1.4 – Schematic representation of the different OM regimes as a function of the ratio between the three main parameters characterizing the OM interaction, g_0, Ω_{m} and κ.

OM regimes	Parameters
Strong-coupling	$g = g_0\sqrt{\bar{n}_{\mathrm{cav}}} \gg \kappa$
Resolved strong-coupling	$g \gg \kappa$ $\Omega_{\mathrm{m}} \gg \kappa$
USC	$g_0 \gg \Omega_{\mathrm{m}}$
Single-photon OM coupling	$\Omega_{\mathrm{m}} \gg \kappa$ $g_0^2/\Omega_{\mathrm{m}}\kappa \gg 1$

TABLE 1.1 – The OM regimes for different values of g_0, Ω_{m} and κ.

The last relation we want to examine is connected to the *single-photon blockade parameter* $D = g_0^2/\Omega_m\kappa$. The presence of a single photon in the cavity mode creates a static deflection of the oscillator $\delta x^{(1)}$, which in turn generates a parametric cavity shift given by $\delta\omega_{\text{cav}}^{(1)} = g_0\delta x^{(1)} = 2D\kappa$, which then exceeds the cavity linewidth if D is larger than one. It is also called "strong dispersive coupling condition" and shows the condition for resolving the optomechanical Kerr-like nonlinearity in the cavity spectrum. When this ratio is bigger than one and the system is in the resolved sideband regime, a single photon in the cavity mode can shift the resonance frequency sufficiently so that a second photon can not enter anymore. This regime can also be called a "photon turnstile". This regime is represented in fig. 1.4 by the zones 1 and 2. Zone 1 satisfy the additional requirement $g_0 \gg \Omega_m \gg \kappa$ and allows the creation of macroscopic mechanical cat states [221, 119].

It is worth mentioning that it may not always be desirable to operate in the resolve sideband regime, especially when quantum optics applications are targeted. We will discuss in more detail in section 5.3.3 some mechanisms that arise in the USC regime when working in the adiabatic cavity limit. For a more detailed description of these exotic regimes, see [18, 221, 240, 167, 119]. We note however that this regimes have not yet been explored experimentally with massive oscillators, but it is worth mentioning the optomechanical implementations based on collective atomic motional resonances in high-finesse optical cavities [145, 31] where such exotic regimes are at play.

1.2.3 Quantum limit in optical position sensing and the standard quantum limit

Exploring the ultimate limits of sensitivity for an optical position readout [241] and the related **quantum noise** requires to take into account the quantum nature of the meter light field.

The pump laser can be described by a pure *coherent state*, defined as

$$\hat{a}\,|\alpha\rangle = \alpha\,|\alpha\rangle \qquad\qquad |\alpha\rangle \equiv \sum_{n=0}^{\infty} e^{-|\alpha|^2/2}\frac{\alpha^n}{\sqrt{n!}}\,|n\rangle \tag{1.2.37}$$

where α is a complex number describing the amplitude and the phase of the electric field, and $|n\rangle$ is the eigenvector of the *number operator* $\hat{N} = \hat{a}^\dagger\hat{a}$ for light. For $\alpha = 0$ this is nothing but the vacuum state. A coherent state presents an intensity distribution which follows a Poissoninan distribution, and verifies $(\Delta N)^2 = |\alpha|^2 = \overline{N}$.

A coherent state is formally a vacuum state displaced by the mean field α in the quadrature space. It thus presents the same fluctuation disk as the vacuum state. Its phase fluctuations $\Delta\theta$ are connected to the angle with which the uncertainty disk is seen from the center of the quadrature space, which decreases as the mean field increases, so that the phase and intensity variances verify

$$(\Delta\theta)^2 = \frac{1}{4\overline{N}}, \quad (\Delta N)^2 = \overline{N} \quad \Rightarrow \quad \Delta N\Delta\theta = \frac{1}{2}. \tag{1.2.38}$$

Similarly, if we consider an average flux of photons $\Phi = \overline{\dot{N}}$ arriving on our detector, the fluctuations of the phase and amplitude noises are white and uncorrelated, with a noise spectral density given by:

$$S_{\theta\theta} = \frac{1}{4\Phi}, \quad S_{\Phi\Phi} = \Phi \quad \Rightarrow \quad \sqrt{S_{\Phi\Phi}S_{\theta\theta}} = \frac{1}{2}. \tag{1.2.39}$$

To continuously detect the position of an oscillator, we can monitor the phase fluctuations imprinted on the reflected beam. If the oscillator moves by a distance δx, the phase is shifted by $\delta\theta = 2k\delta x = \frac{4\pi}{\lambda}\delta x$. This means that quantum phase fluctuations impose a limit on the smallest position fluctuation that can be detected. We can express this limit in term of equivalent noise spectral density for the position readout, given by

$$S_{\delta x}^{\text{shot}} = \frac{S_{\theta\theta}}{4k^2} = \frac{1}{16k^2\Phi}. \tag{1.2.40}$$

This is called the **measurement imprecision**, caused by the shot-noise of the photons impinging *on the detector* and it is inversely proportional to the photons flux. Each photon fully reflected on the oscillator also transfers a momentum $2\hbar k$ to the oscillator, which is the origin of the radiation pressure force. The fluctuations in the photon number impinging *on the oscillator* are thus responsible for a fluctuation of the optical force, causing a so called random **back-action force noise**, since this process can be viewed as the fundamental counterpart of the measurement process that perturbs the position to detect. The power spectral density of this fluctuating force is then given by

$$S_{\text{F}}^{\text{qba}} = 4\hbar^2k^2S_{\Phi\Phi} = 4\hbar^2k^2\Phi. \tag{1.2.41}$$

Those expressions verify

$$\sqrt{S_{\text{F}}^{\text{qba}}S_{\delta x}^{\text{shot}}} = \hbar/2, \tag{1.2.42}$$

which represents a lower bound for an ideal (quantum limited) position sensor.

If we now sum up all the measurements noises involved in the position readout, we obtain for the estimator δx_{tot}:

$$\delta x_{\text{tot}} = \delta x_{\text{signal}} + \delta x_{\text{shot}} + \delta x_{\text{qba}} \tag{1.2.43}$$

where the different terms are respectively the signal one wants to detect, the imprecision noise and the radiation pressure noise. Since the two latter terms are proportional to the phase and intensity fluctuations of the meter beam, which are uncorrelated, and in principle also uncorrelated with the signal to detect, the limiting noise spectral density can be written as:

$$S_{\delta x}^{\text{min}}[\Omega] = S_x^{\text{shot}} + |\chi[\Omega]|^2 S_F^{\text{qba}} = \frac{1}{16k^2\Phi} + 4\hbar^2k^2 |\chi[\Omega]|^2 \Phi. \tag{1.2.44}$$

While the imprecision noise decreases with the injected optical power, the radiation pressure noise instead increases, so there exists a minimal limiting noise called the *Standard Quantum Limit*, obtained for an injected flux of

$$\Phi_{\text{SQL}} = \frac{1}{8\hbar k^2 |\chi[\Omega]|} \tag{1.2.45}$$

which amounts to

$$S_{\delta x}^{\text{SQL}} = \hbar |\chi[\Omega]|. \tag{1.2.46}$$

This expression takes a very simple form, and is only connected to the mechanical susceptibility of the oscillator. The interplay of optical quantum noises is of course modified when employing a Fabry-Perot cavity, the power needed to reach the SQL is decreased by a factor of $\mathcal{F}^2$ ($\mathcal{F}$ being the finesse of the cavity) due to the buildup of the intracavity field, but it does not change the expression of the SQL. Operating with very sensitive

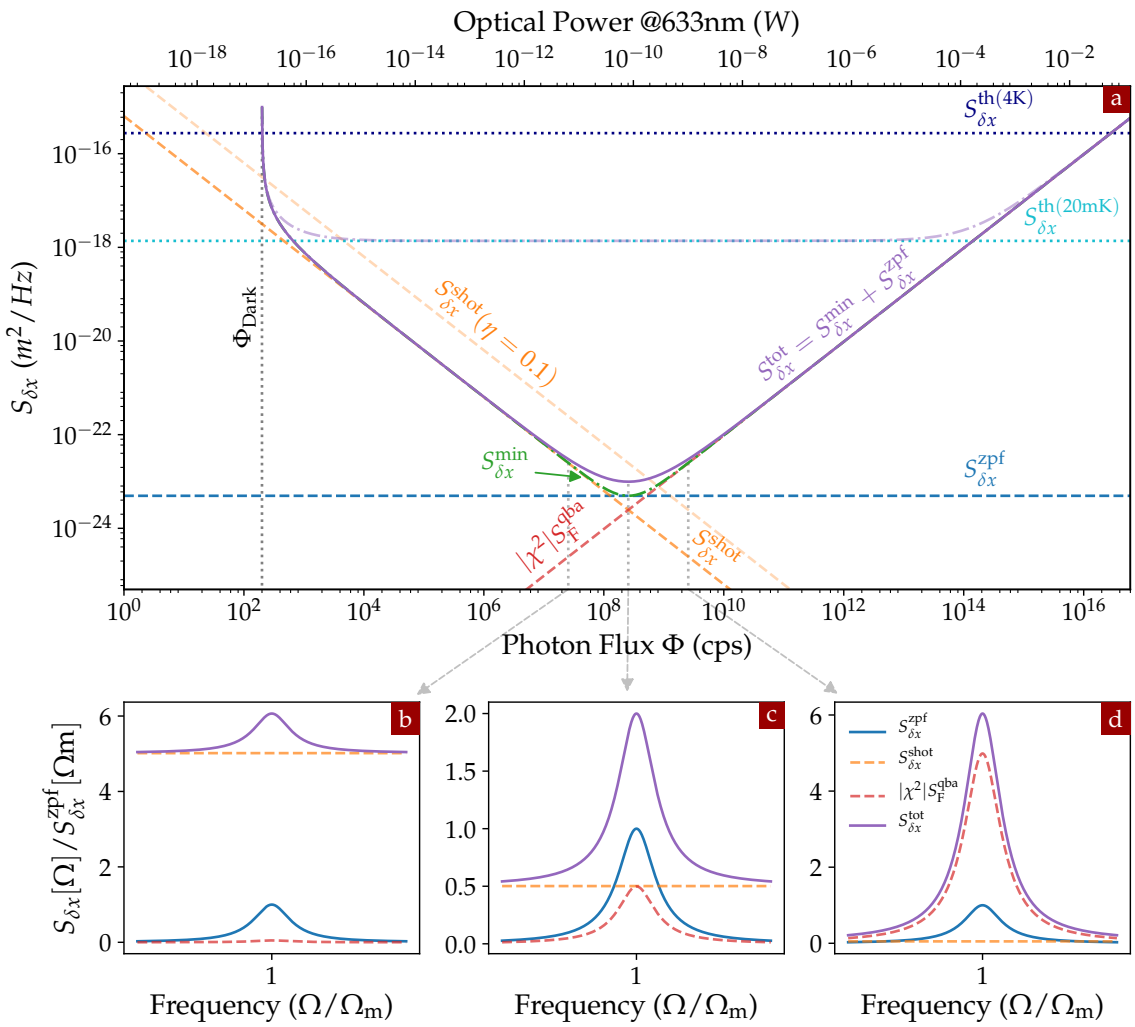

FIGURE 1.5 – The standard quantum limit for the position detection of the vibrations of a nanowire with a resonant frequency $\Omega_{\rm m}/2\pi = 3\,$kHz, a quality factor $Q = 1 \times 10^5$, effective mass $M_{\rm eff} = 6 \times 10^{-15}\,$kg and assuming that it behaves as a perfect mirro. (a) different noise contributions as a function of the photon flux arriving on the detector, including the imprecision noise, the back-action noise, the zero-point-fluctuations and the thermal noise at 20 mK and 4 K. The effect on the shot-noise of a lower efficiency and of the dark count of the detector are also shown. The comparison of the different noise contributions in frequency space is also show for the case of a photon flux lower (b), equal (c) or higher (d) than the optimal value $\Phi_{\rm SQL}$.

force sensors is thus an interesting avenue to realize strongly coupled optomechanical systems operating at the fundamental limits of quantum measurement.

To put numbers on the above considerations, fig. 1.5 represents the different noise contributions expected for a Michelson like readout of the vibrations of a typical nanowire employed in this work. Even if this assumes that the nanowire behaves as a perfect mirror, which is far from reality, the numbers are pretty encouraging and it could be possible to detect its thermal noise at 20 mK with a readout power of well below the femtowatt level. This however raises two important experimental challenges, which are first to operate with such low optical fluxes without being limited by the dark noise of the detectors, and second to realize optics operating at such low temperatures. This will be the topic of chapters 2 and 3 of the manuscript.

1.3 SIC NANOWIRES ULTRASENSITIVE SENSORS

Silicon-carbide nanowires are extremely interesting mechanical oscillators that, thanks to their nanometric cross-section but large refractive index, can be efficiently readout by simple optical means. Indeed their optical cross section can be significantly larger than their actual diameter, since they can host internal optical resonances. These are called "Mie resonances" [238]. Following several studies from the PNEC (*Physique des Nanostructures et Emission de Champ*) group at ILM (*Institut Lumière Matière*) in Lyon, which has extensively investigated their physical properties [151], the nanowires have been employed in the Néel group during the past ten years, in order to develop new strategies to use them as ultrasensitive force sensors or as part of novel hybrid optomechanical systems [16, 156].

In these experiments, a diamond nano-crystal containing a single crystal defect (a nitrogen-vacancy center) was attached to the free extremity of the NW (see fig. 1.6a). The goal was to investigate the parametric coupling to a non-classical two-level system, the spin qubit which could act as a quantum force transducer: in presence of a strong magnetic field gradient, the state of the movable spin becomes dependent on the oscillator's position, thus giving birth to a spin-dependent force, as in a Stern and Gerlach experiment, which is in principle the building brick required to generate non-classical states of motion. Immersing the system in a magnetic field gradient, it was possible to probe a quantitative signature of the nanoresonator motion directly imprinted on the electronic spin dynamics. In a following work [156], during the thesis of S. Rohr [175, 234], the signature of a phononic Mollow triplet was observed and investigated, allowing to synchronize the spin precession on the mechanical motion. The latter is an important step in order to mechanically observe the spin dependent force.

The next objective is to observe the reversed interaction signature, namely the action of the single spin on the nanowire. In order to pursue this objective, a lot of effort has been spent to develop and improve the optical detection of the NW vibrations, as well as its use as an ultrasensitive force sensor.

Given its geometry, the nanowire naturally vibrates along two orthogonal transverse directions, thus enabling its use as a $2D$ vectorial sensor. During the thesis of A. Gloppe [232], sensitivities around $10\,\mathrm{aN}/\sqrt{\mathrm{Hz}}$ were achieved at room temperature and it was

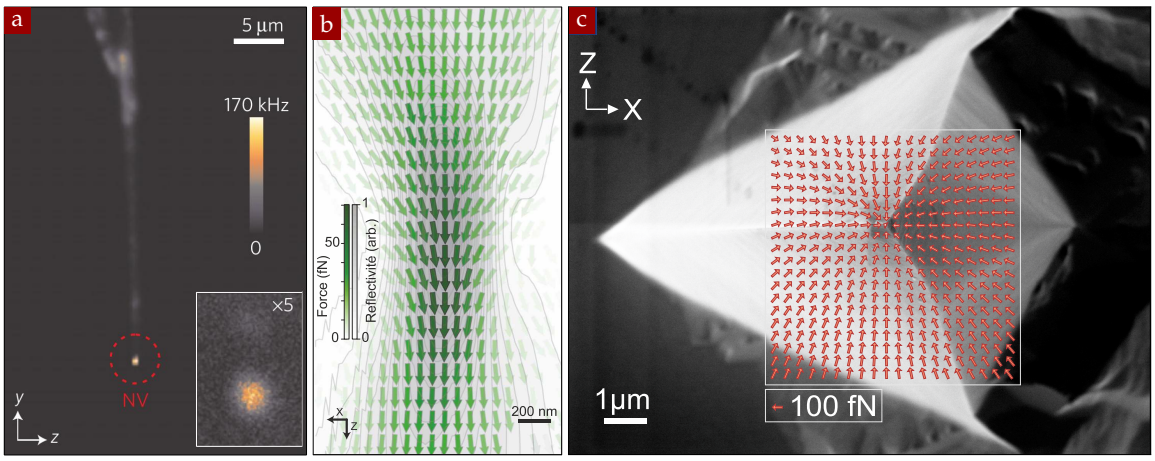

FIGURE 1.6 – SiC nanowires ultrasensitive force sensor: (a) hybrid spin-mechanical system [16]; (b) cartography of an optical force field [86]; (c) cartography of an electrostatic force field [56].

possible to realize a cartography of the optical force applied on the NW by a focused laser beam [86] (see fig. 1.6b). Those measurements were performed by means of a pump-probe response technique, requiring to be able to modulate the intensity of the force field at the mechanical frequency. A more general and universal approach, applicable to any force field that cannot be time modulated (Casimir, Van der Waals, etc.), has been subsequently developed during the PhD of L. Mercier de Lépinay [233]. This was based on the angular and spectral analysis of the NW Brownian motion: it has allowed to map the force field induced by an electrostatic tip positioned below the nanowire [56] (see fig. 1.6c), but also to study the impact of rotational force field on the nanowire dynamics, such as the one observed on the side of an optical waist [117]. We will now briefly detail the principle of the universal vectorial measurement, as well as the motivations that led to this work.

A 2*D* VECTORIAL FORCE SENSOR The way a nanowire is employed to perform a force field measurement is quite similar to the "non-contact" mode of an atomic force microscope (AFM): by monitoring the change of the cantilever resonant frequency, induced by a proximity force generating an appreciable gradient along the cantilever motion, it is possible to measure the gradient of the force along the oscillation direction. The same mechanism applies for a nanowire, but now it is possible to exploit the fact that it oscillates along both transverse directions and is thus sensitive to the spatial variations of the force field experienced along its transverse oscillation plane. By monitoring the frequencies of the two mechanical fundamental eigenmodes, together with their orientations, it is possible to deduce the four components of the force field gradient experienced by the nanowire. Once the gradients are known, it is possible to reconstruct the entire bidimensional vectorial field.

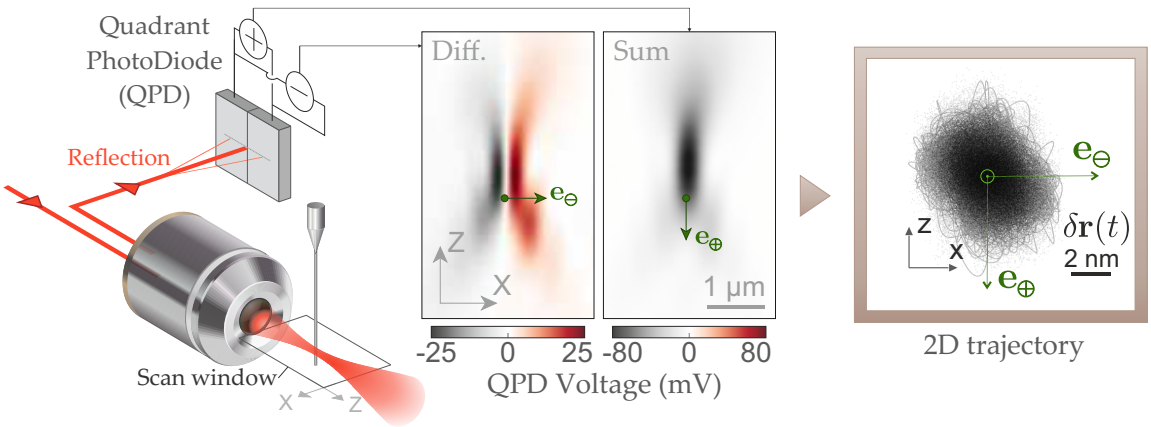

FIGURE 1.7 – Typical readout scheme to probe the NW vibrations. A laser beam is focused on the nanowire by mean of a microscope objective. The reflected light is collected on a quadrant photodiode, whose sum and difference signals provide the two independent measurement channels. It is then possible, for example, to reconstruct the 2*D* trajectory of NW thermal motion.

It is important to note that in order to guarantee the universality of this method, the nanowire vibrations have to be measured in two dimensions, by two independent measurement channels. If it is not the case, it is still possible to compute the force field under the assumption that the two polarizations always remain orthogonal to each other, which is in general not true in presence of rotational force fields. A typical measurement technique to probe the nanowire vibrations, which makes use of the sum and the difference signals of a split photodiode, is shown in fig. 1.7.

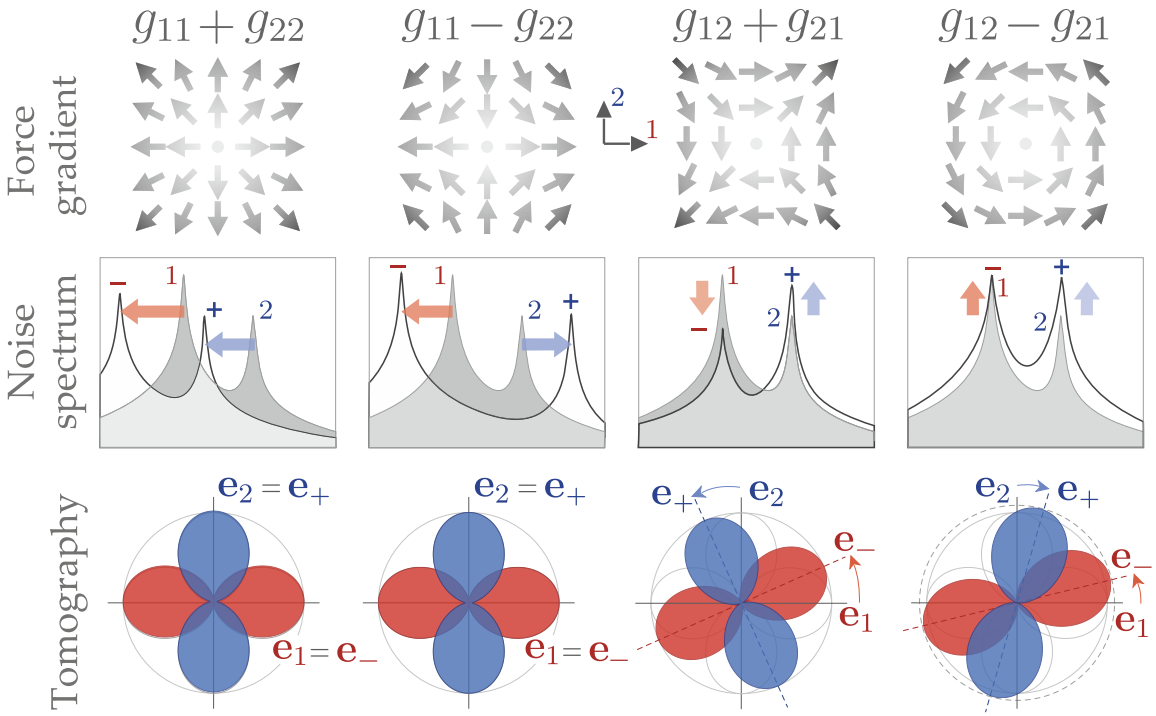

FIGURE 1.8 – Simplified phenomenology of the dressing of the nanowire eigenmodes by the four base elements that can be used to describe any $2D$ force field gradient. The impact on the measured power spectral density as well as on the angular tomography is schematized. A force field gradient can then generate eigenfrequency shifts and rotation of the eigenvectors. The measurement of the perturbation of the nanowire mechanical properties permits to fully reconstruct the local force field gradients.

The bidimensional displacements of the NW extremity immersed in an external force field $\mathbf{F}^{\text{ext}}$, can be described by the equation of motion:

$$\delta\ddot{\mathbf{r}}(t) = -\begin{pmatrix}\Omega_1^2 & 0\\ 0 & \Omega_2^2\end{pmatrix}\delta\mathbf{r}(t) - \begin{pmatrix}\Gamma_1 & 0\\ 0 & \Gamma_2\end{pmatrix}\delta\dot{\mathbf{r}}(t) + \frac{\delta\mathbf{F}_{\text{th}}}{M_{\text{eff}}} + \begin{pmatrix}g_{11} & g_{21}\\ g_{12} & g_{22}\end{pmatrix}\delta\mathbf{r}(t), \tag{1.3.1}$$

where we have introduced a set of 2 Langevin forces independently driving the nanowire along both transverse directions $\delta\mathbf{F}_{\text{th}} = (\delta F_1^{\text{th}}, \delta F_2^{\text{th}})$. The matrices are written in the $(\mathbf{e_1}, \mathbf{e_2})$ orthogonal base of the 2 uncoupled eigenmodes, and we have expanded the force field under investigation around the nanowire rest position $\mathbf{F}^{\text{ext}}(\mathbf{r}) = \mathbf{F}^{\text{ext}}(\mathbf{r_0}) + \delta\mathbf{r}\cdot\boldsymbol{\nabla}\mathbf{F}^{\text{ext}}$, using the 4 components of the force field gradients g_{ij} defined as

$$g_{ij} \equiv \frac{1}{M_{\text{eff}}}\partial_i F_j^{\text{ext}}(\mathbf{r}_0), \tag{1.3.2}$$

$\mathbf{r}_0$ being the static equilibrium position in presence of the force. i, j are a generic set of orthonormal vectors taken in the transverse plane with respect to the nanowire axis, while $1, 2$ refer to the two mechanical uncoupled eigenvectors. M_{eff} is the effective mass of the NW (see section 3.1.2).

It is then possible to establish a $2D$ dressed susceptibility matrix:

$$\delta\mathbf{r}[\Omega] = \chi[\Omega]\delta\mathbf{F}_{\text{th}}[\Omega] \tag{1.3.3}$$

where $\chi[\Omega]$ is given by

$$\chi^{-1}[\Omega] = M_{\text{eff}} \begin{pmatrix} \Omega_1^2 - \Omega^2 - i\Gamma_1\Omega - g_{11} & -g_{21} \\ -g_{12} & \Omega_2^2 - \Omega^2 - i\Gamma_2\Omega - g_{22} \end{pmatrix}. \tag{1.3.4}$$

From there it is then possible to derive the two new dressed eigenfrequencies

$$\Omega_\pm^2 \equiv \frac{\Omega_{1\|}^2 + \Omega_{2\|}^2}{2} \pm \frac{1}{2}\sqrt{\left(\Omega_{2\|}^2 - \Omega_{1\|}^2\right)^2 + 4g_{12}g_{21}} \tag{1.3.5}$$

as well as the two new eigenvectors:

$$\mathbf{e}_- \equiv \frac{1}{\sqrt{g_{12}^2 + \Omega_\perp^4}} \begin{pmatrix} \Omega_\perp^2 \\ g_{12} \end{pmatrix} \qquad \mathbf{e}_+ \equiv \frac{1}{\sqrt{g_{21}^2 + \Omega_\perp^4}} \begin{pmatrix} -g_{21} \\ \Omega_\perp^2 \end{pmatrix}, \tag{1.3.6}$$

where we have defined $\Omega_{1\|}^2 \equiv \Omega_1^2 - g_{11}$, $\Omega_{2\|}^2 \equiv \Omega_2^2 - g_{22}$ and $\Omega_\perp^2 = \left(\Omega_+^2 - \Omega_{1\|}^2\right) = \left(\Omega_{2\|}^2 - \Omega_-^2\right)$. Figure 1.8 pictures a simplified phenomenology of the dressing mechanism of the two mechanical eigenmodes by the four base elements on which can be expanded any $2D$ force field.

As an example, the divergence component of the force field only affects its eigenfrequencies according to

$$\Omega_+^2 + \Omega_-^2 = (\Omega_1^2 + \Omega_2^2) - (g_{11} + g_{22}) = (\Omega_1^2 + \Omega_2^2) - \frac{1}{M_{\text{eff}}}\boldsymbol{\nabla} \cdot \mathbf{F}_{\text{ext}}, \tag{1.3.7}$$

while transverse terms are responsible for a rotation of the eigenvectors. For more details see [233].

TOWARDS LOW-TEMPERATURE EXPERIMENTS The thermal noise sets a limit on the smallest forces that can be detected. In the case of a monochromatic force, its minimal amplitude is given by:

$$\delta F_{\text{min}} = \sqrt{\text{RBW} \times 2M\Gamma k_B T}. \tag{1.3.8}$$

where RBW stands for the resolution bandwidth employed. From this equation is clear that in order to improve this limit there are only few alternatives. The first one consists in using lighter oscillator, which means for NWs shorter and thinner samples: this solution has several limitation, because both parameters strongly impact the vibration frequency and samples with a diameter smaller than 100 nm tend to be rare and extremely difficult to manipulate (they bend and stick to their support very easily). The second alternative is to improve the quality factor of the mechanical resonator: this depends on the material properties and at room temperature our samples hardly exhibit Q-factor higher than 10^5 [19, 228].

The last solution to improve the sensitivity of the probe consists in reducing its temperature. This has been one of the compelling objectives of this work and it will be discussed extensively in chapters 2 and 3.

When it comes to force sensing, operating in a cryogenic environment can have multiple advantages. The sensitivity not only benefits from the reduced temperature of the probe, but also from the increased quality factors that are generally observed at low temperatures. The systems investigated with the nanowire-scanning-probe would also take advantage of the colder environment. Furthermore, the properties of silicon carbide are tabulated in literature only down to approx. 9 K and are yet to be explored at lower temperatures. It is also worth mentioning that the thermal and mechanical behaviour of such small nano-resonators are likely to be very different from the ones of bulk material.

Of course the advantages come at a cost, in particular we will have to overcome several challenges, among which the ability to perform optical measurements at dilution temperature as well as being able to thermalise such nano-sized samples with extreme aspect ratios.

DISPERSIVE OPTOMECHANICS WITH A NANOWIRE Another peculiar aspect of SiC NWs are their large zero-point-fluctuations. From the definition of eq. (1.2.8) it is obvious that the ability to work with nano-resonators in the kHz range and with very low masses, of typical few pg, results in typical values for x_{zpf} of several pm. When looking at the definition of single-photon coupling given above, we see that in order to enter more exotic regimes, such as the USC regime, large values of both the parametric optical frequency shift and x_{zpf} are required. Concerning the former, a good choice would be to make use of a **nanowire-in-the-middle** (NIM) optomechanical configuration, similar to the *membrane-in-the-middle* (MIM) systems. This kind of geometries decouple completely the mechanical and the optical parts of the system, allowing to work with high-finesse optical cavities without compromising either the optical or the mechanical quality factors. In our case, in order to maximize the optical frequency shift, we decided to use a fiber-micro-cavity that allows to minimize the optical mode volume. Reducing the cavity length to around 10 µm, optical frequency shifts of the order of few tens of GHz can be expected, a magnitude that would allow to satisfy the condition $g_0/\Omega_{\mathrm{m}} > 1$. A scheme of this nanowire-in-the-middle configuration is shown in fig. 1.9 and will be thoroughly discussed in chapters 4 and 5.

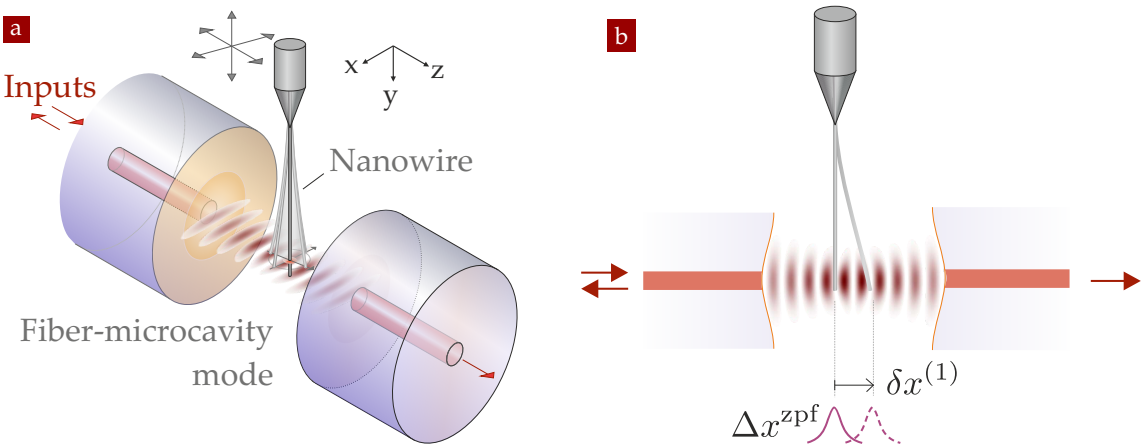

FIGURE 1.9 – (a) scheme of a nanowire-in-the-middle (NIM) system. (b) single-photo recoil in a NIM system.

Part II

NANO-OPTOMECHANICAL FORCE SENSORS AT DILUTION TEMPERATURE

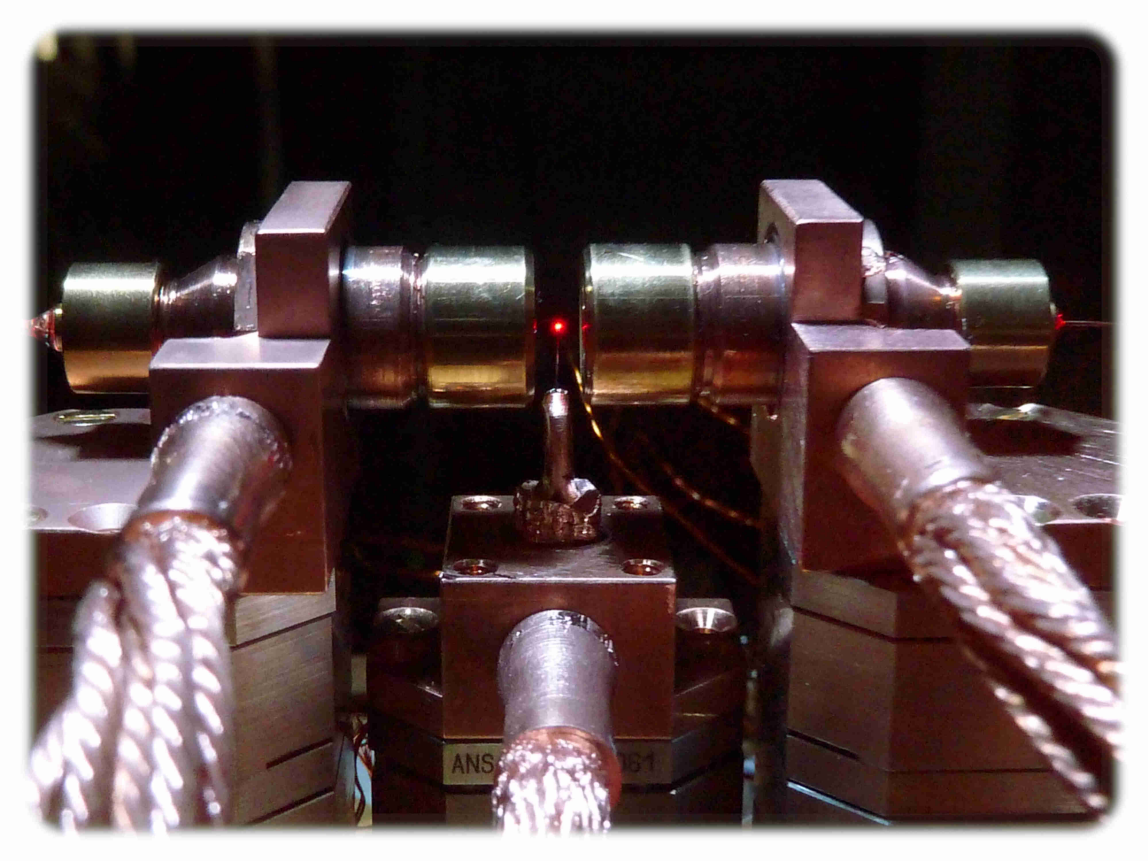

Operating a force sensor at dilution temperatures allows to reduce its thermal noise and further benefits from an increased mechanical coherence, giving rise to exceptional force sensitivities. In the following part we will show how we achieved this result by operating our suspended silicon-carbide nanowires in a SIONLUDI dilution fridge. This requires to eliminate the sources of unwanted vibrations, such as electrical or mechanical noises, and to operate at ultralow optical powers to avoid unwanted laser heating. We will expose the experimental developments that lead us to observe a nanowire thermalised at the base temperature of the cryostat, while exploiting novel optical readout schemes operating in the photon counting regime, where less than a photon is detected per mechanical period. We will discuss their mechanical and thermal properties at low temperatures and report on exceptional force sensitivities for a scanning probe force sensor.

2 THE CRYOGENIC EXPERIMENT

This chapter presents a complete description of the cryostat employed in this work, as well as a full characterisation of the optical components used to probe the nanowires motion at low temperatures. We also describe the signal analysis techniques operating in the photon counting regime developed to enable the use of ultra-low optical powers, together with the control system of the experiment.

CONTENTS

2.1 Force sensing at cryogenic temperatures . . . 25
2.2 The cryostat . . . 27
2.2.1 Dilution fridges . . . 27
Quantum fluids . . . 27
Working principle . . . 29
2.2.2 SIONLUDI: an inverted dilution fridge . . . 33
2.2.3 Measuring and controlling the temperature . . . 37
MMR3 module . . . 38
MGC3 module . . . 39
2.2.4 Environment acoustic isolation . . . 40
2.2.5 Cryostat control and interface . . . 42
2.3 Optical cryogenic head . . . 43
2.3.1 Interferometric objectives . . . 43
2.3.2 Nanowire support . . . 48
2.3.3 Piezo-positioners and scanners . . . 49
2.3.4 Suspended optical head . . . 51
2.4 System control and signal detection . . . 53
2.4.1 Experiment control and interface . . . 53
2.4.2 Optical scheme . . . 54
2.4.3 Vibrations measurements in the photon counting regime . . . 55
Measurement principle . . . 57
Measurement calibration . . . 60

2.1 FORCE SENSING AT CRYOGENIC TEMPERATURES

Operating force probes at low temperatures enables novel physical explorations in a quieter environment, with an increased force sensitivity granted by the reduction of their thermal noise which ultimately limits their performances. Since the invention of the atomic force microscope (AFM), the sensitivity of force sensors was greatly enhanced by using nanomechanical force probes. Nanowire (NW) cantilevers in particular are becoming increasingly popular [27], thanks also to the improved atomic-scale control during the growth of the structure that drastically reduced the number of defects, ultimately improving their sensitivity. Compare to more conventional AFM probes, which are more suitable for revealing larger (in the pN range) forces, NWs are better at discerning weak interaction. Furthermore, their near-degenerate flexural mode doublets allow to image the full vectorial character of the force field [86], enabling for example the distinction among conservative and non-conservative force fields [117]. This kind of probes can also

be functionalized by adding a magnetic tip at their extremity, resulting in an excellent sensor to investigate magnetic field patterns generated above micro-structures such as vortices, domain walls, skyrmions, nuclear spins ensembles etc.

Up to now, the use of nanomechanical force probes has enabled the mechanical detection of ultraweak interactions such as the force exerted by a single electronic spins [177] or molecules [80] and investigations of fundamental processes in condensed matter such as the interaction of a nanoresonator to a superconducting qubit [111]. At cryogenic temperatures, the reduced thermal bath fluctuations often comes along with a decrease of mechanical damping rates which further improves the probe's sensitivity. All those benefits only occur at the condition to read the nanomechanical force sensors without increasing their noise temperature.

This challenge becomes excessively difficult with ultrasensitive nanomechanical force sensors due to the desired decoupling from their mechanical support which is a general condition to achieve large quality factors and to the extreme aspect ratios of commonly employed ultrasensitive geometries in the form of nanotubes, graphene or nanowires [143, 40, 206, 54]. The overall reduction of the heat conductance at low temperatures, which even accelerates below 100 mK, renders this objective even more difficult. In this perspective, the choice of the probe is decisive and one should aim at minimizing its impact on the force sensor. Several approaches making use of electron based readout schemes were already reported, such as atomic quantum point contact [161], SET [110, 112], squids [71, 200], MW cavities [170] or propagating electron-beam [146, 187]. However the spatial integration of the readout imposes serious geometrical constraints on the physics that can be investigated with such probes and in general does not permit preserving a scanning probe capacity.

In the optical domain, successful developments were realized by employing the toolbox of cavity optomechanics [13, 82], making use of an enhanced readout efficiency enabled by the large cavity finesse. However, a natural drawback of this strategy is to increase the overall system absorption, which has for the moment prevented from observing the oscillator thermal noise thermalised to the cryostat base temperature [135]. In those approaches, low phonon number occupancies were obtained by exploiting dynamical backaction cooling, which however does not necessarily help increasing the bare force sensitivity of the system since it simultaneously reduces the mechanical susceptibility of the oscillator.

Several optical detection schemes making use of cavity-free optical interferometric readouts were employed to probe ultrasensitive force sensors at low temperatures, in particular in the field of MRFM [128, 24, 59, 193], but the thermal noise of the probe could not

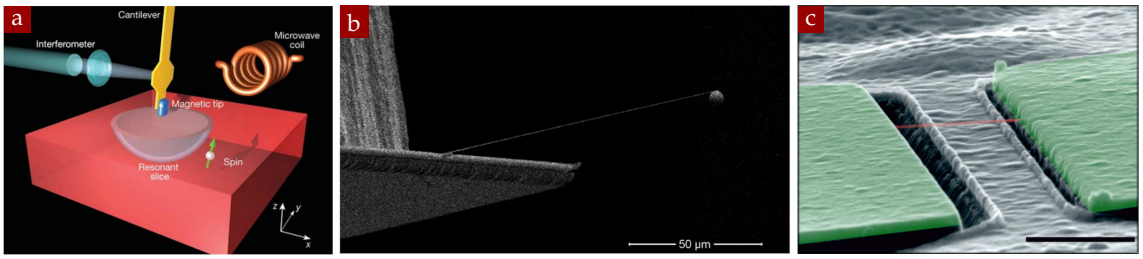

FIGURE 2.1 – (a) scheme of the setup use in [177] for the detection of an individual electron spin by MRFM; (b) SEM image of the silicon resonator with a magnetic sphere attached to its end used in [200] as a force sensor and thermalised at 25 mK; (c) SEM image of a typical nanotube resonator used in [54] that can achieve sensitivity of few zN.

be probed below an effective noise temperature of approx 300 mK. Despite the low light powers employed, the residual light absorption has thus for the moment prevented existing experiments from reaching the sub-100 mK temperature regime. This is however an extremely interesting objective since - beyond increasing the force sensitivity of the nano-optomechanical force probes - it permits investigating the intrinsic mechanical, thermal and physical properties of the systems in their lowest excitation state, and gives access to a new physical richness.

2.2 THE CRYOSTAT

Performing optical measurement at ultralow temperature involves several technical challenges. The further requirement of a mechanically isolated and stable setup to measure the vibration of an ultrasensitive sensor adds complexity to the system. After a brief introduction of some key concepts of the physics of quantum fluids, we will detail the working principle of a SIONLUDI dilution fridge, used to reach the base temperature of 20 mK, the thermometer employed, as well as the suspension assembly used to decouple the optical head where the experiment occurs. For the interested reader, a brief historical excursus on the evolution of cryogenic technology is presented in the insert at page 31.

2.2.1 Dilution fridges

Dilution fridge refrigerators have been invented almost 70 years ago, nonetheless this technology has been constantly improved and optimized since then, still representing a fundamental and unique ingredient for most of ultralow temperature experiments. In order to better understand the operation of the SIONLUDI refrigerator, the main physical properties of ^{3}He and ^{4}He are introduced, together with the basic working principle of a dilution refrigerator.

QUANTUM FLUIDS Helium is a rather extraordinary element, with a lot of exotic and unique properties. As visible in the phase-diagrams in fig. 2.2 ^{4}He (^{3}He) becomes liquid at 4.2K (3.2 K) at room pressure, it presents a transition to the superfliud phase at 2.2 K (1 mK) and it has no triple point, not being able to solidify under its own vapour pressure. Given its closed electronic shell, binding forces between atoms are rather small and only

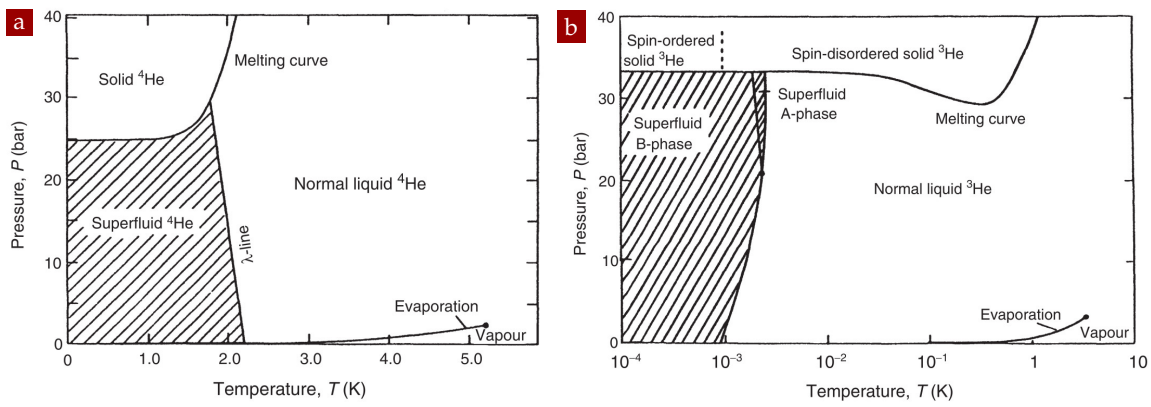

FIGURE 2.2 – Phase diagram of the quantum fluids ^{4}He (a) and ^{3}He (b). Images from [255].

mediated by van der Waals interactions. The two isotopes are then characterized by a small atomic mass m, which is associated to a large quantum zero-point energy E_0, given by

Zero-point energy

$$E_0 = \frac{h^2}{8ma^2} \tag{2.2.1}$$

where h is the Plank's constant, $a = V_m/N_A$, V_m is the molar volume and N_A the Avogadro's number. The combination of these two attributes can explain most of its properties, among which its small density and latent heat of evaporation, the very low boiling point, the quite large vapour pressure and why helium remains liquid even at absolute zero. They also account for the differences in these properties between the two isotopes (see fig. 2.3c). All those physical properties are fundamental to understand low temperature cryogenic systems.

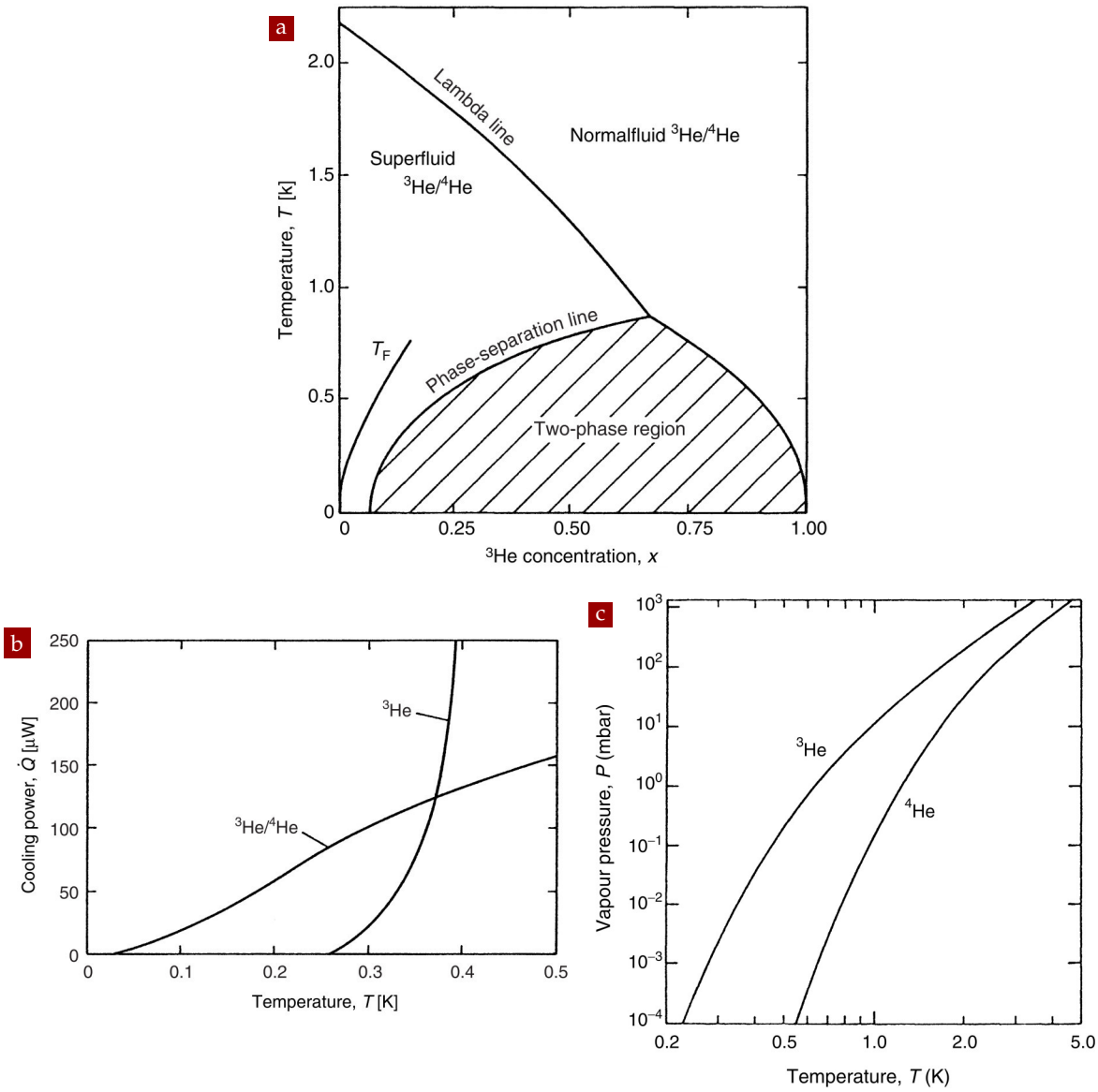

FIGURE 2.3 – Properties of liquid helium: (a) phase diagram of ^{3}He -^{4} He mixture; (b) cooling power of a ^{3}He cryostat vs a dilution fridge; (c) vapour pressure of pure ^{3}He and ^{4}He. Image from [255].

A standard technique to reduce the temperature of a cryogenic liquid below its boiling point consists in pumping away atoms from the vapour phase above the liquid-gas interface: the hottest atoms in the liquid will then evaporate while the others thermalise to a lower temperature. The cooling power of this technique is given by

Cooling power of an evaporation cryostat

$$\dot{Q} \propto LP_{\text{vap}} \propto e^{-1/T} \tag{2.2.2}$$

where L is the latent heat, P_{vap} the vapour pressure and T the temperature. Due to the rapid decay of the vapour pressure at low temperature (see fig. 2.3c), the minimal temperature achievable with standard pump are typically 1.3 K for ^{4}He and 0.3 K for ^{3}He.

Dilution refrigerators are based on a ^{3}He-^{4}He mixture. It is important to remember that the two isotopes are two different quantum objects: ^{4}He atoms are bosons, they obey the Bose-Einstein statistics and undergo the analogue of a Bose momentum condensation into a superfluid state [254]; ^{3}He atoms are fermions, they obey the Fermi-Dirac statistics and at sufficiently low temperatures behave like a Fermi liquid, similarly to the conduction electrons in metals. In a helium mixture with temperature < 0.5 K, the ^{4}He component acts just like an "inert superfluid background", contributing to the volume of the liquid and modifying the effective mass of the resulting interacting Fermi-gas. The phase-diagram of the mixture is shown in fig. 2.3a, where x denotes the ^{3}He concentration.

If we start at $x = 0$, ^{4}He crosses the λ-line at 2.2 K and becomes superfluid. Increasing the concentration reduces the transition temperature due to the ^{3}He "impurities". However, for concentrations higher than 67.5% this transition in not possible anymore and another phenomenon occurs: if the temperature is lower than 0.867 K, the liquid actually separates into two phases. The first is a dilute phase, rich in ^{4}He but poor in ^{3}He; the second is a lighter phase rich in ^{3}He which floats on top of the first and form an interface. Forcing the ^{3}He to flow from the rich to the dilute phase is an endothermic process, on which the working principle of a dilution fridge is based. Interestingly, at zero temperature the concentration of ^{3}He in the dilute phase doesn't vanish, but approaches a constant value[1] of 6.6 % (another peculiar property of the quantum fluid, in apparent contradiction with the 3rd principle), so that even at low temperature there always remains a fixed ^{3}He concentration in the dilute phase which can participate to the cooling mechanism. The cooling power is connected to the enthalpy difference ΔH between the 2 phases, and at low temperatures scales like (see fig. 2.3b):

Cooling power of a dilution cryostat

$$\dot{Q} \propto x\Delta H \propto T^2 \tag{2.2.3}$$

WORKING PRINCIPLE A scheme describing the main components of a dilution refrigerator can be found in fig. 2.4. The mixing chamber is the coldest part, where the two phases of the mixture coexist, the rich phase sitting on top of the dilute phase due to their respective density difference. As stated, the cooling power is provided by the latent heat of mixing, so the goal is to have a constant flux of ^{3}He atoms crossing the phase separation boundary, from the concentrated to the dilute phase. This is achieved by pumping ^{3}He from the dilute phase while constantly providing ^{3}He to the concentrated one. To do so, the mixing chamber is connected to the still, a second chamber normally kept at a temperature around 0.6 K to 0.7 K. Due to the difference in vapour pressure of the two isotopes at this temperature (fig. 2.3c), the vapour

The mixing chamber

[1] It is the value for which the binding energy of ^{3}He atoms in the mixture equals that of pure ^{3}He at 0 K

The still

in the still chamber is almost pure ^{3}He (> 90%), so that a pump will almost only evacuate pure ^{3}He. An osmotic pressure will then be established between the mixing chamber and the still, allowing the ^{3}He atoms to be driven out of the dilute phase.

In order to close the cycle, it is now necessary to reinject the pumped ^{3}He back into the concentrated phase in the mixing chamber, an operation that requires several steps. The ^{3}He gas coming from the room temperature pump is thus precooled by a 4 K stage and will then condense while thermalising in the 1 K pot[2]. A main flow impedance needs to be added between this stage and the still, in order to have enough pressure for the condensation to actually take place. Next, the liquid flows through a heat exchanger in thermal contact with the still, at a temperature of about 0.7 K; a secondary flow impedance allows again to maintain a sufficiently high pressure to prevent reevaporation of the ^{3}He. The cooling power due to the latent heat of evaporation in the still is actually more than the one needed to thermalise the helium from the condenser: an additional heater is needed to keep the temperature at the desired level. Finally a sequence of several heat exchangers (normally a continuous heat exchanger followed by multiple discrete heat exchangers) is needed before the liquid can enter the upper, concentrated phase in the mixing chamber. An important constrain must be taken into account at this point: in order not to have a zero cooling power available from the mixing chamber, the ^{3}He entering the concentrated phase needs to be no more than three times hotter than the mixing chamber itself. Heat exchangers thus constitute one of the most important and crucial parts of a dilution fridge, determining among other things the lowest achievable temperature. Their realization has to cope with Kapitza resistance consideration ([163]), and has to compensate the change in liquid visicositites and conductivities with temperature.[3]

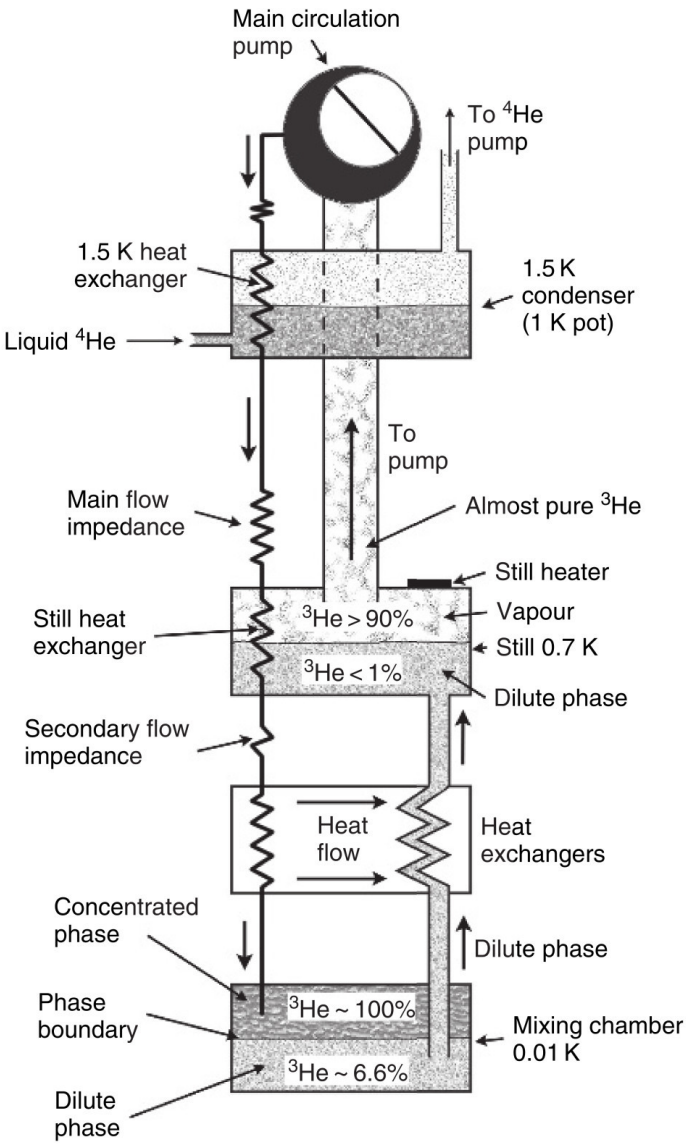

FIGURE 2.4 – Scheme of a dilution refrigerator. Image from [255].

Heat exchangers

[2]This second stage is sometimes replaced by a Joule Thompson expansion that cools the gas down to aprrox. 2 K

[3]More information on the realization and working principle of a DR can be found in [255, 262, 244, 259, 57].

A BIT OF HISTORY

Refrigerators and low-temperature physics developments will soon have a two-centuries-long history, a path full of surprises, remarkable technological advancements and scientific discoveries. Starting with the experiments of Michael Faraday with CO_2 and ammonia in 1820, it actually took almost fifty years until the liquefaction of oxygen and nitrogen was possible. With the results of Pictet and Cailletet in 1877 and the experiments of Wróblewski and Olszewski in 1883, a temperature below 100 K was reached for the first time. Beyond practical applications for refrigeration, scientists were trying to understand whether permanent gases actually exist, that is if all the known substances appear in the liquid and solid form or not. Technical limitations, especially the lack of a sufficiently good thermal isolation, delayed the answer to this question up to the end of the century, when a major breakthrough was done by James Dewar in 1892 with the introduction of the double-walled vacuum flask, which now bears his name. In 1898 this allowed him to reach a temperature lower than 20 K and to liquefy hydrogen.

Born of cryogenics

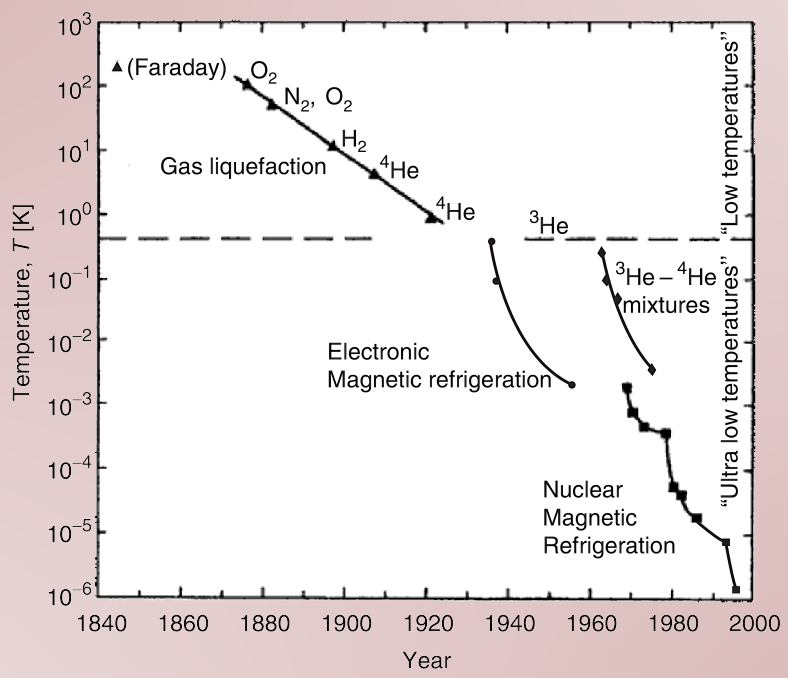

Historical development of refrigerators, image from [255].

In 1868 during a solar eclipse the French astronomer J. Janssen detected new unknown lines in the spectrum of the Sun [98]; shortly after, the English scientist N. Lockyer confirmed the observation and named the new element *Helium* [124]. Nonetheless, it took until 1895 for the element to be observed on Earth, in a gas escaping from the mineral cleveite, discovered by W. Ramsay [168, 169]. Shortly after, when hydrogen liquefation became feasible, a race started between James Dewar and the Dutch physicist Heike Kamerlingh Onnes to obtain helium in liquid form. The race was won by Kamerlingh Onnes in 1908 [102], in Leiden, which is now considered the starting date of low-temperature physics. This also permitted the discovery of superconductivity in 1911 and the first evidence of superfluidity in helium in the early 1920s (which was actually only confirmed independently by P. Kapitza [103] and J. Allen [8] in 1938).

Liquefaction of helium

As time went by, lower and lower temperatures where achieved. The limit of continuous pumping ^{4}He cryostats (based on the latent heat of ^{4}He) was reached by the Leiden group in the early 1930s, a temperature of around 0.7 K. During the same period, the electronic magnetic refrigeration technique was developed: starting from an ^{4}He base temperature, the adiabatic demagnetization of paramagnetic salts allowed for the first time to achieve temperatures well below 1 K, down to the millikelvin region, initially in single shot experiments. Despite the discovery of ^{3}He in 1933 [148], it was only during the 1950s that a sufficient amount of this rare isotope was isolated to operate a cryostat based on ^{3}He evaporation, reaching the 300 mK range.

The invention of the dilution refrigerator

A major breakthrough came from an idea of H. London, proposed in 1951 [218] and fully implemented only ten years later [125]: the dilution refrigerator (DR). It is based on a mixture of ^{3}He-^{4}He and exploits the endothermic process which takes place, for temperatures lower than 800 mK, at the interface between the ^{3}He-rich phase and the ^{3}He-dilute phase; it was first realized in 1965 [217]. Several improvements were made since then, in particular by G. Frossati in the 80s [78, 202], who managed to reach temperatures as low as 2 mK (the actual record for a DR is 1.7 mK [50]). Today, dilution refrigerators represent the only method which provides continuous cooling down to the mK region and constitute a starting stage for nuclear magnetic refrigeration cryostats. This is an evolution of the former electronic magnetic refrigeration principle and the only way currently known to reach temperatures as low as few μK for continuous systems.[a]

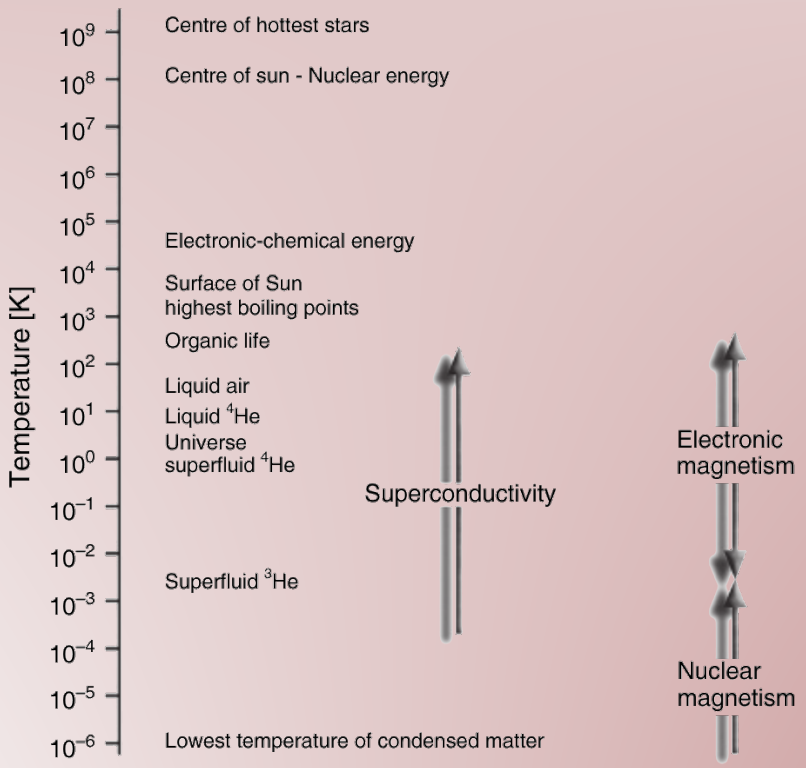

Range of temperature existing in nature or obtainable in the laboratory. Image from [262].

[a] More information can be found in [246, 186, 255].

2.2.2 SIONLUDI: an inverted dilution fridge

The experiment was built on a home made dilution fridge, named SIONLUDI. This name originates from the historical model developed in the group of Alain Benoit, that was used for condensed matter and space related applications (camera).

Our cryostat was the 7th model of a series of 8 cryostats produced in the institute during the 2014-2016 period. These developments were mainly conducted by W. Wernsdorfer, with the help of E. Eyraud who entirely built our platforms during the first part of 2015. Nothing would have been possible without their efforts and the feedback from the different colleagues who had the chance to run those unique systems. We operated the cryostat in the "incubator room" during 1.5 year, and it was subsequently moved to the Z building (room Z110) during the course of my PhD, where it was connected to the new gas handling system. Its development was supervised by E. Eyraud, with the help of F. Lahoucine.

The name SIONLUDI alludes to the fact that it is inverted compared to standard dilution fridge, in the sense that the coldest stage sits on the top, which allows for an easier assembly and access to the optical setup. The mixing chamber is of course not inverted. It can be cooled from room temperature down to 20 mK in roughly 3 hours, enabling the user to perform up to 2 cooling cycles in a day if needed. Its operation is fully automatized and in addition it can be operated remotely, even if a presence in the room is nonetheless recommended. It presents a cooling power of about 200 µW at 100 mK and a rather low ^{4}He consumption ($\sim$ 80 L per week), which requires a single refill per week, during which the cryostat base temperature remains unchanged (however acoustic shocks do not permit to realize satisfying nanomechanical measurements during this 1 h period). It can thus be kept cold for long periods of time, even months or years.

A simple scheme of the cryostat structure in shown in fig. 2.6a: the cryostat presents a plateau structure made of different stages, each one of decreasing temperature from bottom to top. The stages are supported by a set of 3 stainless steel mounts, presenting a minimal thermal conductivity. The lower stages, labelled 90 K, 20 K, 4 K, also support radiation screens, while it is also possible to add a 1 K screen for operations below 20 mK. The cylindrical screens (see fig. 2.5) are made or pure copper with a golden surface.

The different electrical wires, connected at the coldest plate of the cryostat, are running inside those screens and emerge at the periphery of the bottom stage. This includes 9 channels for the thermometers, a heater and the superconducting cabling for the piezo positioners and the scanners. The optical fibers, which also enter from the bottom, present a very limited thermal conductivity and do not require a very elaborate thermalisation.

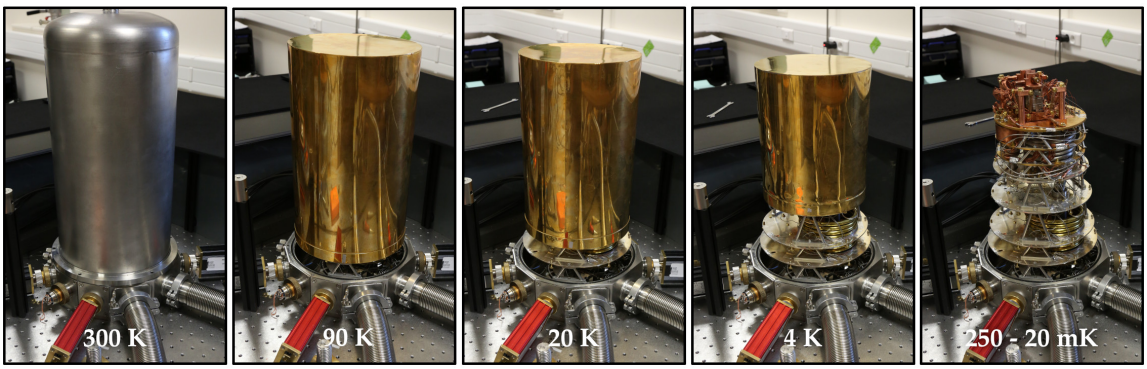

FIGURE 2.5 – Subsequent stages and relative screens employed in the SIONLUDI.

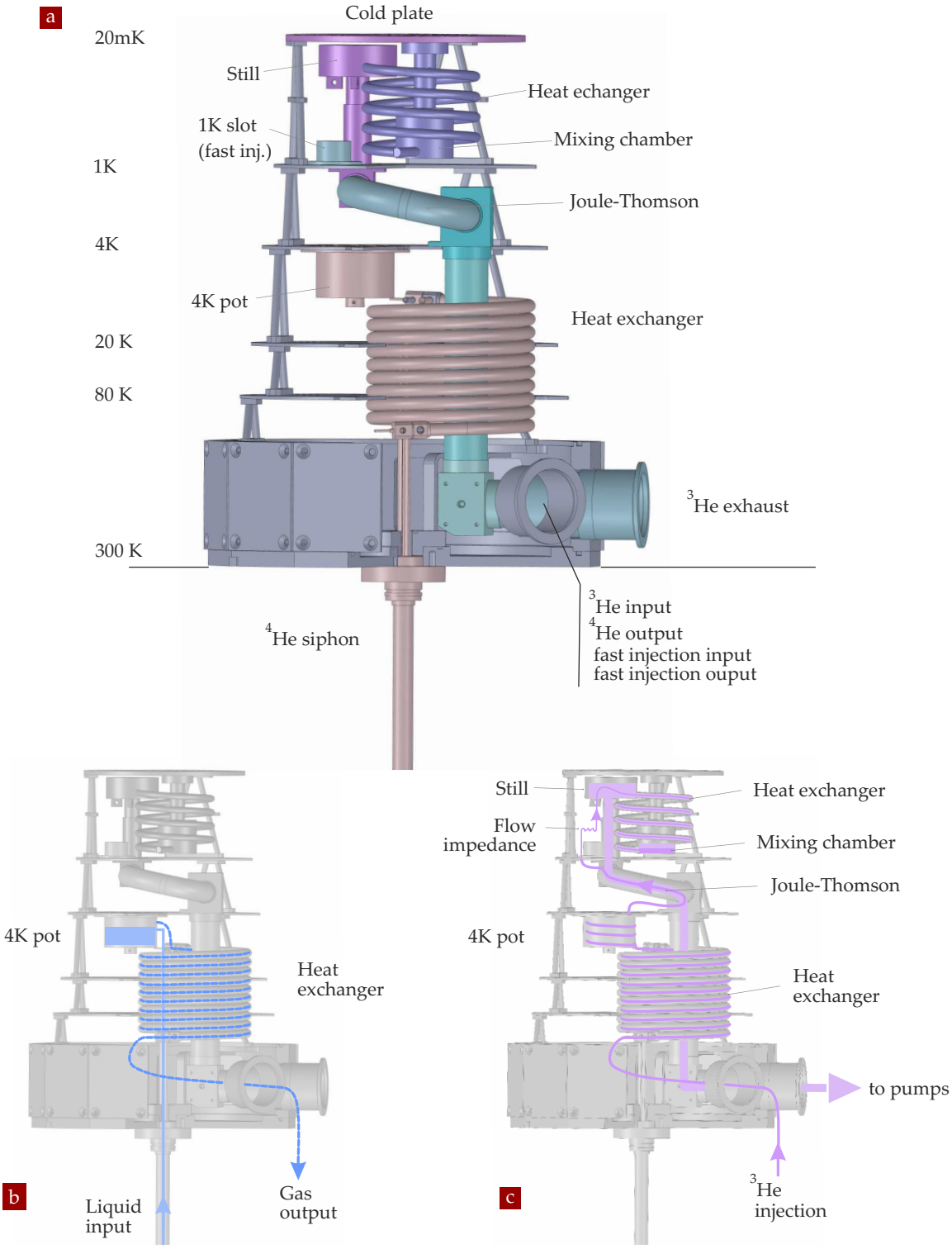

FIGURE 2.6 – Scheme of a SIONLUDI inverted dilution refrigerator: (a) main component of the cryostat and different temperature stages; (b) secondary open-cycle ^{4}He circuit; (c) primary close-cycle dilution circuit.

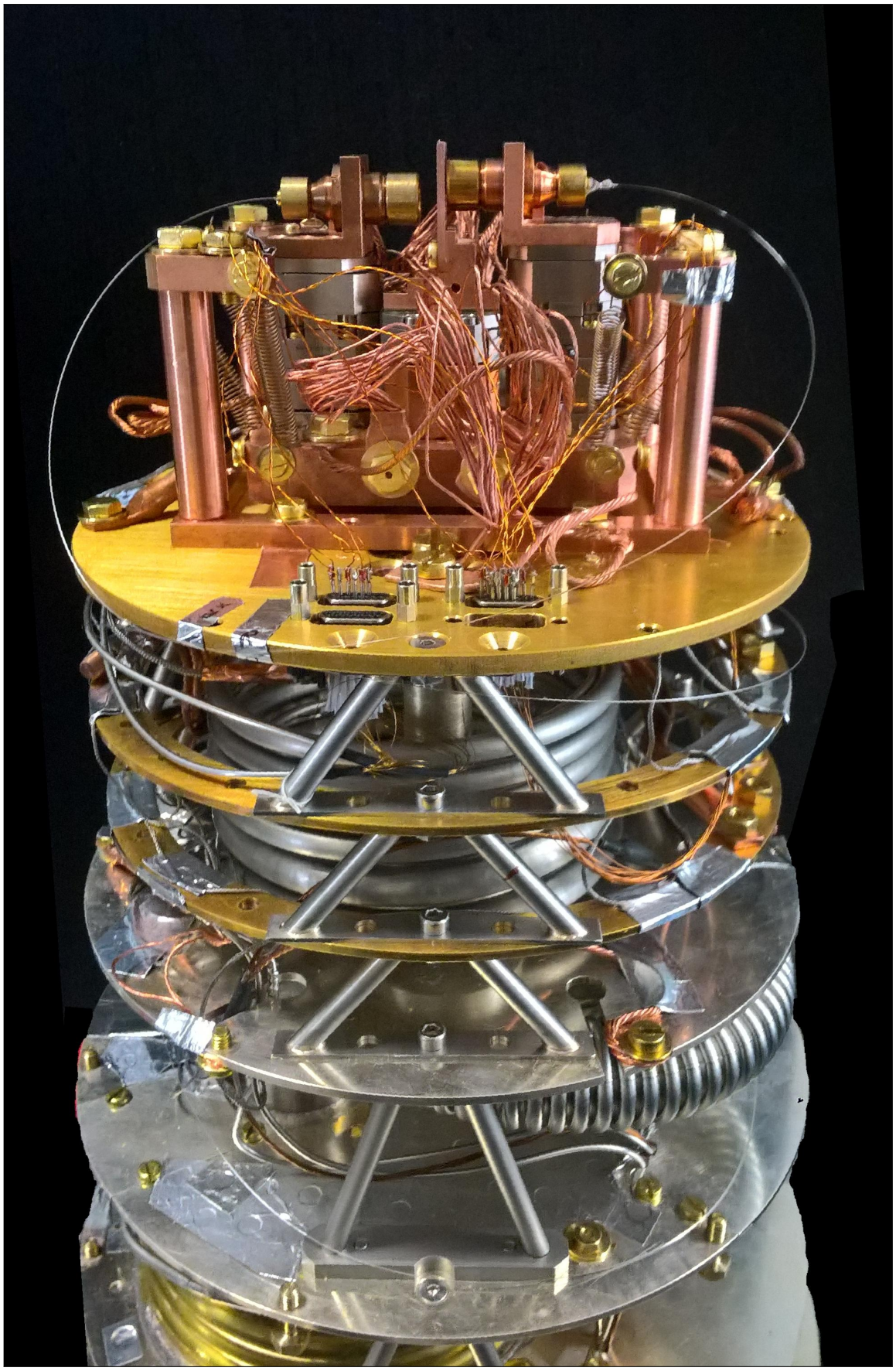

FIGURE 2.7 – Pictures of the SIONLUDI dilution fridge: the different temperature stages, from 80 K to 20 mK are visible, together with the optical apparatus suspended above the cold plate.

The SIONLUDI uses a secondary ^{4}He circuit (fig. 2.6b) to precool the ^{3}He-^{4}He mixture prior to its injection in the dilution section. This is realized first in the continuous counter-flow heat exchanger which evacuates the ^{4}He vapour from the 4 K pot. A 100 L Dewar, positioned below the cryostat and attached to the bottom part of the same optical table, is kept slightly over-pressure at few tens of mbar. It provides a constant flow of ^{4}He into the 4 K pot which serves to cool down the 4 K stage. The vaporized gas is then ejected into the spiral heat-exchanger, which has the double function to precool the mixture entering in the primary circuit and to cool down the two lower stages, respectively at 20 K and 90 K. This is an open-cycle circuit: during steady-state operation a constant flux of about 4 L/min of ^{4}He gas is required (roughly 12 % of the maximum possible flux) and regulated by a mass flow controller. It consumes around 80 L of liquid helium per week, while the average consumption of the system when is not operating is of 1.4 L/d or $\approx$ 10 L/w. An additional pump placed on the output circuit can be employed to ensure a higher ^{4}He flux rate, when the system is cooled down from room temperature or during the filling phases (for which the dewar pressure is reduced).

The ^{4}He circuit

The dilution unit is a closed-cycle circuit in which the ^{3}He-^{4}He mixture circulates. When following the dilution circuit from room temperature (fig. 2.6c), the gas first enters the cryostat head through 12 capillaries located inside the spiral heat exchanger described above; on the way up it gets cooled by the gaseous ^{4}He counter-flow which is escaping the 4 K pot. There are 12 capillaries in total, but only one of them is employed during the standard operation, the other serves for the rapid pre-cooling phase. Just before the 4 K pot, the 11 capillaries constituting the rapid injection circuit are split from the normal injection one and are mixed into one single tube. This gets thermalised on the 1 K stage and then on the still, finally entering the mixing chamber. This tube has a larger cross section and its main purpose is to rapidly precool the top part of the cryostat

The rapid injection

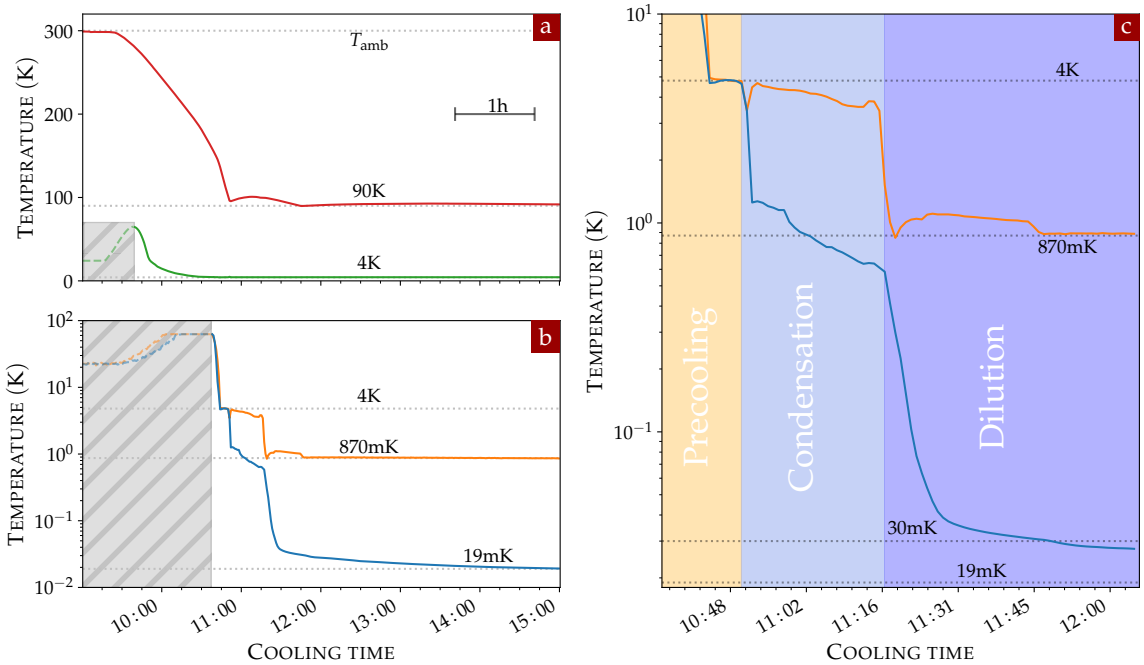

Figure 2.8 – Evolution of the temperature of the main elements during a typical cool down phase, with all the optical components in place. (a) shows the cooling of the 90 K and the 4 K stages. (b) shows the temperature evolution of the still and of the mixing chamber. (c) is a zoom around the moment when the dilution process starts.

down to 4 K. This part of the circuit is not employed during the condensation phase or in the normal operation of the dilution. Instead, the main circuit capillary is thermalised in the 4 K pot, goes through a second heat exchanger, terminated by a flow impedance, and then enters the still (where the ^{3}He is evaporated on the way back). From there it goes through a second continuous counter-flow exchanger and a series of discrete exchangers, finally ending in the mixing chamber, the coldest part of the cryostat. The normal injection handles the condensation of the mixture and the steady-state operation. The dilute phase is pumped out and flows back through the heat exchanger, up to the still (around 800 mK) where the liquid gets evaporated. A ^{4}He stop film is inserted in order to avoid the creation of a superfluid thermal link with the upper temperature areas. Finally, the gas is pumped out of the cryostat through a large diameter tube by the root and primary pumps located in the basement. After the pumps, the circuit goes back to the input port of the cryostat. During the condensation phase, a compressor is employed to inject a large amount of mixture to fill the dilution circuit.

The normal injection

Starting at room temperature, the "rapid injection" is first activated to pre-cool the system. A small quantity of mixture starts to circulate and pre-cool the higher stages. Once the system is thermalised at 4.2 K (in about two hours), an external compressor pressurize the gas in the primary circuit at $\sim$ 4 bar, starting the condensation phase. The pressure gradient generated by the flow impedance gives rise to a Joule-Thomson expansion, lowering the temperature of the gas to about 1 K. When the gas starts to condense, the pressure is progressively reduced and the compressor is finally stopped when it reaches approx. 1000 mbar. The remaining part of the mixture is then slowly injected in the normal circuit. The external pump, together with a root pump, reduces the pressure in the mixing chamber to around 0.1 mbar, allowing another adiabatic expansion and speeding up the condensation process. The liquid gradually fills all the components from the mixing chamber up to the still. Once the system reaches a temperature of $\sim$ 800 mK, the ^{3}He-^{4}He mixture starts to separate in the two phases, as we saw in section 2.2.1. The dilute phase expands from the bottom of the mixing chamber to the still, where the vaporized ^{3}He atoms are pumped out and then reinjected through the normal circuit in the concentrated phase of the mixing chamber: the dilution cooling process begin. The temperature rapidly decreases from 800 mK to about 40 mK, progressively slowing down to finally approach the temperature of 20 mK. The injection pressure in the circuit is around 380 mbar, which is relatively low in comparison to other dilution fridges and permits lowering the vibration level. Figure 2.8 shows the evolution of the temperature of different elements of the cryostat: the data refer to a typical cooling cycle in real experimental conditions.

The cooling cycle

2.2.3 Measuring and controlling the temperature

Low-temperature experiments require a careful and reliable measurement of the system temperature. We employed 3 sets of 3 thermometers, one for the high temperature stages (90 K, 20 K and 4 K), and 2 sets for the low temperature stages of the cryostat and of the experiment. Depending on the temperature range, different types of sensors can be employed. Temperature measurements are here realized by measuring their resistance, which is largely varying with temperature. For the high temperature range, we employ *platinum resistors*, which present a very stable, linear and highly reproducible behavior in the region from 20 K to 300 K. They are manufactured to reach 100 Ω at 0 °C ($Pt100$) and saturate to a constant value around 4 K. At lower temperatures, we employed *carbon*

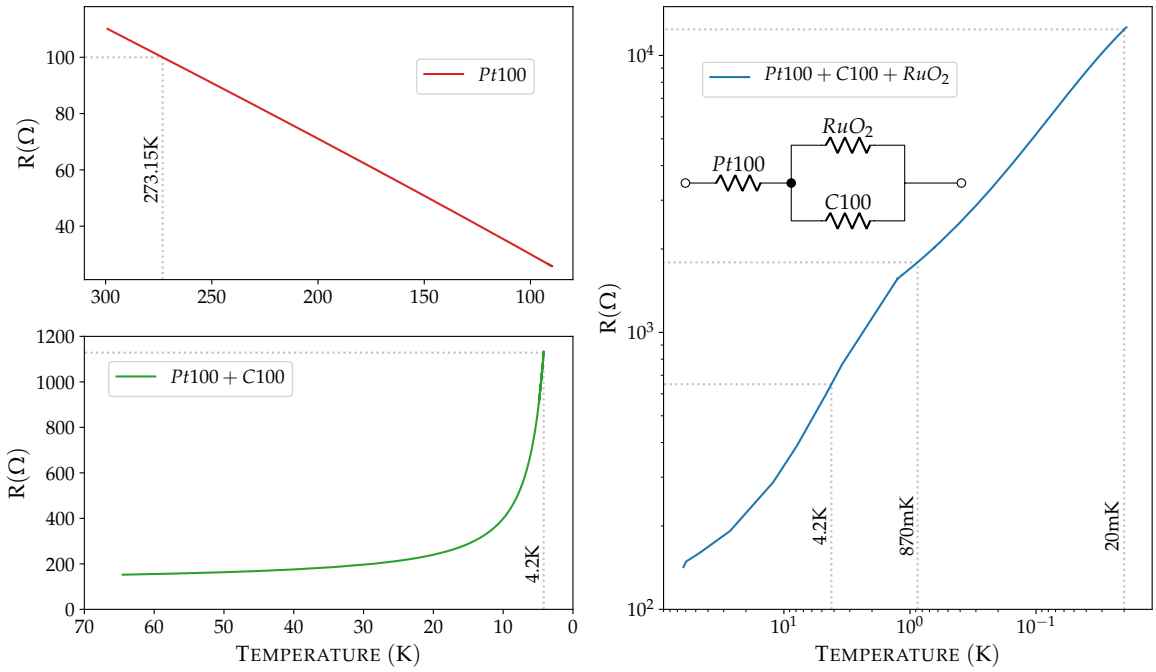

FIGURE 2.9 – Thermometers' resistances: experimental values for the different stages and resistances' scheme for the ultralow temperature ones.

resistor thermometers. The ones employed exhibit an increasing resistance for decreasing temperatures, that finally exponentially diverges at ultra-low temperatures, but are not really reproducible and require an individual calibration. We also make use of *thick-film resistors*, made of ruthenium oxide (RuO_2): they present a much better reproducibility and show a universal temperature dependence given by

$$R(T) = R_0 \exp\left(\frac{T_0}{T}\right)^{-0.345} . \tag{2.2.4}$$

A single platinum $Pt100$ resistor has been used for the 90 K stage, while for the other high temperature stages, a combination of a $Pt100$ with a carbon resistor was employed. For the low temperatures thermometers, a combination of a $Pt100$, a carbon $C100$ and a RuO_2 has been employed, in a configuration shown in the inset of fig. 2.9. This arrangement presents a non-monotonous resistance variation with temperature, it exhibits an inversion around 70 K and it is very convenient in the 10 K - 20 mK range. The temperature dependence of the thermometers' resistances is shown in fig. 2.9. The values at room temperature are: $Pt100(T_{\text{amb}}) = 100\,\Omega$, $C100(T_{\text{amb}}) = 100\,\Omega$ and $RuO2(T_{\text{amb}}) = 1\,\text{k}\Omega$.

Temperature measurement

MMR3 MODULE In order to read the actual values of the resistance thermometers different methods can be used, but typically a Wheatstone bridge is applied: using a four-terminal (or four-wire) sensing, a known reference resistor is compared to the one of interest. In our experiment this is done with a MMR3 (*Module de Mesure de Résistance 3 voies*) module: each module can measure up to three resistances at the same time, it can automatically adapt the injected current in the range $10\,\text{pA} - 20\,\text{mA}$ to enhance the sensitivity or minimize the heating induced by the dissipated readout current in the thermometer ($10\,\text{k}\Omega$ read with $1\,\text{nA}$ generate $10\,\text{fW}$ of heat) and it is capable of measuring values from $1\,\mu\Omega$ to $2\,\text{M}\Omega$.

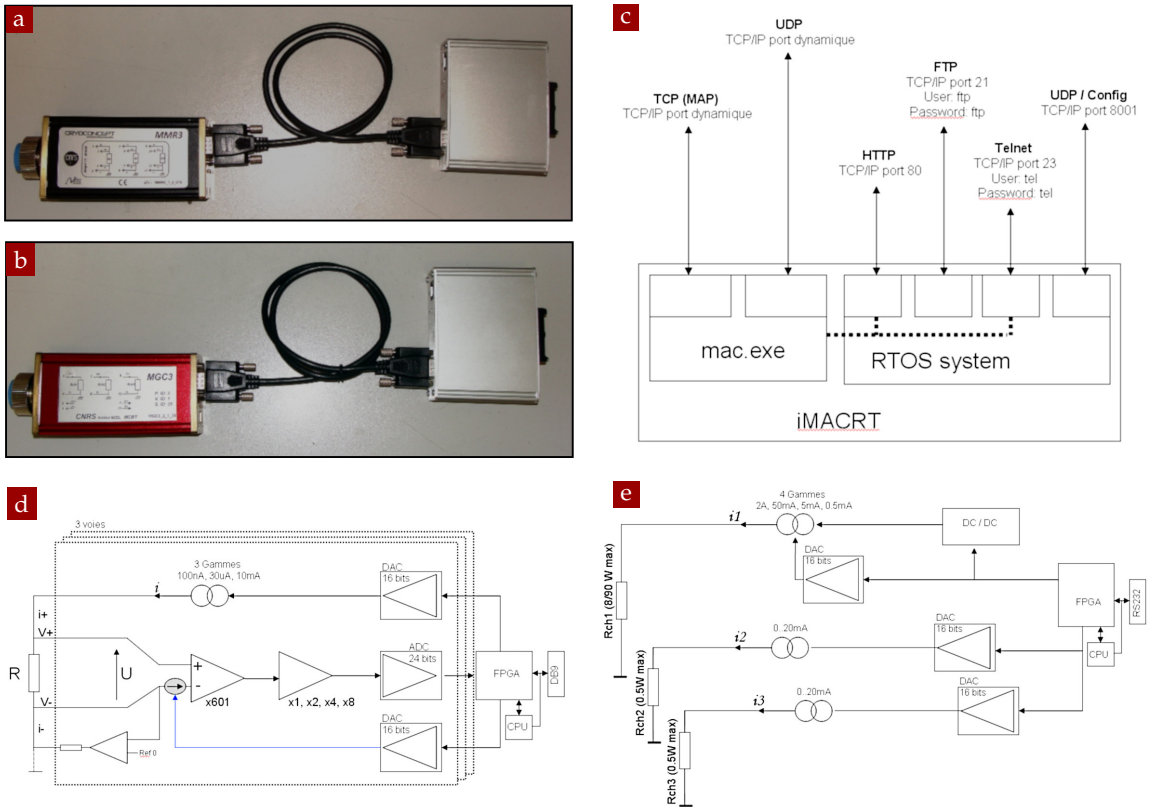

FIGURE 2.10 – The MMR3 and MGC3 controller: images of the components (a and b); schemes of the communication (c), temperature (d) and heater (e) modules.

The MMR3 is serially connected to a communication module MacRT (*Module Autonome pour le Controle et la Régulation de Température*) which serves as an interface and can be used to convert the measured resistance into a temperature. Multiple protocol are employed (HTTP, UPD, TCP) and a graphical interface on the browser can be used to control the instrument.

MGC3 MODULE Another important requirement for the kind of measurement we perform in our experiment (see section 3.2.2), is the possibility to vary the temperature of our sample inside the cryostat, or to adjust the cryostat temperature directly. This is realized with heating resistors placed in the cryostat, directly on the experimental platform or on the cold plate, through which is flowing a current provided by the MGC3 (*Module Générateur de Courant 3 voies*) module. This current generator exploits the Joule effect to locally warm up the system. Again, three parallel circuit can operate three heaters simultaneously, each of which is connected to a PID loop that can work in three different modes: current regulation, power regulation and temperature regulation. The first simply fixes and keeps a constant current through the load. The second, given the value of the resistance, regulates the current in order to produce a constant heating power. Ultimately the third one, for a given value of the resistance and if properly coupled with a MMR3 thermometer, can produce the needed amount of heat to keep the system at a stable assigned temperature. To properly perform the latter as desired, the parameters of the PID must be manually optimized depending on the temperature range to explore (the cooling power of the cryostat is not linear in temperature).

Temperature regulation

2.2.4 Environment acoustic isolation

A key component in the realization of this work, is the ability to measure the small thermal vibrations of a single nanowire at dilution temperatures, without driving the nanowire into an unwanted motion. This is remarkably challenging since the nanowires employed are extremely soft. In particular, if their base is shaken resonantly, it can drive its vibrating extremity very efficiently. We measured that a random noise of a few $\mathrm{pm}/\sqrt{\mathrm{Hz}}$ applied at the mechanical resonance is capable of driving the nanowire up to an effective temperature of approx. 300 mK. This observation imposes stringent conditions on the reduction of the acoustic noise in the experiment. Furthermore, all the low frequency vibrations are impacting the working point of the system, generating heat inside of it, but they can also blur the optical images and create some errors in the measurement schemes. As such, they should also be reduced as much as possible.

To do so, wet dilution fridges present a quieter acoustic environment, in particular compared to dilution fridges based on pulsed tubes to precool the system. The latter has become the typical choice for many groups, mainly due to the shortage of helium on the market, but implies several technical challenges (see [60, 58, 150, 115]) to reduce the level of vibration on the sample. In particular, in our system, the rather low injection pressure ($\approx$ 400 mbar) also allows to reduce the acoustic noise originating from the mixture circulation. The absence of a pump on the ^{4}He circuit also goes in the same direction.

We isolate the cryostat from the acoustic noise produced by the external pumps used to operate it by placing them in a different room (underground). We dampened their vibrations using two solid concrete blocks, which incorporate all the tubes connected to the cryostat (see figs. 2.11 and 2.12). Additional precautions have also been taken: the whole optical table, where the experiment lies together with the refrigerator, stands on a massive concrete platform that is mechanically isolated and disconnected from the rest of the building. Finally the optical table itself is hydraulically suspended and the ^{4}He tank is screwed on the bottom side of the table and is not in contact with the ground, to further prevent any other type of low frequency noise to enter the system.

FIGURE 2.11 – Acoustic isolation and gas handling system of the cryostat: photo of the experimental setup.

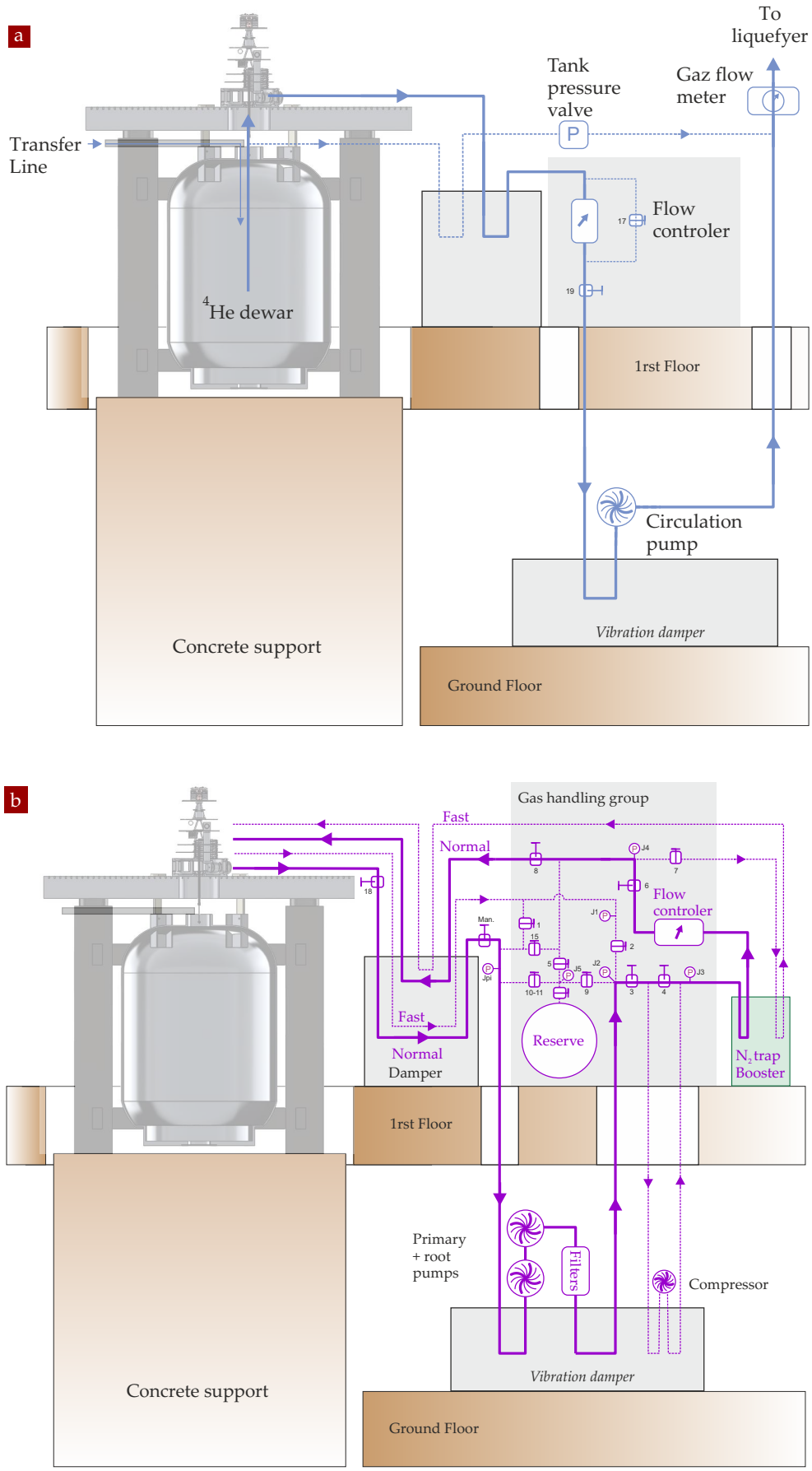

FIGURE 2.12 – Scheme of the gas handling system in real space: (a) scheme of the ^{4}He open-cycle circuit; (b) scheme of the dilution close-cycle circuit.

2.2.5 Cryostat control and interface

Running and operating a dilution cryostat is a rather delicate procedure, for which an independent automaton was developed in the lab, mainly by P. Gandit. It manages all the valves, sensors, pumps and security procedures required for the normal functioning of the refrigerator. The automaton is controlled by means of a Labview software. The interface of the software is displayed in fig. 2.13. The operation of the cryostat can be entirely automatized and realized remotely.

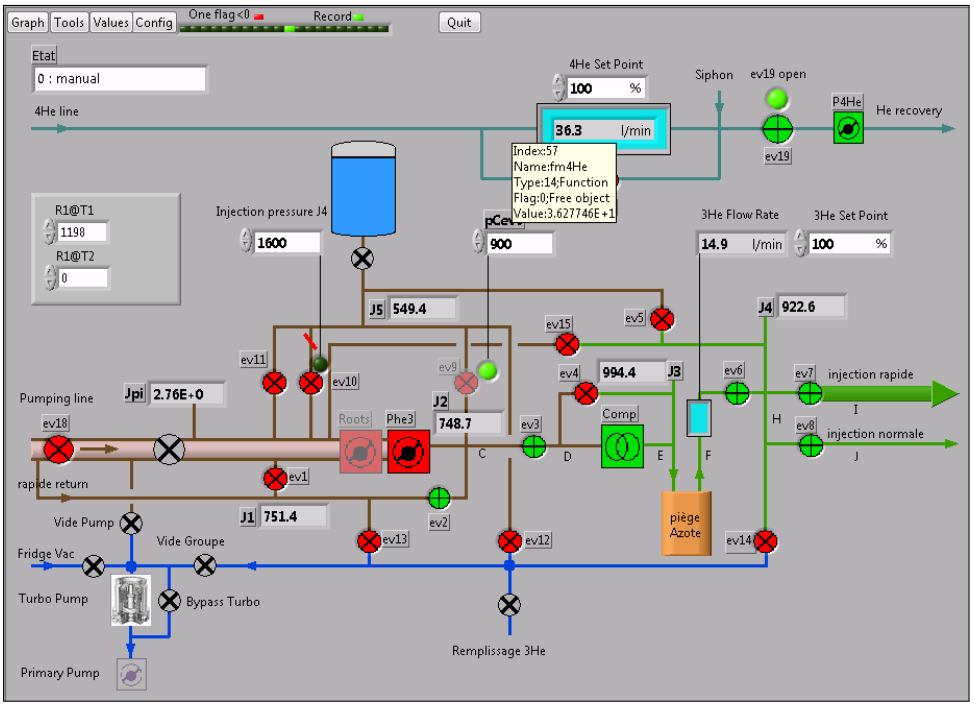

FIGURE 2.13 – Graphical user interface of the Labview software used to control the cryostat operation. The electronically controlled valves are shown as circles ($ev+$number), the pressure measured by the different gauges are shown and labeled as $J1$, $J2$... The flow regulators appear as blue boxes.

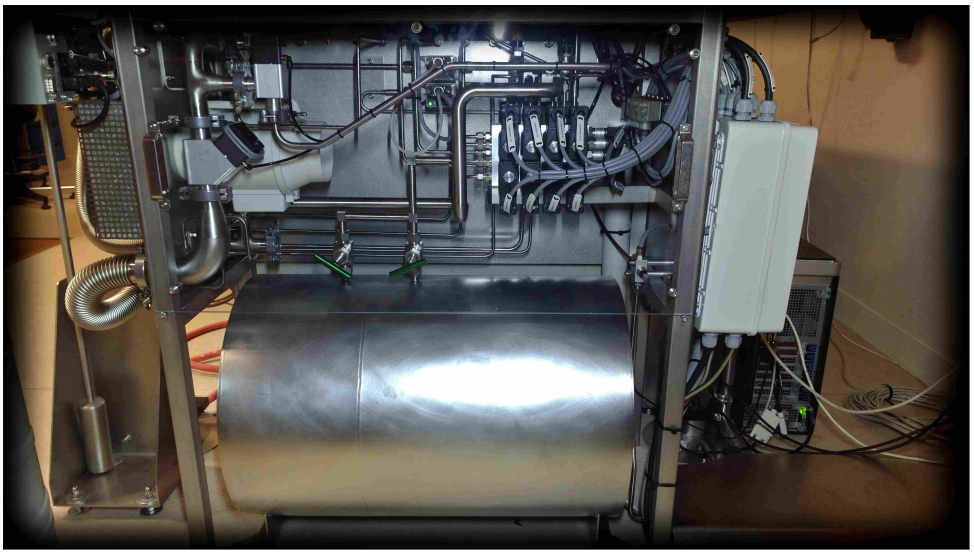

FIGURE 2.14 – ^{3}He reserve and main component (valves, gauges, etc.) of the gas handling group.

2.3 OPTICAL CRYOGENIC HEAD

We describe here the optical head that has been installed on the cold plate of the cryostat. The objective was to verify the possibility to operate our ultrasensitive nanowires at dilution temperatures, to explore their mechanical properties, and to verify the possibility to observe them thermalised at low temperatures.

The principle of the optical head is shown in fig. 2.15. We now describe the setup in greater detail.

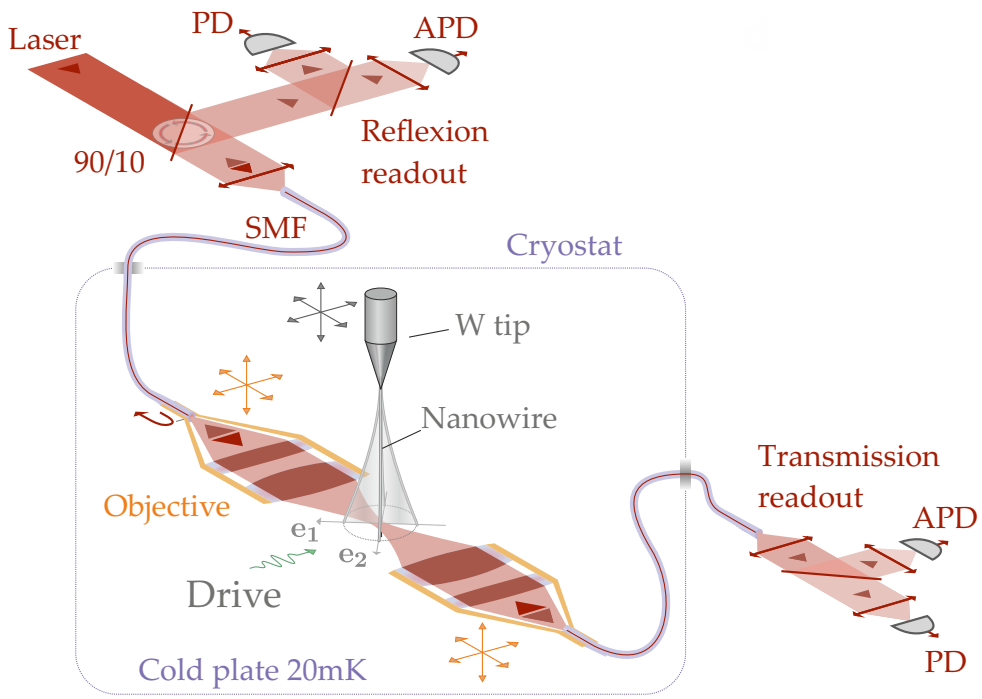

FIGURE 2.15 – Scheme of the optical cryogenic head: through a 90/10 beam splitter the light is injected into the fiber at room temperature. The fiber then reaches the 20 mK cold plate where the objectives focus the laser beam on the nanowire. The light reflected at the fiber interface interferes with the one reflected from the nanowire and is collected back from the same fiber. The transmitted light can also be collected from the second objectives. The two objectives are identical and interchangeable.

2.3.1 Interferometric objectives

Performing optical measurements at low temperature can represent a difficult challenge, especially when working in the sub - 100 mK range, due to the limited cooling powers available at those temperatures (few µW at 20 mK) and to the various technical difficulties. In the group, the optical readout of the nanowire's vibrations was realized using high numerical aperture objectives and free space optics. Employing free space optics has been realized by many groups at dilution temperatures [144, 9, 204, 176, 159, 15, 109, 25, 165, 164, 153]. This is rather delicate in our case since the cryostat undergoes large thermal expansions, which would require a permanent re-alignment during the temperature cycles. Furthermore, the commercial objectives make use of several doublet or triplet lenses whose optical glue can break under thermal cycling. Also, adding optical windows on the screens represents in itself an involved engineering challenge. Those difficulties led us to develop our own optical apparatus, based on optical fibers.

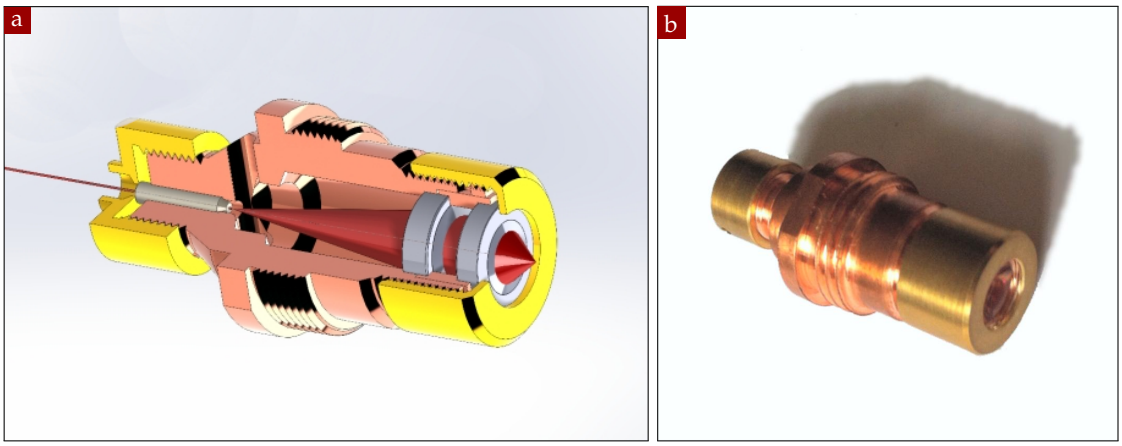

FIGURE 2.16 – Scheme (a) and picture (b) of the cryogenic objective developed to optically probe the vibrations of the nanowires, capable of working continuously and reliably from room temperature to 20 mK.

A couple of interferometric objectives have been developed in order to optically probe the vibrations of our samples. The probe light is focused in a monomode fiber at room temperature, which then enters the cryostat and is carried to the cold plate, where the other fiber extremity injects light in the objective, as shown in fig. 2.15 and fig. 2.16a. Particular care needs to be taken where the fibers enter the vacuum chamber, in order to avoid any leak but at the same time not to damage the fibers themselves. Concerning the thermalisation instead, due to the poor thermal conductivity of glass, no particular attention is needed and we simply attached them on the cold elements with a conductive tape.

A ferrule is used to hold the fiber in place: as shown in fig. 2.16a, the light escaping the fiber extremity is collimated by a first aspheric lens with focal length of 15 mm and is subsequently focused by a second one, with focal length of 3 mm and numerical aperture of 0.72. The overall transmission has been measured around 92% at 633 nm and produces and optical waist of around 500 nm, with a working distance of 2.5 mm. When the nanowire is inserted in the optical spot, part of the light is back scattered into the optical apparatus and makes it possible to realize an optical readout of its nanomotion. The dimension of the objective, the space between the lenses and the focal distances have been chosen to minimise the waist dimension, while keeping a light ($\sim$ 15 g with optics) and compact assembly that can be mounted on our piezo-motors (see section 2.3.3). The overall dimension is around 28 mm, so that 2 of them placed in front of each other can easily fit on the cold head without bending the fibers excessively. Single-mode APC fiber connectors are spliced at the input side of the fibers, in order to minimise parasitic reflections. Numerical simulations under Zemax, realized by C. Felix from the *pole optique et microscopies* in the lab, were run in order to validate our initial design.

The objectives' body and spacers are made of OFHC copper[4], which presents a better heat conductivity at low temperatures, while two brass caps are used to hold the optics. The expansion coefficients for copper, brass, and glass, integrated from 0 to 300 K, are around 3.4, 3.9 and 0.5 mm/m respectively [246, 255]. As such the total contraction of the copper frame is around 100 µm during a cool down, while the corresponding relative length change on the 3 mm thick optics is around 8 µm, which is small enough to neither break the objectives nor create appreciable strain induced birefringence.

[4]Oxygen-free high thermal conductivity copper

The final system is perfectly operational from room to low temperatures and has proven to be capable of sustaining multiple cooling cycles (> 30) without significative change. A prototype is shown in fig. 2.16b. The objective is then screwed on a copper support, which is thermalised to the 20 mK stage using soft copper braids (see fig. 2.23a).

Furthermore, in addition to the already described capabilities, this assembly also exhibits a very practical interferometric behaviour that significantly enhanced the measurement efficiency. Due to the partial reflection on the glass-air interface at the extremity of the injection fiber in the objective, part of the injected light, roughly 4%, is reflected back into the fiber and channelled back to the detectors placed in reflection. This then interferes with the light that, once collimated and focused, is reflected back from the sample (the nanowire in our case). The difference in optical path length between both interfering signals is of $2 \times 22 = 44$ mm, which is significantly smaller than the optical coherence length of our *HeNe* laser (tens of meters), and could be observed with any laser source featuring a spectral linewidth smaller than a few GHz (a pm wide in the visible).

This interference creates a spatial modulation in the reflected signal, with a periodicity $\lambda/2 = 330$ nm along the optical axis, which is significantly smaller than the scale of variations observed in a normal RT setup, which is around the Rayleigh length along the optical axis. This increased slope will then provide larger measurement vectors. The drawback is of course the lack of $2D$ readout capacity, but it can be compensated by the use of 2 objectives simultaneously.

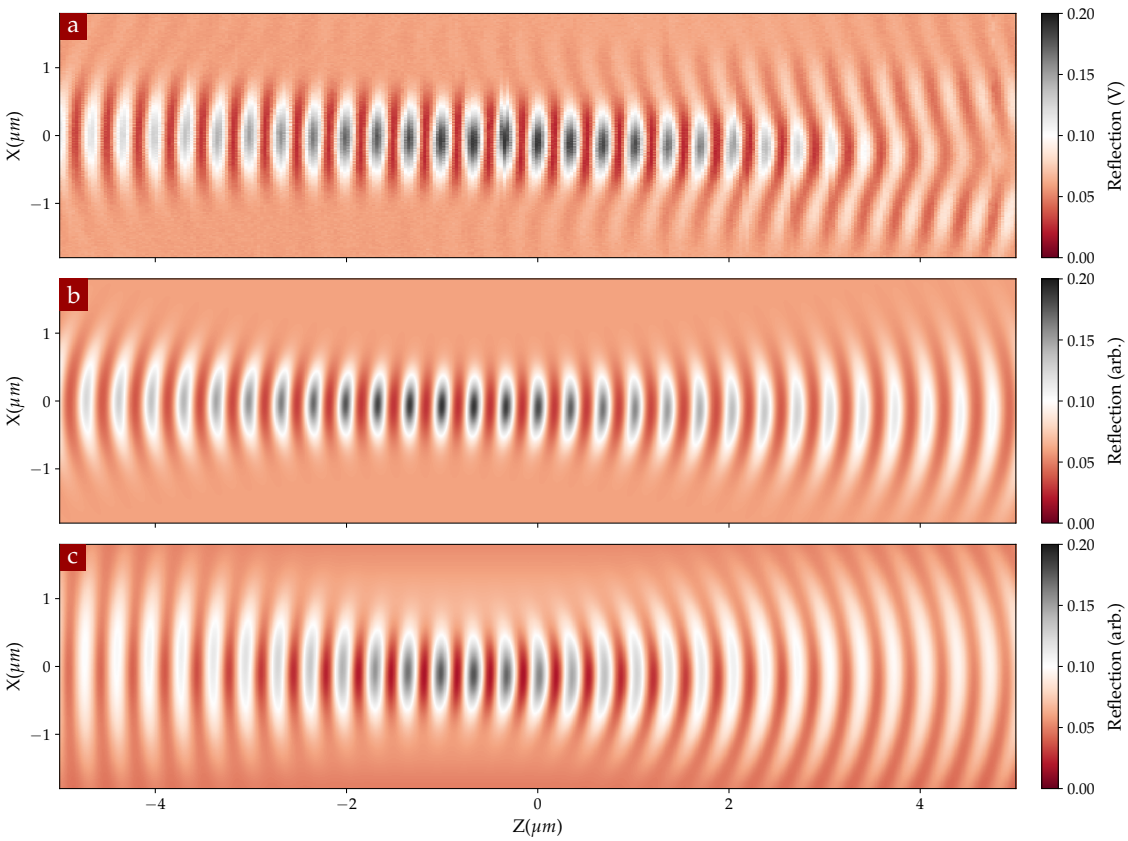

FIGURE 2.17 – Cryogenic objectives interference pattern: (a) experimental signal corresponding to an input power of $\sim 1\,\mu$W; (b) 2D plot calculated using the parameters from the fit: $w_0 \sim 0.7\,\mu$m, $\mu \sim 0.8$; (c) numerical simulation obtained with the *LightPipes* python package, supposing that the fiber's objective reflect $\sim 3\%$ of the injected light, the NW $\sim 2\%$, for a propagating beam with $w_0 = 0.75\,\mu$m.

The objectives have been machined by J. Jarreau from the mechanical workshop. During the mounting process at RT, particular care must be taken to precisely position the fiber along the optical axis. We optimized the distance to the first lens, aiming at producing the smallest possible optical waist, by realizing maps of the interference pattern in the XZ plane by scanning a nanowire in the waist area. Once the desired specifications are achieved, the fiber is fixed in place with the help of a UV glue. A typical XZ map measured in reflection (see setup in fig. 2.15) and obtained after optimization, is shown in fig. 2.17a: the image depicts the measured reflected signal, for a corresponding input power of $\sim 1\,\mu W$. To evaluate the optical waist, this data can be fitted using the expression:

$$I_R = I_0 \left| e^{\varphi_0} + \mu E_{00}(x,z) \right|^2 \tag{2.3.1}$$

where μ controls the contrast of the interference and $E_{00}(x,z)$ is the horizontal projection of the E field of a TM_{00} mode (see eq. (4.2.17) in section 4.2.3). The result is presented in fig. 2.17b. From the fit parameters we can extract a good estimation of the waist in the focal point, for which we usually obtained values between $0.5\,\mu m$ and $0.7\,\mu m$, depending on the collimator and on the wavelength in use. Finally fig. 2.17c presents a numerical simulation performed using the *LightPipes* python package, which as been used to further validate the setup. Note that the experimental data on the side further from the objective present some "ripples" due to non-paraxial effect typical of highly focused beams, that we didn't consider in our analysis.

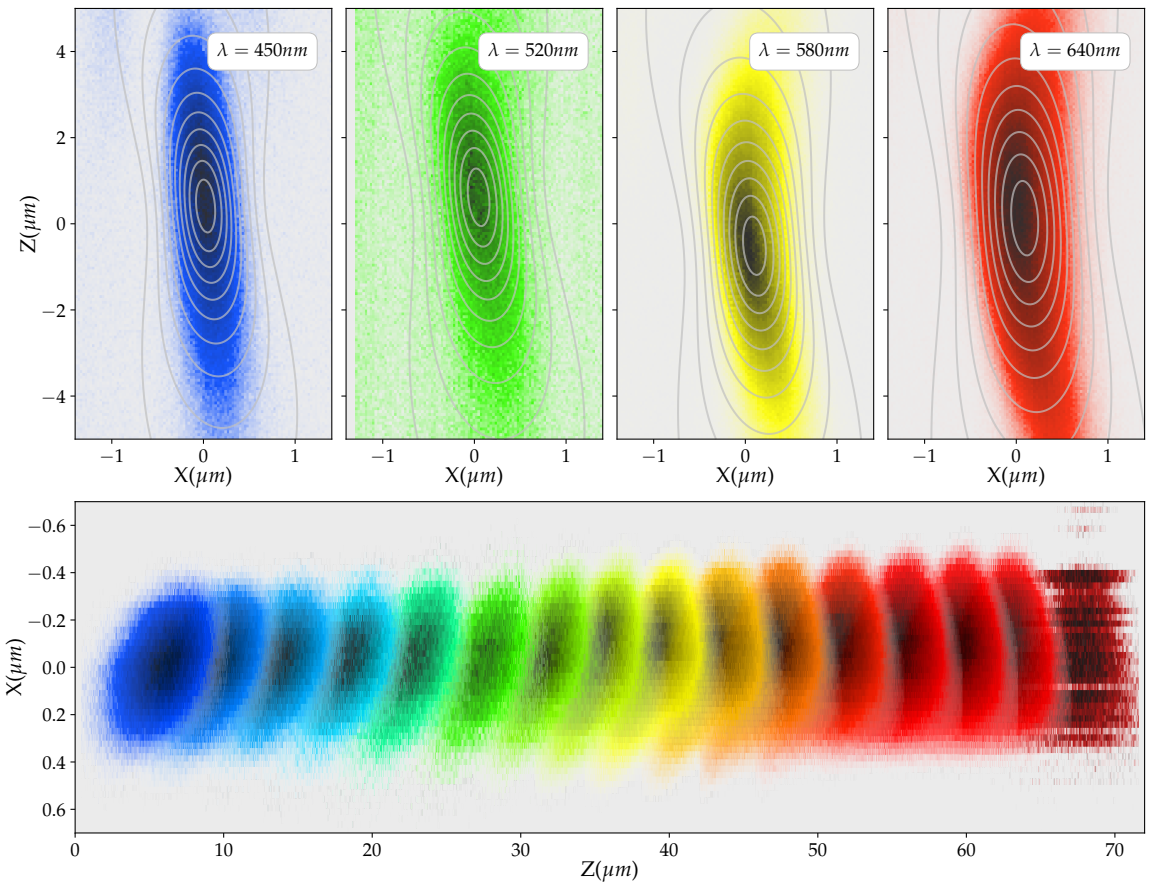

FIGURE 2.18 – Chromatic focal shift of the cryogenic objectives. On the top the XZ map for four different wavelengths and their relative fits are presented. On the bottom a concatenated image illustrates the chromatic focal shift for the following wavelengths: 450 nm, 460 nm, 470 nm, 480 nm, 500 nm, 520 nm, 540 nm, 560 nm, 580 nm, 600 nm, 620 nm, 640 nm, 660 nm, 680 nm, 700 nm, 750 nm.

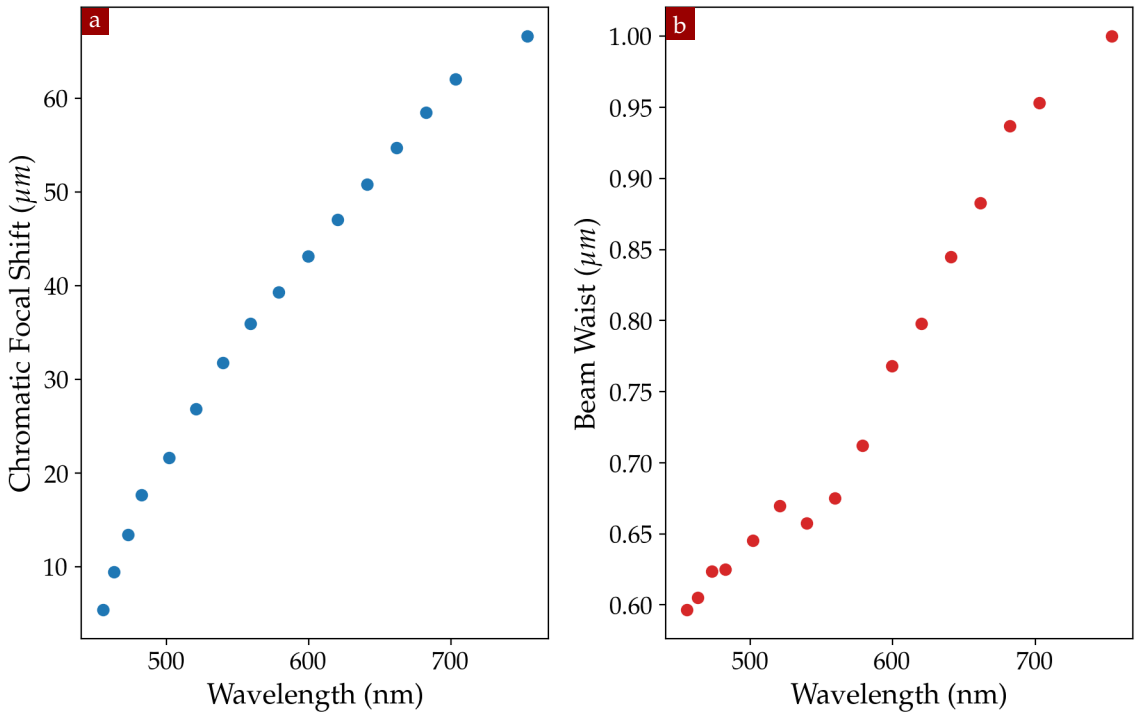

FIGURE 2.19 – Collimator chromatic focal shift (a) and beam waist dimension (b).

Those objectives are thus very interesting for realizing interferometric readouts of the nanowires. However they have a natural drawback, which is their large chromaticity, since they use a single-material aspheric lenses. To characterize the impact of the illumination wavelength on the beam properties, we used a Leukos Supercontinuum laser followed by a tunable monochromator from Leukos as well. Multiple scans have been performed in the wavelength range 450 nm to 750 nm, as displayed in fig. 2.18. On the top, the XZ maps and relative fits for four different wavelengths are presented; on the bottom, a concatenated image to illustrate the chromatic focal shift.

The first thing to notice is the absence of any interference pattern, due to the reduced coherent length of the laser light selected by the optical filters. This can be estimated with the formula [4] $l_c = \sqrt{\frac{2\ln 2}{\pi}}\frac{\lambda^2}{\Delta\lambda}$. For a typical commercial He-Ne laser (with linewidth of a few MHz), such as the one we normally use in our experiment, this gives a coherence length around 70 m. Instead, the Supercontinuum light is filtered by a tunable filter module using a spectral width of $\Delta\lambda \sim 3$ nm, which corresponds to a coherence length range of about 40 µm, too small compared to the path difference of the interferometer.

However, this measurement permits to measure the chromatic focal shift and the beam waist for each wavelength: the results are shown in fig. 2.19. Since the refraction index of glass in reduced at larger wavelengths, the focusing power of the aspheric lens is reduced at large wavelengths, causing a displacement of the waist area away from the lens. In the blue-green region the shift tends to be slightly bigger, of the order of 0.4 µm/nm, and the waist dimensions a bit smaller, typically around 0.65 µm. On the contrary, from the green to the near infrared region the shift are smaller, aroud 0.2 µm/nm, with increasing waist dimension up to $\sim$ 1 µm. Those values are comparable to the ones for similar commercial aspheric lenses and are overall quite good; they are fairly large compared to the axial spot size and this must be taken into account when working with multiple different wavelengths.

2.3.2 Nanowire support

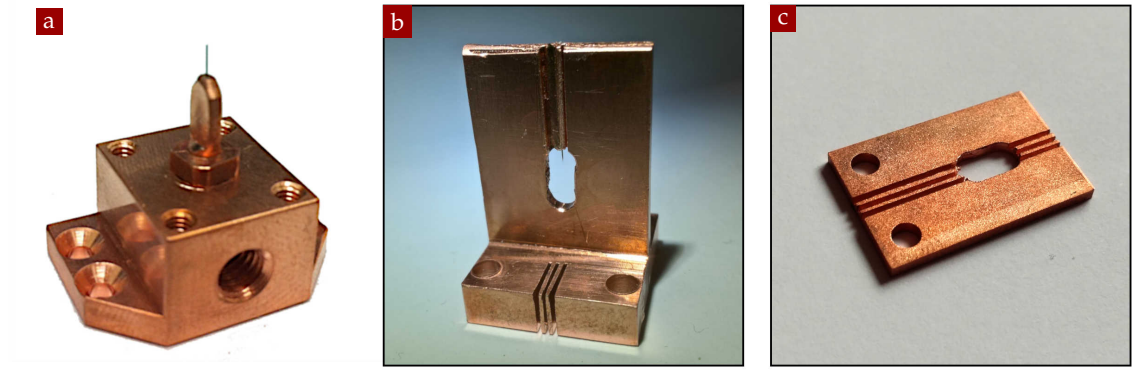

FIGURE 2.20 – First (a), second (b) and third (c) generation of the NW support.

Silicon carbide nanowires are extremely robust in comparison to their size, nevertheless their manipulation and mounting requires some attention. In particular, it is important to take a special care to their proper thermalisation in the cryostat. Due to the extremely small surface contact area between the nanowire and the tungsten support, and the Kapitza resistance appearing between materials having different phonon bands at low-temperature, their thermalisation is not trivial.

First the nanowires are glued on a sharpened tungsten tip, by mean of a carbon paste. The operation can be easily done under an optical microscope with a micro-manipulator. The nanowires employed in the cryostat are rather long ($> 100\,\mu m$) and we make sure that they are glued on a length of at least $50\,\mu m$ and up to $200\,\mu m$ for the longest nanowires employed ($300\,\mu m$). This is done in order to reduce the interfacial resistance, but places stringent conditions on the total length of the nanowire. The tip is then inserted in a highly conductive copper support, which is strongly compressed around it with the help of a hydraulic press, to ensure an optimal thermal connection and maximize the surface contact. Figure 2.20 presents the different generations of supports that have been developed: the first prototype was initially dedicated to only test the optics at dilution

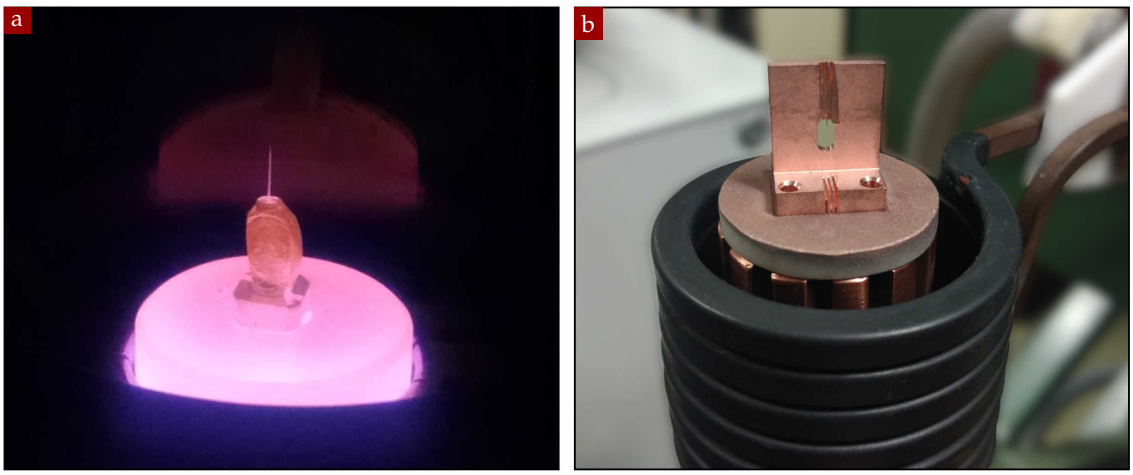

FIGURE 2.21 – Baking of a nanowire: 700 °C (a); induction oven (b).

temperatures, but we kept it cold for 6 months. The second version was developed in order to allow a force sensing geometry, where a test sample could be inserted in the opening. This configuration also protects the nanowire from unwanted shocks, and is aimed at creating a colder environment around the nanowire. The last version permitted a faster sample exchange and its use with the second version of microscope objectives featuring a larger NA (not described here).

Using an induction oven the nanowire, the tip and the support are later baked at a temperature of roughly 700 °C. This process permits to harden the glue, which significantly improves the mechanical quality factors at room temperature (from 1000 to above 10000). However, the best quality factors obtained at dilution temperatures (> 100000) were obtained with the first nanowire, that was not baked.

Finally the support is mounted on the piezo-scanner stage inside the cryostat and is thermally coupled to the 20 mK stage through a soft braid made of ultrapure copper whose extremities are sealed in a copper support using a magneto forming machine.

2.3.3 Piezo-positioners and scanners

The typical dimension of the laser waist is of the order of 0.5 µm, while the typical diameter of nanowire is around 200 nm. A refined alignment of the system is required and needs to be extremely precise and stable over long periods of time, both at room and at low temperature.

To do so we mount each objective on an Attocube's stepper tower to ensure a coarse positioning of the system while the nanowire support is mounted on an Attocube's *XYZ* scanner for fine positioning. The former are composed of two *ANPx*101 (open loop, linear, horizontal) stepper positioner, mounted perpendicular to each other and screwed on top of a *ANPz*101 (open loop, linear, vertical) stepper positioner (see fig. 2.22). These are slip-stick piezo actuators with a travel range of 5 mm, both at room and low temperature; the typical minimum step size is of 50 nm at 300 K (10 nm at 4 K) and the threshold voltage around 40 V. In addition it is possible to apply them a continuous tension and use the fine-positioning mode, with a range of 5 µm at 300 K and 0.8 µm at 4 K. The latter is a *ANSxyz*100*hs* (open loop xyz) scanner: at room temperature it allows to perform $40 \times 40 \times 4.3$ µm scans (respectively in the horizontal and vertical directions), while this range gets reduced to $9 \times 9 \times 2$ µm at low-temperature.

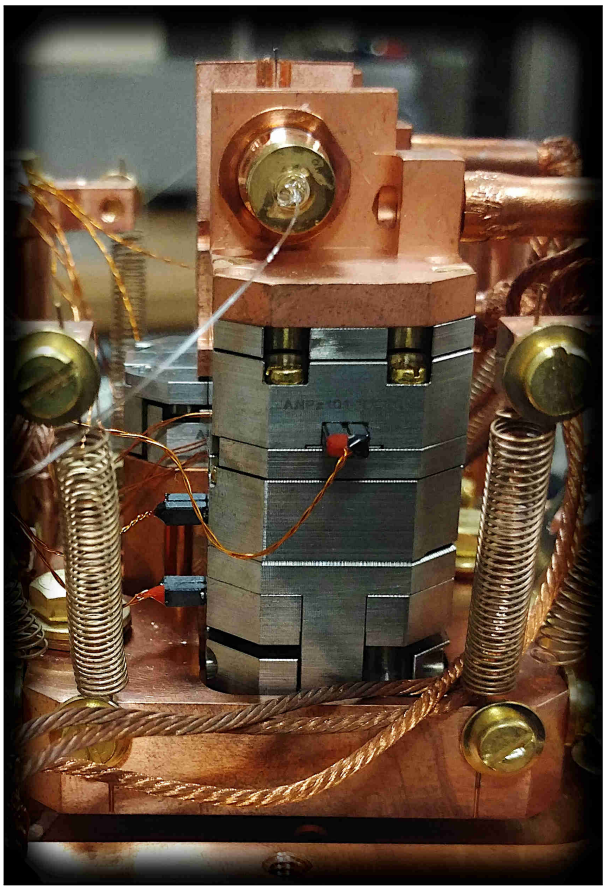

FIGURE 2.22 – Attocube stepper tower mounted on the suspended optical head

In term of reproducibility the steppers exhibit a significative hysteretic behavior in the µm range, sufficient to lose the alignment of the system, while for the scanner, especially at low-temperature, the difference between consecutive scans is of few nm (for a typical scan range of 1 µm). Concerning electrical noise some precautions must be taken: as we will extensively discuss in chapter 3, our samples are extremely sensitive to any source of noise, of mechanical and electrical origin. We observed that both the steppers and the scanner can introduce some appreciable position noise, which results in a false measure of the nanowire effective temperature. The problem can be mainly overcome for the steppers if they are grounded once the system is aligned; for the scanner, instead, it can be reduced by adding a low-pass filter on the control-box amplifier of the attocube. Normally a 3 Hz filter is applied during the mechanical spectrum acquisition, while a 30 Hz or a 300 Hz bandwidth is used when making scanning maps.

A certain attention has been required for the electrical cabling of the piezo elements. As far as the steppers are concerned, in order to preserve a rapid stage motion which is required for the stepping process to occur, it is necessary to provide sharp electric signals on the piezo. Since the latter has an intrinsic capacitance of a few µF, this imposes stringent conditions on the resistances of the cables from the controller to the cold plate. However, using low resistance wires leads to increased thermal flux, which heats up the cold plate. Also, we wanted to use the same wiring to operate the experiment at room and low temperature. To cope with this trade-off, we have employed superconducting wiring, based on NbTi wires from Supercon, with a superconducting temperature of approx 10 K. A first version of the cables used a too thin filament diameter, and it was not possible to operate the steppers at low temperature for long periods of time, because of a transition to the normal phase. Those lines are still mounted in the cryostat and provide electrical connections to the experiment. The final design made use of larger wires, model *SC - SW* - 18/10 - 0.203, which are made of 18 filaments of NbTi (30 µm each) inserted in a CuNi matrix, with a total diameter of 0.203 mm. 16 cables of approx 1 m in length are arranged together and directly go from 300 K to the 4 K plate (approx 20 cm) in order to minimize the cable resistance at low temp. A thermal connection to the different plates permits their efficient thermalisation and in principle the wires become superconductors before the 4 K plate. Above the 4 K stage they are progressively thermalised to the different stages before reaching a canon connector screwed on the bottom side of the top plate. Roughly 50 cm in length are bellow 1 K.

As far as the scanner module is concerned, since its piezo does not operate with pulsed signals, the requirements are less stringent and we employed lower diameters superconducting cables. We used 2 cables for each scan direction (signal and ground) instead of using a common ground, and all of them were inserted in a CuNi capillary running from 300 K down to 20 mK in order to shield them from external electrical perturbations that can shake the piezo stage, but also to protect them physically. To solder the extremities of those thin wires, the insulator was removed using a sharp tool and a copper thin wire was rolled around to facilitate the adhesion of the soldering tin.

Above the cold plate, where heat injection does not matter anymore, thin copper wires were employed from the cannon connector at 20 mK up to the piezo elements, in order not to apply strain on the positioners themselves.

2.3.4 Suspended optical head

Once all the external noise sources are properly suppressed, the internal noise which arises when operating the cryostat must be taken into account.

During the first measurement phases, we operated nanowires oscillating at frequencies smaller than 10 kHz, for which we observed a logarithmic relative frequency increase with the cryostat temperature, which was pointing towards the fact that the nanowire was correctly thermalised to the cryostat. However, we initially observed a too large thermal noise, that could amount up to a few hundreds of mK. A measurement of a 11 kHz nanowire showed the first noise temperatures below 50 mK indicating that we were in the presence of an environment induced noise that was "colored", i.e. presenting a non trivial frequency dependence. After a period spent hunting any possible electrical noise source, we finally realized that the circulation of the He mixture was indeed responsible for this excess of noise: we stopped the injection while still pumping the output port, thus cooling down the still due to the suppression of the hot mixture injection. Once it reached a temperature of 640 mK, we observed a quasi instantaneous reduction of the noise peak, indicating that a far lower temperature could be achieved on a low frequency nanowire. After calibration, its noise temperature dropped from 400 to 40 mK. This and other tests thus pointed towards the importance of decoupling the experiment from the residual cryostat vibrations. Using the scanner piezo as a reference actuator, we determined that a noise strength of $10\,\mathrm{pm}/\sqrt{\mathrm{Hz}}$ at 4 kHz shaking the base of the nanowire was sufficient to drive up to the effective temperatures we observed (400 mK), meaning that the level of vibrations on the cold plate was extremely small.

To compensate for this problem, the whole optical experiment was suspended above the 20 mK stage using a system of 8 springs which act as a low pass vibration filter: fig. 2.23 shows a simple scheme of the suspension and an image of the optical system before and after its implementation. The suspension mechanism has a cut-off frequency around 2 Hz and a loaded quality factor around 10 ($>$ 500 in absence of the thermal links). This parameters should ensure a damping by a factor larger than 100 in amplitude at 4 kHz, thus reducing the excess of noise by four orders of magnitude. The system was found extremely efficient, and effective temperatures around 30 mK could be measured under normal circulating conditions. In practice, even if the vertical and horizontal vibrations are not equally damped, and part of the acoustic noise can still travel through the springs and the thermal links, the suspension was remarkably effective. By reducing the level of vibration on the experiment, it also largely increased the quality of the images, which can now be realized even when the turbo pump used to evacuate the chamber is running. When pumping from room pressure, we also found that it largely reduces the relative displacements of the nanowire with respect to the optical waist, due to the reduction of static deformations on the base plate.

The force elongation curves for the springs were realized using an encoded displacement platform (the vertical axis on a numeric milling machine) and a balance supporting its lower extremity. Their individual stiffness is around 39 N/m, providing an estimated resonant frequency of 2.8 Hz when loaded with 1 kg, the approximate mass of the suspended optical head, when including the thermal links. These 8 Copper-Beryllium springs are placed with a slight angle in order to ensure a self centering of the optical head within the vertical posts.

Finally, a RuO_2 thermometer (from N. Roch) was installed to measure the suspended head temperatures. The latter was fixed on the cold plate using a stainless steel membrane, which presents a negligible conductivity at low temperatures, and thermally con-

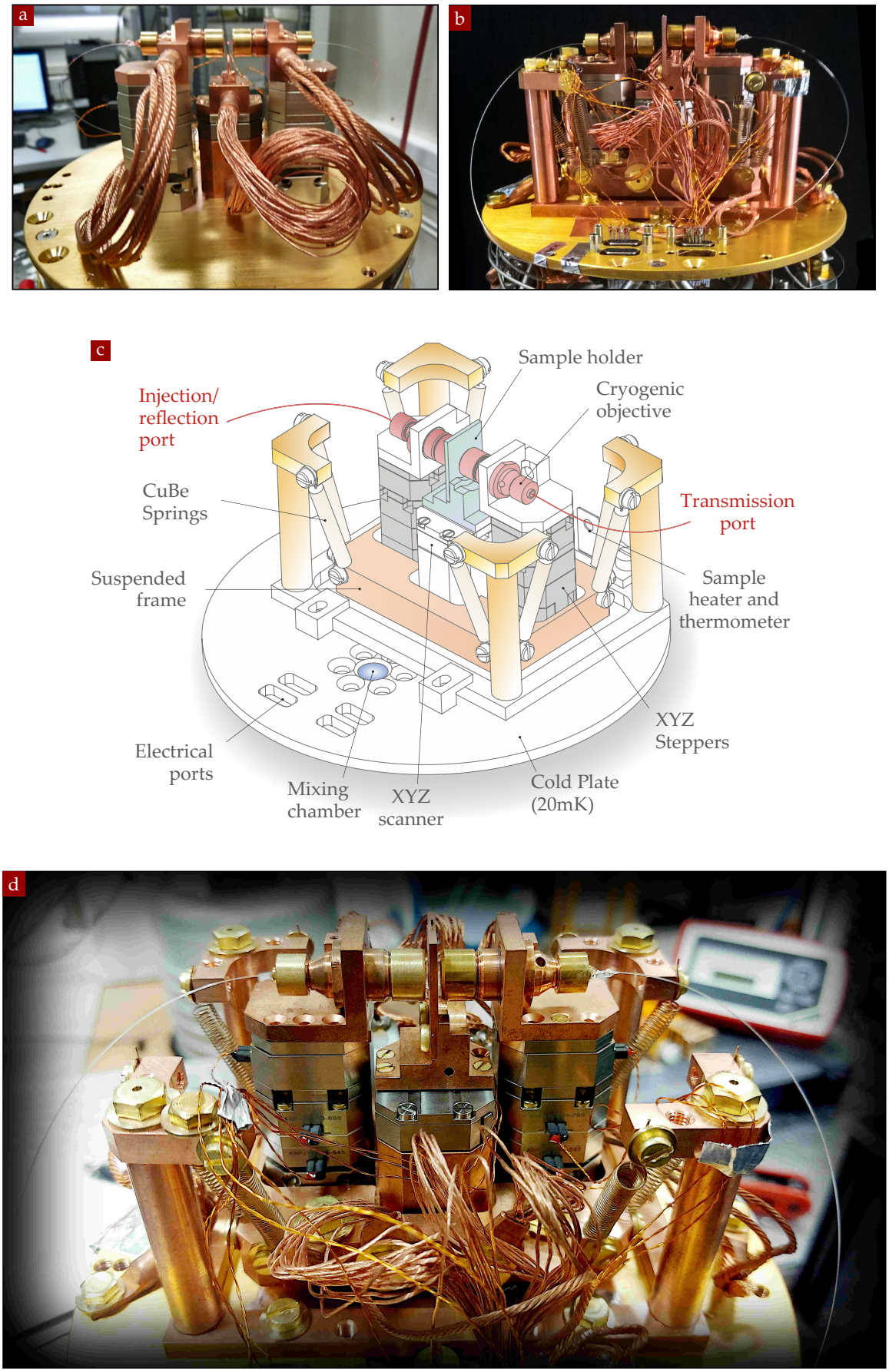

FIGURE 2.23 – Cryostat optical head: without suspension (a), with suspension (b,d), scheme (c).

tacted to the suspended head with flexible ultrapure copper braids. A heater was similarly installed, connected to the experiment base in order to warm up the experiment platform while minimizing the temperature elevation on the cold plate temperature. In presence of all those elements, the temperature of the experimental platform was measured at around 27 mK while the cold plate was measured at 22 mK. Furthermore, the thermal decoupling system installed with the heater allows to reach sample temperatures above 300 mK while keeping the cold plate below 100 mK.

To conclude, we also noted that when knocking on the optical table to shake the suspended platform, we could observe a direct temperature burst of up to 50 mK on the sample thermometer, lasting up to a few seconds, while the cold plate temperature did not show any measurable change. We note that if the 1 kg suspended head is lifted by 1 mm, this corresponds to a gravitational energy increase of 10 mJ, which would be dissipated in 100 s using a cooling power of 100 µW.

2.4 SYSTEM CONTROL AND SIGNAL DETECTION

Moving away from the cryostat itself, we will now illustrate the control system that we employed to operate both the refrigerator and the piezo-motor on top of it. We will then focus on the generation, control and detection of the optical signal. To conclude, we will detail the calibration process that we developed to operate in the photon-counting regime, that, as we will explain in section 3.2, in one of the main requirement of our experiment.

2.4.1 Experiment control and interface

The actual experiment, concerning the stepper-motor, the scanner, the laser power and the signals acquisition, is controlled by mean of the *Nano-Imaging-Lab* (NIL) software, a custom python-based program developed in the HQNOM group[5]. The software has a modular structure that can be adapted depending on the instruments required for the specific experiment. In the present case, a main module was use to communicate with a *National Instrument PCI-6323e* acquisition card which offers multiple input channels (with a maximum sample-rate per channel of 250 kS/s/n, where n is the number of channels), as well as two counters (used for the acquisition of the photon counter signal, see below) and four output signals. Three of them are use to control the Attocube's scanner to adjust the NW XYZ position. The clock of the card is used to synchronise the input and output signals as well as the other instruments. A second module permits to move the stepper-motor (which can also be manually activated throught the Attocube's control box). Additional modules enable the communication with an Agilent MXA $N9020$ spectrum analyser, an Agilent $E5061B$ network analyser and a lock-in amplifier (Zurich Instrument HF2LI). The laser power is adjusted and modulated via an acousto-optic-modulator (AOM), electronically controlled by the output of the network analyser or by mean of the last DC output of the main DAC card. The interface of the program is shown in fig. 2.24. Finally, a scripting module permits to launch generic tasks involving multiple instruments. This can be used to realize noise measurements at different points in space,

[5]Following a first implementation made by A. Gloppe, this software has been mainly created by L.M. de Lépinay, with subsequent contribution from the author, B. Besga and from P. Heringlake.

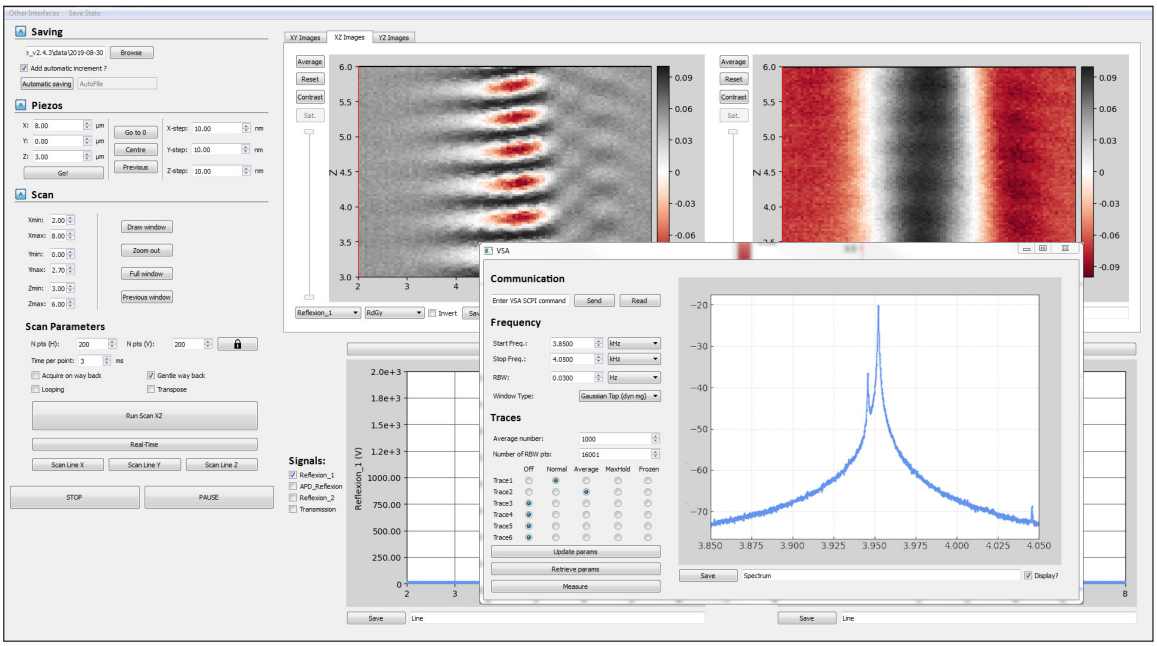

FIGURE 2.24 – User graphical interface of the NIL software.

to realize a power or temperature sweep while recording mechanical signals, or locking the nanowire position on the side of an interference fringe.

2.4.2 Optical scheme

The readout of the NW mechanical vibrations is realized by a visible He-Ne 633 nm red laser (2 mW), which is significantly far away from the optical bandgap of 3C (4H) silicon carbide at 525(385)nm, in order to minimise the energy absorption from the probe light.

The laser intensity that we will normally inject into the fiber ranges from few hundreds of femtowatts to few nanowatts. In order to generate such small laser power as well as to vary it over several order of magnitude, we first employ two subsequent combinations of a half waveplate, a polarizing beam splitter (PBS) and a polarizer (cfr. the scheme in fig. 2.15). This permits to highly reduce the light intensity and to allow a first coarse regulation. A narrow-line filter is placed at the output of the laser to suppress unwanted radiation. The polarizers placed in front of each PBS compensates for the non-ideal behavior of the cube and the non perfectly linear polarization state of the laser. The optical power is then finely adjusted by an AOM. Even if it shows a power cancellation larger than 60 dB, it is employed to vary the injected power over more than three orders of magnitude. If larger power spans are required, we use neutral density filters inserted in regions of low optical power in order to minimize parasitic fluorescence and the impact of thermal deformations.

Given the symmetry of the setup, both fibers entering the cryostat can be used to illuminate the nanowire and to collect the reflected or transmitted light. A 90:10 non-polarizing cube is placed before the fiber injection, allowing to collect $\sim$ 90% of the reflected light. A switchable mount is employed at the entrance of the second fiber, that can be used to measure the transmitted light or, when combined with a 99:1 fibered beam-splitter, to perform reflection measurement. The fiber injection is realized with an aspheric lens with focal length $f = +4.03$ mm (C340TMD-A).

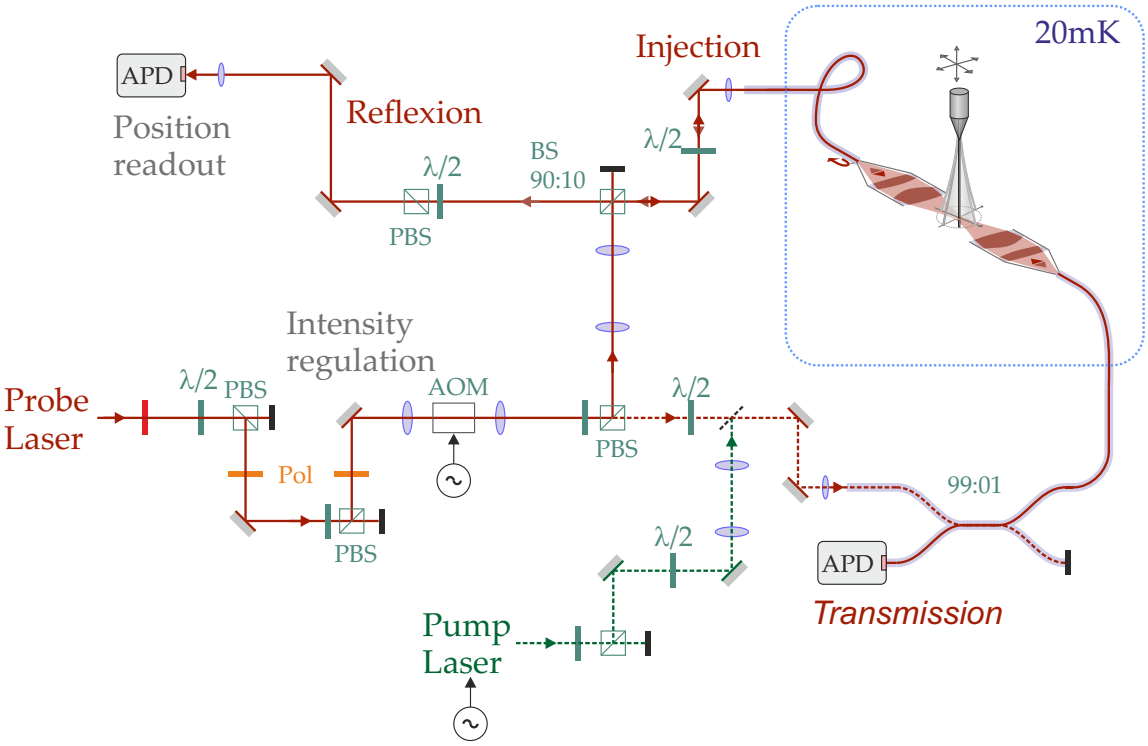

FIGURE 2.25 – Scheme of the optical setup.

In order to enable pump-probe measurements at different wavelengths, which facilitate the pump cancellation in the probe channel, one of the objectives was realised using a Thorlabs SM600 single mode fiber (operating wavelength 633-780 nm), while for the second we employed a Thorlabs SM450 (operating wavelength 488-633 nm). The coupling efficiency to the input port of the fiber, the propagating losses in the entire system (fiber plus the objective), the coupling efficiency between the two objectives and the overall transmission efficiency (for a beam propagating in both directions), are reported in table 2.1 for both wavelengths.

λ(nm)	η_r	fib$_r$+Obj$_1$	Obj$_1 \leftrightarrow$ Obj$_2$	fib$_g$+Obj$_2$	η_g	$T_{r\to g}$	$T_{g\to r}$
633	92%	86%	30%	62%	87%	14.5%	14%
515	80%	62%	30%	46%	75%	6.7%	6.4%

TABLE 2.1 – Efficiency of the coupling to the input fibers, full transmission of the objectives, including the 4% reflexion on the fiber output, objective to objective transmissions and overall transmission of the system. Note that while the first objective was fully optimized, the second one was repaired after a problem in the splice and could not fully recover. Also in the experiment we had no angle adjustment which could have permitted to increase the objective-objective transmission.

2.4.3 Vibrations measurements in the photon counting regime

In section 2.3.1 we showed the typical interference pattern $\mathbf{\Phi}_R(\mathbf{r})$ obtained on the reflection channel when scanning a nanowire in the horizontal XZ plane of a laser beam, around the waist area of our cryogenic objective. The expected $\lambda/2$ axial periodicity is used to calibrate the piezo displacements at any temperature. This is important since they exhibit a substantial temperature dependence and the total scan span is reduced by a factor of around four from RT to low temperature. We adopt the same contraction coefficient

along the two horizontal axes. For the vertical axis, since we use extralong nanowires, a precise calibration is less important, and we only adopt the manufacturer's parameters. We now expose the calibration steps required to exploit the nanowire induced intensity fluctuations to probe its vibrations.

Looking at fig. 2.26c, when the NW extremity is positioned on a slope of the interference pattern $\mathbf{\Phi}_R(\mathbf{r})$, its transverse vibrations $\delta\mathbf{r}(t)$ around its rest position $\mathbf{r}_0$ are dynamically encoded as temporal variations of the reflected photon flux $\mathbf{\Phi}_R(\mathbf{r}_0 + \delta\mathbf{r}(t))$, which can be written at first order: $\delta\mathbf{\Phi}_R(t) = \nabla\mathbf{\Phi}_R|_{\mathbf{r}_0} \cdot \delta\mathbf{r}(t)$. This provides a $1D$ measurement channel of the nanowire vibrations $\delta r_\beta(t) = \mathbf{e}_\beta \cdot \delta\mathbf{r}(t)$, projected on a normalized measurement vector defined by $\mathbf{e}_\beta \equiv \nabla\mathbf{\Phi}_R|_{\mathbf{r}_0}/|\nabla\mathbf{\Phi}_R|_{\mathbf{r}_0}|$. The latter is measured by a routine computing the local tangent plane to the surface $\mathbf{\Phi}_R(\mathbf{r})$ [86, 56].

Compared to room temperature measurements, the calibration of the measurement vector is done very slowly, first in order to let the oscillator reach its stationary rest state, (inverse damping rate of a few tens ms at 20 mK). Also, we average the signals over a sufficiently long measurement time in order to limit the variance of the photon flux measured in each point. The slope measurement algorithm also records the variance of the measurement sequence.

To compute the measurement vector, we measure the reflected flux at different points around the measurement position. We generally stay 100 ms per point, each measurement sequence is made on a set of approx 10 points arranged in a matrix around the central point and is repeated $\sim$ 10 times. The total acquisition time for a proper measurement vector at sub-pW fluxes typically lasts for 30 s. Repeated measurements give a reproducibility of a few % which is rather low when considering the optical powers engaged, but represents the main limiting factor in the precision of the noise temperature measurement.

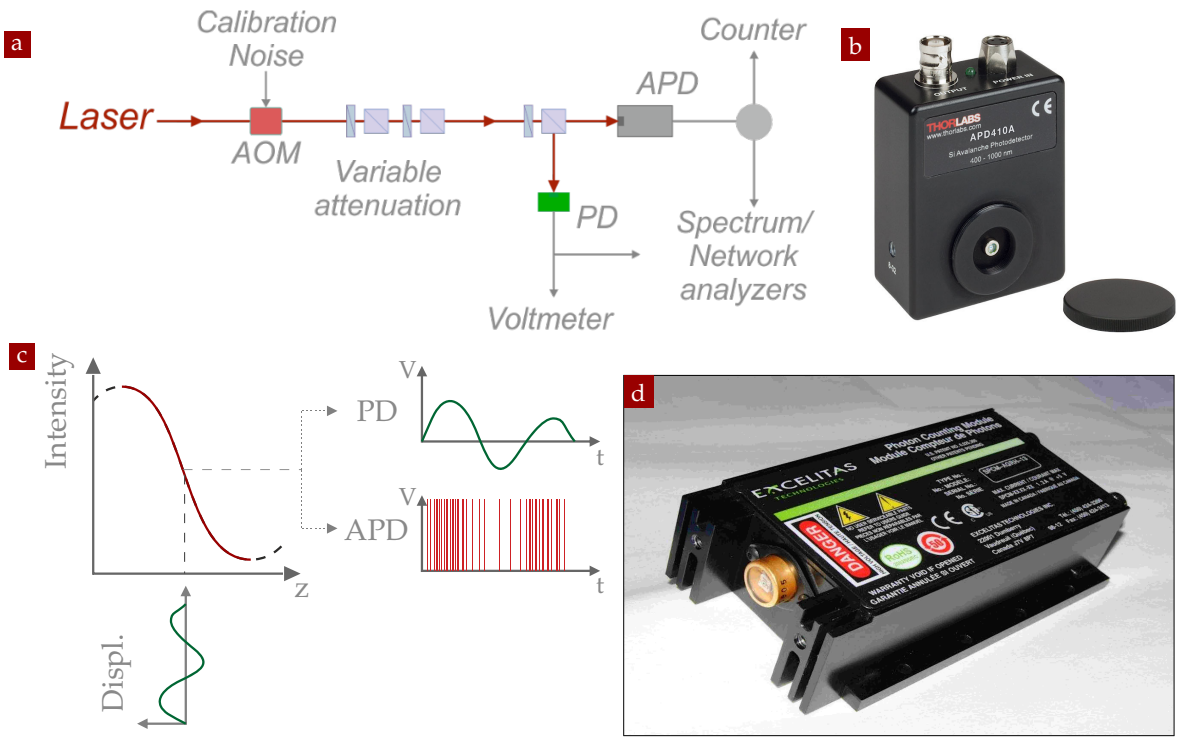

FIGURE 2.26 – Scheme of the setup used to calibrate the photon counter spectrum signal (a). The standard photodiode used for the calibration (b). Schematic comparison of the difference between the PD and APD signal (c). The single photon counter used in the experiment (d).

In the room temperature experiments of the group [86, 56], the nanowires vibrations are recorded on continuous detectors, providing a map of the time-averaged reflected intensity ($P_R(\mathbf{r})$), instead of a photon flux map $\mathbf{\Phi}_R(\mathbf{r})$. We will see in section 3.2 that in order to avoid optical heating of the nanowire due to residual absorption, it is necessary to operate at ultralow (sub-pW) injected optical powers. Normally in this situation the NW induced intensity fluctuations would be hidden by the detector's dark noise. To circumvent this limitation we employed a single photon counter, specifically an *Excelitas SPCM-AQRH*-15 avalanche photodiode, operated in Geiger mode and featuring an approx 50 cps dark count rate[6], corresponding to ≈ 15 aW in the visible.

In real time, the output signal of the APD is made of a sequence of voltage pulses, and the vibrations of the oscillator in the interference map modulate the sequence of photon detection time. One can intuitively understand that the autocorrelation function of the pulse sequence is directly connected to the autocorrelation function of the oscillator position. However the proper connection between both signals requires a bit of investigation, as well as the impact of shot noise in such a measurement sequence.

Figure 2.26c schematically compares the signal of a standard photodiode to that of a photon-counter: instead of a continuous varying voltage signal, we now a have a sequence of single photon pulses, whose density vary over time. This kind of signals are called pulse-density-modulation (PDM). They can be averaged over a measurement gate time, to obtain a mean photon flux (in cps or Hz^{-1}), analysed with time stamping devices to acquire the full temporal statistics or alternatively resolved with a spectrum analyzer, which is the case we are currently interested in. However, a proper conversion coefficient η (in V/cps) must be determined to extract the projected displacement noise spectral density, that is $S_{\delta\mathbf{r}_\beta}[\Omega] = S_V[\Omega]/(\eta^2|\nabla\mathbf{\Phi}_R|_{\mathbf{r}_0}|^2)$.

MEASUREMENT PRINCIPLE The photon-counter output signal is made of a series of voltage pulses:

$$V_R(t) = \sum_i V_\pi(t - t_i) \tag{2.4.1}$$

where the pulses are defined by the height V_π and their duration T_π as:

$$V_\pi(t) = V_\pi \qquad \text{if} \quad 0 < t < T_\pi, \qquad 0 \quad \text{otherwise.} \tag{2.4.2}$$

The probability $dp(t)$ to detect a photon between t and $t + \delta t$ depends on the position of the nanowire extremity $\mathbf{r}(t) = \mathbf{r_0} + \delta\mathbf{r}(t)$ in the interference map $\mathbf{\Phi}_R(\mathbf{r})$:

$$dp(t) = dt\,\mathbf{\Phi}_R(\mathbf{r_0} + \delta\mathbf{r}(t)) \simeq dt\mathbf{\Phi}_R(\mathbf{r_0}) + dt\ \nabla\mathbf{\Phi}_R|_{\mathbf{r_0}} \cdot \delta\mathbf{r}(t). \tag{2.4.3}$$

In practice, the signals are acquired over a duration T, their spectral density is computed for each segment and subsequently averaged. The autocorrelation function of the signal recorded during a single acquisition (of duration T) is given by:

$$C_{V_R}(\tau) \equiv \frac{1}{T}\int_0^T dt V_R(t)V_R(t-\tau) = \sum_i \int_0^T \frac{dt}{T} V_\pi(t-t_i)V_\pi(t-t_i-\tau) + \sum_{i\neq j}\int_0^T \frac{dt}{T} V_\pi(t-t_i)V_\pi(t-t_j-\tau) \tag{2.4.4}$$

[6] cps stands for *counts-per-second*

where we split the sum into equal and different photon arrival times and the sums run on all the photon collected during an acquisition T. The first integral does not depend on t_i and is associated to the autocorrelation function of the pulse shape:

$$C_\pi^T(\tau) \equiv \int_0^T \frac{dt}{T} V_\pi(t) V_\pi(t-\tau). \tag{2.4.5}$$

It can be computed:

$$C_\pi^T(\tau) = \frac{V_\pi^2 T_\pi}{T}\left(1 - |\tau|/T_\pi\right) \qquad \text{if} \quad |\tau| < T_\pi, \qquad 0 \quad \text{otherwise.} \tag{2.4.6}$$

Using a change of variables $t \to t + t_i$, the second integral is indeed equal to $C_\pi^T(\tau - t_i + t_j)$. The first sum is simply proportional to the number of photons recorded during the acquisition, which amounts in average to $\mathbf{\Phi}_R(\mathbf{r_0})T$. The signal autocorrelation function is then:

$$C_{V_R}(\tau) = \sum_i C_\pi^T(\tau) + \sum_{i \neq j} C_\pi^T(\tau - t_i + t_j). \tag{2.4.7}$$

Finally, the noise spectral density of the signal computed by the spectrum analyzer is:

$$S_{V_R}[\Omega] \equiv \int d\tau C_{V_R}(\tau) e^{i\Omega\tau}. \tag{2.4.8}$$

It makes use of the Fourier transform of the pulse autocorrelation function:

$$C_\pi^T[\Omega] \equiv \int d\tau C_\pi^T(\tau) e^{i\Omega\tau} = \frac{T_\pi^2 V_\pi^2}{T} \mathrm{sinc}^2\left(\Omega T_\pi/2\right) \tag{2.4.9}$$

where the sinus cardinal function produces a cutoff in frequency at the inverse of the pulse duration (approx 20 MHz typically).

Experimentally, we average several acquisition sequences, which permits to both average over many noise realizations, but also to average over many realizations of the pulses sequences for an "hypothetical" given mechanical trajectory. This means that the first term, which is proportional to the number of photon detection during the acquisition time and does not depend on mechanical trajectories, will then become: $\mathbf{\Phi}_R(\mathbf{r_0})TC_\pi[\Omega]$. It represents the shot noise contribution and can thus be written:

$$S_{V_R}^{\text{shot}}[\Omega] = \mathbf{\Phi}_R(\mathbf{r_0}) T_\pi^2 V_\pi^2 \,\mathrm{sinc}^2\left(\Omega T_\pi/2\right). \tag{2.4.10}$$

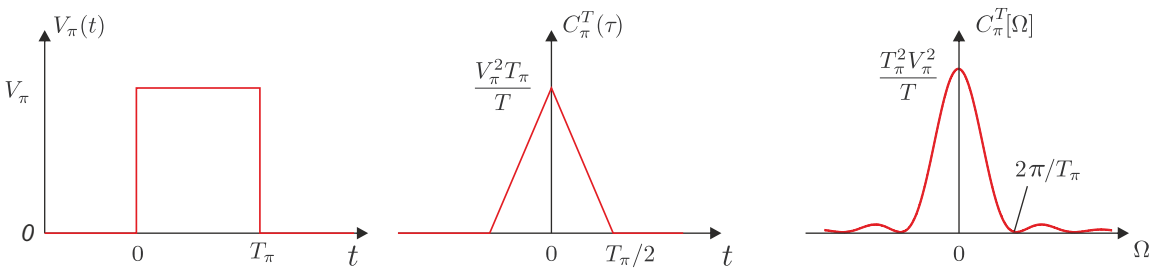

FIGURE 2.27 – Pulse shape and autocorrelation function of the photon-counter output signal.

The second integral on different photon arrival times, is averaged as

$$S_{V_R}^{\text{signal}}[\Omega] = \int d\tau \int_0^T dt_1 \int_0^T dt_2 e^{i\Omega\tau} C_\pi^T(\tau - t_1 + t_2) \langle \mathbf{\Phi}_R(t_1) \mathbf{\Phi}_R(t_2) \rangle \tag{2.4.11}$$

where we replaced the sum over different times by an integral form, weighting the time of arrival by the mean probability to detect a photon at a corresponding time: $dp(t)$ introduced above. The symbol $\langle ... \rangle$ stands for average over many realizations of the noise. We can expand at first order:

$$\mathbf{\Phi}_R(t_i) = \mathbf{\Phi}_R(\mathbf{r_0}) + \left| \mathbf{\nabla \Phi}_R|_{\mathbf{r_0}} \right| \delta r_\beta(t_i) \tag{2.4.12}$$

When computing the product, the terms linear in δr_β will average to zero, while the first static term is not of dynamical interest. As such the second integral can be written:

$$S_{V_R}^{\text{signal}}[\Omega] = \left| \mathbf{\nabla \Phi}_R|_{\mathbf{r_0}} \right|^2 \int d\tau \int_0^T dt_1 \int_0^T dt_2 e^{i\Omega\tau} C_\pi^T(\tau - t_1 + t_2) \langle \delta r_\beta(t_1) \delta r_\beta(t_2) \rangle. \tag{2.4.13}$$

If we now employ a change in variable: $\tilde{\tau} = \tau - t_1 + t_2$, we obtain:

$$S_{V_R}^{\text{signal}}[\Omega] = \left| \mathbf{\nabla \Phi}_R|_{\mathbf{r_0}} \right|^2 \int d\tilde{\tau}\ e^{i\Omega\tilde{\tau}} C_\pi^T(\tilde{\tau}) \int_0^T dt_1 dt_2 \langle \delta r_\beta(t_1) \delta r_\beta(t_2) \rangle e^{i\Omega(t_1 - t_2)}. \tag{2.4.14}$$

The first integral is simply $C_\pi[\Omega]$ as defined above, while the second double integration can be computed by using the autocorrelation function of the projected oscillator position:

$$C_{\delta r_\beta}(t_2 - t_1) = \langle \delta r_\beta(t_1) \delta r_\beta(t_2) \rangle \tag{2.4.15}$$

whose Fourier transform is the noise spectral density of the oscillator's position

$$S_{\delta r_\beta}[\Omega] \equiv \int d\tau C_{\delta r_\beta}(\tau) e^{i\Omega\tau}, \tag{2.4.16}$$

which is the quantity we are interested in recording experimentally. The last temporal integration simply gives an additional T contribution which cancels the one present in $C_\pi[\Omega]$. Finally, the last integral gives:

$$S_{V_R}^{\text{signal}}[\Omega] = \left| \mathbf{\nabla \Phi}_R|_{\mathbf{r_0}} \right|^2 \frac{C_\pi^T[\Omega]}{T} S_{\delta r_\beta}[\Omega]. \tag{2.4.17}$$

This leads to:

$$S_{V_R}[\Omega] = T_\pi^2 V_\pi^2 \text{sinc}^2 \left(\Omega T_\pi / 2 \right) \left(\mathbf{\Phi}_R(\mathbf{r_0}) + \left| \mathbf{\nabla \Phi}_R|_{\mathbf{r_0}} \right|^2 S_{\delta r_\beta}[\Omega] \right). \tag{2.4.18}$$

This formulation is rather explicit, the shot noise level is proportional to the received photon flux, while the signal part is transduced by the slope of the interference map. The overall signal is filtered for frequencies larger than $1/T_\pi$ (tens of MHz). In our experiments, we are only interested in the mechanical signals found at low frequency, so that the conversion between the voltage noise spectral density measured by the spectrum analyzer in the frequency representation ($S_\pi^f = 2\pi S_\pi[2\pi f]$) can be written as:

$$S_{\delta r_\beta}[\Omega] = \frac{S^f_{V_R}[\Omega]}{\eta^2 \left| \nabla \mathbf{\Phi}_R \big|_{\mathbf{r_0}} \right|^2}, \tag{2.4.19}$$

with $\eta = \sqrt{2\pi}\ T_\pi V_\pi$. This conversion factor between voltage and flux amounts to $\eta \approx 3.9 \times 10^{-8}\,\mathrm{V/Hz}$ using $T_\pi = 15\,\mathrm{ns}$ and a 3.3 V pulse magnitude produced by the photon counter, followed by a 10 dB attenuator ($V_\pi = 1.04\,\mathrm{V}$). We will see that this estimation provides a good order of magnitude for the η conversion factor.

In practice, however, there are many limitations such as the finite sampling rate of the spectrum analyzer (100 MS/s used), impedances mismatching or other sources of pulses distortions, so that it is necessary to properly calibrate the "volt to clics" η conversion factor. We also note that all the devices that record the vibrations of the nanowire, such as the spectrum analyzer, the network analyzer, the lock-in detection or the oscilloscope all present a 50 Ω input impedance, so that the same calibration factor will be used as soon as one wants to extract calibrated mechanical signals out of the avalanche photodiode photon fluxes. This is also the role of the photon splitter unit developed by C. Hoarau which permits to identically split the APD output into multiple equivalent TTL outputs channels, without being impacted by impedance management considerations.

Moreover, the equivalent shot noise level can be expressed as:

$$S^{\mathrm{shot}}_{\delta r_\beta}[\Omega] = \frac{\mathbf{\Phi}_R(\mathbf{r_0})}{\left| \nabla \mathbf{\Phi}_R \big|_{\mathbf{r_0}} \right|^2} \tag{2.4.20}$$

where it is clear that to minimize this imprecision noise level, one should try to maximize the measurement slope, while trying to operate at minimal mean optical flux.

MEASUREMENT CALIBRATION To determine the exact conversion coefficient we set up a small experiment (see fig. 2.26a): a known calibrated noise (mechanical) signal is numerically simulated and played with a wave generator to create a voltage control signal, which is sent to an AOM and simulate an artificial intensity modulated mechanical signal. The light intensity is varied by mean of half-waveplate plus a PBS cube and is then (asymmetrically) split and simultaneously collected with a standard photodiode (*Thorlabs APD410A/M*) and with the photon-counter. The measured signals are finally registered with a spectrum analyzer.

We now expect the PSD to be constant, once normalized by the incident power on each sensor, given that the calibration noise used is identical on each channel. The results for the two detectors are shown in figs. 2.28a and 2.28c. We can notice that the photon counter behaves linearly across the whole power intensity range, starting to exhibit some problem only when close to its saturation limit (higher than few million counts), or at low intensity when limited by the *noise imprecision measurement*. Given a typical quantum detection efficiency of 65% (@ 633 nm) and the result of section 1.2.3, this low limit is not the best our detector can achieve. Indeed, in order to perform the calibration and measure the signal with both detectors at the same time, it was necessary to add a neutral density filter in front of the APD. The effect is to displace the whole *noise imprecision measurement* limit toward higher intensity. The standard photodiode has a different behaviour instead. Despite not being limited by the dark noise and still being able to measure a signal, the results become unreliable for signals lower than few tens of mV.

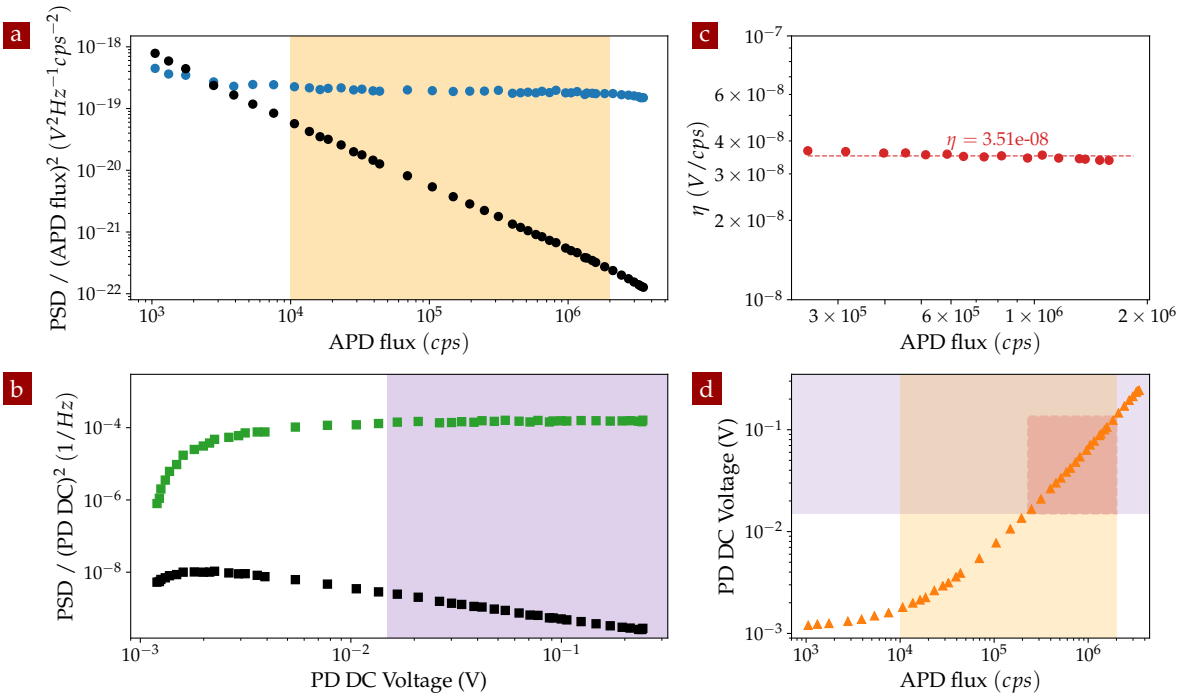

FIGURE 2.28 – Experimental calibration of a noise signal measured with a photon counter: (a) calibration noise measured with the photon counter; inside the yellow region the APD behaves linearly as expected. For higher power saturation problems can occur, while for lower ones can be limited by the shot noise. (b) calibration noise measured with the standard photodiode; inside the purple region the PD behaves linearly. (c) the calibration coefficient η is obtained from the square-root of the ratio of the noise measured with the two photo-detectors. (d) relation between the DC components of the signals measured with the two photo-detectors, with their respective zone of linearity. The points inside the intersection between these two regions (red zone) are the ones used to estimate the calibration coefficient η.

The large difference in the value of the PSD of the two sensors is indeed the reason why the calibration is needed: assuming the value of the standard photodiode to be correct [86, 56], the values returned from the photon-counter are off of several order of magnitude. Restraining the data to the working range of the two detectors (cfr. fig. 2.28d), the square root of the ratio of the two measurements gives the calibration coefficients we are looking for (see fig. 2.28b): $\eta = 3.51 \times 10^{-8}$ V/cps, which is in good agreement with the above estimation.

3 OPERATION OF A FORCE SENSOR AT DILUTION TEMPERATURE

The present chapter presents the main results obtained in the dilution experiment. After a brief description of the NWs physical, mechanical and thermal properties, the dependence of their thermal noise on the cryostat temperature and on the optical probe power are discussed, together with the achieved force sensitivities and thermal transport properties.

CONTENTS

3.1 SiC nanowires force sensors . . . **64**
3.1.1 Physical Properties and their temperature dependence . . . 64
3.1.2 Mechanical properties . . . 66
Flexural vibrations . . . 66
Effective Mass . . . 71
Force sensitivity and SQL . . . 73
3.1.3 Optical properties . . . 74
3.2 Brownian thermometry . . . **76**
3.2.1 The Brownian thermal motion . . . 76
3.2.2 Dependence on the cryostat base temperature . . . 79
3.2.3 Optical heating . . . 81
3.2.4 Frequency and quality factor temperature dependence: TLS signature . . . 82
Frequency . . . 83
Damping rate . . . 84
Two-level tunneling systems . . . 85
3.3 Low temperature heat transport at the nanoscale . . . **86**
3.3.1 The low temperature heat transport regimes . . . 86
3.3.2 Static heating of the nanowire at cryogenic temperatures . . . 90
3.4 Response measurement and force sensitivity . . . **92**
3.5 Comparison across multiple samples . . . **95**

3.1 SIC NANOWIRES FORCE SENSORS

Silicon carbide nanowires are the resonator we employed in this work and have become the workhorse of the results achieved in our group in recent years [16, 232, 156, 56, 117]. Here we briefly describe the physical, mechanical and optical properties of these objects, focusing our attention on the main parameters that must be taken into account when preparing a force sensor for particular applications.

3.1.1 Physical Properties and their temperature dependence

Known since the XIX century and studied since the beginning of '900 [226], silicon carbide combines a series of superior physical properties which makes it an ideal material for numerous electronical and optoelectronical applications (in particular high temperature, high power and high frequency electronics), as well as for the realization of micro- and nano-mechanical structures [247, 223, 251, 260].

Silicon carbide is the only chemically stable form of silicon and carbon, with a crystalline structure which consists in a close-packed stacking of double layers of Si and C atoms. Depending on the layers' orientation during the stacking process, a large number of crystallographic forms, called polytypes[1], exists. The cubic form is denoted 3C-SiC or beta silicon carbide (β-SiC). Hexagonal (H) and rhombohedral (R) types are commonly referred to as α-SiC, with 4H and 6H the most common ones. Most polytypes are metastable and can transform into others at temperatures as low as 400 °C. The phase-diagram of SiC is shown in fig. 3.1a.

Silicon carbide is a relative light density material, with a volumetric mass density $\rho = 3210\,\mathrm{kg/m^3}$ in the crystalline form. It presents a rather large Young's modulus E, in the range 392 - 448 GPa, and a Poisson's ratio $\nu = 0.45$. As a consequence, mechanical resonators realized with this material exhibit really interesting properties [43], resulting in light oscillators with high quality factors, particularly suitable as force sensor, as we will see. It is a semiconductor material with a optical bandgap of 385, 405 and 525 nm respectively for the form 4H, 6H and 3C. The typical refractive index is $n \sim 2.7$ in the visible domain.

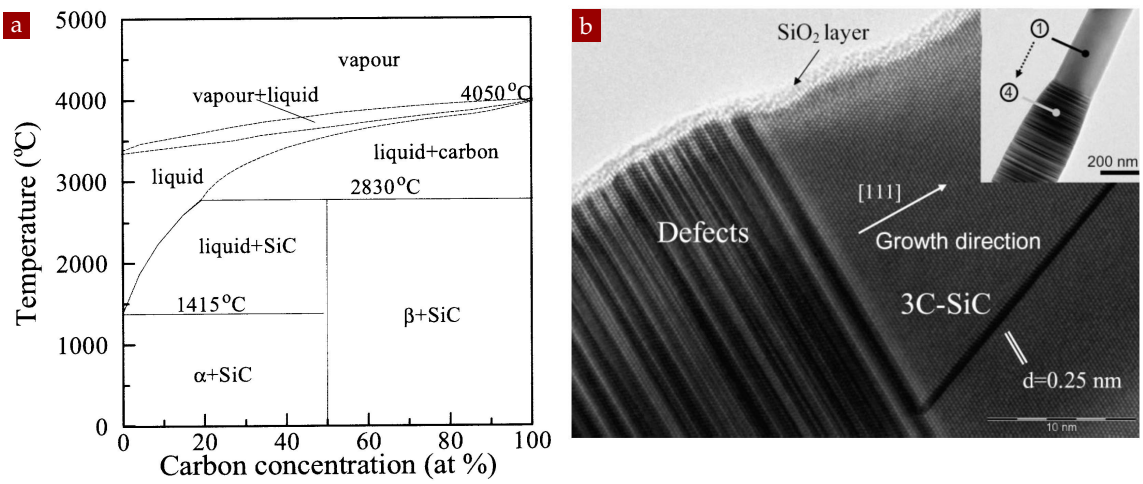

FIGURE 3.1 – (a) Phase diagram of silicon carbide [251]. (b) TEM image of a silicon carbide nanowire [19].

[1]Polytypism is a one-dimensional polymorphism that is a result of the stacking sequence.

The original nanowires employed in this work have been made at the *Laboratoire Multimatériaux et Interfaces* in Lyon [228]. They are chemically grown with a method similar to the chemical vapor deposition (CVD) [19]: a polypropylene carbon source, together with a silicon source (silicon dioxide SiO_2 and silicon), are heated up to 1400 °C for 10 h under an Argon flux. Through a vapour-solid (VS) growth mechanism, the NWs will then condense on a graphite support. Commercially available SiC nanowires, prepared through a lithium-based intercalation method, have also been employed, the latter are found in the 3C phase.

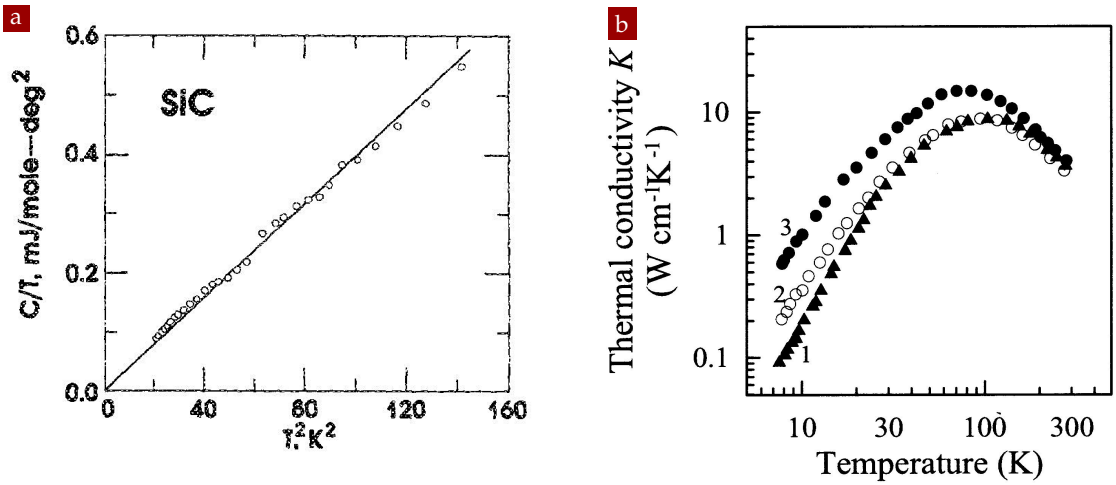

FIGURE 3.2 – (a) Specific heat of SiC between 4 and 12 K. Data from [123]. (b) Thermal conductivity of SiC as a function of the temperature, data from [219]; at low temperature different polytypes behave differently (1 → 4H-SiC, 2 → 3C-SiC, 3 → 6H-SiC)

Concerning its thermal properties, silicon carbide exhibits an excellent thermal conductivity: on one side this allows to probe our resonator with a relatively intense optical beam (10 mW at ambient pressure, up to 500 µW in vacuum) without damaging risk; on the other side this makes it ideal for high power and high temperature electronics application. Its material properties have however been essentially studied in the high temperature range, while not many data can be found regarding the behaviour at low temperature and are completely absent for temperatures lower than 4 K. The dependence of the thermal conductivity on the temperature and polytype is shown in fig. 3.2b [219, 141]. For 3C its value is $\kappa_{ph} = 360\,\mathrm{W/(m \cdot K)}$ at 300 K and $\kappa_{ph} = 23\,\mathrm{W/(m \cdot K)}$ at 9 K (the latter is poly-3C). For 6H it is $\kappa_{ph} = 490\,\mathrm{W/(m \cdot K)}$ at 300 K and $\kappa_{ph} = 70\,\mathrm{W/(m \cdot K)}$ at 9 K [251]. Regarding the specific heat, usually the same value $C_p = 690\,\mathrm{J/(kg \cdot K)}$ (at 300 K) is used for all polytypes. The only available data at low temperature are from [123], as shown in fig. 3.2a, resulting in a value of $C_p = 1 \times 10^{-3}\,\mathrm{J/(kg \cdot K)}$ at 4 K for α-SiC (comparable to the value of pure silicon [77, 244]).

The last property we are interested in is the light absorption coefficient[2] α. It varies with the polytypes, with the temperature and on the employed wavelength. The values for 6H-SiC as a function of the wavelength for different temperatures are reported in fig. 3.3a, while a comparison among the three main polytypes at 4 K is shown in fig. 3.3a. From previous work [232, 233], we know that in the case of SiC nanowires the absorption is typically of few percent. However the absorption can be highly affected by the presence of defects along the crystal (see fig. 3.1b) and can also be artificially enhanced by internal optical resonances in the nanowire.

[2]The absorption coefficient is defined so that the light intensity at depth x of a beam traversing a material is given by $I(x) = I_0 e^{-\alpha x}$.

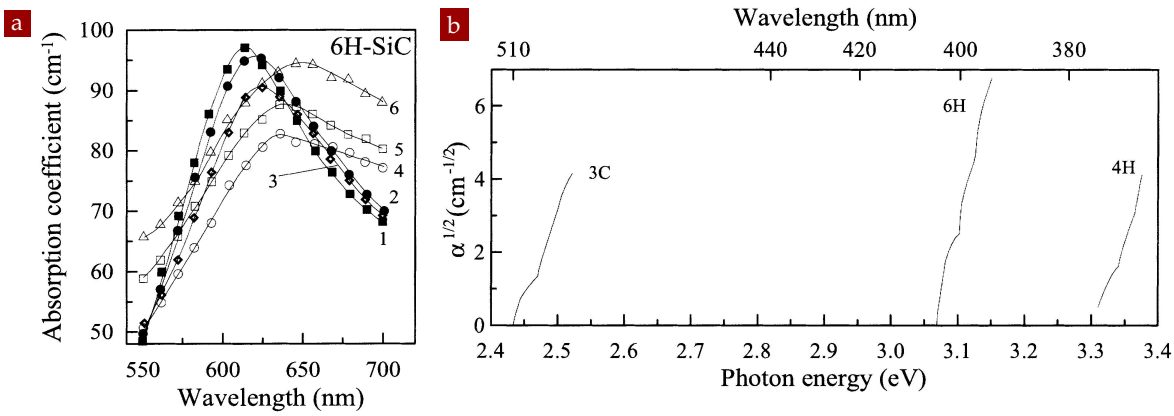

FIGURE 3.3 – Absorption coefficient for a SiC crystal: (a) 6H-SiC dependence on the wavelength and temperature (1 → 78 K, 2 → 300 K, 6 → 1500 K) [64, 247]; the absorption coefficient measured at 78 K and 633 nm is around 90 cm^{-1} or 9000 /m, leading to a bulk absorption of 900 ppm for a 100 nm thickness. (b) difference among the most common polytypes at 4 K [222].

The knowledge of the thermal conductivity, of the specific heat and of the optical absorption coefficient at low temperature is important because they directly impact the thermal properties of the nanowire in response to an absorbed amount of light (see section 3.3).

ρ (kg/m^3)	E (GPa)	ν	n	κ_{ph} (W/(m · K)) 300 K 3C	300 K 6H	9 K 3C	9 K 6H	C_p (J/(kg · K)) 300 K	4 K
3210	392 – 448	0.45	2.7	360	490	23	70	690	1×10^{-3}

TABLE 3.1 – Physical properties of silicon carbide: density, Young modulus, Poisson's ratio, refractive index, heat conductivity and heat capacity.

3.1.2 Mechanical properties

SiC nanowires constitute excellent mechanical resonators. We now present how their deformations can be described by making use of the *Euler-Bernoulli beam theory* and we derive the eigenfrequency, the mode profile and the effective mass of the first fundamental modes[3]. We describe how these properties depend on the NW length (L) and radius (R) and estimate the expected force sensitivity at low temperature.

FLEXURAL VIBRATIONS The large aspect ratio of our nanowires permits to employ [233, 232] the Euler-Bernoulli equation, which assumes a slim beam ($L/2R > 10$) and negligible rotational inertia and shear deformation to describe the dynamics of SiC nanowires. It is given by

$$EI_z \frac{\partial^4 u}{\partial y^4}(y,t) + \rho A \frac{\partial^2 u}{\partial t^2}(y,t) = 0, \tag{3.1.1}$$

where $u(y,t)$ expresses the transverse displacement of the NW, while x and z are the transverse coordinates (see fig. 3.4). The other parameters are the Young's modulus E,

[3]For more details and the generalization to other geometries, see [243, 258, 89, 256].

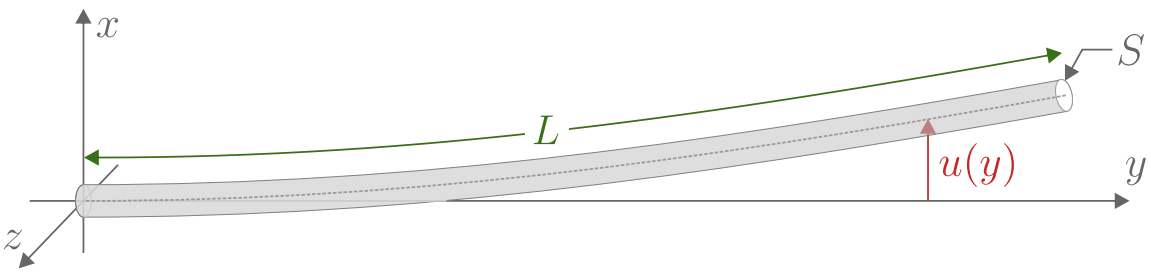

FIGURE 3.4 – Conventions for the *Euler-Bernoulli* description.

the geometric moment of inertia I_z, the mass density ρ and the cross sectional area A. For a cylinder of radius R, the moment of inertia is given by $I_z = \iint_A dxdz\, z^2 = \frac{\pi R^4}{4}$.

The solution of this equation can be expressed as a sum of normal modes, each of which can be separated into a position and a time-dependent amplitude:

$$u(y,t) = \sum_{n=1}^{\infty} u_n(y) a_n(t). \tag{3.1.2}$$

Here n is the mode number and $u_n(y)$ describes the mode profile. In case of a stationary regime where the beam oscillates at pulsation Ω, we obtain:

$$\frac{\partial^4 u_n(y)}{\partial y^4} - \beta_n^4 u_n(y) = 0 \tag{3.1.3}$$

with β_n the *wavenumber* equal to

$$\beta_n^2 = \Omega \sqrt{\frac{\rho A}{E I_z}}. \tag{3.1.4}$$

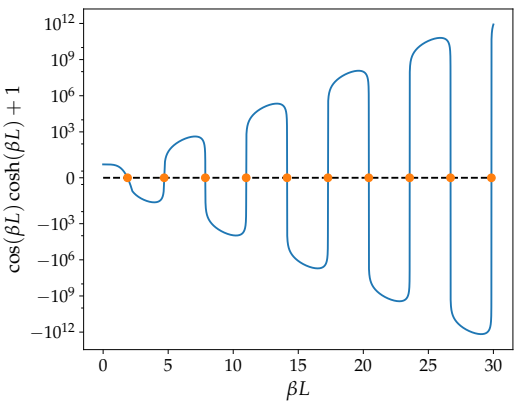

FIGURE 3.5 – Graphical solution to compute the wavenumber β_n.

n	$\beta_n L$	$(2n-1)\pi/2$	Ω_n/Ω_0	Ω_n/Ω_{n-1}
1	1.8751	(1.5708)	1.000	-
2	4.6941	(4.7124)	6.267	6.267
3	7.8548	7.8540	17.547	2.800
4	10.9955	10.9956	34.386	1.960
5	14.1372	14.1372	56.843	1.653
6	17.2788	17.2788	84.913	1.494
7	20.4204	20.4204	118.595	1.397
8	23.5619	23.5619	157.896	1.331
9	26.7035	26.7035	202.809	1.284
10	29.8451	29.8451	253.336	1.249

TABLE 3.2 – Wavenumber $\beta_n L$ for the first 10 modes.

A general solution to eq. (3.1.3) can be written in the form

$$\begin{aligned} u_n(y) &= A_n e^{\beta_n y} + B_n e^{-\beta_n y} + C_n e^{i\beta_n y} + D_n e^{-i\beta_n y} = \\ &= A_n \cos\beta_n y + B_n \sin\beta_n y + C_n \cosh\beta_n y + D_n \sinh\beta_n y \end{aligned} \tag{3.1.5}$$

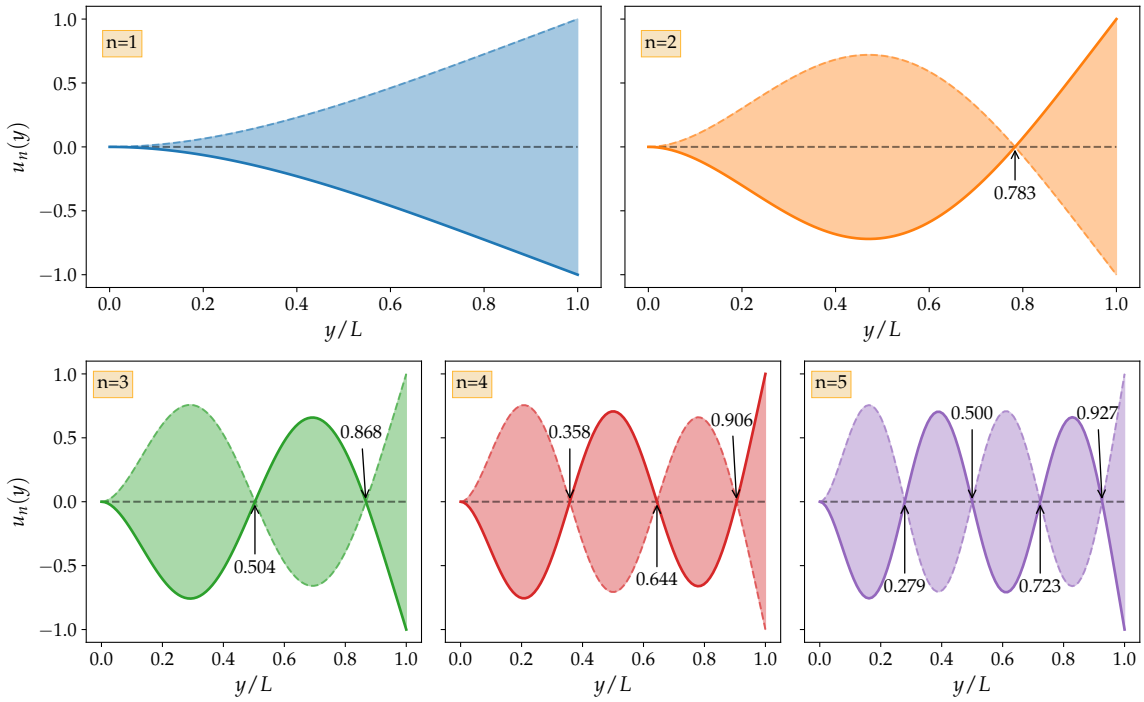

FIGURE 3.6 – Normalized mode-shape $\phi_n(y)$ of the first 5 fundamental modes. Each longitudinal mode can vibrate along both transverse orientations and is thus 2 times degenerated.

where the constants A_n, B_n, C_n and D_n and the wavenumber β_n have to be determined from initial conditions. For a singly-clamped beam (or cantilever), the boundary conditions are

$$u_n(0) = \frac{\partial}{\partial y} u_n(0) = \frac{\partial^2}{\partial y^2} u_n(L) = \frac{\partial^3}{\partial y^3} u_n(L) = 0, \tag{3.1.6}$$

for which we find that β_n obeys the relation

$$\cos \beta_n L \cosh \beta_n L + 1 = 0. \tag{3.1.7}$$

The solutions to this equation can be found numerically (see fig. 3.5) and are reported in table 3.2 for the first 10 modes. As shown, for $n \geq 3$ a good approximation is given by $\beta_n L \approx (2n-1)\pi/2$. Reporting eqs. (3.1.6) and (3.1.7) into eq. (3.1.5) leads to

$$u_n(y) = A_n \left[\cos \beta_n y - \cosh \beta_n y - \frac{\cos \beta_n L + \cosh \beta_n L}{\sin \beta_n L + \sinh \beta_n L} (\sin \beta_n y - \sinh \beta_n y)\right]. \tag{3.1.8}$$

The normalized shapes ($u_n^{\text{norm}}(y) = u_n(y)/u_n^{\max}$, where $u_n^{\max} = u_n(L)$) of the first 5 fundamental modes are shown in fig. 3.6.

We can now use eq. (3.1.4) to compute the eigenfrequencies of a NW of given length L and radius R:

$$\Omega_n = (\beta_n L)^2 \sqrt{\frac{E}{\rho} \frac{R}{2L^2}}. \tag{3.1.9}$$

Figure 3.7 presents a response spectrum of the sample $NW1$ (see below), which was realized by driving the nanowire with an electrostatic tip mounted on the transmission piezo tower, fed by a DC plus a swept modulation tone (see fig. 3.8). This sample has a fundamental frequency around 3 kHz. Starting from this value, we can use table 3.2 to estimate the tabulated frequencies of the first 10 modes and compare them to the measured ones.

As we can see from table 3.3, the agreement is good, at percent level, which justifies our original assumption. Note however that each nanowire vibrates in a transverse plane in two orthogonal transverse directions. This means that each mode is degenerated in the ideal case and split into two different values in reality, due to the non-perfect cylindrical symmetry of the nanowire geometry (or due to its clamping asymmetry). Making use of eq. (3.1.9) we can also verify that the measured frequency agrees with the length and the diameter of the NW measured in a scanning electron microscope. The same equation can also be used to create a map of the expected fundamental frequency for varying NW dimensions (see fig. 3.9a).

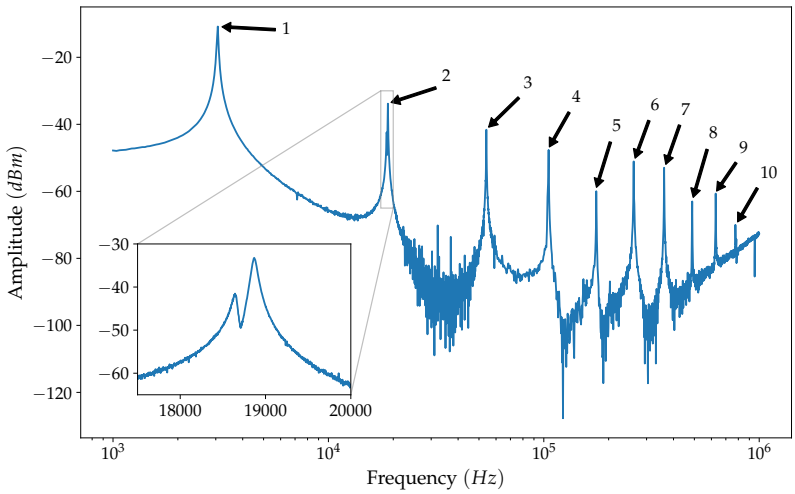

FIGURE 3.7 – Response spectrum of the sample $NW1$ measured under electrostatic actuation. Each peak is 2-fold degenerated, as can be verified by zooming on each of them to extract the frequency of each transverse eigenmode.

n	Ω_n^{Theo}	Ω_n^{Pol1}	Ω_n^{Pol2}
1	3.06	3.05	3.06
2	19.18	18.64	18.87
3	53.70	53.69	54.09
4	105.22	103.25	105.17
5	173.94	171.43	175.34
6	259.83	261.32	262.77
7	362.91	361.99	365.50
8	483.16	486.40	488.48
9	620.60	617.50	628.00
10	775.21	775.42	783.28

TABLE 3.3 – Frequency (in kHz) of the first 10 fundamental modes of the sample $NW1$.

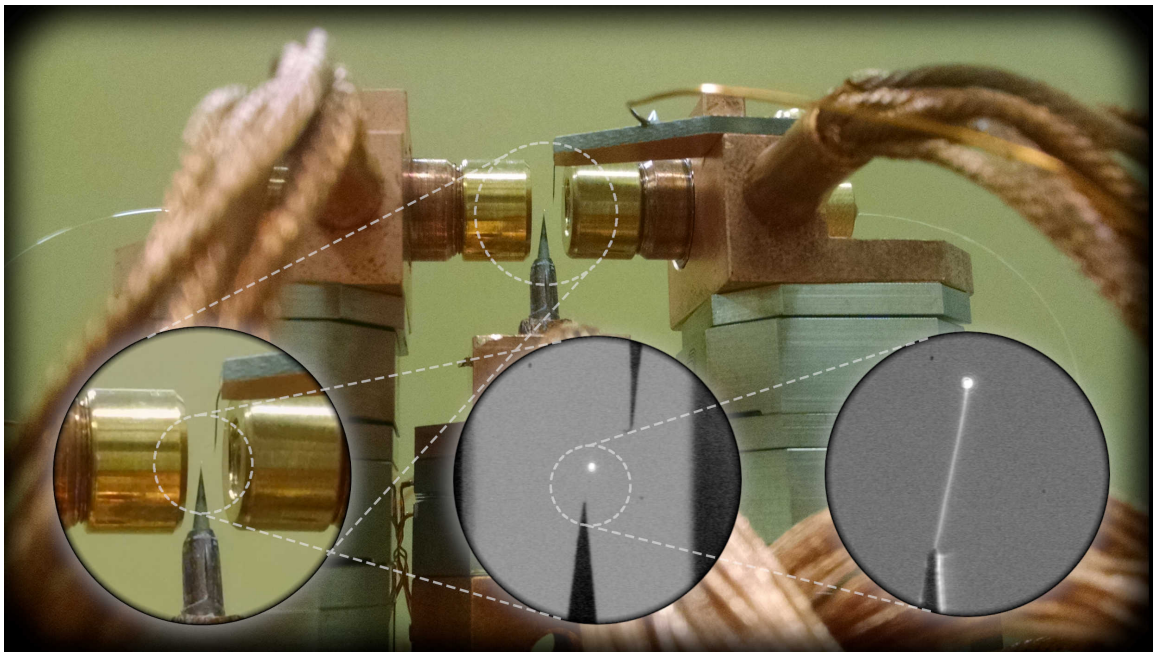

FIGURE 3.8 – Electrostatic tip mounted on the transmission piezo tower and used to drive the nanowire motion.

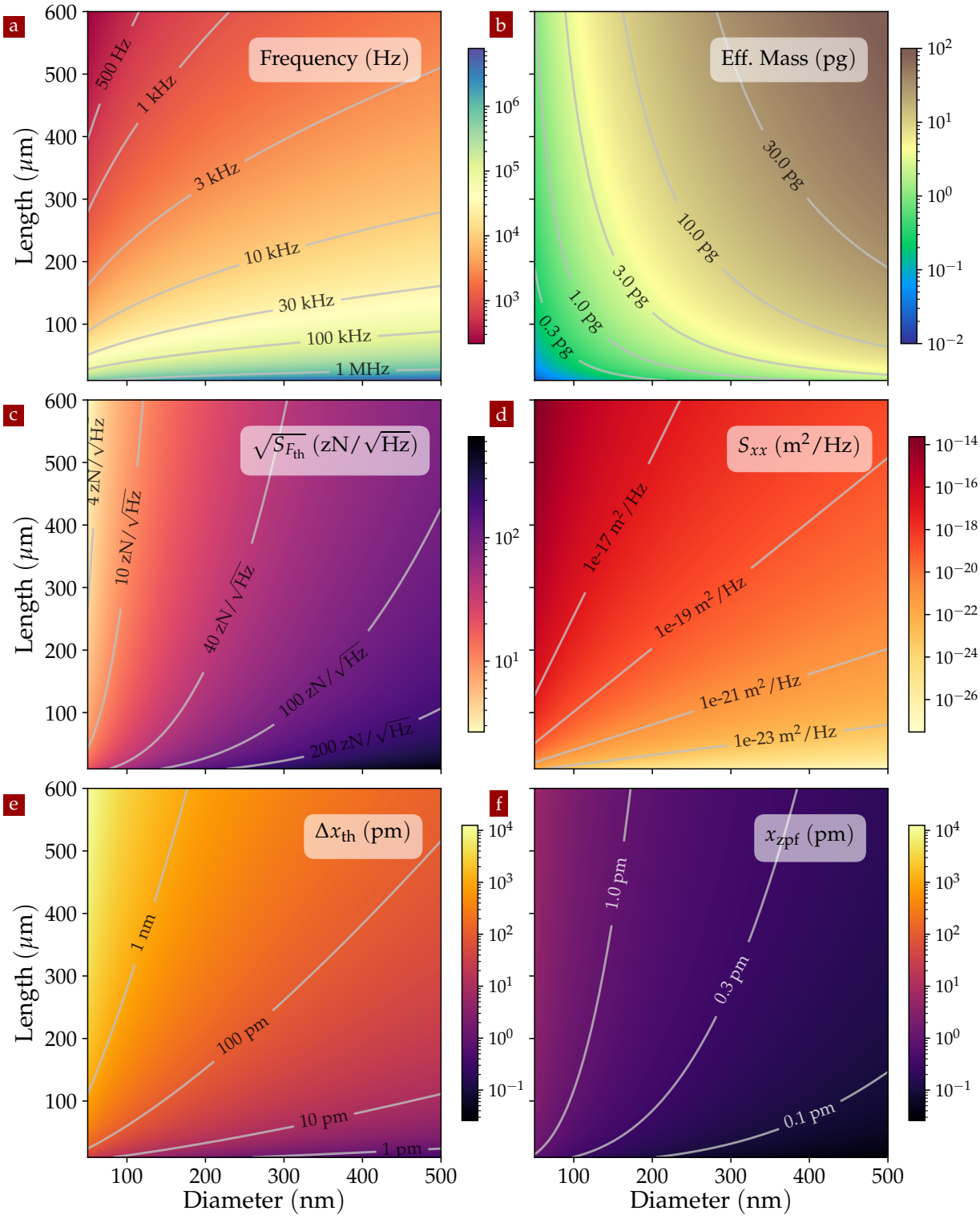

FIGURE 3.9 – (a) frequency of the fundamental transverse mode, (b) effective mass, (c) best force sensitivity, (d) typical power spectral density, (e) variance and (f) *zero-point-fluctuations* as a function of the geometrical properties of the nanowire ($L = 10$ - $600\,\mu$m, $D = 50$ - $500\,$nm). (c), (d) and (e) has been computed supposing a temperature of $20\,$mK and a quality factor of 1×10^5.

EFFECTIVE MASS We saw in section 1.2.1 that the power spectral density of the thermal noise of a harmonic oscillator can be expressed as

$$S_{\delta x}[\Omega] = \frac{2\Gamma k_B T}{M\left((\Omega_m^2 - \Omega^2)^2 + \Gamma^2\Omega^2\right)}. \tag{3.1.10}$$

In order to describe a continuous $3D$ vibrating structure as an equivalent harmonic oscillator, it is necessary to introduce the notion of *effective mass* [158, 13, 100, 188, 7, 68], which takes into account the efficiency of the probe laser to readout the resonator 3D deformation profile, and convert it into a scalar temporal modulation of the collected probe light. This conversion must be done while insuring that the equipartition theorem is preserved for the equivalent oscillator. In our case we use local optical readouts that can be assimilated to a point-like measurement of the vibrations of the nanowire. We generally position the laser at the extremity of the nanowire, but one can also investigate the deformation profile all along the nanowire. In that situation, this implies that the effective mass will be a function of the position at which the measure is performed.

In the case of a point-like measurement, the effective mass is introduced by comparing the kinetic (or potential) energy of the $3D$ vibration profile to the one of the equivalent

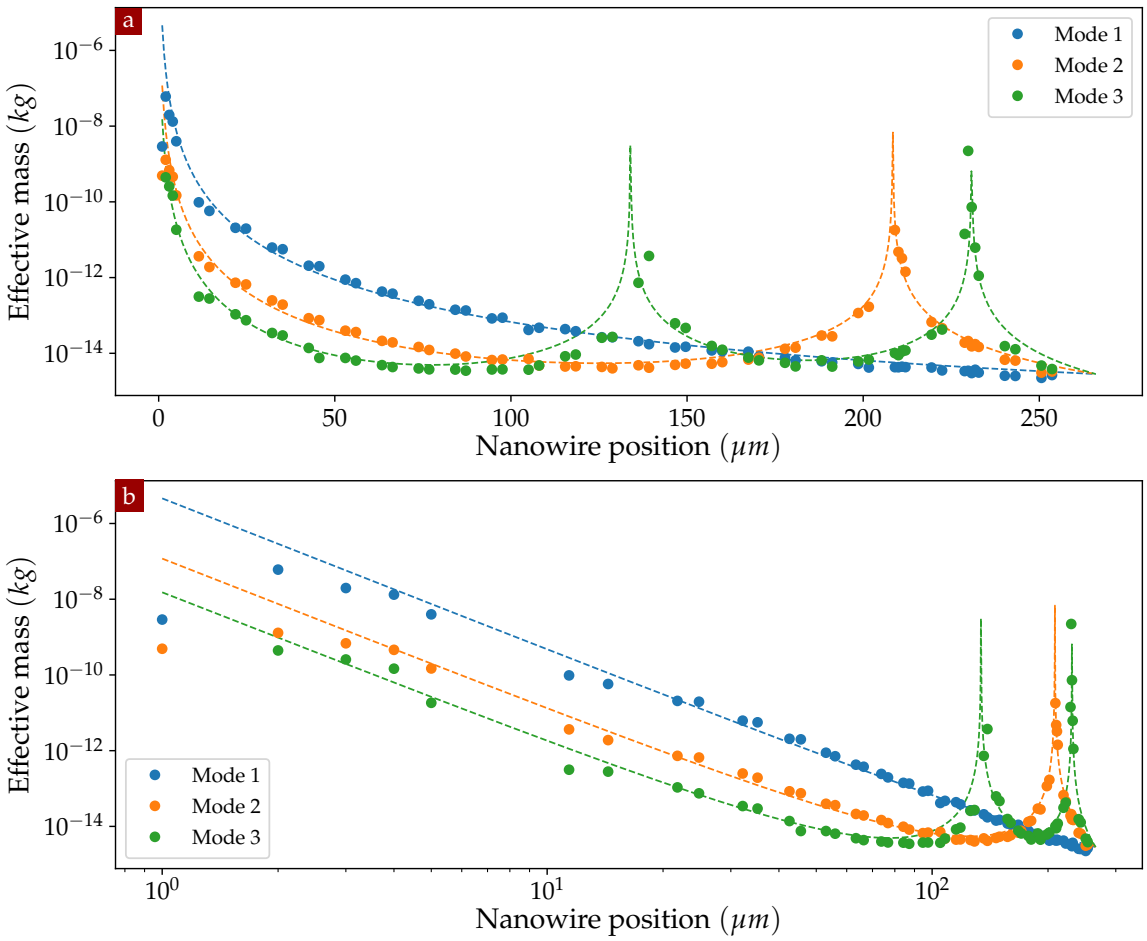

FIGURE 3.10 – Comparison between the expected theoretical values for the effective mass of a nanowire of length $L \approx 270\,\mu m$ and diameter $D \approx 130\,nm$ and the measured ones for the first three modes of $NW1$, as a function of the position along the NW. (a) linear scale; (b) logarithmic scale.

harmonic oscillator [158, 89, 258]. In the case of a laser positioned at the elevation y_0, the effective mass of mode n reads

$$M_{\text{eff},n} = M \int_0^L \frac{1}{L} \frac{u_n(y)^2}{u_n(\mathbf{y_0})^2} dy, \tag{3.1.11}$$

where M is the geometrical mass of the resonator ($M = \rho_{\text{SiC}} L \pi R^2$). In the usual case where the NW is measured at its extremity, the effective mass of the n flexural mode amounts to:

$$M_{\text{eff},n}/M = \int_0^L \frac{1}{L} \frac{u_n(y)^2}{u_n(L)^2} dy = \frac{1}{4}, \tag{3.1.12}$$

which is true for all the normal modes. The dependence of the effective mass of the fundamental mode of the nanowire with its geometrical dimensions is shown in fig. 3.9b.

In fig. 3.10 we show a comparison between the expected theoretical value obtained from eq. (3.1.11) for a nanowire of length $L \approx 270\,\mu\text{m}$ and diameter $D \approx 130\,\text{nm}$, and the effective mass for the first three modes of $NW1$ measured at different vertical positions. In each point, a thermal noise spectrum is acquired and calibrated, and a fit permits to determine the local effective mass. Those measurements are realized at 300 K and permit to map the spatial profile of the first vibrational modes. As expected the effective mass increases when approaching a mechanical node where the rms noise amplitude gets reduced. The solid lines are an estimation of the effective mass given the theoretical mode profiles (eqs. (3.1.8) and (3.1.10)). Furthermore, once calibrated this kind of measurements allows to infer with a good precision at which position along the nanowire the measure is performed, which is particularly useful when it is not possible to realize a direct image of the system, such as in the cryostat, or when the positioners are not very reliable, which is the case of the steppers.

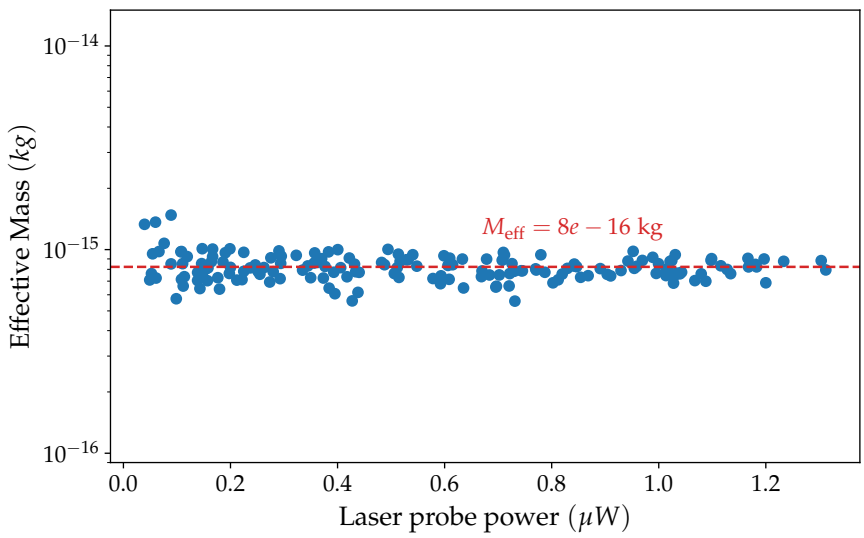

FIGURE 3.11 – Estimation of the effective mass of the sample $NW2$ at 300 K, where no absorption induced heating is observed.

In order to verify that the noise temperature is not perturbed by the light (via absorption or optomechanical effects), one has to realize the above measurement for varying optical powers. Figure 3.11 presents the results of such a measurement. Thermal noise spectra are acquired for increasing powers of the probe laser beam and the variation of the effective mass is reported as a function of the optical power. The detector employed here is a continuous photodiode, in order to operate with large optical powers,

but similar measurements are realized with the photon counters. For this dataset, no optical perturbation is observed. Since the effective mass only depends on the longitudinal mode shape, it is in principle not supposed to vary with temperature. However this needs to be verified at low temperatures. As we will see, a verification can be done by sweeping the cryostat temperature and operating at minimal optical powers.

FORCE SENSITIVITY AND SQL Making use of eq. (1.2.31), we can now estimate the force sensitivity we can expect when using a singly-clamped nanowire resonator thermalised at 20 mK:

$$\delta F_{\text{min}} = \sqrt{S_{F_{\text{th}}}[\Omega]} = \sqrt{2M_{\text{eff}}\Gamma k_{\text{B}}T}. \tag{3.1.13}$$

This values represents the smallest monochromatic force modulation that can be detected in 1 s above the thermal noise. The result, as a function of the NW geometry, is shown in fig. 3.9c, where we employed a quality factor of 1×10^5 in agreement with our experimental observations (see below). Sensitivities of the order of few tens of zepto-Newton can be expected with thin and ultralong oscillators.

However, a major challenge when dealing with such a sensor is the capability to detect their motion while ensuring their proper thermalisation. Figure 3.9d shows the noise spectral density expected at resonance: $S_x[\Omega_{\text{m}}]$ as a function of the nanowire dimensions.

In particular, combining this result with the ones from sections 1.2.3 and 2.4.3, it is possible to compute the minimum photon flux impinging on our detector which is required to probe the thermal motion of a SiC nanowire at 20 mK, before being masked by the imprecision noise. This limit will be very important in our case, because as we will see a higher value corresponds not only to a lower imprecision noise, but also to a higher optical heating effect of the laser probe. If the laser heats the sensor more than the desired operating temperature (20 mK in our case), the resulting force sensitivity will be reduced. The minimum values of the flux are reported in fig. 3.12.

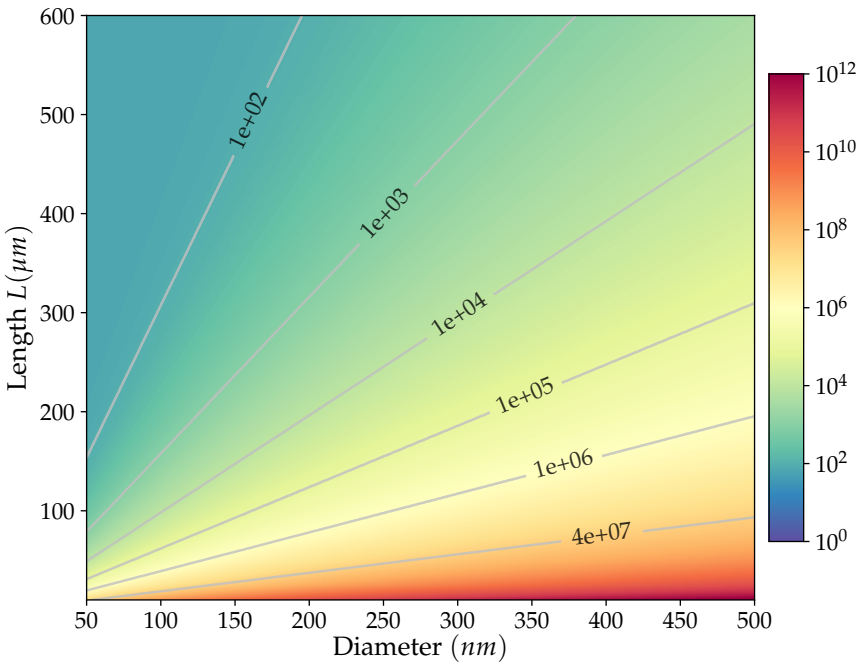

FIGURE 3.12 – The minimum photon flux impinging on the detector required to probe the thermal motion of a SiC nanowire thermalised at 20 mK, before being masked by the imprecision noise, as a function of the NW geometry.

3.1.3 Optical properties

Silicon carbide is a large bandgap material, with a gap ranging from below 400 to 515 nm for its most common allotropic phases (4H/6H and 3C phases respectively) and presents a rather large refractive index, around 2.7 in the visible. For the diameters we employed, in the 100 - 400 nm range, this allows to sustain internal optical resonances for optical wavelengths in the visible. Those internal modes are called **Mie resonances**, and can be computed analytically [238] in the case of an infinite cylinder illuminated by a monochromatic radiation. The original theory assimilates the incoming light field to a plane wave, and permits to compute the fields inside and outside of the nanowire, for any polarization of the incoming light field, and any orientation of its Poynting vector. It is then possible to describe the scattering properties of the nanowire to any incoming light field by expanding it on the plane wave basis, as we will do in the cavity optomechanics section.

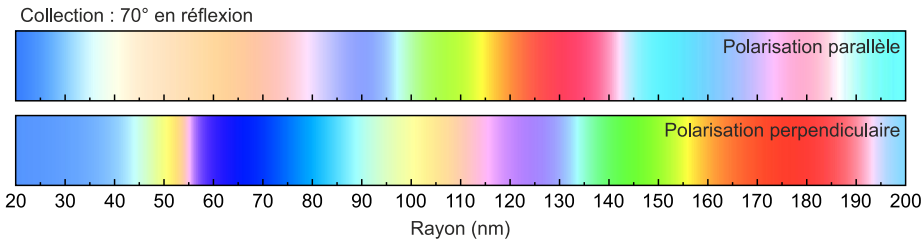

FIGURE 3.13 – Theoretical visible color chart computed for the SiC NWs radius range of interest and for the microscope objective used during the samples' selection.

In our experiments, we make use of the first internal Mie resonances, whose spatial profile is described by the cylindrical harmonic functions. We have seen in the above section that minimizing the nanowire diameter is the key ingredient to increase the nanowire force sensitivity, and naturally fully controls the light-nanowire interaction. It is thus important to precisely determine the diameters of the nanowires we employ, which is done by simply observing the nanowires under a white-light microscope objective, and determining their color for both polarizations of the incoming light source. This requires to take carefully into account the chromatic rendering of the CCD camera and of the screen employed, and leads to the color chart shown in fig. 3.13, established in ref. [233] when employing the 50x/0.55NA objective of the Zeiss microscope in the Nanochemistry room.

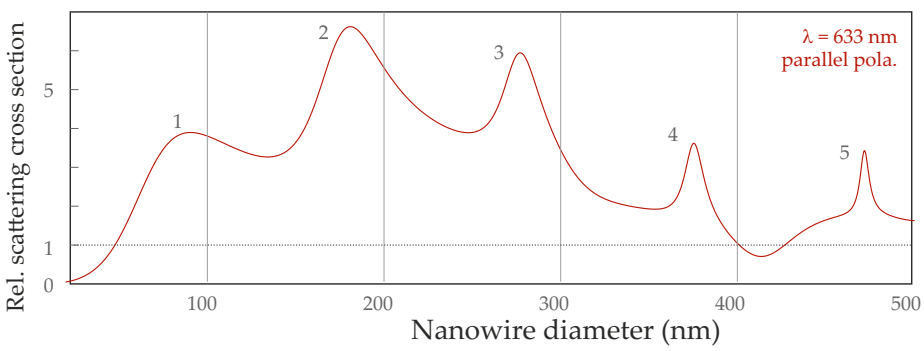

FIGURE 3.14 – Total scattering cross section (normalized by geometric cross section) as function of the nanowire diameter for a probe wavelength of 633 nm and a parallel polarisation, aligned with the nanowire axis. The first Mie resonances are visible, they structure the nanowire optical response and permit to significantly enhance the light-nanowire interaction.

The color chart is obtained under white light illumination. In our experiments we employ monochromatic laser sources, and the Mie resonances will largely structure the light-nanowire interaction. As an example, the total scattering cross section (integrated over all scattering directions) obtained for a 633 nm laser wavelength and parallel polarisation is shown in fig. 3.14, for increasing nanowire diameters. The cross section is normalized to the nanowire geometric cross section.

Using the Mie-scattering resonances [238, 233], it is possible to compute the quantity of light reflected towards the illuminating objective or in any other orientations, and to refine the estimation of the optical contrast expected for our nanowires, which governs the readout efficiency. Figure 3.15 regroups all of the meaningful parameters that enter into play when searching a nanowire for a dedicated experiment. If one seeks a very large force sensitivity, he should target to operate with a small nanowire diameters, lower than 130 nm, and as long as possible. Unfortunately this kind of nanowires are a bit delicate to find and catch since they are quite often largely folded in the powder. However, in order to operate with a large SNR at low temperatures, it is easier to do so with larger, but extremely long, nanowires which are easier to find.

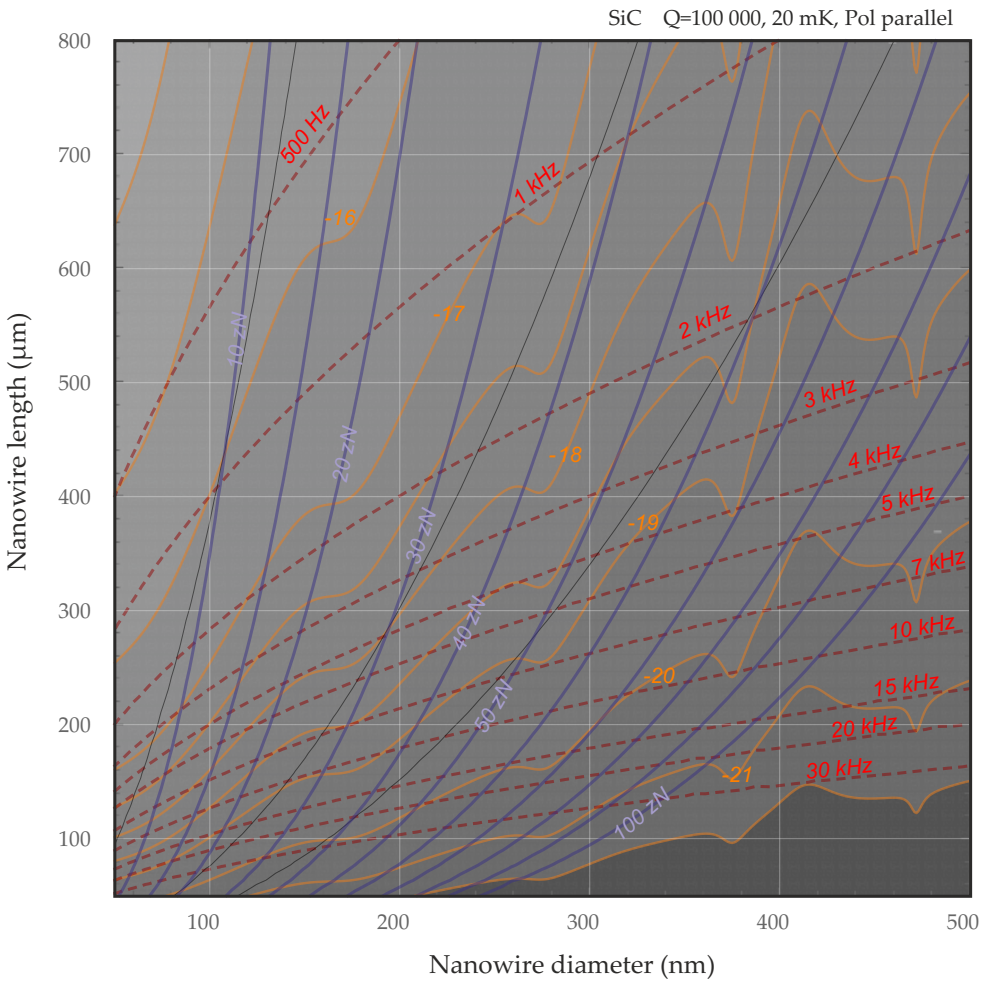

FIGURE 3.15 – Abacus of the nanowires properties expected at dilution temperatures as a function of their length and diameter. In red their fundamental resonance frequency (400 GPa Young modulus). In blue the force sensitivity expected at 20 mK using a constant quality factor of 10^5. In orange, the resonant noise spectral density ($S_{\delta r}[\Omega_m]$) expected at 20 mK with similar Q factor using a 633 nm probe laser. The modulations observed in those traces are due to the reflectivity changes due to the internal Mie resonances in the nanowires (parallel polarisation).

3.2 BROWNIAN THERMOMETRY

We now present the measurements and the results obtained on the thermal noise of a SiC nanowire at ultralow temperature. After discussing the concept of Brownian thermal motion and the way we describe it through its power spectral density, we analyze the Brownian temperature as a function of the intensity of the probe laser. We then compare these results to the ones obtained when recording the thermal motion as a function of the cryostat base temperature. We proceed by analyzing the mechanical frequency and quality factor as a function of the (effective) temperature of the resonator, as well as the force sensitivity that we have achieved for the different samples.

3.2.1 The Brownian thermal motion

Following the discussion of sections 1.2.1 and 3.1.2, we know that each of the resonant modes of the nanowire can be described as a dumped-driven harmonic oscillator couple to an environment at temperature T. This results in random transverse position fluctuations of the NW extremity[4], which have already been tracked and recorded in previous work of the group [233].

These fluctuations spread over a distance $\Delta x_{\text{th}} = \sqrt{k_B T / M\Omega_m^2}$, which is temperature dependent, so that the readout of the nanowire thermal noise can provide information on its vibrational temperature. For completeness, fig. 3.16a shows a numerical simulation of the temporal evolution of this thermal motion for a 300 µm long, 200 nm thick NW thermalised at 20 mK, with a fundamental frequency of $\sim$ 3.5 kHz, a quality factor of 1×10^5 and effective mass of $\sim 7.5 \times 10^{-15}$ kg. Figures 3.16b to 3.16f presents a graphical

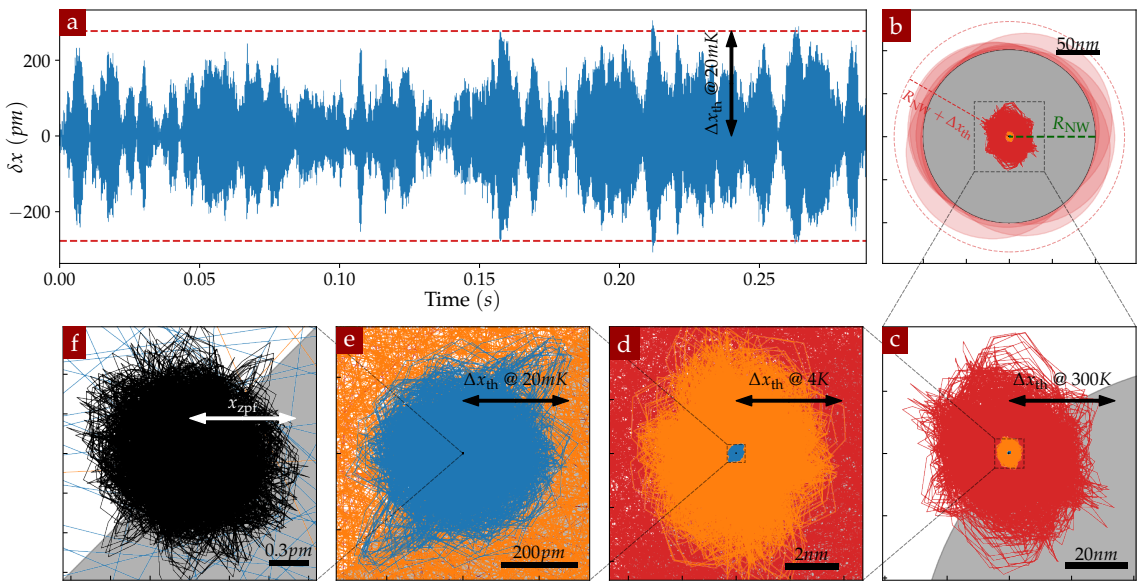

FIGURE 3.16 – Simulation of the Brownian thermal motion of a SiC nanowire: (a) temporal evolution of the position of the resonator extremity, for a 300 µm long, 200 nm thick NW thermalised at 20 mK. (b) comparison between the NW diameter and the spreading of the thermal fluctuations at 300 K. (c), (d), (e) comparison of the spreading of the thermal fluctuations among 3 different temperatures (300 K, 4 K and 20 mK) and with the zero-point-fluctuations (f).

[4]Given the extreme aspect ratio we are allowed to neglect the deformations along the vertical direction $\Delta h \approx \Delta x_{\text{th}}^2 / L$, which is roughly one million times smaller than the laser probe waist dimension.

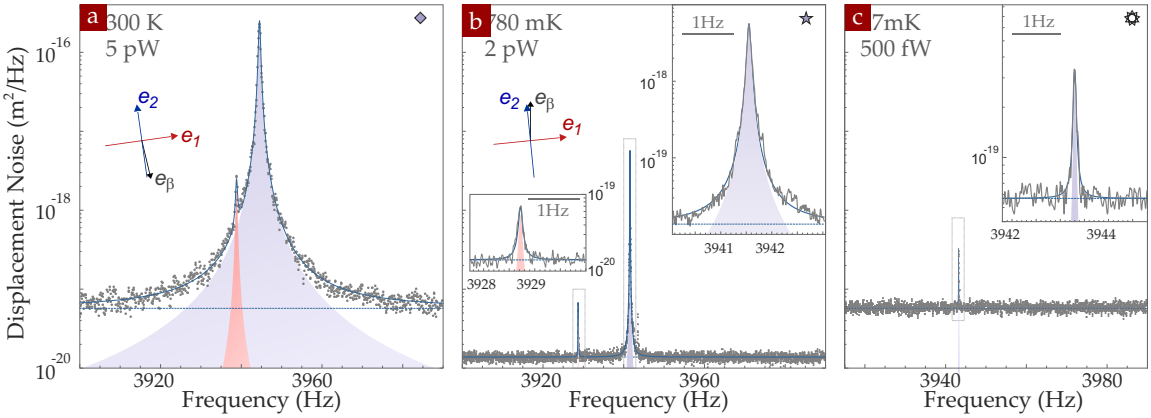

FIGURE 3.17 – Typical position noise spectral density $S_{\delta r_\beta}$ for the sample $NW3$ thermalised at 3 different base temperature of the cryostat: (a) 300 K, (b) 780 mK and (a) 27 mK. The (effective) temperature reduction traduces in a smaller area of the spectrum, while simultaneously it is possible to observe an increased mechanical quality factor at low temperature. The orientation of the eigenmodes on the contrary does not seems to be affected by a change in temperature.

comparison between the diameter of a NW with $R = 100$ nm and its Brownian motion, for temperatures ranging from 300 K down to its fundamental quantum state. This "cartoon" pictures permit to visualize the different dimensions at play in the experiment. For those ultrasensitive force sensors, the Brownian motion spreading at room temperature is comparable to their diameter, and fig. 3.16b gives an idea of the blurring effect caused by their thermal motion.

Experimentally, The nanowire oscillations are converted in an intensity signal modulation through a projection along the measurement vector $\mathbf{e}_\beta$(see sections 2.3.1 and 2.4.3): the signal is recorded with the help of a spectrum analyzer and the typical position noise spectral density $S_{\delta r_\beta}$ obtained is shown in fig. 3.17, for three different sample temperatures[5]. Both mechanical polarizations are clearly visible and the unitary measurement vector $\mathbf{e}_\beta$, in general aligned with the optical axis, is also reported. This is also almost aligned with the high frequency mode ($\mathbf{e}_2$), which explains the large asymmetry observed between peaks' heights. This permits to maximize the peak amplitude at low temperatures. We note that in our mounting process, we aim at placing the nanowire in the plane transverse to the optical axis, and after the hydraulic sealing, we cannot rotate the nanowire anymore. When doing so, we almost systematically observed that one of the eigenmode's orientations was quasi-aligned with the optical axis, suggesting that the lifting of the frequency degeneracy is likely to be governed by the clamping conditions.

The mechanical noise spectrum can be fitted with the expression

$$S_{\delta r_\beta}[\Omega] = \sum_{m=1,2} \frac{2\Gamma_m k_B T}{M_{\text{eff}}} \frac{(\mathbf{e}_m \cdot \mathbf{e}_\beta)^2}{(\Omega_m^2 - \Omega^2)^2 + \Gamma_m^2 \Omega^2} + S_{\delta r_\beta}^{\text{shot}} \tag{3.2.1}$$

where the fitting parameters are the mechanical frequencies $\Omega_{1,2}/2\pi$, the damping rates $\Gamma_{1,2}$ and eigenmode orientations $\mathbf{e}_{1,2}$. The effective mass is estimated at room temperature using the above described procedure, and subsequently checked at all possible tempera-

[5]With sample temperature we indicate the temperature measured by the thermometer close to the sample holder. It usually matches the cryostat base temperature (measure on the mixing chamber), except for temperatures lower than 30 mK, with the first reaching a minimum of 27 mK while the latter can go down to 20 mK. This must not be confused with the Brownian effective temperature extracted from the calibrated spectrum.

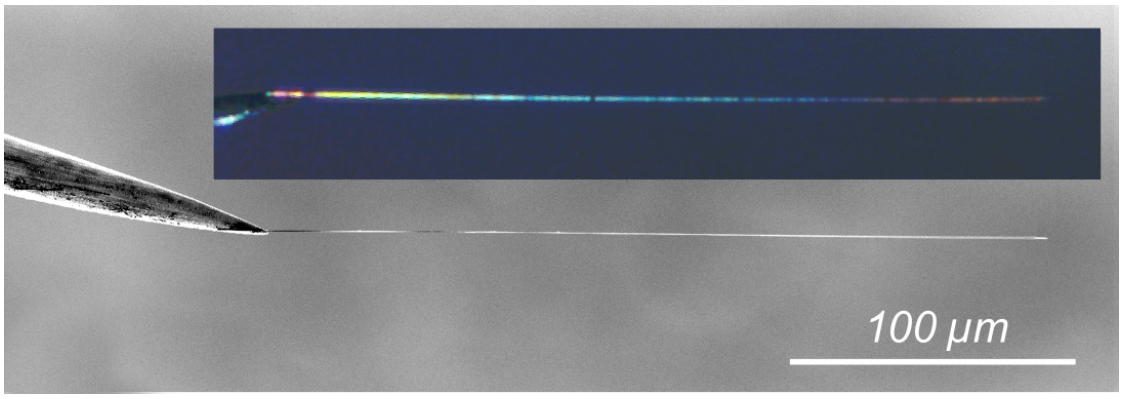

FIGURE 3.18 – SEM and optical (inset) image of the sample $NW1$.

tures, after having verified that the NW is not heated by residual light absorption. Due to the reduction of heat conduction efficiency at low temperatures, this becomes harder and harder to ensure at low temperatures (see below). The area of the spectrum gives access to the effective noise temperature of the mode. Usually the T/M_{eff} ratio presents a spreading around 10%, mainly due to the imprecision obtained on the measurement vector.

From fig. 3.17, we can make several observations: first the eigenmodes' orientations remains unchanged at cryogenic temperature (this has been verified across all the measured samples). On the contrary, the quality factor increased by a factor ~ 10 (see below for a systematic study). The only exception is sample $NW1$, whose Q factor at room temperature was rather low (100) while exhibiting the highest registered value at low T (150000): this was the only sample which had not been backed before the cool process to harden the carbon glue.

It is also worth pointing out that the power employed to readout the nanowire at room temperature is of only 5 pW, measured at the fiber input, so that it is around 4 pW on the nanowire. Despite those ultralow powers, 6 orders of magnitude below the one usually employed in our RT experiments (µW), a very large signal to background ratio is observed (37 dB) above the flat shot noise limited background $S^{\text{shot}}_{\delta r_\beta}$, due to the almost negligible dark count rate of the APD.

At 780 mK the increased Q factor compensates for the reduced thermal motion and both peaks are still visible, but a resolution bandwidth of 30 mHz is required in order to resolve the thermal noise peaks (usually between 20 and 50 mHz are employed depending on the samples). At this temperature the effective mass in unchanged within 10% and the eigenmode orientations are also unchanged, which both suggests that the eigenmodes longitudinal spatial profile is not modified, as expected for a singly-clamped beam of uniform temperature. This may not be the case in presence of an inhomogeneous temperature profile inside the nanowire, if its mechanical properties are temperature dependent (e.g. stiffest at its support than at its vibrating extremity).

Figure 3.17c shows the thermal noise spectrum when the system is cooled down to 27 mK: the injected power is now reduced to $\approx$ 500 fW and the reflected photon flux drops to a few kcts/s. This is comparable to the mechanical frequency (meaning one photon or less per mechanical oscillation), nonetheless it is still possible to preserve a SNR larger than unity, at the cost of long averaging time (around 30 minutes here and up to a few hours for larger Q). When the signal maximum gets close the noise background, it becomes difficult to correctly estimate the mechanical linewidth. In that situation we generally rely on response measurements (see below), from which we extract the me-

Sample	L(µm)	D(nm)	$\Omega_m/2\pi$(kHz)	$Q@T_{amb}$	$Q@LT$	M(pg)	δF_{min}(zN/$\sqrt{\text{Hz}}$)
*NW*1*	270	130	3.05 – 3.06	100	120 000	2.7	–
*NW*2	245	210 - 130	11.49 – 11.58	10 000	95 000	0.8	40
*NW*3*	300	300	3.92 – 3.95	10 000	100 000	20	59
*NW*4	210	160	5.84 – 5.90	14 000	80 000	2.6	–

TABLE 3.4 – Main NW samples employed in the cryogenic setup. *conical

chanical linewidth that is subsequently used in the thermal noise fits. To estimate the corresponding uncertainty on the effective temperature, we fit the data with an imposed damping rate, testing a ±10% variation around the best fit value. This result in an effective temperature of the nanowire vibration noise of 32 ± 2 mK, while the cryostat base temperature was 22 mK and the sample temperature, measured with the deported thermometer, at the level of 27 mK.

Those results were obtained on the suspended setup. Identical measurements realized on the same nanowire, one month before the installation of the suspensions, could not reach noise temperatures below 400 mK. We identified the source of artificial noise by stopping the injection in the cryostat, while continuing to pump on the output port. This lead to a cooling of the still, and probably a reduction in the evaporation rate and an immediate suppression of the excess of noise (40 mK was measured under those conditions).

In table 3.4 we report the most important parameters of the main samples that were studied in this work (among a total of 10 different nanowires which were cooled down, some staying cold for more than 3 months). The previous spectra have been obtained with the sample *NW*3. Figure 3.18 presents a SEM (and optical) image of the sample *NW*1.

3.2.2 Dependence on the cryostat base temperature

To investigate the proper thermalisation of the nanowire, it is important to investigate the dependence of the vibration noise temperature as a function of the cryostat temperature, while operating with minimal optical powers. An eventual thermal decoupling between the two systems will then more clearly appear. The temperature of the cryostat can be raised by passing current through a 1 kΩ resistor. However the continuous temperature range over which the dilution fridge can be operated is rather limited since long operations above 150 mK (hours) may lead to instabilities in the cryostat behaviour which can only be circumvented by a warming up to 4 K and a recondensation. This is both time consuming, and can sometime generates appreciable drifts in the system. To avoid those

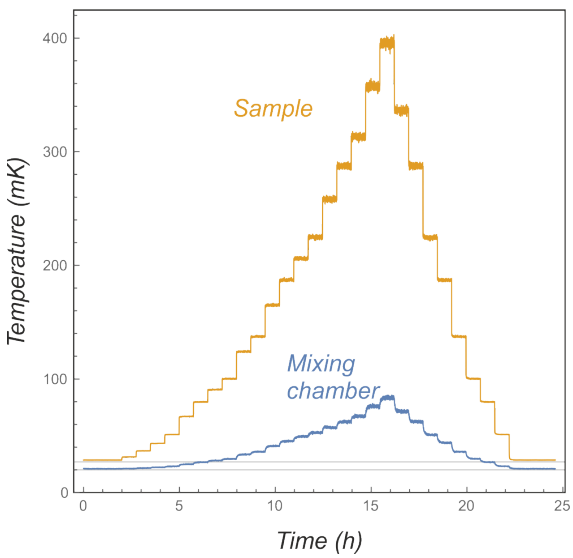

FIGURE 3.19 – Comparison between the heating curve of the sample holder and that of the mixing chamber.

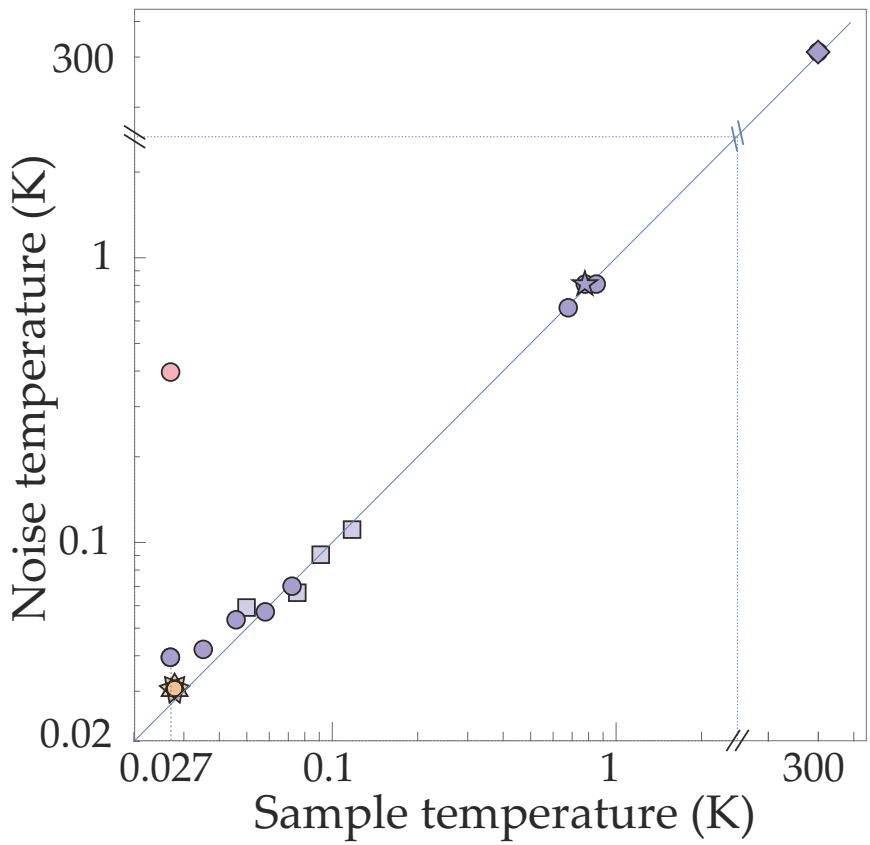

FIGURE 3.20 – Dependence of the noise temperature on the cryostat temperature for the sample *NW*3. Different measurements are shown, with suspension (stars/squares) and without while stopping (circles) or not (red circle) the mixture injection, using optical power in the 100 - 300 fW range. The lowest noise temperature obtained is around 32 ± 2 mK, for a sample temperature of 27 mK and a base temperature of 20 mK.

problems, it is preferable to warm up only the experimental platform, while trying to minimize the temperature increase of the cold plate. To do so, we make use of the thermal bridge between the heater, the optical platform and the cold plate, see fig. 3.19. It allows to warm up the cryostat temperature up to 400 mK while keeping the cold plate below 150 mK. For higher temperature scans, we can lower the pumping strength by turning off the roots pump, or play with the quantity of mixture employed and the heater to span the full temperature range between 20 mK and 4 K. As far as the noise temperature is concerned, the results are well reproducible under thermal cycling, however this can not be the case for the mechanical frequency: sometimes when realizing a large temperature cycle (above $\sim$ 200 mK), we could observe a slight frequency shift, typically increasing by one linewidth.

Figure 3.20 summarizes the results obtained with the same nanowire at different temperatures, with and without the vibration isolation system. Here follows a brief history of our progress towards observing the nanowire quasi-thermalised to the base temperature of the cryostat.

The effective mass was determined at room temperature, as exposed above by verifying the absence of optical heating. In our initial experiments, even if the nanowire was known to be well thermalized from the analysis of its frequency shifts (see below), we could not measure low noise temperatures. Instead we found large fluctuations around 100 - 400 mK, with a tendency to increase for lower cryostat temperatures. However, at larger temperatures, around 780 mK, the nanowire was found well thermalised over an

important optical power range (100 fW-10 pW). After many search and try, where we hunted possible sources of noise, mainly of electrical origin, we identified that it came from the circulation of the mixture itself. Indeed, the mixture injection can be temporary stopped (for a period of around 20 - 30 min while keeping pumping on the output port) before the base temperature of the cryostat starts to increase again when all the mixture has been completely evacuated from the mixing chamber. As soon as the still temperature was lowered from 800 to 650 mK (due to the absence of warm mixture input), which takes around two minutes, the excess of thermal noise almost disappeared on the non-averaged spectrum. This duration was sufficient to record a properly averaged mechanical spectrum and to determine its noise temperature. The latter was found significantly colder, around 40 mK. These are represented respectively by the red and blue circles in the plot. Based on measurements of the oscillator response to a coherent motion imposed on the piezo scanner, we could estimate that the cryogenic circulation was responsible for an equivalent noise of the nanowire support of a few $\mathrm{pm}/\sqrt{\mathrm{Hz}}$, which is relatively weak but sufficient to resonantly drive our ultrasensitive resonator at those extremely large noise amplitudes. This excess of noise, which is ultimately dissipated by the viscous damping force, is responsible for an additional dissipated power of $\Gamma k_B T_{\mathrm{noise}}$, which is of a few yW for a noise temperature of 400 mK, and is thus completely negligible compared to the optical powers employed . We reproduce those "single shot" measurements for increasing sample temperatures, which are represented by the squares in fig. 3.20.

Following those observations, we designed a mechanical decoupling stage with the help of D. Dufeux, L. Del-Rey and E. Eyraud, which was realized by J. Jarreau and incorporated in the setup (see section 2.3.4), to decouple the experiment from the cryostat. The stars and the dots in the figure represent a set of measurements realized using the sample $NW3$ after the suspension mechanism was installed: this not only matches well with the previous results obtained in the "injection-stopped" mode, but has also allowed to reach the lowest noise temperature recorded so far, with a value around 32 ± 2 mK (the spectrum in fig. 3.17c refers to this measure).

3.2.3 Optical heating

In the previous sections we mentioned that the light intensity employed to probe the NW motion should be as small as possible. Here we investigate how the noise effective temperature varies as a function of the injected power, which was varied using the acousto-optic modulator. The results relative to $NW3$ are shown in fig. 3.21.

In those measurements, we had to record the local measurement vector for each power, but we did not need to recalibrate the piezo scanning range since the cryostat temperature was left unchanged (the cooling power is orders of magnitude larger than the injected optical powers). By varying the input power from 100 fW to hundreds of pW, the noise temperature was raised from 32 to 700 mK, with a very peculiar power dependency. Ultralow optical powers are required to observe noise temperatures below 100 mK, which is reached when injecting around 1 pW. The initial slope (dashed line) can be written $T_{\mathrm{eff}} = 100\,\mathrm{mK}(P_{\mathrm{in}}/10.7\,\mathrm{pW})^{1/2}$, which is sub-linear due to the fact that the heat conduction efficiency increases with temperature. We do not experimentally reach the flat behaviour expected at infinitely small optical powers, where the noise temperature becomes power independent. According to the above expression, it should arise for injected powers around 50 fW, for which the signal to noise is smaller than unity. At larger optical powers, above 1 pW, the heating slope gets reduced and acquires a $P^{1/5}$ de-

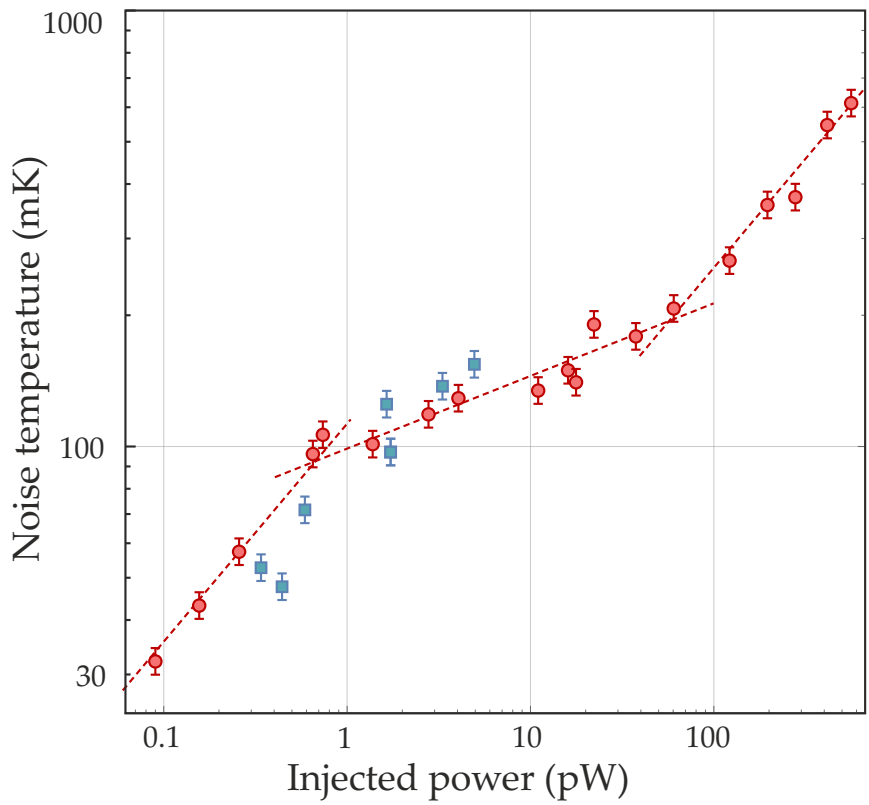

FIGURE 3.21 – Brownian noise temperature of $NW3$ (in red) as a function of the injected power. In the range 100 - 200 mK the effective temperature exhibits a $P^{1/5}$ power dependence, while for lower and higher temperature it varies as $P^{1/2}$. For comparison the measured values for $NW2$ have been also added (in blue).

pendence, which suggests that the heat conduction mechanism increases significantly in efficiency in the 100 - 200 mK temperature range. Finally a $P^{1/2}$ slope is observed above 200 mK, which corresponds to injected powers above 100 pW. We will come back in section 3.3 on the possible origin of this peculiar optical power behaviour. The interesting thing, however, is that it has been possible to replicate this kind of power dependence over at least three different samples (the ones for which we have reliable values at this power/temperature).

A natural question that arises is the connection between the above measured noise temperature and the physical temperature of the nanowire. Stated in another way, when we reach a noise temperature of 700 mK, what is the physical temperature of the nanowire. We will now try to get more insight on that question by investigating the mechanical properties of the nanowire and their temperature dependence.

3.2.4 Frequency and quality factor temperature dependence: TLS signature

The mechanical properties of the nanowire, such as its mechanical resonance frequency and damping rate, are largely unexplored at low temperatures. To understand the above introduced optical heating effects, is interesting to compare the results obtained by varying the injected probe power with the ones achieved while scanning the cryostat temperature. When the optical power is small enough, the temperature profile within the nanowire is supposedly homogeneous, while in presence of optical heating, a temperature gradient is likely to arise along the nanowire.

Figure 3.22 shows how both the frequency and the quality factor evolve with temperature from room temperature down to 20 mK. This figure combines 1) measurements taken while cooling the cryostat (open circles above 4 K) from 300 K to $T > 4$ K, 2) measurements taken while increasing the sample temperature (open circles from 20 mK to 400 mK), 3) measurements taken while increasing the optical power for a cryostat operated at 20 mK (full circles). In that case the horizontal axis represents the noise temperature of the mode. These measurements are taken on $NW4$ oscillating at 5.8 kHz.

FREQUENCY When lowering the temperature from 300 K to 4 K, both eigenmodes increase in frequency by 20 Hz, showing the slight stiffening of the young modulus of SiC. Below 1 K however, the slope gets reversed and one observes a characteristic logarithmic decrease of the oscillation frequency, given by:

$$\Delta\Omega_m/\Omega_m = 2.5 \times 10^{-6} \ln\left(\frac{T}{100\,\mathrm{mK}}\right) \tag{3.2.2}$$

We note that the overall variation between 20 mK and 1 K is more or less comparable to the mechanical linewidth.

What is also noticeable is that the frequency shifts induced by light absorption follow the same trend as the one obtained while varying the cryostat temperature. One can understand this observation with the following arguments: when the heat conduction efficiency increases with temperature, all the temperature gradients are pushed towards the upper extremity of the nanowire. This is due to the fact that its lower extremity, where the laser is positioned, is warmer and thus presents a higher conductance, which does not allow a large temperature gradient to establish. As such, the temperature profile within the nanowire is expected to be more homogeneous than in the case of a temperature independent conductance. Its mechanical properties are then expected to be similar to the ones obtained by simply increasing the cryostat at the corresponding temperature.

The logarithmic frequency increase observed below 1 K is typical of amorphous materials and we will come back on that later. This phenomena has a very practical experimental interest when trying to minimize the nanowire temperature: for example, one can simply track the resonance frequency and minimize it while moving the readout laser vertically to identify regions of smaller light absorption.

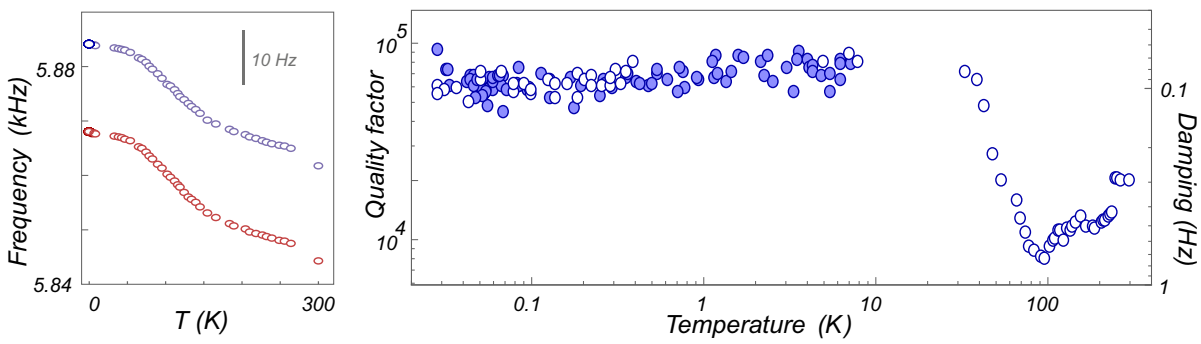

FIGURE 3.22 – Temperature dependence of the mechanical frequency and damping rate for the sample $NW4$, from room to dilution temperature. The open circles are obtained at minimal optical powers (sub pW) while varying the cryostat temperature. The full circles are measured for increasing optical powers (from 100 fW to 10 nW, cryostat set at 20 mK) and are plotted as a function of the measured effective noise temperature.

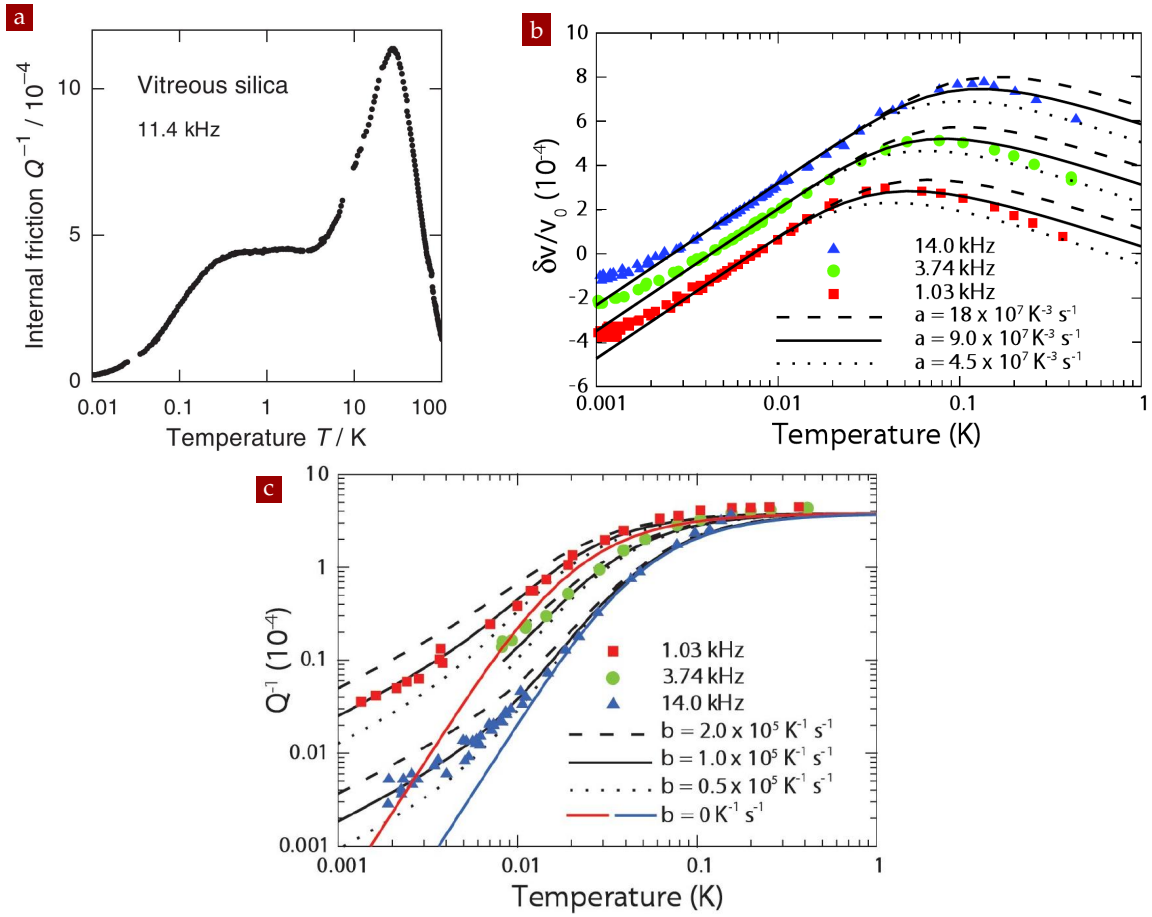

FIGURE 3.23 – Mechanical property of amorphous material at low temperature: (a), (c) quality factor (image from [244] and [75]); (b) relative change in sound velocity (image from [75]).

We note however that while the oscillator frequency is a very good relative temperature indicator, it can suffer from the fact that the minimal frequency may evolves after a thermal cycle above $\sim$ 200 mK. When this happens, in general we observe a blue frequency shift by typically one linewidth (100 mHz) after having raised the nanowire temperature. This signature is also commonly observed in amorphous materials (sometimes called "aging"). Longer "heating" period and particularly high temperature (above 1 K) increase the probability for this phenomenon to happen.

DAMPING RATE The behaviour of the quality factor is rather different: from the room temperature values, $Q \sim 20000$, it actually gets reduced down to a temperature around 90 K, where it reaches a minimal value of $Q \sim 7000$. At lower temperatures, it starts to increase again, down to around 10 K, when it reaches a plateau around $Q \sim 80000$. This peculiar behaviour is actually well known in amorphous glass material [198, 45, 244], caused by thermally activated relaxation processes which modify the internal friction of the material itself (see fig. 3.23a).

Below 10 K, the nanowire reaches a plateau value, which is universally observed in amorphous systems, but at a smaller value of $Q \sim 2500$. However, in comparison to the usual improvement of the quality factor expected at even lower temperatures, the quality factor of almost all the nanowires investigated up to now have never shown such an improvement. This could be explained by the fact that we have reached a quality factor limited by other mechanisms, such as clamping losses, but is not yet fully understood.

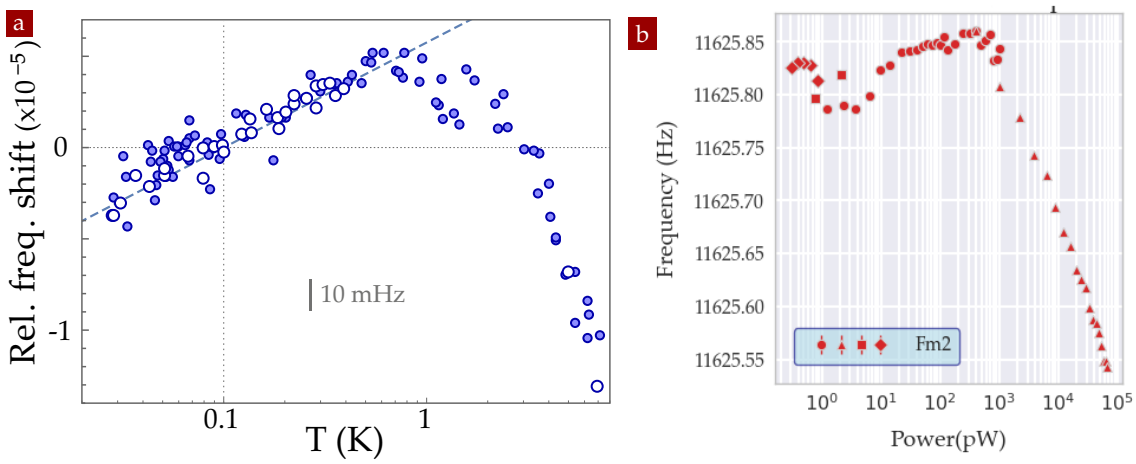

FIGURE 3.24 – Frequency versus optical power for different nanowires: (a) *NW*4, (b) *NW*2. The inversion in the slope occurs for a noise temperature around 800 - 1000 mK. The larger scatter observed on the 11 kHz nanowire is due to a too large thermal cycling, which leads to systematic frequency upshifts (of less than a mechanical linewidth) when the temperature is increased beyond 400 - 500 mK.

TWO-LEVEL TUNNELING SYSTEMS Those observations present multiple similarities with the mechanical properties of amorphous materials, described by an assembly of the two-level tunneling systems[6] [11, 155, 244, 75, 216, 44, 215, 162, 243, 121, 253] (TLSs), see figs. 3.23b and 3.23c. However, the plateau we observe is between 80000 and 100000, depending on the sample, which is around 40 times higher than the universal value of $\approx$ 2500 for amorphous materials. Concerning the frequency shifts, they follow $\Delta\Omega_m/\Omega_m \approx C\ln(T/T_0)$, with the constant value $C \approx 2.5 \times 10^{-6}$, which is also two orders of magnitude smaller than the universal value. Usually this constant is directly connected to the density of structural defects involved: those observations would thus suggest that only a fraction of the nanowires behaves as an amorphous material. This is in agreement with the few nanometers oxide crust present on the surface, which can be revealed in TEM imagining (see fig. 3.1b).

The good agreement we found between the two kinds of scan (temperature and optical) in fig. 3.24 is far from trivial. Indeed, some recent studies in the group of L. Bellon [83] have shown that this is not the case when the internal temperature profile in a cantilever is non homogenous. This comes from the fact that the power spectral density of the force noise can be viewed as a spatial integral of the contributions of local Langevin force vectors distributed along the mode profile.

Having a largely varying thermal conductance ensures that the effective temperature within the nanowire is almost homogeneous, except in the clamping region. Also, the oxide crust is present all along the nanowire, which ensures that this source of dissipation is rather homogeneous along the nanowire. Finally, since we operate with low frequency modes, the deviation of the Q factor from the plateau appears at temperatures below 150 mK (according to recent work in the group of E. Collin at Néel, the magnitude of the deviation appears to depend on the dimensionality of the system, in our case

[6] Even if its precise origin is still under debate, the concept of TLSs is often illustrated as an atom or a group of atoms that can have two stable configurations in their energy landscape, like in a double well potential. These groups of atoms can transit between the two conformations via quantum tunneling between the two states (low temperature regime) or via thermal activation above the barrier (high temperature regime). Those transitions impact the deformability of the material, and are thus introducing energy losses for the phonons propagating in the material.

it should be weaker than what has been measured with larger systems, see fig. 3.23c). This quasi-independence of the clamping losses induced by amorphous defects in temperature, makes that the local dissipation strength, dominated by TLS contributions in principle, will not depend on the nanowire local temperature, which is another argument to understand the good agreement found between both approaches.

In a close future when we will try to improve the quality factor of the nanowires by trying to remove the oxide crust, the situation may be largely different. For the moment, we found that laser induced heating is a proper way to artificially warm up the nanowire, with the advantage that it does not perturb the dilution process.

3.3 LOW TEMPERATURE HEAT TRANSPORT AT THE NANOSCALE

In order to better understand how the heat propagates inside the SiC nanowire we present here some fundamental concepts on thermal transport at low temperature in nano systems. This section is a brief review of the different regimes that are in principle at play in our system. The proper understanding of the heating mechanism in our system will require some additional measurements that are presented at the end of this section.

3.3.1 The low temperature heat transport regimes

A solid with a regular crystalline structure hosts collective vibration modes of its lattice described by individual excitations called *phonons*.

The phonons in a solid are involved in the transport of heat and the mechanism is governed by two characteristic lengths. These are the mean-free-path (MFP) Λ and the phonon dominant wavelength λ_{dom}. The first is the average distance over which a phonon travels between two successive inelastic collisions. The second is defined as the maximum of the phonon's spectral density distribution, given by a black-body-like expression:

$$u(\lambda, T) = \frac{2hv_s^2}{\lambda^5} \frac{1}{e^{\frac{hv_s}{\lambda k_B T}} - 1}, \tag{3.3.1}$$

so that $u(\lambda, T)d\lambda$ represents the volumic energy density of phonons having a wavelength between λ and $\lambda + d\lambda$. v_s is the speed of sound in the material (for SiC we used $v_s = 13\,000\,\text{m/s}$, as from [247]). Figure 3.25 shows a density plot of the the phonon spectral density as a function of the phonon wavelength λ and of the temperature T. The dominant wavelength can be expressed as [230]:

$$\lambda_{\text{dom}} = \frac{hv_s}{2.82\, k_B T}. \tag{3.3.2}$$

The specific heat of SiC can be well described by the Debye model, which at low temperature can be written

$$C_V = \frac{2\pi^2}{5} \frac{k_B^4}{\hbar^3 v_s^3} T^3, \tag{3.3.3}$$

whose unit is J/kgK. The T^3 dependence is characteristic of $3D$-bulk solid, but in general it scales as T^d, where d is the dimension of the system. To know if a system can be considered as a $3D$, $2D$ or $1D$ object, one should compare its dimensions to the dominant

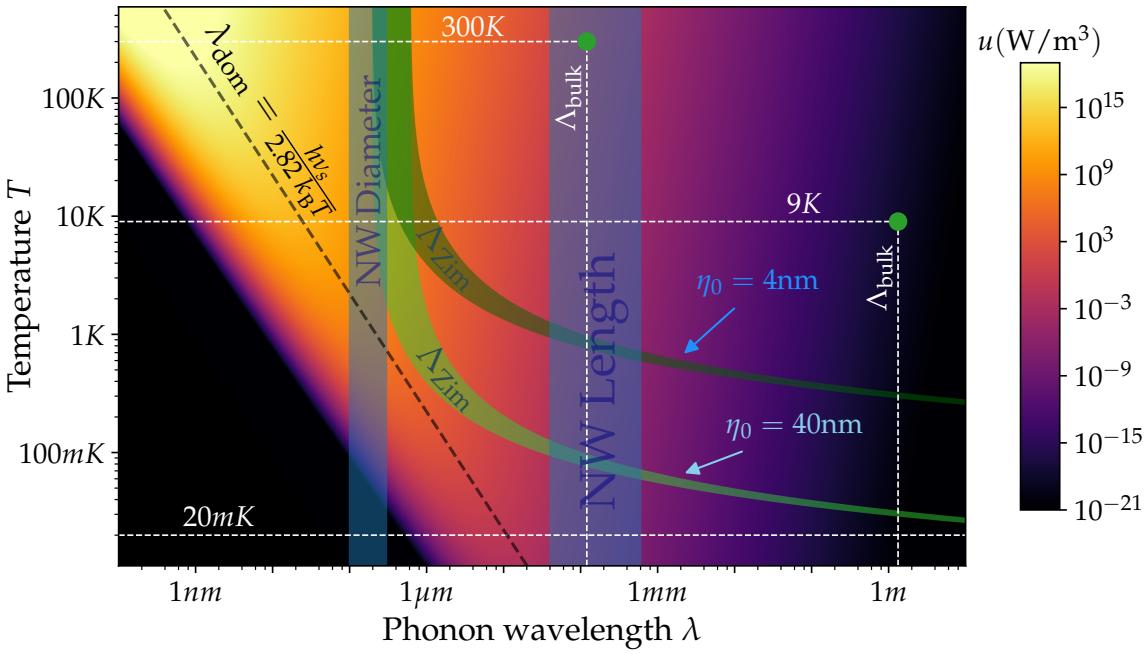

FIGURE 3.25 – Phonon spectral density distribution as a function of the phonon wavelength λ and the temperature T. For each temperature, the maximum value is defined as the *dominant wavelength* λ_{dom} (black dotted line). The two vertical stripes represent the typical width and length of our nanowires. The two green curves illustrate how the MFP in the Ziman model Λ_{zim} varies at different temperatures and for two different values of the surface roughness ($\eta_0 = 4\,\mathrm{nm}$ and $\eta_0 = 40\,\mathrm{nm}$). The two green dots show the values of the MPF Λ computed with the kinetic equation when using the values tabulated in literature for the specific heat and the conductivity (see table 3.1). Given its size, the value at 9 K is most probably false.

phonon wavelength λ_{dom}. Inspecting the plot of fig. 3.25, we expect our nanowire specific heat to follow a $3D$ regime at temperatures higher than $\approx 1\,\mathrm{K}$ and a $1D$ regime below.

An essential quantity which describes how a material conducts the heat, is the thermal conductivity κ_{ph}, which is associated with the diffusive regime of heat propagation. When a heat flux is settled in the nanowire, it is connected to the temperature gradient according to the Fourier's law:

$$j_{\mathrm{th}} = -\kappa_{ph}\frac{dT}{dx}. \tag{3.3.4}$$

The *kinetic equation* connects the MFP, the specific heat and the heat conductivity by:

$$\kappa_{ph} = \frac{1}{3}C_{ph}v_s\Lambda_{ph}, \tag{3.3.5}$$

where Λ_{ph} is the MFP for the bulk material. This implies that for the thermal conductivity of a $3D$ solid at low temperature (as the diffusive regime still holds) we can expect (supposing the MFP and the sound speed constants) the same T^3 dependence on the temperature as for the specific heat. One can also use this formula to estimate the MFP for the bulk material, making use of the tabulated values of κ_{ph} and C_{ph}. Starting from the value reported in table 3.1, these are represented by the green dots in fig. 3.25 for the temperature of 300 K and 9 K. It is very important to notice that at room temperature those values are already much larger than the typical dimensions of our samples, meaning that the reasoning based on $3D$ bulk materials is not appropriate.

It is then mandatory to examine how the geometry of the system can affect its thermal properties. It is usually more appropriate to describe the heat transport of the system by mean of the thermal conductance, defined as

$$K = \kappa_{ph} \frac{S}{L}, \tag{3.3.6}$$

where S and L are respectively the section and the length of the system along the heat flow. This allows for a consistent and better comparison among different geometries and among different heat propagation regimes (diffusive or ballistic).

When one of the dimensions of the system becomes smaller then the phonon MFP, the Debye diffusive model is not suitable anymore and new constraints must be taken into account. This is done by the **Casimir model** [35], which postulates that the MFP of the phonon is limited by the geometrical boundaries, in our case $\Lambda_{\text{cas}} = D$, where D is the diameter of the NW. This is based on the hypothesis of infinitely (or perfectly) rough surfaces, where the scattering of the phonons is completely inelastic, so that every time one hits a surface, its coherence is destroyed. The surfaces act as a black-body in optics, they fully absorb the incoming phonons which are then re-emitted in random directions. This hypothesis is fulfilled when the phonon dominant wavelength is much smaller than the average surface roughness η, $\lambda_{\text{dom}} \ll \eta$. Our silicon carbide nanowires present a surface roughness of few nanometers and sometime some diameter modulations with a periodicity in the 100 nm - 5 µm range. Furthermore the oxide crust are not really homogeneous. As such we expect a great variability on the temperture range where the Casimir model holds, which should extend in principle from 300 K down to 100 K for homogeneous wires, but from 300 K down to 500 mK for largely inhomogeneous nanowires (cfr. fig. 3.25). In principle, however, the Casimir criteria should not hold at the smallest temperature achieved.

In the case of a cylindrical-shaped conductor, the thermal conductance in the Casimir regime can be expressed as [22, 230]

$$K(T) = 3.2 \times 10^3 \left(\frac{2\pi^2 k_{\text{B}}^4}{5\hbar^3 v_s^3} \right)^{(2/3)} \frac{S\Lambda_{\text{cas}}}{L} T^3. \tag{3.3.7}$$

As we can see, compared to the standard diffusive model the MFP Λ_{cas} sets now a major constraint given by the dimension of the system, as it has been experimentally investigated in the case of silicon nanowires [118, 92, 227].

However, the hypothesis of infinitely rough surfaces, behaving as strong incoherent phonon diffuser, does not hold as we keep lowering the temperature: the dominant phonon wavelength keeps growing and the surface scattering regime is not fully inelastic anymore. In particular, in the extreme opposite case when $\lambda_{\text{dom}} \gg \eta$, the surface acts as a perfectly smooth mirror. This transition regime is known as the **Ziman regime** [265].

Ziman proposed a phenomenological parameter, p_{spec}, which represents the phonon probability of specular (elastic) reflection. When a phonon impinges on the surface, it can be either absorbed and then scattered in a random direction, or specularly reflected, conserving its energy and its coherence. The case $p_{\text{spec}} = 0$ will correspond to the Casimir regime, while $p_{\text{spec}} = 1$ is the case of a perfectly smooth surface. The expression for the thermal conductance will be the same as for the Casimir regime eq. (3.3.7), with the MFP Λ_{cas} replaced by:

$$\Lambda_{\text{zim}} = \frac{1 + p_{\text{spec}}}{1 - p_{\text{spec}}} \Lambda_{\text{cas}} \tag{3.3.8}$$

This expression diverges in the case of perfectly smooth surfaces ($p_{\text{spec}} = 1$), implying that the mean free path is not limited anymore by the lateral dimensions of the nanowire in case of mirror-like reflections.

Following references [92, 230, 236], the roughness of a surface is described by a probability distribution $P(\eta)$, so that the specular probability evaluated for the dominant phonon wavelength can be written

$$p_{\text{spec}}(\lambda_{\text{dom}}) \simeq \int_0^{\lambda_{\text{dom}}/4\pi} P(\eta) d\eta. \tag{3.3.9}$$

This traduces that it is only the defects with dimensions smaller than λ_{dom} that behave specularly. For a mean roughness η_0, we can adopt the following distribution:

$$P(\eta) = \frac{1}{\eta_0} e^{-\eta/\eta_0}, \tag{3.3.10}$$

With such a distribution the MFP will be given by

$$\Lambda_{\text{zim}}(T) = \left(\frac{2 - e^{-\lambda_{\text{dom}}(T)/4\pi\eta_0}}{e^{-\lambda_{\text{dom}}(T)/4\pi\eta_0}} \right) \Lambda_{\text{cas}}, \tag{3.3.11}$$

whose temperature dependence is depicted by the green curves in fig. 3.25 for two different mean roughness: $\eta_0 = 4\,\text{nm}$ and $40\,\text{nm}$ (the plot axes are reversed and we plot the Ziman MFP [horizontal axes] as a function of the temperature [vertical axis]).

That plot of the Ziman MFP tells us how the MFP for the most populated phonons evolve with temperature. Since it diverges at low temperatures, at some point the MFP gets larger than the nanowire length itself. This transition occurs between 100 mK and 1 K depending on the surface roughness. The system thus enters the so called **ballistic regime**, for which the nanowire behaves exactly like a $1D$ acoustic guide. As such, for temperatures below 1 K, two important things happen: first, the dominant wavelength λ_{dom} becomes comparable to the cross section of the NW and the system should exhibit a transition from $3D$ to $1D$; second, the MFP increases up to the same order of magnitude as the NW's length. As a consequence, at the lowest temperature achieved there is no more phonon incoherent scattering along the nanowire, which raises questions about the proper definition of a temperature in that regime. Note however that the value of the MFP strongly depends on the roughness of the system: if we assume an average roughness of 40 nm instead of 4 nm, the system becomes fully ballistic at around 200 mK.

When operating in this regime, the thermal conductance is usually compared to the *quantum of thermal conductance* [171], given by

$$G_q = \frac{\pi^2 k_{\text{B}}^2}{3h} T. \tag{3.3.12}$$

This represents the maximum possible contribution of each populated phonon mode to the conductance of a $1D$ waveguide, reached in case of perfect transmission (note that in a $1D$ channel there are only four acoustic branches [147], one dilatational, one torsional, two flexural). It is universal, independent of the material and of the statistics of the carriers (electrons, photons, anyons, phonons). Experimentally, it has been really difficult to probe this limit for phonons [183, 184], mainly because the distance between the test conductors employed was too short. In that view, our nanowires could help investigating this peculiar regime.

Finally, when cooling the system to dilution temperatures, the dominant wavelengths enter the µm range and approach the dimension of the crystal defects observed on inhomogeneous nanowires: if they still have any kind of impact on the system behaviour, they should become completely transparent beyond this point.

As a summary, there are many parameters that enter into play in the proper understanding of the thermal behaviour of our nanowire and a systematic study will help understand in greater detail the different regimes exposed above. This will be the subject of future developments in the group, where we will aim at realizing pump-probe measurements of the dynamical propagation of heat waves generated by a second pump laser. The transition from a diffusive to a ballistic regime should present a very peculiar signature in the thermal response of the nanowire.

3.3.2 Static heating of the nanowire at cryogenic temperatures

In this section we aim at interpreting the optical heating measurements and evaluating the overall nanowire conductance that can be extracted out of those measurements.

When positioning the laser at the nanowire extremity ($y = L$), the absorbed light power P_{abs} generates a heat flux in the nanowire, propagating towards its support, which, in absence of lateral thermal loss, is constant all along the resonator and equals to $j_{\text{th}} = -P_{\text{abs}}/S$. The heat flux emitted by a perfect black-body having the surface of the nanowire is given by the Stefan-Boltzmann law, $\sigma T^4 \pi D_{\text{NW}} L_{\text{NW}}$, and amounts to $\sim 5\,\text{aW}$ at $1\,\text{K}$ ($\sigma = 5.7 \times 10^{-8}\,\text{W/m/K}^4$). This value is significantly smaller than the injected optical powers, but must indeed be compared to the absorbed power itself, that we will estimate below. We adopt a $1D$ description for the nanowire. If one assumes that it is possible to define a temperature all along the nanowire length, which may become non valid when the mean free path becomes comparable to the nanowire length, then at each point we can connect the heat flux to the temperature gradient using the Fourier's law:

$$j_{\text{th}} = -\kappa_{ph} \nabla T \tag{3.3.13}$$

where κ_{ph} is the local heat conductivity. By integrating this equation all along the nanowire, we obtain:

$$\int_0^L j_{\text{th}} dy = -P_{\text{abs}} \frac{L}{S} = -\int_0^L \kappa_{ph}(T(y)) \nabla T dy \tag{3.3.14}$$

where we have made explicit the temperature dependence of the heat conductivity. When realizing a change of variable $y \to T(y)$, which can safely be assumed to be monotonous, we obtain:

$$\frac{A_{\text{abs}} P_{\text{opt}} L}{S} = \int_{T_{\text{cryo}}}^{T_{\text{NW}}} \kappa_{ph}(T) dT \tag{3.3.15}$$

where we have assimilated the temperature of the nanowire's vibrating extremity to the noise temperature measured, in view of previous discussions on mechanical properties. As we will see below, this model leads to a rapid increase of the heat conductivity at low temperatures, so that all the temperature gradients that may exist within the nanowire will likely be located close to the clamped extremity. We have also introduced the absorption coefficient A_{abs} (intensity related), while P_{opt} is the injected power. We can also make the equivalent nanowire heat conductance $K(T)$ appear in the above expression,

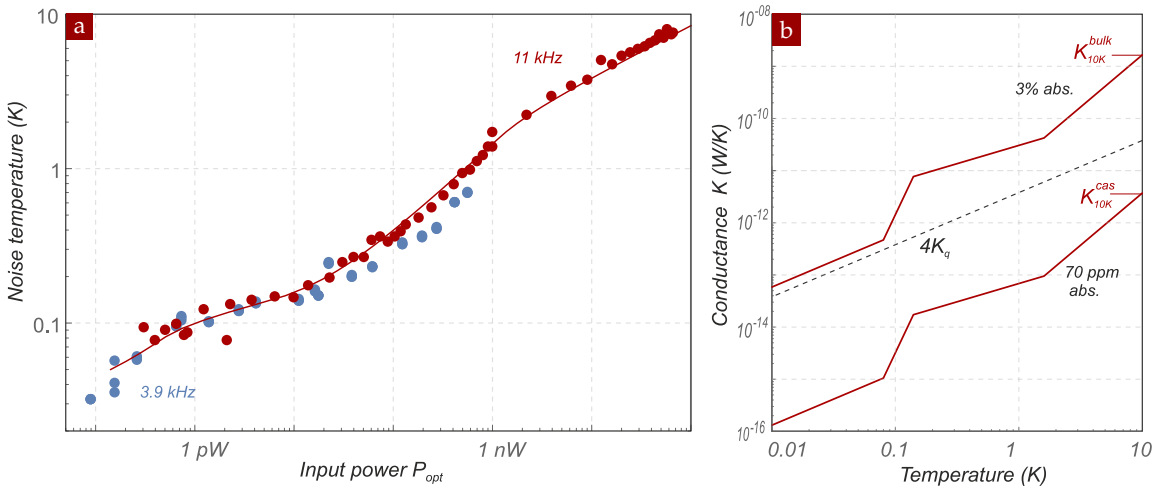

FIGURE 3.26 – Analysis of light induced heating of the NW: (a) noise temperatures as a function of the injected power for $NW2$ (11 kHz) and $NW3$ (3.9 kHz) in red and blue respectively. The solid line is a fit to the 11 kHz data, using the thermal conductance shown in the right panel. (b) the 2 different thermal conductance profiles derived, assuming that the conductance at 10 K is given by the bulk expression (above) or by the Casimir formula (below). This choice impacts on the estimated absorption coefficient, which is respectively of 3% or of 70 ppm. The quantum conductance for four channels is shown as a dashed line.

which would be the one measured if the temperature profile was homogeneous within the nanowire:

$$A_{\text{abs}} P_{\text{opt}} = \int_{T_{\text{cryo}}}^{T_{\text{NW}}} K(T) dT. \tag{3.3.16}$$

This expression can be used to analyze the optical heating curves ($T_{\text{NW}} = f(P_{\text{opt}})$) such as the one shown for $NW3$ above, or the one obtained on $NW2$ and shown in fig. 3.26a, where we have employed an even larger optical power in order to warm up the nanowire up to approx. 10 K.

The exact absorption coefficient is in principle not known and potentially varies with the laser position on the nanowire. We note that it can also evolve with temperature: in that case, it will have to be evaluated at the nanowire's extremity temperature ($A_{\text{abs}} \rightarrow A_{\text{abs}}(T_{\text{NW}})$). The thermal properties of silicon carbide are not known, even for bulk material, below 4 K. We will then use the above equation to adjust the nanowire conductance $K(T)$ and will force it to equal the expected conductance at 10 K, from which we will estimate the absorption coefficient at that temperature. From the above expression, if the heat conductance scales as $K(T) = K_0(T/T_0)^{\mu}$, then the nanowire temperature will evolve as $T_{\text{NW}} \propto {P_{\text{abs}}}^{1/(1+\mu)}$ for sufficient temperature increase. So the changes in the heating slopes in the log-log plots are in principle due to a change in the conductance regime, if we assume that the absorption coefficient remains unchanged.

Our different measurements realized on different nanowires suggest that the heating patterns do present some systematic turning points, around 100 mK, 200 mK and 2 K, across which the power law of the heating process changes. To adjust the measurements, we will thus adopt a segmented conductance profile, presenting changing power laws

between the above intervals. The conductance obtained from this procedure is shown in fig. 3.26b and evolves as:

$$K(T) = \begin{cases} K_{10\,\mathrm{K}} \cdot (T/10\,\mathrm{K})^2 & 1.6\,\mathrm{K} < T < 10\,\mathrm{K} \\ K_{1.6\,\mathrm{K}} \cdot (T/1.6\,\mathrm{K})^{0.7} & 140\,\mathrm{mK} < T < 1.6\,\mathrm{K} \\ K_{140\,\mathrm{mK}} \cdot (T/140\,\mathrm{mK})^5 & 80\,\mathrm{mK} < T < 140\,\mathrm{mK} \\ K_{80\,\mathrm{mK}} \cdot (T/80\,\mathrm{mK})^1 & 20\,\mathrm{mK} < T < 80\,\mathrm{mK} \end{cases} \tag{3.3.17}$$

with $K_{1.6\,\mathrm{K}} = K_{10\,\mathrm{K}} \cdot (1.6/10)^2$, $K_{140\,\mathrm{mK}} = K_{1.6\,\mathrm{K}} \cdot (0.14/1.6)^{0.7}$ and $K_{80\,\mathrm{mK}} = K_{140\,\mathrm{mK}} \cdot (0.08/0.14)^5$. The fitting constant obtained is of $K_{10\,\mathrm{K}}/A_{\mathrm{abs}} = 5 \times 10^4\,\mathrm{pW/K}$. Since we do not know properly the nanowire conductance at 10 K, we can make two different hypotheses, one where it is given by the Casimir expression, and one where it is given by the bulk expression.

When taking into account the nanowire parameters, and assuming a Casimir regime for the conductance at 10 K, given by eq. (3.3.7), we can estimate: $K_{10\,\mathrm{K}} \approx 3.5\,\mathrm{pW/K}$. As a consequence, this permits to evaluate the absorption coefficient at 10 K, at the level of $A_{\mathrm{abs}} = 70\,\mathrm{ppm}$. Here again this value is difficult to compare to any known measurement. However, if we estimate the heat conductance at 10 K from the bulk values of the conductivity ($\kappa_{10\,\mathrm{K}} = 30\,\mathrm{W/m/K}$ which gives $K^{\mathrm{bulk}}_{10\,\mathrm{K}} = 1.5\,\mathrm{nW/K}$), we would have obtained a 3% absorption. Both curves are shown in fig. 3.26b.

As a conclusion, we have exposed a method aiming at estimating the heat conductance of the nanowires. The different nanowires investigated present the same relative trend in temperature. However the value obtained for their conductivity can be found above or below the quantum of conductance at all temperatures below 10 K. In the future, we should find a better determination of the nanowire conductance to complete this investigation. The pump-probe methods developed in the group [185, 235] should in principle help getting new insights on the physics involved at those temperatures. It will also be probably necessary to develop a model in which one averages the contributions of each phonon modes since, when the mean free path approaches the dimensions of the nanowire, the contribution of long wavelength phonon modes will stop meaningfully contributing to the overall heat conduction. The group of O. Bourgeois at Institut Néel is specialized in the investigation of heat transport in nano-structures at low temperatures and their input will be beneficial to help clarifying the very peculiar heat transport properties of our nanowires.

3.4 RESPONSE MEASUREMENT AND FORCE SENSITIVITY

All the results we presented above were focused on the detection and exploitation of the thermal motion of the nanowires. Those measurements are in general relatively lengthy and limited by the time required to average the signal. In order to realize force field measurements using the recent techniques developed in the group, one can rely on coherently driven trajectories instead of random thermal noise trajectories. Here we expose the nanowire response to an external perturbation, which can be an electrostatic or optical force, but also a piezo-electric actuation sent to the nanowire piezo support. A pump-probe or a driving scheme [232, 233], similarly to the one we will present in sections 5.3.1 and 5.3.2, is now described.

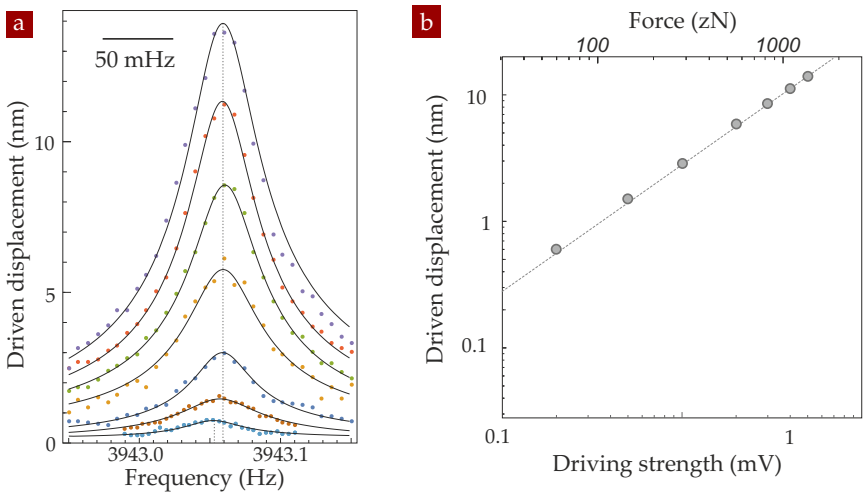

FIGURE 3.27 – Response measurement at dilution temperature for the sample *NW*3. (a) Response measurements obtained for increasing piezo actuation voltage. The resonant driving amplitude is reported in (b). The linearity of the system is well verified, with equivalent driving force spanning from 59 zN to 2.9 aN.

In the case of a piezo actuation, a voltage modulation is applied on the piezo-scanner used to displace the NW in the optical probe field, along its Z direction. The modulation signal is injected after the amplifier and the DC filters (16 Hz) so that it can resonantly drive the nanowire. This generates an equivalent oscillating driving force $\delta F_{\mathrm{drv}} \cos(\Omega t + \phi)$. A vectorial network analyser (VNA) is used to measure the steady state driven trajectory of the nanowire projected along the measurement vector $\mathbf{e}_\beta$, $\delta r_\beta[\Omega]$, while the driving frequency is swept across the eigenmode resonances. At the same time, the signal can also be recorded on a spectrum analyzer, to keep track of the behaviour of the non-driven eigenmode to estimate the mechanical perturbations induced by the actuation tone. The response signal is calibrated with the same "clic-to-volt" procedure exposed above. The amplitude and the dephasing of the response can be fitted with the norm and argument of the expression:

$$\delta r_\beta[\Omega] = \frac{(\mathbf{e}_\beta \cdot \mathbf{e}_1)(\delta \mathbf{F}_{\mathrm{drv}} \cdot \mathbf{e}_1)}{M_{\mathrm{eff}}(\Omega_1^2 - \Omega^2 - i\Omega\Gamma_{\mathrm{m}})} \tag{3.4.1}$$

Figures 3.27a and 3.27b show the amplitude of the response signals obtained on NW2 while sweeping the force drive across the high frequency mode, which is almost aligned with the optical axis. The different curves are obtained for increasing force modulation strength, which generates a larger oscillation amplitude. Each curve is made of 57 frequency points, we employed a resolution bandwidth of 50 mHz and the total time needed for each sweep was around 20 minutes. Several sweeps are averaged, from 2 to 5 depending on the SNR, and the sample temperature is around 28 mK. Figure 3.27b reports the force amplitude recorded as a function of the modulation voltage sent on the piezo scanner. Since it requires 100 V to scan 9 µm in space at low temperatures, the mV modulation depth would represent an equivalent oscillation amplitude of 9 pm of the nanowire fixed extremity, knowing that the actuation mechanisms presents a significant cutoff in frequency, which varies from sample to sample due to the change in the arrangement of the thermal links used to cool down the sample.

Those measurements permits to illustrate the linearity of the actuation mechanism, and the possibility to detect monochromatic forces of a few tens of zeptonewton (59 zN here).

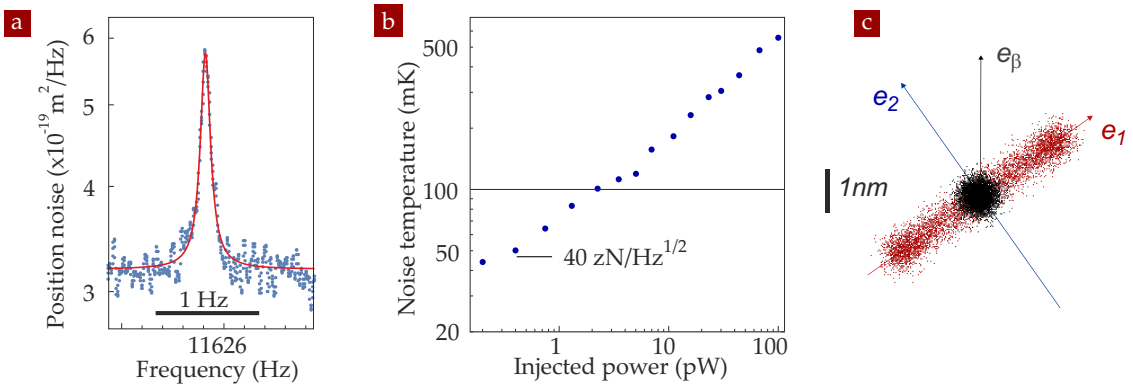

FIGURE 3.28 – Response measurement at dilution temperature for the sample $NW2$. (a) Thermal noise spectrum of $NW2$ measured at 42 mK using 200 fW, providing a 40 zN/$\sqrt{\text{Hz}}$ force sensitivity. (b) Noise temperature of the eigenmode for increasing optical power, while driving the other lateral mode with a 1 aN force strength. (c) Schematic representation of this measurement: the thermal motion of the second mode is measured while actively driving the first.

From such a measurement, we can also analyse the impact of the driving on the oscillator's dynamics: the frequency shifts measured between the 2 lowest drive tones amounts to 6 mHz, and 8 mHz between the extrema. Using the frequency-temperature dependence exposed above, this relative frequency shift of $\delta f_m / f_m = 2 \times 10^{-6}$ can be translated into a maximum 2 mK temperature increase induced by the driving (the measurement realized at the lowest drive amplitude was obtained using a slightly smaller optical intensity, which explains the quasi totality of the 6 mHz upshift). As mentioned above, the power dissipated for an oscillatory motion of 14 nm at 3.94 kHz amounts to 1 zW approximately, which is significantly smaller than the optical power employed (200 fW here).

The two eigenmodes of the nanowire can be equivalently employed for force detection but also for noise thermometry, at the condition that their motion can be efficiently readout. The eigenmodes of the $NW2$, oscillating around 11 kHz were not perfectly aligned with the optical axis, so that it was possible to readout both of them down to low temperatures (as opposed to $NW3$). We used that opportunity to realize a measurement in which we actively drove one mode and recorded the thermal noise of the second mode, see fig. 3.28. Even if those measurements were realized without the suspension apparatus, the circulation noise was sufficiently low at 11 kHz not to fully prevent the system from thermalising, and we could observe a noise temperature of 40 mK on the probe mode, while driving the second mode at an amplitude of a few nm, which is sufficient to obtain a very large SNR in a force measurement. Those 2 measurements thus demonstrate that the 2 modes can be largely decoupled, and that the noise temperature of the second mode is almost not affected by the coherent driving tone of the first.

Finally, we underline that $NW2$, when thermalised at 40 mK, permitted to obtain the largest force sensitivity in our measurements, of $\sim$ 40 zN/$\sqrt{\text{Hz}}$. This value, even if largely above what has been measured with quasi molecular oscillators such as doubly clamped nanotubes [143, 54], is however significantly lower than what has been observed on other scanning force sensors [82, 128, 24, 59, 193, 200, 135], with the interest of preserving a vectorial sensing capacity even at dilution temperatures. Those results were only made possible by the conjunction of optical readout methods operating in the photon counting regime, and of a proper decoupling of the nanowire from parasitic electric and acoustic noises. We also point out that the quality factor of our probes is in principle still limited by the amorphous crust, which could be removed with proper surface treatment based on annealing under hydrogen.

3.5 COMPARISON ACROSS MULTIPLE SAMPLES

Most of the results presented above were achieved using a specific nanowire, *NW*3, for which we were able to record a complete set of measurements. To further validate our results and the measurements techniques we developed, we present here a short comparison with some remarkable results obtained with other samples.

The temperature scan presented in fig. 3.20 has been performed with most of the samples we studied. In all cases, we never measured an appreciable difference between the sample and the noise temperatures. Figure 3.29 shows the result for *NW*2 and *NW*4: for both mechanical polarizations of both samples, the agreement between the temperature above 150 mK is rather good. Despite the fact that the suspension of the optical head was not yet in place at the time, given its slightly higher frequency ($\sim$ 11 kHz) *NW*2 was not affected by the driving due to the circulating mixture and it was possible to reach noise temperature around 40 mK (see section 3.4). This suggests that the environment vibration noise is not spectrally homogeneous. However, in the temperature scan a residual heating of the probe laser limited its noise temperature to $\sim$ 80 mK. *NW*4 on the contrary was measured with minimal optical power and with the optics already suspended above the cryostat cold plate: the analysis revealed that at this frequency ($\sim$ 5.8 kHz) a residual driving effect due to the helium circulation was still present (reduction of the noise temperature when stopping the mixture injection) and that further improvements to the suspension mechanism are needed to work properly at all frequencies of interest.

Figure 3.30 depicts a power scan realize with *NW*4, for intensity ranging from 100 fW to few tens of nW, to be compared with the results in fig. 3.26 for *NW*2 and fig. 3.21 for *NW*3. Ignoring the values for noise temperature lower than 100 mK, due to the driving problem stated before and to a too small SNR, the measurements between 100 mK and 200 mK exhibits also in this case a power dependence $P^{1/5}$, while from 200 mK up to 10 K we find again the $P^{1/2}$ behaviour. Figure 3.30a also show the calibrated amplitude and background of the measured spectra, from which we extract the noise temperature: note that these results are the sum of two consecutive overlapping set of measurements. Indeed, for an injected power of $\approx$ 0.5 nW the photon counter gets saturated and a neutral density must be added in front of it, in order to work at higher power. The consequence

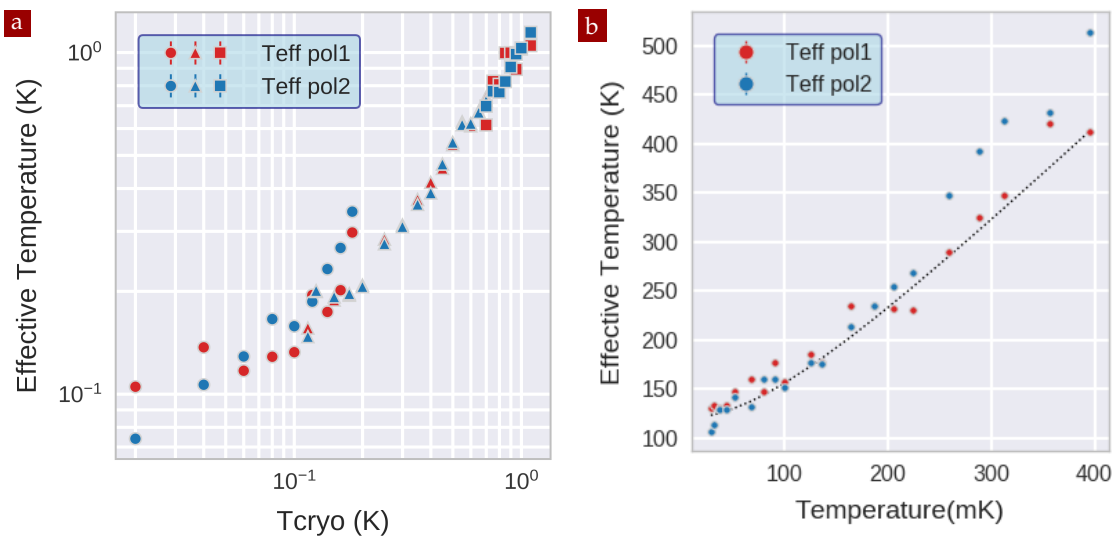

FIGURE 3.29 – Comparison between the sample temperature and the noise temperature for *NW*2 (a) and *NW*4 (b).

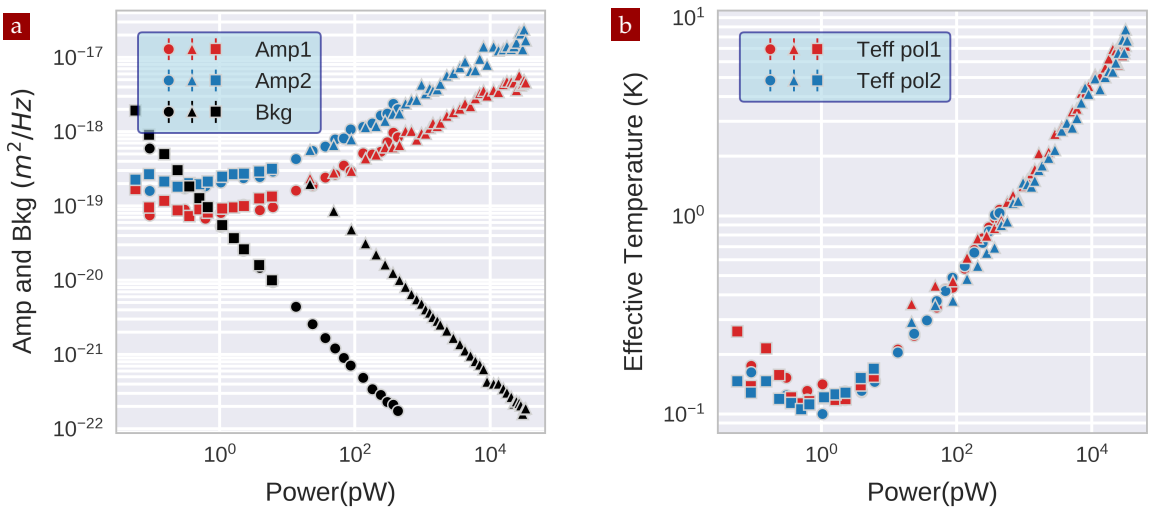

FIGURE 3.30 – Power scan realize with $NW4$: the amplitutes and the background for the two mode (a) as well as their effective temperature (b) are presented. Different symbols refer to subsequent scans realized for different power range.

are two distinct sets of points for the background, whose linear behaviour clearly exhibits the imprecision shot noise limit of our detector (and how it is affected by a decrease in the readout efficiency, caused in this case by the neutral density).

HOW MUCH IS A ZEPTO-NEWTON?

One **zepto-Newton** corresponds to 1×10^{-21} N. In order to grasp the meaning of this quantity, we present here a little cartoon, where some typical physical systems are compare to their equivalent in which the reciprocal distance has been increased until the attractive force is reduced to ~ 1 zN. Three gravitational examples (Sun-Earth, Earth-Man, Man-Man) and an electrostatic one (proton-electron) are provided. The radiation pressure force has also been added for comparison.

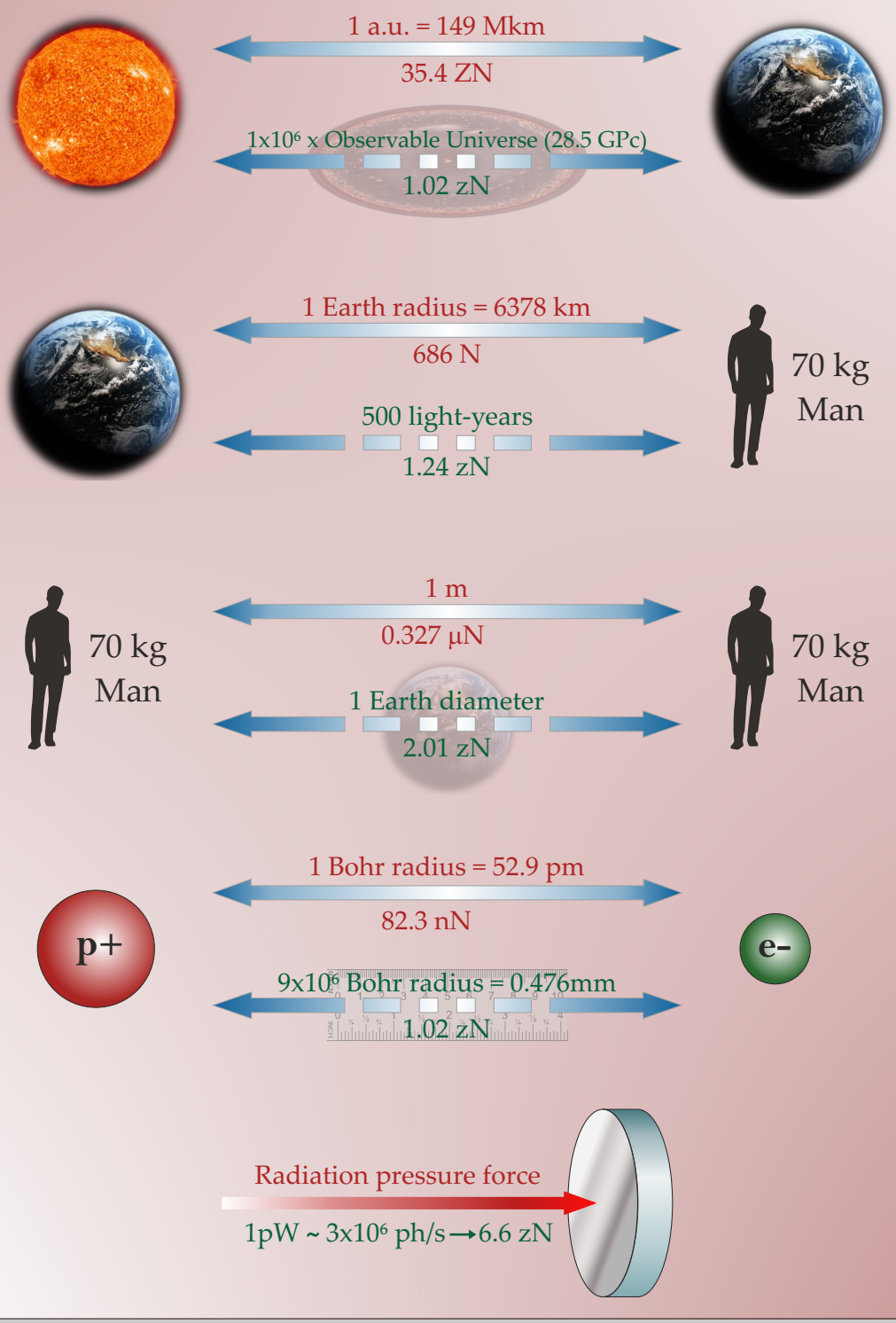

Part III

CAVITY-OPTOMECHANICS IN THE ULTRA-STRONG COUPLING REGIME

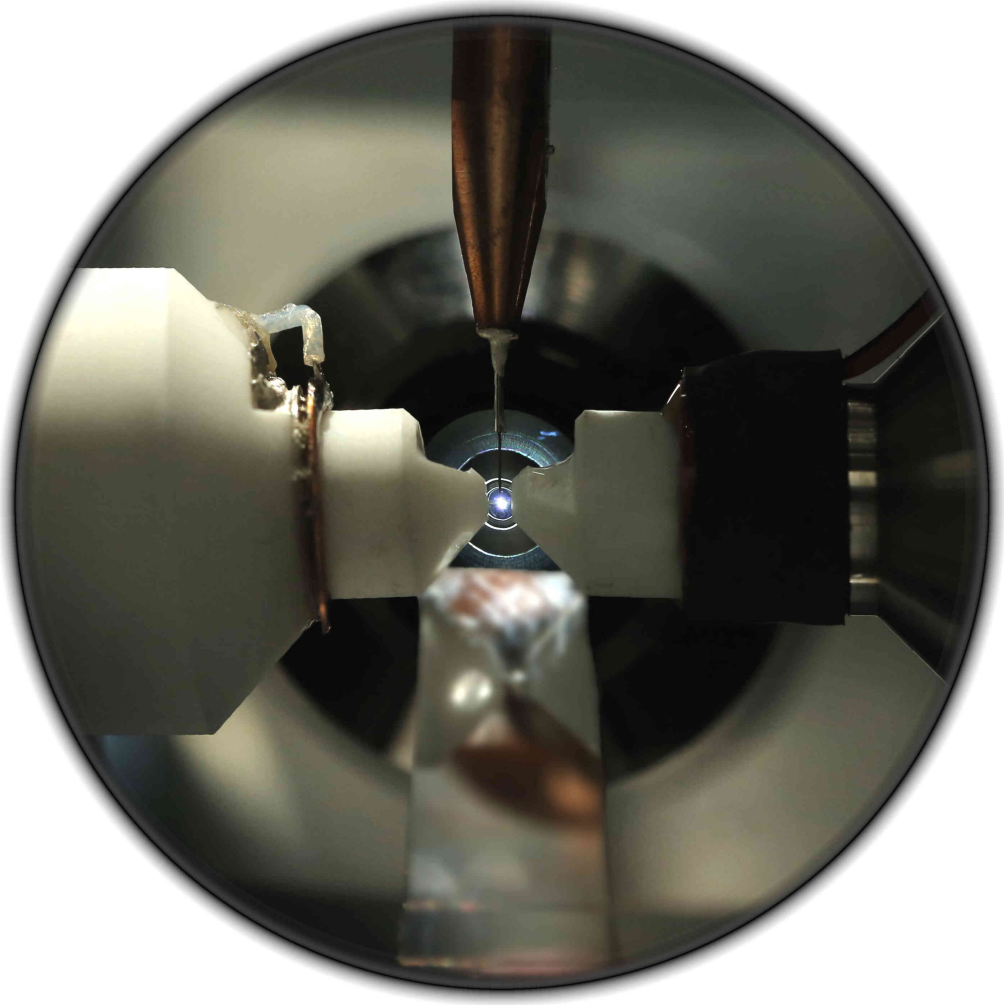

A *nanowire-in-the-middle* is a novel cavity nano-optomechanical system that consists in inserting the vibrating extremity of a suspended nanowire with sub-wavelength sized diameter, in a high finesse fiber micro-cavity. The combination of its small optical mode volume, of the extreme force sensitivity of the nanowires and of the large optomechanical interaction strength that we will demonstrate makes this system very interesting for further explorations in the field of cavity nano-optomechanics. In particular we will show in this part that one can reach the so-called ultrastrong coupling regime, where one single intracavity photon can displace the oscillator by more than its zero point fluctuations. After having described the experimental platform, we will investigate how the nanowire perturbs the intracavity field by mapping the cavity properties as a function of the nanowire position within the standing wave. This permits to quantify and spatially map the optomechanical interaction strength, which acquires a vectorial character. Furthermore we will explore the interaction in the reversed direction by mapping the intracavity optical force field experienced by the nanowire and we will compare our results with dedicated numerical simulations.

4 FIBER-CAVITY OPTOMECHANICS

The following chapter describes the basic theory of a resonator-in-the-middle optomechanical approach, introducing the basic description of an optical cavity, of a membrane-in-the-middle configuration and its comparison to the nanowire-in-the-middle case. The experimental setup as well as the evaluation of the optomechanical coupling strength is explained.

CONTENTS

4.1 Mechanical resonators in the middle of an optical cavity . . . **102**
4.2 Optical cavity basics . . . **104**
4.2.1 The transfer matrix formulation . . . 104
4.2.2 The Fabry-Perot cavity . . . 105
4.2.3 High-finesse fiber optical cavity . . . 107
4.3 MIM: membrane in the middle . . . **110**
4.3.1 Reflection and transmission of the cavity . . . 110
4.3.2 Intra-cavity field . . . 112
4.3.3 Force on the membrane . . . 115
4.4 NIM: nanowire in the middle . . . **116**
4.4.1 Nanowire in a Gaussian beam . . . 116
4.4.2 Transfer matrix of a NIM system . . . 118
4.4.3 Frequency shift of the cavity resonance . . . 118
4.4.4 Optical cavity mode imaging . . . 119
4.4.5 Intracavity field and optical force on the nanowire . . . 120
4.5 Experimental implementation . . . **122**
4.5.1 General overview . . . 122
4.5.2 Functionalized fibers . . . 124
4.5.3 Fiber supports . . . 126
4.5.4 Nanowire support . . . 129
4.5.5 Vacuum chamber . . . 130
4.5.6 Vibration and thermal insolation . . . 130
4.5.7 Optical scheme . . . 131
4.5.8 Experiment control and interface . . . 135
4.6 Optomechanical coupling in a NIM . . . **136**
4.6.1 Bare cavity resonances . . . 136
4.6.2 Optomechanical interaction . . . 140
4.6.3 The ultrastrong coupling regime . . . 145
4.6.4 Coupling to higher-order optical modes . . . 145

4.1 MECHANICAL RESONATORS IN THE MIDDLE OF AN OPTICAL CAVITY

The canonical implementation of cavity optomechanical systems, based on an axial Fabry-Perot with a deformable end mirror, has proven to be extremely effective to describe most of the existing experiments in optomechanics. However this approach is not ideal when one wants to operate with mechanical resonators of small dimensions since it becomes impossible to preserve a decent cavity finesse in this configuration. An alternative to this canonical approach is to separate the mechanical and optical degrees of freedom. As such, several strategies were developed to operate with nanomechanical systems: they can be inserted in the evanescent field of a microcavity [13], or make use of other confined optical modes such as in photonic crystals [39, 178, 116]. The group of J. Harris implemented an interesting approach named *membrane-in-the-middle*, where they inserted a poorly reflective membrane inside a cavity mode, which provided an interesting way to realize optomechanical coupling with weakly interacting oscillators, that compensate for this potential optical drawback with an enhanced mechanical susceptibility. This approach was then followed by several groups, and many nanoresonators were subsequently employed, such as nanowires or CNTs. The "three-mirror system", suggested in some notable works in the 80s [138, 134], has lead to the idea of the *resonator in the middle* configuration, where a high quality factor thin membrane or a nanoscale resonator (NWs, CNTs) are placed in the middle of an high-finesse Fabry-Pérot optical cavity.

In the canonical case, the high finesse requirement implies the need for a resonator larger than the photon's wavelength and thick enough to guarantee a good reflectivity. As a consequence, this sets a lower limit on how small and light the mechanical component can be, and thus limits their mechanical susceptibility. With the new configuration the optical and the mechanical component are now completely independent: on one side this enables to employ resonators with at least one dimension below the optical diffraction limit, such as carbon nanotube and nanowires; on the other side there are no compromises in the choice of the optical cavity. The resulting systems have led to remarkable results both with thin SiN membranes [197, 99, 93] and with nanorods [74, 220]. However, for the moment the rather large mass of SiN membranes and the limited interaction of the nanotubes or nanowires employed, have limited the coupling strength. We will see that the large refractive index of silicon carbide permits to largely enhance the interaction strength.

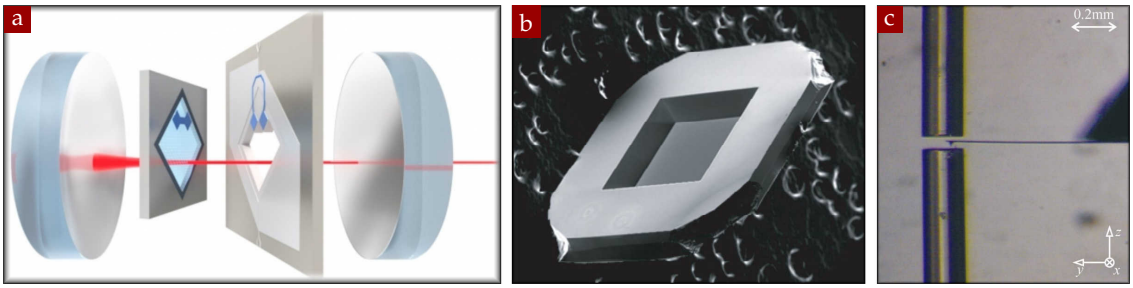

FIGURE 4.1 – (a) artistic representation of the system studied in [93]; (b) SEM image of the SiN membrane employed in a MIM experiment [197]; (c) a dispersive optomechanics experiment made with a nanorod and a fiber micro-cavity [220].

In those systems, the optomechanical interaction usually presents both a dispersive contribution (when the position fluctuations are causing a modulation of the cavity resonance frequency) and a dissipative contribution (when the position fluctuations are causing a modulation of the cavity loss rate), depending on the choice of the nano-resonator employed and the cavity geometry [73, 212, 126, 120, 207, 208]. The purely dispersive case occurs when the mechanical resonator simply shifts the cavity resonance, while all the photons are scattered into the same cavity mode, without absorption or scattering towards an external loss channel or towards other cavity modes. This is in principle the case when using membranes positioned close to a node of the cavity, due to their small absorption and to the fact that they can be aligned to minimise the light scattering out of the cavity mode. Nanowires and carbon nanotubes are instead more prone to also generate a dissipative coupling, due to absorption or scattering outside the mode. The dissipative optomechanical mechanism has been less investigated up to now, since the attention has been more focused on lossless systems, but it is inherent to the use of sub-wavelength sized nanomechanical oscillators, and we will see that it does not necessarily represent a drawback. It has indeed been proven that this kind of coupling could be used, in the bad-cavity limit, to cool the mechanical resonator into its quantum ground-state [70, 84, 211, 172, 53].

In the realization of a *resonator-in-the-middle* system, the optomechanical coupling increases thanks to a reduced mass of the mechanical oscillator but also to a smaller optomechanical interaction volume. The latter in particular can be achieved by employing fiber Fabry-Perot (FFP) micro-cavities [105, 191, 96]. These have been originally developed in the group of J. Reichel and have proven to be a powerful tool in the domain of cavity quantum electrodynamics (CQED) [199, 49, 203]. Thanks to their integrated and compact nature, their high-finesse, their small optical mode volume and good mode matching, besides optomechanics [74, 220, 76] they have found applications in many other systems, such as single-atom trapping [81], coupling to Nitrogen-Vacancy centers [5, 6, 104] and single or multiple ions [190, 189, 34].

4.2 OPTICAL CAVITY BASICS

We will now introduce the basic notions and the common notations that we will use in the following sections to describe on optical cavity. Starting by introducing the transfer matrix formalism, which will be a key ingredient for the description and simulation of the NIM system (section 4.4), we will present the main parameters used to characterize a Fabry-Perot cavity, such as its resonance, linewidth and finesse, and then some specific use-cases when dealing with a Gaussian beam in a high-finesse fiber-cavity.

4.2.1 The transfer matrix formulation

When it comes to describe the evolution of the light field across an optical system, it is common to use a matrix formalism. An example being the *ABCD ray transfer matrix*, which is widely used to describe the propagation of geometrical optical rays through paraxial optical elements [261, 106]. Another example are the *S scatter matrix*, which can be used to describe the reflection and refraction of light at a boundary between two dielectric media (see fig. 4.2a). Being n_1 and n_2 the refractive index of the latter, the output fields E_r and E_t can be expressed as a function of the input fields E_i and E_v as

$$\begin{pmatrix} E_t \\ E_r \end{pmatrix} = S \begin{pmatrix} E_i \\ E_v \end{pmatrix} \quad \text{with} \quad S = \begin{pmatrix} t_{12} & r_{21} \\ r_{12} & t_{21} \end{pmatrix}, \tag{4.2.1}$$

where t_{ij} and r_{ij} are given by the Fresnel formulas[1]

$$t_{ij} = \frac{2n_i}{n_i + n_j}, \qquad r_{ij} = \frac{n_i - n_j}{n_i + n_j}. \tag{4.2.2}$$

This formalism can be very useful in simple cases to calculate the transmitted and reflected fields. However, when dealing with a large number of successive layer (or successive cavities, as in our case), the analysis can become very complex due to the large amount of equations involved. The alternative is to use the *M characteristic transfer matrix* [264, 248, 239, 3], which instead relates the fields on the right side of the interface to the fields on the left side. The advantage is that this matrix can than be cascaded, one for each subsystem, greatly simplifying the computation of the output field. The previous expression can then be rewritten as

$$\begin{pmatrix} E_t \\ E_v \end{pmatrix} = M \begin{pmatrix} E_i \\ E_r \end{pmatrix}, \quad \text{with} \quad M = \frac{1}{t_{21}} \begin{pmatrix} 1 & r_{21} \\ -r_{12} & 1 \end{pmatrix}. \tag{4.2.3}$$

This results holds also for the fields amplitude A ($E = Ae^{-i\omega t}$). It is possible to define the $M_{n,L}$ *propagation matrix*: in the slowly varying envelope approximation (SVEA), the field amplitude at position $z_0 + L$ can be expressed in terms of the amplitude at z_0:

$$\begin{pmatrix} A_1(z_0 + L) \\ A_2(z_0 + L) \end{pmatrix} = M_{n,L} \begin{pmatrix} A_1(z_0) \\ A_2(z_0) \end{pmatrix} \quad \text{with} \quad M_{n,L} = \begin{pmatrix} e^{iknL} & 0 \\ 0 & e^{-iknL} \end{pmatrix} \tag{4.2.4}$$

where k is the wave vector in the vacuum ($k = 2\pi/\lambda$), while n is the refractive index of the medium. Note that in our convention A_1 is propagating in the positive direction ($+z$) while A_2 propagates in the negative one ($-z$).

[1] Here and in the following sections for simplicity we will only consider the case of normal incidence.

As a simple example, we can compute the reflection and transmission coefficients of a layer with refractive index n and width L (see fig. 4.2b). It is straightforward to write for the fields amplitude

$$\begin{pmatrix} A_t \\ A_v \end{pmatrix} = M \begin{pmatrix} A_i \\ A_r \end{pmatrix} = M_{n,1} M_{n,L} M_{1,n} \begin{pmatrix} A_i \\ A_r \end{pmatrix} \tag{4.2.5}$$

where the transfer matrix for the two interfaces are given by $M_{1,n} = \begin{pmatrix} 1 & r_{n1} \\ -r_{1n} & 1 \end{pmatrix}$ and $M_{n,1} = \begin{pmatrix} 1 & r_{1n} \\ -r_{n1} & 1 \end{pmatrix}$, $M_{n,L}$ being the same as before. Using the notation $r_{1n} = -r_{n1} = r$, $\phi = nkL$ and developing the calculation, the reflected and transmitted amplitudes are

$$A_t = C_t A_i + C_r A_v \tag{4.2.6a}$$
$$A_r = C_r A_i + C_t A_v, \tag{4.2.6b}$$

where

$$C_r = \frac{M_{12}}{M_{22}} = \frac{(1-n^2)\sin\phi}{2in\cos\phi + (1+n^2)\sin\phi} \tag{4.2.7a}$$
$$C_t = \frac{1}{M_{22}} = \frac{2in}{2in\cos\phi + (1+n^2)\sin\phi} \tag{4.2.7b}$$

are the coefficient we were looking for. The relative intensity coefficients are given by $C_R = |C_r|^2$ and $C_T = |C_t|^2$ and satisfy the energy conservation $C_R + C_T = 1$.

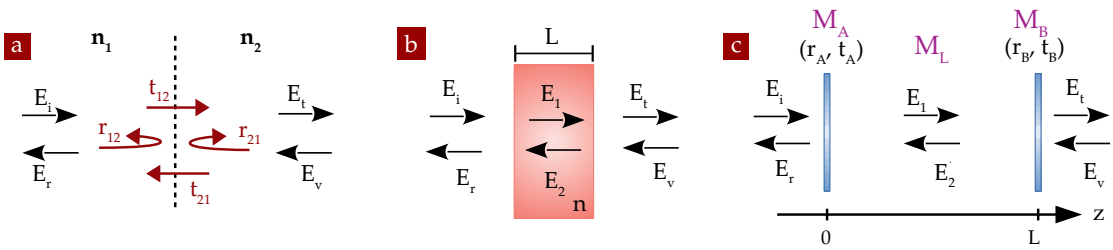

FIGURE 4.2 – Scheme of the electric fields and of the reflection and transmission coefficients at the interface of two dielectric materials (a), for a layer of refractive index n (b) and for a planar Fabry-Perot cavity (c).

4.2.2 The Fabry-Perot cavity

A completely analogous approach can be used to describe a simple Fabry-Perot optical cavity, as the one schematized in fig. 4.2c. Again, E_i and E_v represent the incident fields, E_r and E_t the reflected and transmitted ones and E_1 and E_2 the fields inside the cavity, which we now suppose travel in vacuum. The two interfaces of the single layer case are now replaced by cavity mirros, each one of which is described by its reflection and transmission coefficients, respectively (r_A, t_A) and (r_B, t_B). To compute the output field we can then reuse eq. (4.2.5), where now we have

$$M_A = \frac{1}{t_A}\begin{pmatrix} 1 & -r_A \\ -r_A & 1 \end{pmatrix}, \qquad M_B = \frac{1}{t_B}\begin{pmatrix} 1 & r_B \\ r_B & 1 \end{pmatrix} \qquad \text{and} \qquad M_L = \begin{pmatrix} e^{i\varphi} & 0 \\ 0 & e^{-i\varphi} \end{pmatrix}, \tag{4.2.8}$$

with $\varphi = kL$. Among the multiple possible choices, the expression for M_A and M_B has been chosen in agreement with the energy conservation and the continuity of the field at the boundaries. Proceeding as before it is easy to obtain the element of the transfer matrix M,

$$M = \begin{pmatrix} M_{11} & M_{21} \\ M_{21} & M_{22} \end{pmatrix} = \frac{e^{i\varphi}}{t_A t_B} \begin{pmatrix} 1 - r_A r_B e^{-2i\varphi} & -r_A + r_B e^{-2i\varphi} \\ r_B - r_A e^{-2i\varphi} & -r_A r_B + e^{-2i\varphi} \end{pmatrix} \tag{4.2.9}$$

from which we can then compute the reflection and transmission coefficients as $C_r = E_r/E_i = -M_{21}/M_{22}$ and $C_t = E_t/E_i = 1/M_{22}$, obtaining the usual Airy's formulas.

It is then of practical use to compute the intensity reflection and transmission coefficient and to express them in terms of the intensity reflection coefficient of the mirrors, $R_A = |r_A|^2$ and $R_B = |r_B|^2$:

$$C_R = \frac{R_A + R_B - 2\sqrt{R_A R_B}\cos(2\varphi)}{1 + R_A R_B - 2\sqrt{R_A R_B}\cos(2\varphi)} \tag{4.2.10a}$$

$$C_T = \frac{(1 - R_A)(1 - R_B)}{1 + R_A R_B - 2\sqrt{R_A R_B}\cos(2\varphi)} \tag{4.2.10b}$$

for which it is straightforward to check the energy conservation[2] $C_R + C_T = 1$. Note that the transmission (reflection) has a maximum (minimum) for $R_A = R_B$, which corresponds to the impedance matching condition for the cavity $\eta_{\text{imp}} = 1$.

A typical transmission signal for a Fabry-Perot cavity presents a series of equally spaced resonances (see fig. 4.21). Pumping the cavity with a fixed laser frequency $\omega_{\text{cav}} = 2\pi c/\lambda$, the resonant lengths can be obtain from eq. (4.2.10b) and are given by $L_n = n\frac{\lambda}{2}$, with $n \in \mathbb{N}$. Similarly, for a fixed cavity length L, we find a series of resonant frequencies: $\omega_n = n\frac{\pi c}{L}$. In the frequency domain, the pulsation difference between two successive resonances is known as the free spectral range (FSR) and is given by

$$\omega_{\text{FSR}} = \frac{\pi c}{L}. \tag{4.2.11}$$

Using eq. (4.2.10) we can then compute the FWHM of the peaks, which are given in the length and in the frequency domain respectively by

$$\Delta L = \frac{\lambda}{2\pi} \frac{1 - \sqrt{R_A R_B}}{(R_A R_B)^{1/4}} \tag{4.2.12a}$$

$$\Delta\omega = \frac{c}{L} \frac{1 - \sqrt{R_A R_B}}{(R_A R_B)^{1/4}} \equiv \kappa \tag{4.2.12b}$$

Another important quantity which we will extensively use in the following chapters to characterize the optical cavity is the *Finesse*.[3] This is defined as the ratio between the FSR and the cavity linewidth, that is

$$\mathcal{F} = \frac{\omega_{\text{FSR}}}{\kappa} = \frac{\lambda/2}{\delta L} = \pi \frac{(R_A R_B)^{1/4}}{1 - \sqrt{R_A R_B}}, \tag{4.2.13}$$

and it is linked to the mean number of round trips of a photon in the cavity N by the relation $\mathcal{F} = \pi N$. The lifetime of a photon in the cavity is $\tau^{(1)} = N(2L/c) = 2/\kappa$ instead.

[2]For a simple model which includes losses in the system, see the three-mirror ring-cavity inset (page 157).

[3]This must not be confused with the *coefficient of finesse* $F = \frac{4\sqrt{R_A R_B}}{(1-R_A)(1-R_B)}$ (with $\mathcal{F} = \pi\sqrt{F}/2$), or with the optical cavity quality factor $Q_c = \frac{\omega_{\text{cav}}}{\kappa}$.

In most of the cases of interest, we assume to work with high-reflectivity cavity mirrors, so that $T_A = 1 - R_A$ and $T_B = 1 - R_B$ satisfy the condition $T_A, T_B \ll 1$. Considering a cavity of fixed length L and a laser frequency $\omega = \omega_n + \Delta$, where Δ is the detuning from a cavity resonance (and for a symmetric cavity $R_A = R_B = R$), the transmission intensity eq. (4.2.10b) reads as

$$C_T(\Delta) \approx \frac{1}{1 + \frac{4R}{(1-R)^2}(\frac{\Delta L}{c})^2} = \frac{1}{1 + (\frac{2\Delta}{\kappa})^2}, \tag{4.2.14}$$

which has the usual Lorentzian form. The same thing can be done for the reflection expression. Later we will extensively use this formulation (see section 4.6.1).

The transfer matrix formalism can also be very useful in order to compute the intra-cavity field of the optical cavity, which for example we will need to estimate the force applied on the resonator in a NIM system (see section 4.4). Once we have computed the amplitude of the reflected field A_r, making use of eq. (4.2.9) we can use the same formalism to propagate the field through the left mirror only:

$$\begin{pmatrix} A_1 \\ A_2 \end{pmatrix} = M_A \begin{pmatrix} A_i \\ A_r \end{pmatrix}. \tag{4.2.15}$$

Here A_1 and A_2 are the amplitudes of the intra-cavity field defined at $z = 0$ (that is the position of the left mirror), which we can then use to obtain the field at any point z inside the cavity through

$$E_{\text{cav}}(z,t) = (A_1 e^{ikz} + A_2 e^{-ikz}) e^{-i\omega t}. \tag{4.2.16}$$

4.2.3 High-finesse fiber optical cavity

The high-finesse fiber Fabry-Perot cavity (FFPC) that will constitute a key ingredient of our experiment is an example of a stable two-mirror resonator, trapping a Gaussian beam. Basic definitions of this kind of system that we will frequently use, both in our simulation and to describe and to analyze our experiment, are given below[4].

GAUSSIAN BEAM The Hermite-Gaussian modes form a complete set for the resonant modes trap in a two-mirror cavity. However, for our purposes we will only focus on the fundamental Gaussian mode TM_{00} in the paraxial approximation, whose electric field will be written as

$$\mathbf{E}^{00}_{(\pm)} = \rho(\mathbf{r}_\perp, z) e^{\pm i\varphi(\mathbf{r}_\perp, z)} \mathbf{e}, \tag{4.2.17}$$

where $\mathbf{e}$ indicates the linear polarization vector of the field and $(\pm)$ means that the mode is propagating in the $\pm z$ direction. The amplitude and phase of the field read

$$\rho(\mathbf{r}_\perp, z) = A_0 \frac{w_0}{w(z)} e^{-\frac{\mathbf{r}_\perp^2}{w^2(z)}}, \qquad \varphi(\mathbf{r}_\perp, z) = kz - \Psi(z) + k\frac{\mathbf{r}_\perp^2}{2R(z)} \tag{4.2.18}$$

where the waist $w(z)$ at position z, the Gouy phase $\Psi(z)$ and the radius of curvature of the beam $R(z)$ are given by

$$w(z) = w_0 \sqrt{1 + \left(\frac{z}{z_R}\right)^2}, \qquad \Psi(z) = \arctan\left(\frac{z}{z_R}\right), \qquad R(z) = z\left[1 + \left(\frac{z_R}{z}\right)^2\right]. \tag{4.2.19}$$

[4]More details can be found in [261, 106, 105, 191, 96, 229, 231].

w_0 is the waist of the Gaussian beam, $z_R = \pi w_0^2/\lambda$ is the Rayleigh range and $A_0 = \sqrt{2/\pi w_0^2}$ a normalization factor (ensuring that $\int d\mathbf{r}_\perp |\mathbf{E}^{00}_{(\pm)}|^2 = 1$).

STABLE TWO-MIRROR RESONATORS A cavity of length L, composed of two concave mirrors with radius of curvature $\mathcal{R}_1$ and $\mathcal{R}_2$, as depicted in fig. 4.3a, can be characterized by the parameters $g_i = 1 - L/\mathcal{R}_i$, with $i = \{1, 2\}$. The stability condition of the resonator reads $0 \leq g_1 g_2 \leq 1$ and is summed up by the diagram in fig. 4.3b, where different values of the radius of curvature give rise to different kind of cavity. For our case, that of a symmetric resonator, with $\mathcal{R}_1 = \mathcal{R}_2 = \mathcal{R}$ and thus $g_1 = g_2 = g = 1 - L/\mathcal{R}$, the waist is in the middle of the cavity ($z_1 = z_2 = L/2$) and the Rayleigh range is given by

$$z_R = \frac{L}{2}\sqrt{\frac{1+g}{1-g}}. \tag{4.2.20}$$

From previous equations we can then obtain for the spot size of the waist at the center and on the mirrors of the cavity

$$w_0^2 = \frac{L\lambda}{\pi}\sqrt{\frac{1+g}{4(1-g)}} = \frac{\lambda}{2\pi}\sqrt{L(2\mathcal{R}-L)}, \qquad w_1^2 = w_2^2 = \frac{L\lambda}{\pi}\sqrt{\frac{1}{1-g^2}} = \frac{L\mathcal{R}\lambda}{\pi}\sqrt{\frac{1}{L(2\mathcal{R}-L)}}, \tag{4.2.21}$$

from which we can directly see that these values are determined by the geometric parameter of the cavity. They are presented in fig. 4.3c as a function of the cavity length L, for a fix value of the radius of curvature $\mathcal{R} = 30\,\mu\text{m}$.

It is also important to recall the expression for the mode volume of the cavity [12], for the smaller values of which correspond larger values of the optomechanical coupling:

$$V_\text{m} = \frac{\pi}{4} w_0^2 L = \frac{L\lambda}{8}\sqrt{L(2\mathcal{R}-L)}. \tag{4.2.22}$$

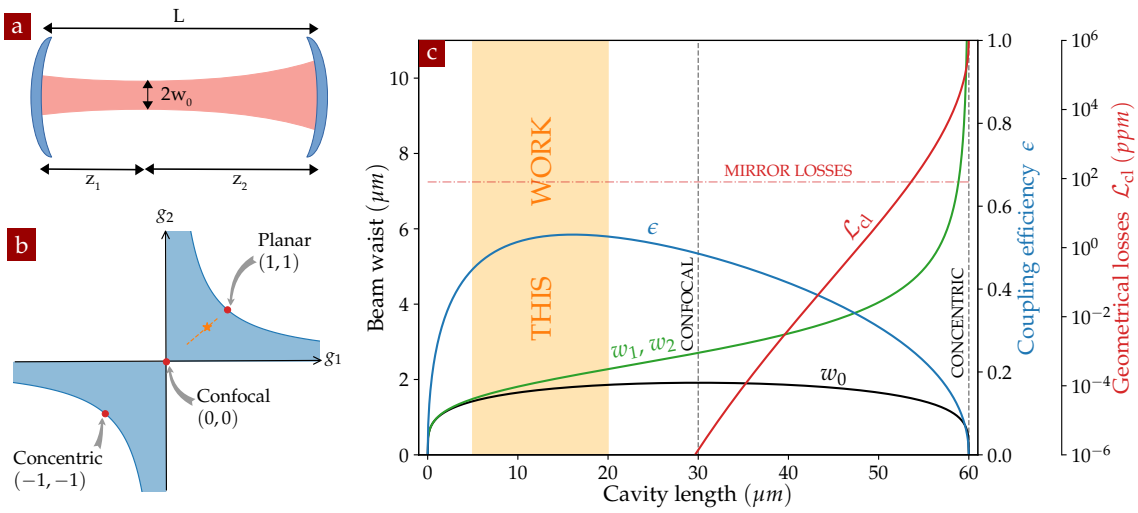

FIGURE 4.3 – Scheme of an optical cavity with concave mirrors (a) and its stability diagram (b); the orange dotted line represents the working region in our experiment. Cavity mode waist (black line) and spot size on the mirrors (green line) as a function of the cavity length (c). The coupling efficiency ϵ (blue line) and the geometrical clipping losses $\mathcal{L}_\text{cl}$ (red line) are also shown for comparison. The zone in yellow represents the typical cavity dimension that we have explored in this work: we can see that we have been working around the maximum of the coupling coefficient, while the losses of the cavity should be dominated by the mirror coating (red dotted line) and not by clipping effect.

We also note that for an optical cavity made with two fibers, the total cavity length is the sum of three contributions, namely

$$L = L_{\text{geo}} + 2\, z_t + 2\, \alpha_{\text{ml}}\, \lambda/2, \tag{4.2.23}$$

where L_{geo} is the geometrical distance between the two fiber, $z_t = \mathcal{R} - \sqrt{\mathcal{R}^2 - (D/2)^2} \simeq D^2/8\mathcal{R}$ is the depth of the mirror on the fiber surface (D being the diameter of the mirror), while the third term takes into account the penetration of the field in the multilayer, with $\alpha_{\text{ml}} \simeq 1.6$ [94, 96]. These last two term are important and need to be taken into account when dealing with µm-size cavity because they represent a lower bound of the attainable length.

FIBER COUPLING AND CLIPPING LOSSES The simulation of a FFPC, as well as the design of this kind of structure, required the analysis of the system efficiency, in particular the coupling between the cavity and the fiber mode as well as the geometrical losses.

The first can be estimated as the power transmission coefficient between two Gaussian modes [101]:

$$\epsilon = \frac{4}{\left(\frac{w_0^f}{w_0} + \frac{w_0}{w_0^f}\right)^2 + \frac{(z_0 - z_0^f)^2}{z_R z_R^f}}. \tag{4.2.24}$$

w_0, z_0 and z_R are the waist dimension, the waist position and Rayleigh range of the cavity mode, w_0^f, z_0^f and z_R^f the ones of the fiber mode[5]. The value of the coupling efficiency as a function of the cavity length, for a cavity with radius of curvature $\mathcal{R} = 30\,\mu\text{m}$ and mirrors' diameter $D = 10\,\mu\text{m}$ is shown in fig. 4.3c.

The same image also pictures the intensity of the clipping losses for a single reflection on a mirror cavity, that we can express as

$$\mathcal{L}_{\text{cl}} = e^{-2\left(\frac{D/2}{w_m}\right)^2} \tag{4.2.26}$$

where w_m is the dimension of the cavity bream on the mirror. Other sources of geometrical losses, due for example to a system misalignment or to an incorrect centering of the fiber core with respect to the mirror center, are not analyzed here and can be found in [101, 229].

PROPAGATION MATRIX FOR A GAUSSIAN BEAM IN A CAVITY Moving from the results of section 4.2.2 for a planar Fabry-Perot cavity, we show here that the same formalism of the characteristic transfer matrix can be applied to the case of a Gaussian beam propagating between two concave mirrors.

Given the amplitude, the radial and the axial position, it is possible to fully determine the field of a TM_{00} mode at position $\mathbf{r}$. We can then rewrite eq. (4.2.17) separating the spatial envelope from the phase propagation on the optical axis, thus

$$\mathbf{E}_{(\pm)}(\mathbf{r}) = \rho(\mathbf{r}_\perp, z) e^{\pm ik \frac{\mathbf{r}_\perp^2}{2R(z)}} F_{(\pm)}(z)\mathbf{e}, \tag{4.2.27}$$

[5]Given the dimension of beam waist w^f at the fiber output and its relative radius of curvature $R^f = \mathcal{R}/(n_f - 1)$ (where n_f is the refractive index of the fiber), these values can be obtain inverting eq. (4.2.19):

$$w_0^{f\,2} = w^{f\,2} \Big/ \left[1 + \left(\frac{\pi w^{f\,2}}{\lambda R^f}\right)^2\right], \qquad z^f = R^f \Big/ \left[1 + \left(\frac{\lambda R^f}{\pi w^{f\,2}}\right)^2\right] \tag{4.2.25}$$

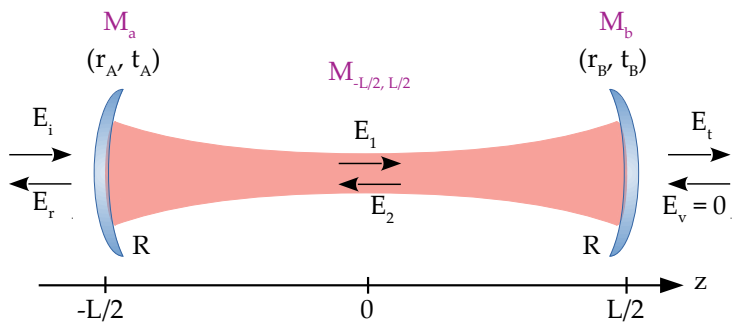

FIGURE 4.4 – Characteristic transfer matrix for a symmetric cavity made of two concave mirrors.

where

$$F_{(\pm)} = A_{\pm} e^{\pm \varphi_0(z)}, \qquad \varphi_0(z) = kz - \Psi(z) \tag{4.2.28}$$

will be defined as the *reduced* field. It will thus be possible to express the propagation of the Gaussian beam, between two point z_1 and z_2, in term of transfer matrix as

$$\begin{pmatrix} F_{(+)}(z_2) \\ F_{(-)}(z_2) \end{pmatrix} = M_{z_1,z_2} \begin{pmatrix} F_{(+)}(z_1) \\ F_{(-)}(z_1) \end{pmatrix}, \qquad \text{with} \qquad M_{z_1,z_2} = \begin{pmatrix} e^{i[\varphi_0(z_2)-\varphi_0(z_1)]} & 0 \\ 0 & e^{-i[\varphi_0(z_2)-\varphi_0(z_1)]} \end{pmatrix}. \tag{4.2.29}$$

The propagation of a Gaussian beam through a cavity, as the one schematized in fig. 4.4, will then be described through the characteristic transfer matrix formalism as

$$\begin{pmatrix} F_t \\ F_v \end{pmatrix} = M \begin{pmatrix} F_i \\ F_r \end{pmatrix} \qquad \text{where} \qquad M = M_B M_{-L/2,L/2} M_A. \tag{4.2.30}$$

M_A and M_B are defined as in eq. (4.2.8), while for $M_{-L/2,L/2}$ we use the definition above. Also in this case, the intensity reflection and transmission coefficients will be obtained from the matrix elements as

$$C_R = \left| \frac{-M_{21}}{M_{22}} \right|^2, \qquad C_T = \left| \frac{1}{M_{22}} \right|^2. \tag{4.2.31}$$

4.3 MIM: MEMBRANE IN THE MIDDLE

In order to properly understand the behaviour of a "resonator-in-the-middle" system, we will start by discussing the main characteristics of a membrane-in-the-middle setup, allowing us to introduce and familiarize with some of the basic concepts that we will encounter studying a NIM.

4.3.1 Reflection and transmission of the cavity

Consider the system portrayed in fig. 4.5: a thin membrane of width L_m and refractive index n is inserted in the middle of a planar Fabry-Perot cavity. The center of the cavity is at $z = 0$, the membrane positioned at $z = z_0$ and the two mirrors respectively at $z_A = -L/2$ and $z_B = L/2$, where L is the total length of the cavity, while L_A and L_B indicate the length of the two sub-cavities at the left and right of the membrane respectively. In this configuration, when the cavity length changes, both mirrors are

displaced in order to keep the center at zero (to see how a different coordinates system can affect the simulation or the experimental results, see the inset on page 113).

We start by considering the limit case of a perfectly reflective membrane, which means that the system is separated in two independent sub-cavities of length $L_A = L/2 - L_m/2 + z_0$ and $L_B = L/2 - L_m/2 - z_0$. Each one of them can then satisfy the resonant condition $\omega_{n_i} = n_i \frac{\pi c}{L_i}$, with $i = [A, B\,]$ and $n_i \in \mathbb{Z}$, which leads to

$$L_A^{\text{res}} = n_A \lambda + L_m - 2z_0 \qquad \text{(left sub-cavity)} \tag{4.3.1a}$$
$$L_B^{\text{res}} = n_B \lambda + L_m + 2z_0 \qquad \text{(right sub-cavity).} \tag{4.3.1b}$$

This values are represented by the diagonal dashed lines in fig. 4.6 (purple for the left sub-cavity, green for the right one) and show that only when the resonance condition is matched for both sub-systems (crossing points) it is possible to have a transmission signal out of the cavity.

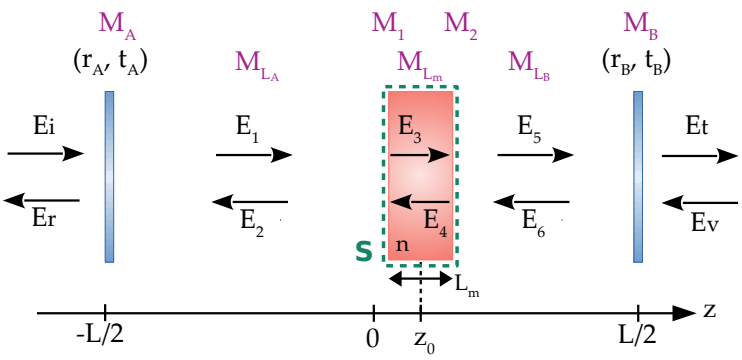

FIGURE 4.5 – Scheme of a membrane in the middle of a Fabry-Perot planar cavity.

We can now apply the characteristic transfer matrix formalism (section 4.2.2) to the case of the membrane in the middle. In this case we will have to consider not only the propagation matrices of the cavity mirrors (M_A, M_B) and the propagation through the two sub-cavities (M_{L_A}, M_{L_B}), but also the propagation matrices of the two interfaces of the membrane (M_1, M_2) as well as the field propagation through the membrane itself (M_{L_m}). Proceeding as before, we have for the input and the output fields

$$\begin{pmatrix} A_t \\ A_v \end{pmatrix} = M \begin{pmatrix} A_i \\ A_r \end{pmatrix} \qquad \text{with} \qquad M = M_B M_{L_B} M_2 M_{L_m} M_1 M_{L_A} M_A \tag{4.3.2}$$

where

$$M_A = \frac{1}{t_A}\begin{pmatrix} 1 & -r_A \\ -r_A & 1 \end{pmatrix}, \qquad M_B = \frac{1}{t_B}\begin{pmatrix} 1 & r_B \\ r_B & 1 \end{pmatrix},$$

$$M_1 = \frac{1}{\tilde{t}_m}\begin{pmatrix} 1 & -r_m \\ -r_m & 1 \end{pmatrix}, \qquad M_2 = \frac{1}{t_m}\begin{pmatrix} 1 & r_m \\ r_m & 1 \end{pmatrix},$$

$$M_{L_A} = \begin{pmatrix} e^{ikL_A} & 0 \\ 0 & e^{-ikL_A} \end{pmatrix}, \quad M_{L_B} = \begin{pmatrix} e^{ikL_B} & 0 \\ 0 & e^{-ikL_B} \end{pmatrix}, \quad M_{L_m} = \begin{pmatrix} e^{iknL_m} & 0 \\ 0 & e^{-iknL_m} \end{pmatrix},$$

with $r_m = (1-n)/(1+n)$, $t_m = 2/(1+n)$ and $\tilde{t}_m = 2n/(1+n)$.

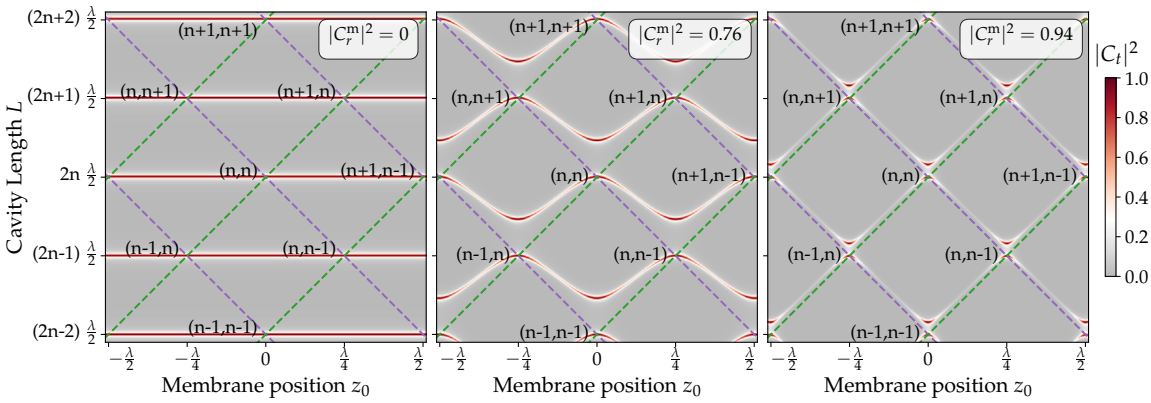

FIGURE 4.6 – Theoretical intensity transmission coefficient for a MIM system as a function of the cavity length L and the membrane position z_0, obtained for a 20 nm-thick membrane, three different membrane reflection coefficients ($|C_r^m|^2 = 0,\ 0.76,\ 0.94$), cavity mirrors with $R_A = R_B = 0.9$ and $\lambda = 780$ nm.

Supposing the cavity being pumped only from the left side ($E_v = 0$), it is then easy to obtain the reflection and transmission coefficients as we have previously shown,

$$C_r = \frac{-M_{21}}{M_{22}}, \qquad C_t = \frac{1}{M_{22}}, \tag{4.3.3}$$

and from them the intensity reflection and transmission coefficients. The results of the calculation of the latter, for a 20 nm-thick membrane and three different values of the membrane reflection coefficients ($|C_r^m|^2 = 0,\ 0.76,\ 0.94$), as a function of the membrane position and the cavity length, are pictured in fig. 4.6. In the case of a perfectly transparent membrane ($|C_r^m|^2 = 0$), the system is equivalent to that of a simple Fabry-Perot (cfr. section 4.2.2). For increasing values of $|C_r^m|^2$, the resonance conditions of the two sub-cavities are overlapped for a smaller range of membrane positions and cavity lengths: the greater this value, the more the system tilts towards the case of a perfectly reflecting membrane (dashed lines). For $|C_r^m|^2 \to 1$, the cavities' linewidths tend to zero and the system results to be resonant only at the crossing points.

4.3.2 Intra-cavity field

As in the case of the Fabry-Perot cavity (cfr. eq. (4.2.15)), we can use the transfer matrix to estimate the intra-cavity field, both in the two sub-cavity as well as inside the membrane. Once the amplitude of the reflected field A_r is obtained, we can compute the amplitude of the inner fields as

$$\begin{pmatrix} A_1 \\ A_2 \end{pmatrix} = M_A \begin{pmatrix} A_i \\ A_r \end{pmatrix} \tag{4.3.4a}$$

$$\begin{pmatrix} A_3 \\ A_4 \end{pmatrix} = M_1 M_{L_A} M_A \begin{pmatrix} A_i \\ A_r \end{pmatrix} \tag{4.3.4b}$$

$$\begin{pmatrix} A_5 \\ A_6 \end{pmatrix} = M_2 M_{L_m} M_1 M_{L_A} M_A \begin{pmatrix} A_i \\ A_r \end{pmatrix}. \tag{4.3.4c}$$

Note that this expressions are valid by defining the fields' amplitudes on the left side of the sub-cavities.

COORDINATES SYSTEM AND ASYMMETRIES

When analyzing a MIM system different signatures and asymmetries can arise depending on the working parameters. One example are the different coordinates systems of the simulations presented here and of the experimental results presented in section 4.6, as depicted in the scheme at the bottom. The first is defined relatively to the middle of the cavity, chosen as $z = 0$, with both mirrors moving with respect to it when the cavity length change. In the second, given an initial cavity length L_0, only one mirror is displaced (ΔL), while the membrane is positioned with respect to a rest position $\tilde{z}_0$. The two sub-cavities lengths will then be defined as

$$L_A = -\Delta L + \tilde{z}_0 + \Delta\tilde{z} - L_m/2$$
$$L_B = L_0 - \tilde{z}_0 - \Delta\tilde{z} - L_m/2$$

while the resonant conditions are now

$$\Delta L^{res} = \tilde{z}_0 + \Delta\tilde{z} - L_m/2 - n_A\ \lambda/2$$
$$\tilde{Z}^{res} = L_0 - \tilde{z}_0 - L_m/2 - n_B\ \lambda/2.$$

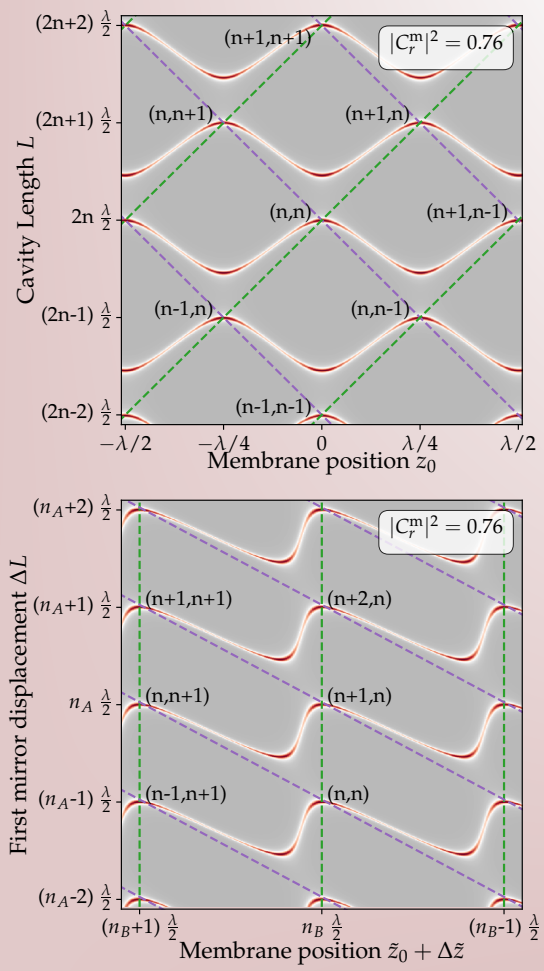

Comparison of the frequency shift of the transmission signal between the simulation and the experimental coordinates system.

The comparison of the two coordinates system is shown in the plot of the right, where the second clearly becomes (artificially) asymmetric. However if the frequency shift is small compared to the FSR, this effect is small and we will be allowed to neglect it in our analysis. We showed in the text that pumping the cavity from one side introduces other (in this case physical) asymmetries, for example when computing the intracavity fields. A difference of reflectivity between the cavity mirrors can also lead to an asymmetric behaviour. We will not describe these aspects in detail here, but they must all be taken into account when simulating and analysing the experimental results.

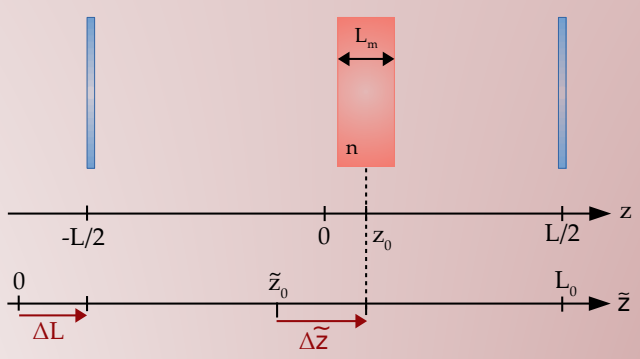

Comparison scheme of the simulation and experimental coordinates system.

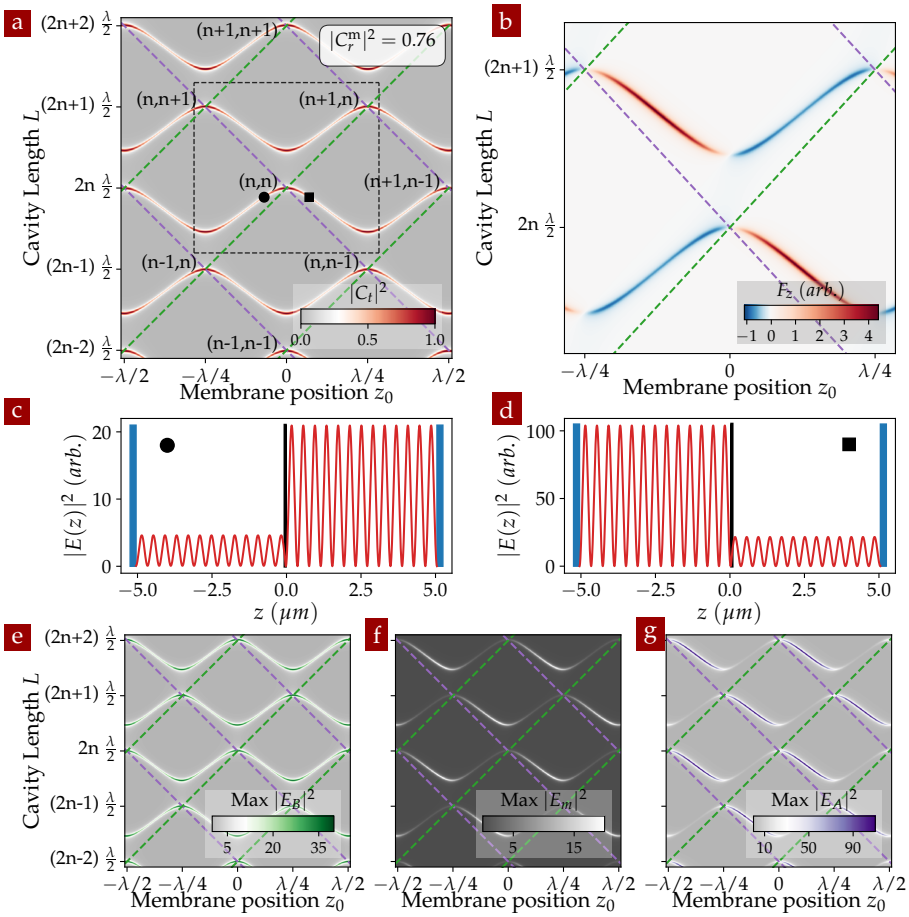

FIGURE 4.7 – Given a map of intensity transmission coefficient of a MIM system (a), the intracavity field on the left (●) and on the right (■) of a crossing point are shown in (c) and (d). The map of the maximum of the intracavity field on the right, membrane and left sub-cavity is presented respectively in (e), (f) and (g). A zoom of the map of the force applied on the membrane around the crossing point is given in (b).

Then, the electric field in the three sub-system is given by

$$E_A(z) = A_1\, e^{ik(z+\frac{L}{2})} + A_2\, e^{-ik(z+\frac{L}{2})} \tag{4.3.5a}$$

$$E_m(z) = A_3\, e^{ik(z-(z_0-\frac{L_m}{2}))} + A_4\, e^{-ik(z-(z_0-\frac{L_m}{2}))} \tag{4.3.5b}$$

$$E_A(z) = A_5\, e^{ik(z-(z_0+\frac{L_m}{2}))} + A_6\, e^{-ik(z-(z_0+\frac{L_m}{2}))}. \tag{4.3.5c}$$

This calculation allows for example to understand qualitatively the split in energy around a crossing point observed in fig. 4.7c and fig. 4.6. For the lower energy branch the system presents a node of the electric field inside the membrane, while for the higher ones it presents an antinode. For decreasing values of $|C_r^m|^2$, the former becomes an even mode of the unperturbed cavity, preserving its energy given the almost negligible field inside the membrane; the latter progressively becomes an odd mode of the unperturbed cavity, showing a more important field inside the membrane (given the lower reflectivity) and thus an higher energy.

It is also interesting to examine the electric field for two different positions of the membrane, symmetric with respect to a node, as shown in fig. 4.7c and d. When the membrane is on the left (right) of the crossing point, the system approaches the ascending (descending) branch, which means it satisfies better the resonant condition of the right

(left) sub-cavity. This is in agreement with an electric field mainly localized in the right (left) sub-cavity. However, the intensity of the light transmitted through the system is equal for both position, because it is proportional to the electric field in the right sub-cavity, which stays the same. On the contrary, the field on the left sub-cavity varies more than an order of magnitude, due to the asymmetry of the optical pumping. This can also be seen from figs. 4.7e to 4.7g: they represent the maximum of the intensity of the electric field, respectively inside the right sub-cavity, inside the membrane and inside the left sub-cavity. The first reproduces the behaviour of the intensity transmission coefficient, as stated. The third exhibits a large variation of the electric field when the system approaches the ascending or descending branch. Similarly does the one inside the membrane, although the overall intensity will now also depend on the physical properties of the membrane (refractive index, width).

4.3.3 Force on the membrane

Finally, we briefly introduce a method to estimate the optical force applied on the membrane, once all the intra-cavity fields are known. We start by expressing the force applied on an object immersed in an electromagnetic field, contained in a volume $\boldsymbol{\mathcal{V}}$ and enclosed by a surface $\boldsymbol{\mathcal{S}}$ [249], as

$$F_\alpha = \oint_{\boldsymbol{\mathcal{S}}} \sum_\beta T_{\alpha,\beta} n_\beta dS \tag{4.3.6}$$

with $\alpha \in \{x, y, z\}$ and where we considered that the electromagnetic energy contained in $\boldsymbol{\mathcal{V}}$ does not change with time. In the right term of the equation, $\mathcal{S}$ is the integration surface, $\mathbf{n}$ is the outward normal vector to $\mathcal{S}$ and $T_{\alpha,\beta}$ is the Maxwell stress tensor defined by

$$T_{\alpha,\beta} = \epsilon_0 \left[E_\alpha E_\beta + c^2 B_\alpha B_\beta - \frac{1}{2}(\mathbf{E}\cdot\mathbf{E} + c^2 \mathbf{B}\cdot\mathbf{B})\delta_{\alpha,\beta} \right]. \tag{4.3.7}$$

The case of our interest is illustrated in fig. 4.5, where the membrane is enclosed by the surface $\boldsymbol{\mathcal{S}}$. Taking the time-average of eq. (4.3.6) and exploiting the symmetry of the problem which leads to an optical force along the z-axis, we obtain at a simple expression for the force applied by the electromagnetic field on the membrane:

$$\mathbf{F} = \epsilon_0 S(|A_1|^2 + |A_2|^2 - |A_5|^2 - |A_6|^2)\mathbf{e}_z. \tag{4.3.8}$$

Here S is the surface of the membrane. Making use of the characteristic transfer matrix to estimate the amplitude of the fields, we can then calculate the value of the force applied on the membrane for different positions inside the cavity, as shown in fig. 4.7b. As we can see, its shape is similar to that of the transmission, given the fact that both are non-zero when the intra-cavity field is non-zero. The calculated force is negative on an ascending branch, positive on a descending one. This is in agreement with what we observed in the previous section: the direction of the force is determined by which sub-cavity has the more intense field. The asymmetry of the absolute value of the force is also originated by the difference on the maximum possible value of the amplitude of the sub-cavities fields (see figs. 4.7e and 4.7g), which is in turn caused by the cavity being pumped from the left side. Note anyway that this difference tends to become very small when the reflection coefficient of the membrane is small, which is a case very close to the one of the NIM system that we will study in the following sections.

4.4 NIM: NANOWIRE IN THE MIDDLE

Moving from the simple model of membrane in the middle of a planar Fabry-Perot cavity, we will now introduce a simple toy-model that can describe qualitatively the experimental evidence that we will present in section 4.6 and chapter 5. The NW will be modelled as a parallelepiped with square section, inserted in the fundamental optical mode of a two-mirror cavity. We will then use the characteristic transfer matrix formalism to compute the reflected and transmitted fields. A scheme of the system is depicted in fig. 4.8. A more quantitative model, base on the Mie resonances of an infinite, sub-wavelength sized cylinder, will be briefly discussed in section 5.3.3, together with some preliminary results.

4.4.1 Nanowire in a Gaussian beam

We start by considering the cavity being resonant with a single optical mode, the fundamental TM_{00} mode. This way, only the projection of the reflected and transmitted field on this mode will contribute to the intracavity field, while the orthogonal part will be interpreted as losses.

The NW is modeled with a square cross section of dimensions L_x, L_z, it is semi-infinite in the y direction and its extremity will be identified by the coordinates $\mathbf{r}_0 = (x_0, y_0, z_0)$. In order to obtain the transfer matrix of the NW immersed in the Gaussian mode, the idea is to model the interaction as a *shadow effect*, including a position dependence for the reflection and transmission coefficients of the NW layer ($z \in [Z - L_z/2, Z + L_z/2]$), see fig. 4.8.

In this layer, the reflection and transmission coefficients r_{NW} and t_{NW} depend on $\mathbf{r}_\perp$ as

$$r_{\mathrm{NM}} = \begin{cases} C_r & \text{if} \mathbf{r}_\perp \in \mathrm{NW} \\ 0 & \text{if} \mathbf{r}_\perp \notin \mathrm{NW} \end{cases} \tag{4.4.1a}$$

$$t_{\mathrm{NM}} = \begin{cases} C_t & \text{if} \mathbf{r}_\perp \in \mathrm{NW} \\ e^{ikL_z} & \text{if} \mathbf{r}_\perp \notin \mathrm{NW} \end{cases}. \tag{4.4.1b}$$

Here, C_r and C_t are the reflection and transmission coefficients of a layer of width L_z and refractive index n, given by eq. (4.2.7). Our expression assumes a plane wave propagation in the effective layer, which is valid for $L_z \ll z_R$ and $z_0 \ll z_R$, allowing to neglect the Gaussian beam divergence.

Noting $E_i = A_i E^{00}_{(+)}(\mathbf{r}_\perp, z)$ the incident field in the TM_{00} mode and considering $z_0 \ll z_R$, the reflected and transmitted field by the NW can be expressed as

$$E_r(\mathbf{r}_\perp, z) = r_{\mathrm{NW}} A_i E^{00}_{(-)}(\mathbf{r}_\perp, z) \tag{4.4.2a}$$

$$E_t(\mathbf{r}_\perp, z) = t_{\mathrm{NW}} A_i E^{00}_{(+)}(\mathbf{r}_\perp, z). \tag{4.4.2b}$$

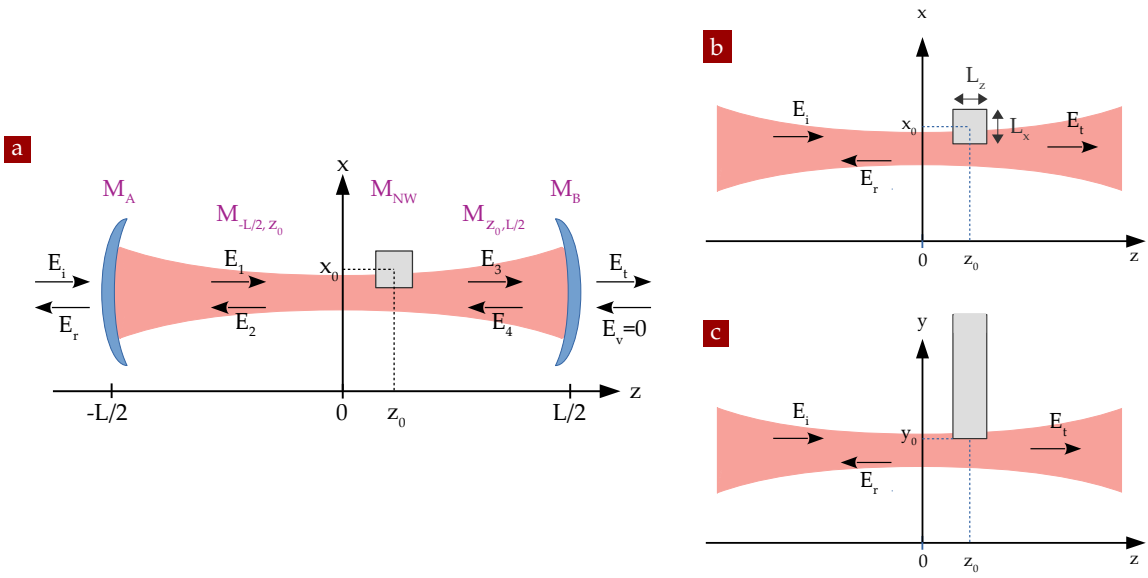

FIGURE 4.8 – Scheme of the simple NIM system model: (a) transfer matrix formalism; (b) and (c) scheme of the coordinates system of a NM inside a Gaussian beam.

The NW effective reflection and transmission coefficients of the fundamental Gaussian mode, towards the same mode, can then be obtained from the previous field through a projection operation:

$$r_{00}^{00}(\mathbf{r}_0) = \langle E_{(-)}^{00} | E_r \rangle \, / A_i = \iint d\mathbf{r}_\perp \, r_{\mathrm{NM}}(\mathbf{r}_\perp) \, \rho^2(\mathbf{r}_\perp, z_0 - L_z/2) \tag{4.4.3a}$$

$$t_{00}^{00}(\mathbf{r}_0) = \langle E_{(+)}^{00} | E_t \rangle \, / A_i = \iint d\mathbf{r}_\perp \, t_{\mathrm{NM}}(\mathbf{r}_\perp) \, \rho^2(\mathbf{r}_\perp, z_0 + L_z/2), \tag{4.4.3b}$$

where ρ is the field amplitude as defined in eq. (4.2.18).

Making use of the error function[6] and solving the integral we arrive at the final expression

$$\begin{aligned} t_{00}^{00}(\mathbf{r}_0) = e^{ikL_z} + \frac{1}{4}\left[C_t - e^{ikL_z}\right]\left[1 - \mathrm{erf}\left(\frac{\sqrt{2}}{w(z_0)}Y\right)\right] \\ \times \left[\mathrm{erf}\left(\frac{\sqrt{2}}{w(z_0)}(X + L_x/2)\right) - \mathrm{erf}\left(\frac{\sqrt{2}}{w(z_0)}(X - L_x/2)\right)\right] \end{aligned} \tag{4.4.4a}$$

$$\begin{aligned} r_{00}^{00}(\mathbf{r}_0) = \frac{C_r}{4}\left[1 - \mathrm{erf}\left(\frac{\sqrt{2}}{w(z_0)}Y\right)\right] \\ \times \left[\mathrm{erf}\left(\frac{\sqrt{2}}{w(z_0)}(X + L_x/2)\right) - \mathrm{erf}\left(\frac{\sqrt{2}}{w(z_0)}(X - L_x/2)\right)\right]. \end{aligned} \tag{4.4.4b}$$

For the waist at position z_0 we use the equation $w(z_0) = w_0\sqrt{1 + (z_0/z_R)^2}$ and we made the additional approximation $w(z_0 + L_z/2) \approx w(z_0 - L_z/2) \approx w(z_0)$.

[6]The error function is defined as $\mathrm{erf}(x) = \frac{2}{\sqrt{\pi}} \int_0^x e^{-t^2} dt$.

4.4.2 Transfer matrix of a NIM system

Having clarified how to obtain the reflection and transmission coefficients of a NW interacting with a Gaussian beam, we can add up the result of sections 4.2.1, 4.2.3 and 4.3.1 to obtain the transfer matrix describing the NIM system depicted in fig. 4.8a. Proceeding as before, for the reduced Gaussian fields we have

$$\begin{pmatrix} F_t \\ F_v \end{pmatrix} = M \begin{pmatrix} F_i \\ F_r \end{pmatrix} \qquad \text{with} \qquad M = M_B M_{-L/2,z_0} M_{\mathrm{NW}} M_{z_0,L/2} M_A, \tag{4.4.5}$$

where the transfer matrices of the system will now be defined as

$$M_A = \frac{1}{t_A}\begin{pmatrix} 1 & -r_A \\ -r_A & 1 \end{pmatrix} \qquad M_B = \frac{1}{t_B}\begin{pmatrix} 1 & r_B \\ r_B & 1 \end{pmatrix} \tag{4.4.6a}$$

$$M_{-L/2,z_0} = \begin{pmatrix} e^{i[\varphi_0(z_0)-\varphi_0(-L/2)]} & 0 \\ 0 & e^{-i[\varphi_0(z_0)-\varphi_0(-L/2)]} \end{pmatrix} \tag{4.4.6b}$$

$$M_{z_0,L/2} = \begin{pmatrix} e^{i[\varphi_0(L/2)-\varphi_0(z_0)]} & 0 \\ 0 & e^{-i[\varphi_0(L/2)-\varphi_0(z_0)]} \end{pmatrix} \tag{4.4.6c}$$

$$M_{\mathrm{NM}} = \frac{1}{t_{00}^{00}}\begin{pmatrix} t_{00}^{00\,2} - r_{00}^{00\,2} & r_{00}^{00} \\ -r_{00}^{00} & 1 \end{pmatrix}, \tag{4.4.6d}$$

with $\varphi_0(z) = kz - \Psi(z)$ and $\Psi(z)$ the Gouy phase.

As in the other cases, the intensity coefficients will be derived from

$$C_R = \left|\frac{-M_{21}}{M_{22}}\right|^2 \qquad C_T = \left|\frac{1}{M_{22}}\right|^2 \qquad C_S = 1 - C_R - C_T, \tag{4.4.7}$$

where in this case we also added the intensity coefficient for the scatter field (derived using the energy conservation principle), as a result of the light scattered out of the cavity (or in this case out of the TM_{00} mode).

4.4.3 Frequency shift of the cavity resonance

Making use of the model presented in the previous sections, we are now able to numerically compute the intensity transmission, reflection and scattered coefficient for any cavity length and any nanowire position. Figure 4.9 shows these three quantities for a scan of the nanowire ($L_x = L_z = 30\,\mathrm{nm}$, $n = 2.7$) across the cavity mode, both on transverse plane ((a), X scan) and along the optical axis ((b), Z scan).

Concerning the Z scan (realized at $X = Y = 0$), we observe, similarly to the MIM system, a periodic oscillation of the resonant cavity length in agreement with the standing wave profile of the intra-cavity field. When the nanowire is at a node of the field, the interaction with the optical field is small and there is no shift of the cavity resonance. On the contrary, when the nanowire is at an anti-node the interaction with the optical field is strong and the shift of the cavity resonance is maximum. The main difference with the membrane system is that the transmission intensity drops rapidly when the nanowire is at an anti-node of the field. This happen because in these position a large amount of intra-cavity photons are scattered out of the cavity mode by the nanowire, as shown in the scattered map (right). This also leads to a finesse degradation.

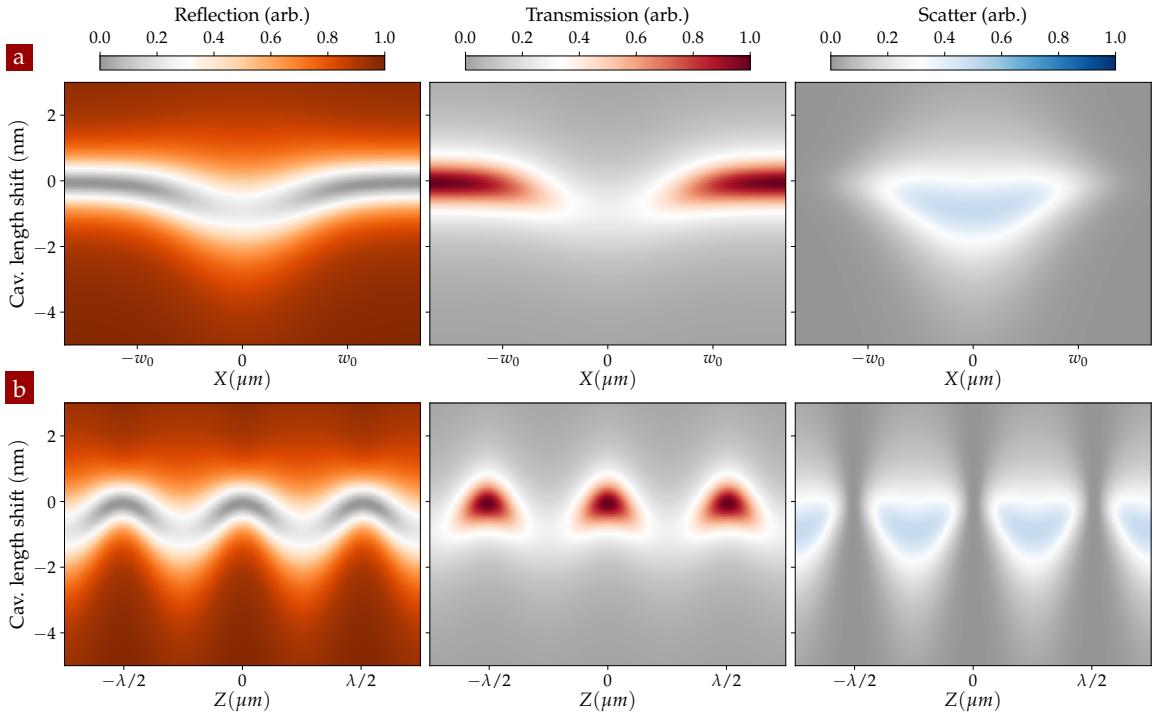

FIGURE 4.9 – Simulation of the optical frequency shift in a NIM system when the nanowire is scanned across an even mode of the cavity. Reflection, transmission and scatter signal for a scan on the transverse (X) plane (a) or along the optical (Z) axis (b). The simulations have been performed for a NW partially entered in the optical mode, with dimensions $L_x = L_z = 30\,\text{nm}$, in a cavity of average length $L = 12.13\,\mu\text{m}$, mirrors with radius of curvature $\mathcal{R} = 28\,\mu\text{m}$ and reflectivity $R_A = R_B = 0.99$, and using a wavelength $\lambda = 800\,\text{nm}$.

Concerning the X scan (realized at $Y = 0$ and $Z = \lambda/4$, in a anti-node of the field), we observe a Gaussian-shape shift of the resonant cavity length, in agreement with the spatial profile of the intra-cavity mode, since we are working with the fundamental mode TM_{00}. As expected, the maximum of the shift of the cavity resonance happens when the NM is placed at the center of the optical mode, which also corresponds to the position with the minimum transmission and the maximum scattered signal.

4.4.4 Optical cavity mode imaging

An alternative experimental situation we are interested to simulate is when we keep the system at resonance (through a feedback-lock), while scanning the nanowire across the optical mode. To do this, for any simulated position of the nanowire in the cavity, we adjust the cavity length to match the resonance condition. In practice, for any NW position, we scan the cavity length and perform a fit of the transmission coefficient. Its maximum gives the resonant cavity length which we then use to compute the other quantities (reflection, scatter, intra-cavity field, force etc.). The width can also be used to compute the cavity finesse.

In fig. 4.10 we present the results for a nanowire partially inserted in the optical mode and scan through the XZ plane. The transmission, scatter and correction signals (which corresponds to the cavity length shift) are shown. In this case the NW almost does not perturb the optical mode, acting as a good probe of the intra-cavity field and allowing to make an "image" of the standing wave pattern. Similarly to what we observed before,

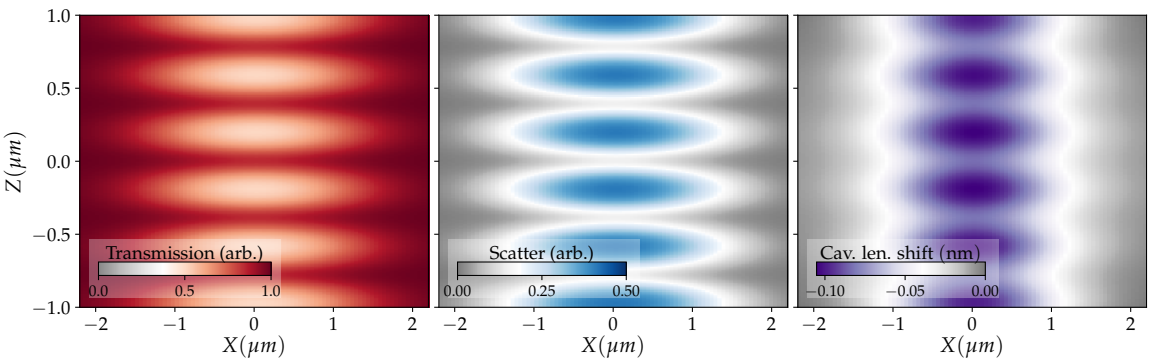

FIGURE 4.10 – Mode imagining simulation of the resonant mode TM_{00}: the transmission, scatter and correction signals have been computed for a NW 1.8 µm away from the optical axis in the Y direction, with dimension $L_x = L_z = 115$ nm, a cavity length $L = 12.44$ µm, mirrors with radius of curvature $\mathcal{R} = 28$ µm and reflectivity $R_A = R_B = 0.994$, and wavelength $\lambda = 770$ nm.

when the NW is at a node the interaction is small, the transmission is close to one and no photon is scattered out of the cavity. Inversely, when it is at an anti-node the interaction is stronger, the transmission rapidly dropped and there is a maximum of scattered photons.

4.4.5 Intracavity field and optical force on the nanowire

Following the same steps illustrated in sections 4.3.2 and 4.3.3, it is possible to estimate the intracavity field for the NIM system, as well as the optical force acting on the nanowire.

Once the reduced reflected field F_r is known, we can estimate the field amplitudes at the left of the two sub-cavities through

$$\begin{pmatrix} F_1(-L/2) \\ F_2(-L/2) \end{pmatrix} = M_A \begin{pmatrix} F_i \\ F_r \end{pmatrix} \tag{4.4.8a}$$

$$\begin{pmatrix} F_3(z_0 + L_z/2) \\ F_4(z_0 + L_z/2) \end{pmatrix} = M_{\mathrm{NM}}\, M_{-L/2,z_0}\, M_A \begin{pmatrix} F_i \\ F_r \end{pmatrix}. \tag{4.4.8b}$$

Equation (4.2.29) then gives the reduced Gaussian fields for both propagation directions and in both sub-cavities:

$$F_1(z) = F_1(-L/2)e^{ik(z+\frac{L}{2})-i[\Psi(z)-\Psi(-\frac{L}{2})]} \tag{4.4.9a}$$

$$F_2(z) = F_2(-L/2)e^{-ik(z+\frac{L}{2})+i[\Psi(z)-\Psi(-\frac{L}{2})]} \tag{4.4.9b}$$

$$F_3(z) = F_3(z_0 + L_z/2)e^{ik(z-z_0-\frac{L}{2})-i[\Psi(z)-\Psi(z_0+\frac{L_z}{2})]} \tag{4.4.9c}$$

$$F_4(z) = F_4(z_0 + L_z/2)e^{-ik(z-z_0-\frac{L}{2})+i[\Psi(z)-\Psi(z_0+\frac{L_z}{2})]}. \tag{4.4.9d}$$

The total Gaussian field can then be obtained from eq. (4.2.27):

$$\mathbf{E}_A(\mathbf{r}_\perp, z) = \rho(\mathbf{r}_\perp, z)\left[F_1(z)e^{ik\frac{\mathbf{r}_\perp^2}{2R(z)}} + F_2(z)e^{-ik\frac{\mathbf{r}_\perp^2}{2R(z)}}\right] \quad \text{for} \quad z < z_0 - L_z/2 \tag{4.4.10a}$$

$$\mathbf{E}_B(\mathbf{r}_\perp, z) = \rho(\mathbf{r}_\perp, z)\left[F_3(z)e^{ik\frac{\mathbf{r}_\perp^2}{2R(z)}} + F_4(z)e^{-ik\frac{\mathbf{r}_\perp^2}{2R(z)}}\right] \quad \text{for} \quad z > z_0 + L_z/2. \tag{4.4.10b}$$

While later we will only consider the instantaneous component of the force, it is worth mentioning that the knowledge of the field inside of the nanowire, that can be obtained with the same proceeding as that of the membrane, is essential to study delayed forces, linked to thermal effects and absorption of the light, which will constitute the subject of future investigations.

In analogous fashion to what we have done in the case of the membrane, the optical force applied by an electromagnetic field on an object contained in a close surface $\mathcal{S}$, is given by

$$F_\alpha = \oint_{\mathcal{S}} \sum_\beta T_{\alpha,\beta} n_\beta dS, \tag{4.4.11}$$

where $T_{\alpha,\beta}$ is the Maxwell tensor. The z component of the force then reads

$$F_z = \oint_{\mathcal{S}} T_{z,z} n_z dS = \sigma_0 (u_L - u_R), \tag{4.4.12}$$

where $u_{L,R}$ are given by

$$u_L = \epsilon_0 (|F_1|^2 + |F_2|^2) \tag{4.4.13a}$$
$$u_R = \epsilon_0 (|F_3|^2 + |F_4|^2) \tag{4.4.13b}$$

and take into account the amplitude of the field (remember that F_i are the *reduced* fields we defined in section 4.2.3), while σ_0 is given by

$$\sigma_0 = \int_{\mathbf{r}_\perp \in \mathrm{NW}} d\mathbf{r}_\perp e^{-2\left(\frac{\mathbf{r}_\perp}{w_0}\right)^2} \tag{4.4.14}$$

and characterizes the overlap between the nanowire and the Gaussian beam.

4.5 EXPERIMENTAL IMPLEMENTATION

After having introduced the theoretical motivations of the "Nanowire in the Middle" approach, we will now describe its experimental implementation.

Inserting a nanowire in the middle of a fiber microcavity of small mode volume is indeed a real experimental challenge: the nanowires employed are extremely long and soft and there is not much space left between the fiber faces when the cavity length approaches 10 µm. This is why we decided to operate with a fully adjustable system, in which both the fiber cavity and the nanowire can be tuned and optimized in vacuum.

In this section we will describe the experimental system: after giving a general overview, we will present the fiber, the nanowires and the optical setup, as well as the software control and acquisition system.

4.5.1 General overview

Using a high finesse and small mode volume microcavity imposes serious constraints on the experimental implementation. A 10-µm-long-microcavity features a free spectral range of $c/2L = 15\,\text{THz}$, corresponding to a wavelength separation of 32 nm in the near infrared (800 nm). For a finesse of 10 000, the spectral linewidth is of $\Delta\nu = FSR/F = 1.5\,\text{GHz}$, corresponding to a cavity length change of $\Delta L = L\,\Delta\nu/\nu = 40\,\text{pm}$. Such a small cavity length change is thus sufficient to bring the cavity out of resonance, meaning that a greater system stability must be achieved.

In parallel, the alignment of the cavity requires a very refined adjustment of the lateral fiber positions, which has to be done in vacuum. In order to tune the cavity at resonance and maintain it for long periods, it is necessary to make use of a piezo element to control the overall cavity length, with a bandwidth sufficient to compensate for the fast fluctuations of the cavity length.

As far as the nanowire is concerned, it is necessary to have both coarse and fine positionings along three directions of space. Operating at low pressure is required to lower the acoustic damping rate of the nanowire vibrations to benefit from larger mechanical quality factors. It also permits to reduce the contamination of the mirror surface, preserving the optical properties of the microcavity over a longer duration. It is worth mentioning that during the pumping phase, the vacuum chamber employed gets slightly deformed, leading to a reproducible $\sim 20\,\mu\text{m}$ spatial drift of the nanowire's position with respect to the fiber (and of one fiber with respect to the other).

Finally, to operate such a tunable system, it is necessary to employ a good imaging system, that allowed to correctly preposition all three key elements (fibers and nanowire) with respect to each others. A long working distance imaging system is thus required.

As usual, it is delicate to conciliate a high mechanical stability and a great tunability. Our choice finally converged on an almost entirely tunable experiment, where both the fiber and the nanowire can be independently adjusted, which lead us to develop an external isolation in order not to suffer from external perturbations.

An overview of the experiment is shown in fig. 4.11. The injection fiber is mounted on a ring piezo to dither the cavity length, and is fixed on the bottom of the vacuum chamber. It serves as a spatial reference for the rest of the experiment. The second fiber, called the transmission fiber is mounted on a motorized XYZ translation stage and on a gimbal mirror mount with manual micrometric screw to control the angle between both fibers. It is also mounted on a fast piezo ring to dither the cavity length for locking purpose. The

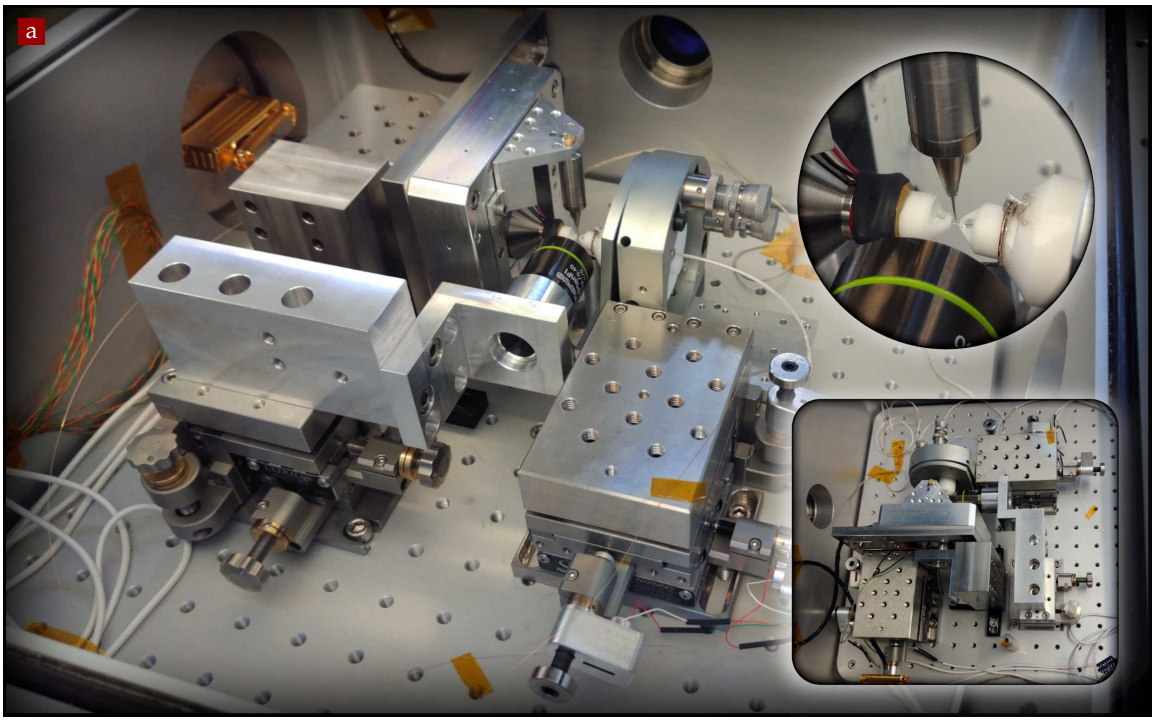

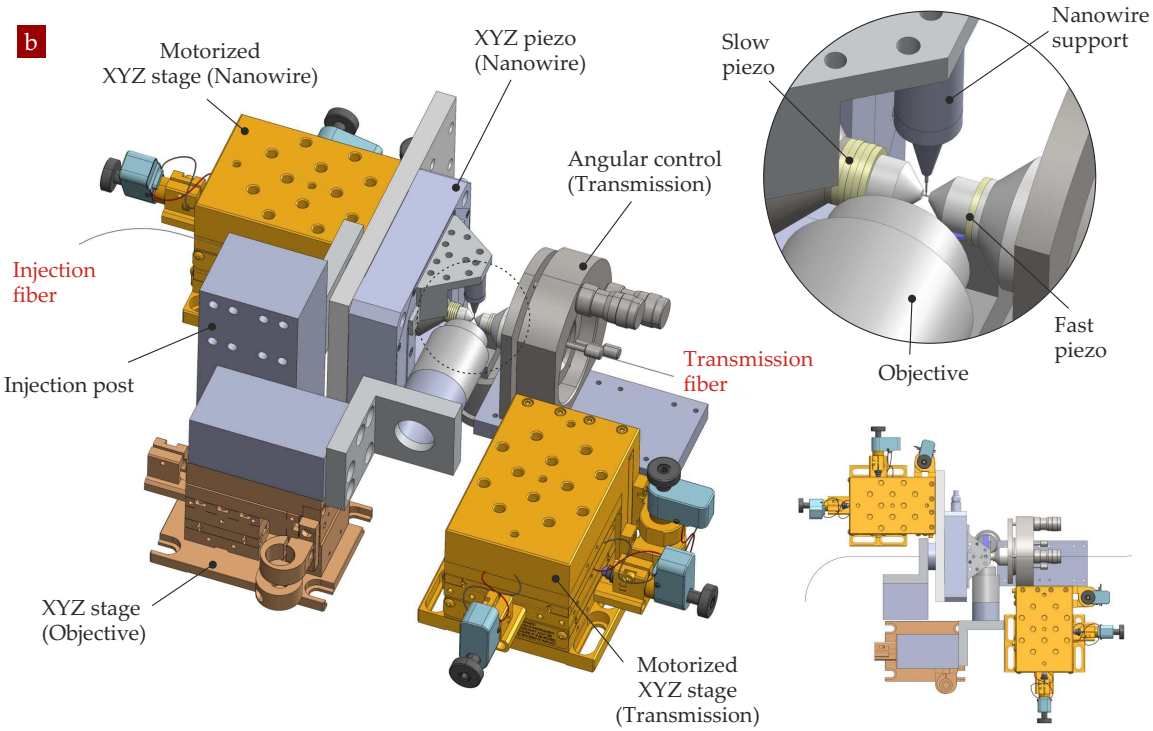

FIGURE 4.11 – Overview of the experimental setup: (a) image of the interior of the vacuum chamber; (b) scheme of the setup.

nanowire is mounted on a XYZ motorized translation stage, supporting an XYZ piezo stage used for precise positioning of the nanowire extremity in the cavity mode. A lateral microscope objective (20× /0.4NA or 50× /0.55NA) with long working distance (10 mm) allows to monitor the respective position of each element with a camera located outside of the chamber. It also serves to collect the light scattered out of the cavity mode by the nanowire. On the other lateral side a camera can be used for additional control, while an inclined mirror permits to monitor the experiment from the bottom side.

We now describe in greater detail the different experimental developments.

4.5.2 Functionalized fibers

The fibers were produced by C. Vaneph at the beginning of his PhD in the Atom-chip group at LKB Paris. These are copper-coated single-mode fibers[7] made of amorphous fused silica (SiO_2). The fabrication process consists of two steps: first the surface is modelled by irradiation with a CO_2 laser, shaping the future mirror by laser ablation. Second, a multilayer dielectric deposition is realized on its laser machined extremity, forming a low loss Bragg mirror. The fibers are then individually characterized and sorted depending on the envisioned experiment.

LASER ABLATION The modelling process is realized with sequences of CO_2 laser pulses, focused on a fiber extremity. The CO_2 laser wavelength of $\sim 10.5\,\mu m$ is close to the resonance vibration modes of the $Si - O - Si$ bound, causing an absorption of roughly 85% of the incident light that locally melts and shapes the fiber surface. Multiple phenomena must be taken into account to describe the heat propagation in the system (conduction,

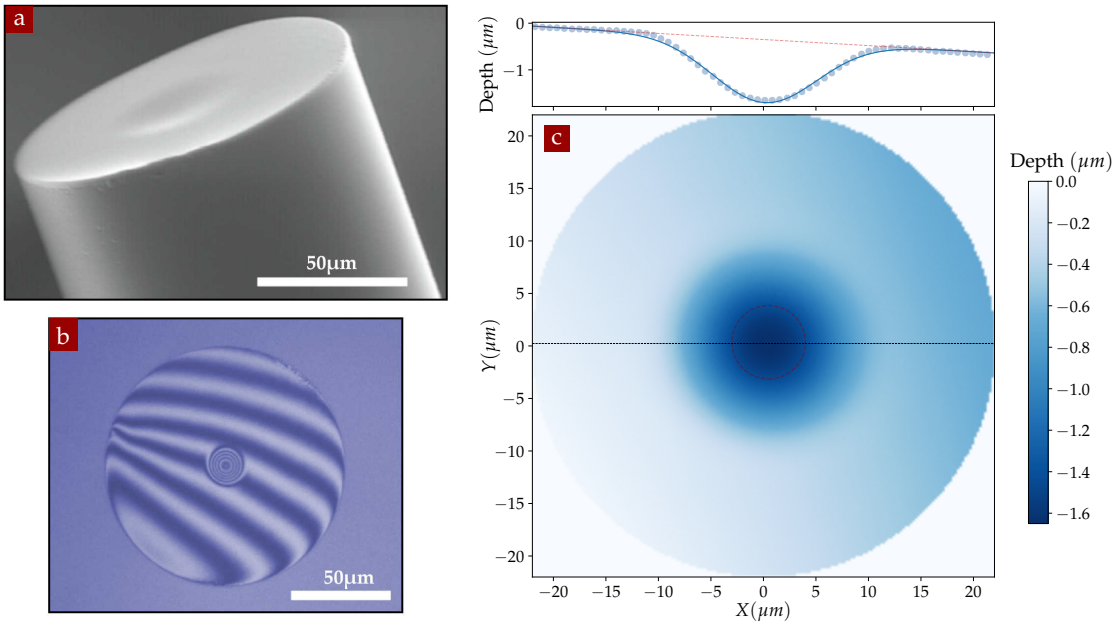

FIGURE 4.12 – Laser ablation of a fiber extremity: SEM image of a fiber mirror (a) (courtesy of the Atom Chips Group [96]); optical profilometry of a fiber with same dimension as Cav2, static mode (b), phase-shift mode (c). The dotted circle shows the fiber core, with MDF of 7 µm. An horizontal cut has been fitted with a Gaussian function (plus a linear offset), with a width of $\sim 5\,\mu m$.

[7]Oxford electronics SM800-125CB

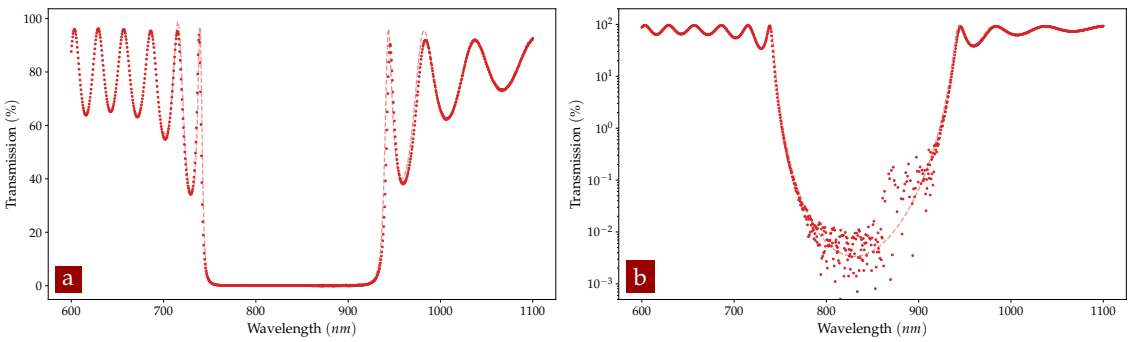

FIGURE 4.13 – Transmission property of the Bragg mirror measured with the help of a LaserOptik spectrometer, both in linear (a) and logarithmic (b) scale.

radiation, convection, evaporation), usually requiring numerical simulation to predict the final mirror shape [96, 154, 95, 231, 229]. The ablation process depends essentially on the laser power, on the waist dimension and on the pulse duration. A result of this process is shown in fig. 4.12a.

The melting process is responsible for an excellent surface roughness, smaller than 1 nm rms [231] (measured with an atomic force microscope), which is an important starting point to reduce optical scattering on the fiber extremities. After fabrication, the etched fibers are pre-characterized by optical means. In particular, an interferometric image is produced in order to evaluate the surface curvature. Among the possible problems that may arise are the elliptical character of the surface and the off-centering with respect to the fiber core. An interferometric imaging permits to determine the mirror curvature, and its principal orientations. The centering of the curvature on the fiber core is also detemined: if too large, it will impact the mode coupling efficiency from the fiber to the cavity mode, and the overall system efficiency.

For a single mode fiber with a mode field diameter around 7 µm and cavity parameters comparable to the one employed in this work, an off-centering value around 3 to 4 µm is enough to reduce the coupling by a factor $1/e$. In order to minimise this effect, a red diode laser is injected into the fiber and used as reference to align the CO_2 before the irradiation, resulting in typical off-centering smaller than 1 µm. Other parameters must also be taken into account when aiming for small losses and high finesse, such as the clipping losses: the lateral extension of the mirrors should be sufficiently large compared to the mode dimensions. In practice the curved surface presents a lateral extension around 10 µm, which is sufficiently large for the optical waists employed, around 2 µm in our experiments.

COATING DEPOSITION The shaped fibers are then sent to an external company to deposit the Bragg mirror (DBR). This consist of a succession of thin films of 2 dielectric material with different refractive index (SiO_2 ($n = 1.479$) and Ta_2O_5 ($n = 2.078$) at 830 nm). Each film has a thickness of $\lambda_0/4$, where λ_0 is the mirror central wavelength. For our fibers, the central wavelength was set at 830 nm and a total of 32 layers were deposited. The expected reflectivity was 99.992% at 830 nm, corresponding to a maximum finesse $\mathcal{F} = 2\pi/2(1-R) \sim 39000$ for a symmetric cavity. The transmission properties of the mirror were measured with a spectrometer (see fig. 4.13). The coating has been realized by ATFilms using Ion Beam Sputtering (IBS) technique in UHV conditions (this is the reason for example for the copper coating of the fibers employed).

SURFACE CHARACTERISATION An optical profilometer is employed to determine the surface curvature, with a lateral resolution limited by optical diffraction. This makes use of an interferometric objective and of an electroluminescent diode to reconstruct the interference pattern between the reference surface (inside the objective) and the fiber surface. It can be used in static mode, to image the interference rings (see fig. 4.12b), or in phase-shift mode, which permits to quantify the surface curvature (confront fig. 4.12c). The resulting image can be fitted to characterize the mirror surface, namely the radii of curvature and their principal orientations, the diameter and the maximum depth. Those measurements allow to establish the stability diagram of the cavity, to determine its ellipticity and the clipping effect due to the finite lateral extension of the etched surface, which are limiting when realizing long microcavities. On the contrary, a too large depression depth is a limiting factor for the creation of short microcavities, as well as the light penetration in the mirror coating.

Depending of the fabrication parameters (he laser power can be set from 300 mW to 3 W, the exposition time from 4 to 120 ms, the waist can range from 21 to 93 µm) it is possible to largely tune the mirror parameters. The radii of curvature can spread between 20 µm and 2 mm, diameters between 5 to 60 µm and depression depth from 10 nm to 5 µm.

FIBER SAMPLES Once processed, our colleagues at LKB sorted out the produced fibers and sent us four couples of them, presenting radii of curvature ranging from 28 to 90 µm.

We realized the experiment with two different microcavities, the first one using 50 µm radii of curvature, and the second one, with which all the following results were obtained, using a couple of 26 - 29 µm ROC fibers. The parameters for the two sets of fiber are reported in table 4.1.

Cavity	Sample	ROC1(µm)	ROC2(µm)	Diameter(µm)	Off-centering1/2(µm)
Cav1	S4-F11	43	46	9	1/0.3
	S4-F12	48	51	9	1/0.6
Cav2	S4-F29	26	29	10	0.2/0.1
	S4-F30	28	29	10	0.2/0.1

TABLE 4.1 – Parameters of the fiber mirrors employed for the cavity setup. The result presented in this manuscript have been obtained with the Cav2 samples.

4.5.3 Fiber supports

Traditionally, fiber microcavity setups were using 2 fibers glued on a compact support, incorporating a shear piezo stage for cavity length control, which requires a refined fiber prepositioning and permits to produce compact microcavities. The requirement to insert long and soft nanowires inside the cavity mode, lead us choosing a more tunable approach, in which the 2 fibers are mounted on separate supports. This approach is less compact but more tunable. We chose it to progressively investigate the experiment and found it to be satisfying for room temperature, while it will need to be reconsidered for low temperature operations.

MACOR SUPPORT The assembly process starts by gluing the fiber on a machined truncated-cone made of Macor. This is a hard ceramic compatible with ultralow vacuum which can

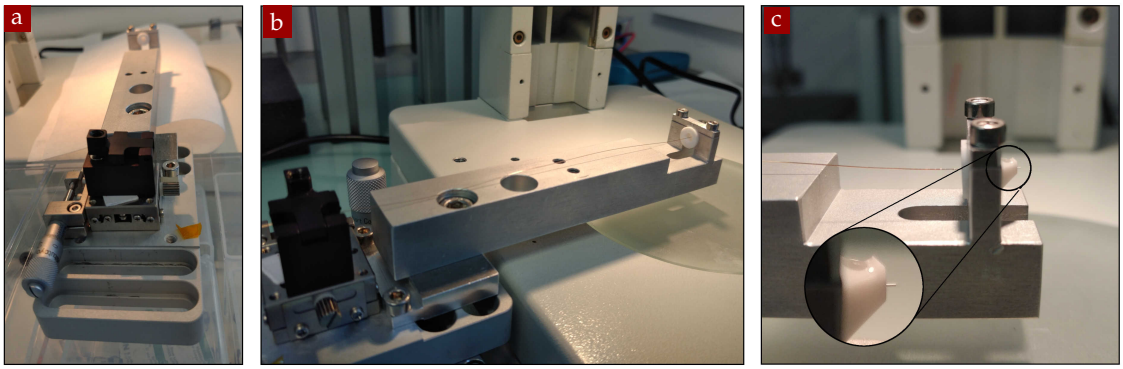

FIGURE 4.14 – View of the aluminium support made to glue the fibers below a binocular (b): a translator (a) is used for the fine positioning at the extremity of the Macor cone (c).

be finely machined. It is an electrical insulator so that it does not create contacts between the faces of the ring piezo elements on which it is mounted.

The cone has a diameter of 8 mm at the base and 0.6 mm at the top; a $\sim$ 250 µm hole is drilled to let the fiber through. An additional larger side hole allows the insertion of the glue in the middle of the central fiber channel. Its back face presents a bevel to allows its proper centering on the supporting ring piezo element.

The mounting is realized on a specifically-made aluminium support (see fig. 4.14). The fiber is slid through the cone from the front side (to protect the mirror end) and set in place under a binocular with the help of a manual translator that moves the fiber axially (fig. 4.14a and b). We try to have the fiber emerging by 300 - 400 µm above the cone extremity, but at the same time avoiding a too long overhanging for the system stability. Also, this distance can not be too small, to avoid the glue gliding on the fiber mirror due to capillarity (see the inset in fig. 4.14c).

Once the fiber is prepositioned, a small droplet of glue is dropped through the side hole with the help of a syringe. We used the Norland Optic Adhesives *NOA*61 which can be cured with a UV lamp in 5 to 10 minutes. We try to avoid a direct exposure of the fiber coating to the UV light, in order not to damage it or create parasitic electrostatic charges which can attract dust. More glue is then applied through the back side of the cone to strengthen the bond. This second step is repeated until the cone is completely filled.

PIEZOS AND STEPPER-MOTOR Once glued on the cones, the fibers are then mounted on the rest of the support, which consists of a ring piezo element and of a final holder.

The injection fiber is glued on a ring piezo stack (Physik Instrument) (fig. 4.15b), which is subsequently glued on a stainless steel support (fig. 4.15a). The latter is then screwed on the bottom plate of the vacuum chamber. The piezo stack allows to move the fiber along the cavity axis on a distance of $\sim$ 1.1 µm, with a maximum voltage of 220 V. This corresponds to roughly 2.5 times half of the infrared wavelengths employed. It is also a range sufficient to completely compensate for the long term drifts observed in the system over one day, so that it can be used for long term locking purpose. This piezo is suitable for low frequency operations, with a (unloaded) cutoff frequency around 50 kHz.

The transmission fiber is glued on a fast piezo ring, mounted on a Macor holder (fig. 4.15c). The latter is screwed on a gimbal mount, fixed on XYZ Newport motorized stage (fig. 4.15d and e). The gimbal mount allows to adjust the angle between the

two fibers, both in the horizontal and vertical planes, while the motorized stage is used for the lateral and axial alignment (each axis has a displacement range of 12 mm and the piezo motors can realize steps as small as 50 nm, albeit with a moderate reproducibility) of one fiber with respect to the other. The piezo ring is used to dither the cavity length to generate the error signal for the cavity lock (see section 5.1). It is driven up to an amplitude of ± 5 V, generating a length modulation of up to 1 nm and can be employed up to ~ 1 MHz.

Note that our system is completely symmetric and the cavity can be injected from both sides; however it is more convenient experimentally to fix the injected port and allow for the transmission port to move.

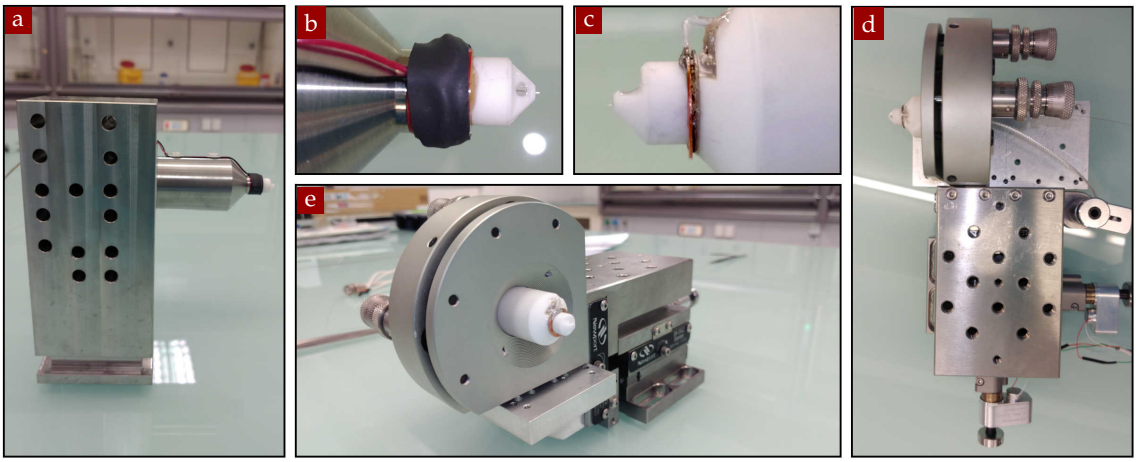

FIGURE 4.15 – Optical fiber support: (a) stand for the reflection fiber; (b) and (c) slow and fast piezos; (d) and (e) stand for the transmission fiber.

FIBER CONNECTORIZATION The fiber samples come in pieces long around 50 cm, that need to be connected with a longer fiber so that the light can be injected and transmitted in and out of the vacuum chamber. A supplementary length of 1 to 2 meters per fiber has been added. The quality of this splicing process is crucial because it can potentially impact the optical properties of the cavity by creating spurious standing waves (or induce meaningful optical losses if badly done). We used a commercial fusion splicer (Ericson FSU15FA) and P3-830A-FC fibers from Thorlabs, with an outer APC connector to reduce spurious reflections. The target value for the losses estimated by the machine must be around 0.01 - 0.02 dB. The splicing follow the standard procedure: first the fiber coating is removed (chemically or mechanically); the extremity is precisely cleaved and then both fibers are inserted in the splicer and fused with the proper settings. The LKB fiber samples present a copper coating, that can be attacked chemically with iron chloride ($FeCl_3$) for around one minute and then cleaned with isopropanol. Potential residues of a thin carbon film can be removed after being burnt with a lighter and a subsequent alcohol cleaning.

4.5.4 Nanowire support

In the choice of the nanowire, several aspects have to be taken into consideration. First it should be long enough to be inserted in a short fiber microcavity without touching the upper part of the fibers (125 µm in diameter). This leads to overall lengths larger than 70 µm. The nanowire has to be relatively straight and attached as well as possible in the prolongation of the tungsten tip. To do so, we employ very sharp tips, which permit such an alignment. Second, its diameter, at least at its vibrating extremity, has to be precisely chosen to maximize the optomechanical coupling strength. We will discuss those aspects in section 4.6.2, but in general, it is desirable to operate with a diameter in the 100 - 180 nm range. The selection method is realized as explained in the low temperature section 3.1.3.

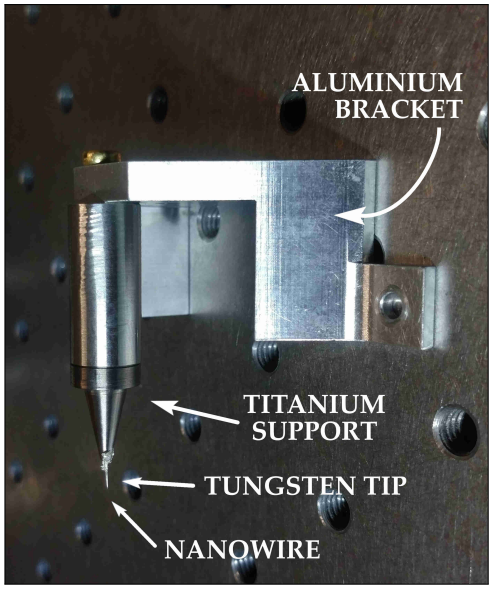

FIGURE 4.16 – Ensemble of the NW support.

The tungsten tip is glued with a conductive silver paste in a conical titanium support, which is screwed on a bracket (fig. 4.16). The latter is connected to a XYZ piezo stage featuring $30 \times 30 \times 10$ µm travel range in each orientations. This hollow piezo stage is surrounding the injection fiber mount and coarse positioned using a motorized XYZ translation stage (see fig. 4.11), which permits to position the nanowire in all three directions with respect to the fibers.

The nanowire may not be aligned with the tungsten tip axis, due to its gluing on the conically etched support. The mechanical support of the nanowire can be rotated in order to bring the nanowire in the plane perpendicular to the optical axis. This adjustment must be extremely well done in order to operate with short microcavities, otherwise it would be impossible to bring the nanowire in the cavity field without touching the fibers. This alignment is realized with the lateral camera view. As a consequence, the nanowire may not always be perfectly vertical, which can be compensated by using tilted scan axes (electronic rotation in the XY plane to ensure that the scan axes remain aligned with the nanowire axes).

To improve mechanical quality factors, the nanowire and its support are baked in vacuum at a temperature of $\sim 700\,°C$. This permits to reach quality factors around 10 000 at low pressure, below 1×10^{-3} mbar.

The parameters of the NW samples employed in this work are reported in table 4.2. All the results discussed in the following will refer to NW2, if not specified otherwise.

Sample	L(µm)	d(nm)	$\Omega_m/2\pi$(kHz)	Q	M_{eff}(pg)	x_{zpf}(pm)	Δx_{th}(nm)
NW1	180	250	$10.7 - 11$	–	–	–	–
NW2	70	130	$50 - 60$	2000	0.7	0.47	7.0
NW3	90	160	$27.2 - 27.6$	2700	2	0.39	8.4

TABLE 4.2 – Main NW samples employed in the cavity setup.

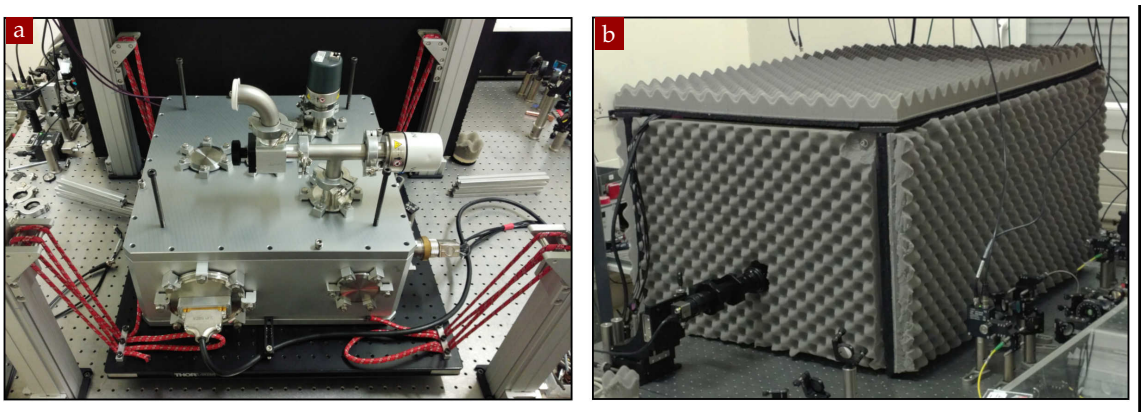

FIGURE 4.17 – Vacuum chamber and system isolation: (a) enclosure suspended from the table; (b) acoustic (and thermal) isolation chamber.

4.5.5 Vacuum chamber

We showed in section 3.1.2 that the mechanical damping rates of the nanowires are very much affected by the environment pressure and typically become only limited to their intrinsic value for pressures below 10^{-3} mbar. The experiment is conducted in a $40 \times 40 \times 15$ cm vacuum chamber, as shown in fig. 4.17a. Combining a primary and a turbomolecular pump permits to achieve pressures down to 10^{-5} mbar inside the enclosure. However, the vibrations due to both pumps preclude the stability of the optical microcavity, since it goes out of resonance for relative fibers separation changes of a few tens of picometers. The pumping system needs to be turned off and disconnected during the alignment and the measurement process. After disconnecting the pumps the pressure in the chamber can be maintained below 0.01 mbar for a day or two, sufficient for most data-acquisition sequences.

We realized efficient fiber vacuum feedthroughs using a common gaz tube connector system (Swagelok) soldered on stainless steal vacuum flange. The tube is replaced by a teflon cylinder drilled in the middle to host the fiber. A screw permits to compress the outer part of the connector on the teflon, which seals the fiber input. If needed, a bit of epoxy glue can be added. Vacuum pressure is monitored on a gauge placed on the cover plate, while multiples electrical feedthroughs serve to convey signals for the two dithering piezos, for the XYZ nanowire piezo stage and for the six motors.

4.5.6 Vibration and thermal insolation

After having checked that the cavity could be safely aligned with the above described setup, we rapidly experienced the need for largely reducing the vibration noise of the environment, as well as for improving its long term stability: we typically observed mechanical drifts of 1 µm/°C, which correspond to a few cavity FSR, knowing that the temperature stabilization of the room cannot be ensured at a level better than ±3 °C per day.

To do so, the whole vacuum chamber was mounted on a breadboard, which was suspended with the help of bungee cables, in order to reduce the acoustic vibration impinging on the experiment. The dominant sources of noise are the human traffic in the corridors and lifts, the pumps in close-by labs and the one arising from the close-by

instruments (laser chiller, fans from electronic devices). The total mass of the loaded chamber and breadboard is around 100 kg: we employed bungee cables from Sandow Technics, with diameter of 6 mm and surrounded by a textile cover. Four folded cables at each angle of the breadboard, sixteen in total, with an unloaded length of 20 cm, allowed to safely lift the chamber using a 15 cm elongation. The cables were suspended on four pillars, slightly displaced to ensure a self-centering in the horizontal directions. The effective oscillation frequency is around 1 - 2 Hz in the horizontal direction and 2 - 3 Hz vertically.

Furthermore, we built an acoustic isolation chamber around the experiment to provide an isolation against air vibrations, using plane tree wood boards cover with two layers of foam, providing an attenuation larger than 20 dB and 15 dB respectively. This acoustic chamber also serves as a thermal isolation layer, which stabilizes the experiment temperature by mitigating the fluctuations of the air conditioning system of the room. Figure 4.17 shows images of the suspension and thermal isolation box.

In presence of those two apparatus, it became possible to satisfyingly lock the microcavity at resonance over days, in order to accomplish the long imaging measurement sequences exposed below. The thermal drifts were also largely attenuated, below 100 nm per day, which was sufficient to make long acquisition maps without moving too much in the standing wave pattern. The most critical measurements were also launched overnight or over a weekend to benefit from a quieter environment.

4.5.7 Optical scheme

INFRARED PUMP LIGHT Our pump laser is a Ti:Saphhire laser, a Solstis SRX model from M-Squarred, pumped by a 532nm 10W laser from Light House Photonics (model Sprout). It is tunable from 700 to 1000 nm and provides more than 2 W of IR light one the range of interest. The laser linewidth can be reduced using an external reference cavity, down to 50 kHz rms (in 100 µs). The overall laser tunability can be achieved using the internal birefringent filter, etalon and piezo elements, which permit to cover the full spectral range. For the experiment described in this work, we will adjust coarsely the laser wavelength, lock the internal etalon and lock the laser cavity length on the external reference cavity. A diode laser from Toptica, tunable from 770 to 805 nm was also employed. The peak reflectivity of the fiber coating is around 830 nm and present large variations in the 760 - 830 nm band, see fig. 4.13, which is of great interest in order to tune the cavity finesse. In the experiment, we only pick around 30 mW of IR light.

The pick-up is first injected in an optical fiber which serves as spatial filter to clean the beam profile. A polarizer placed at the fiber output permits a better determination of the laser polarization. The beam is then sent through a half waveplate and a polarizing beam splitter (PBS) cube, which serves as a coarse intensity controller. The addition of a polarizer permits to compensate the non-ideal behaviour of the cube, resulting in an actual regulation of the power down to null intensity. An acousto-optic-modulator (AOM) from AA Opto-Electronic (MT200-IR, 200 MHz carrier) serves to electronically control the intensity sent to the microcavity. Depending on the experimental needs, this is can be controlled by a DC output of the main DAC card, or by the output channels of a vectorial network analyser (Agilent) or a synchronous demodulator (Zurich Instrument HF2LI), if a dynamical modulation of the light intensity is needed.

Two additional lenses ($f = +100$ mm) are positioned before and after the AOM to optimize the spot-size on the crystal. With this configuration, the AOM bandwidth is

around 10 MHz. At this point the light goes through a 90 : 10 non-polarizing cube: 10% of it is sent to the cavity, so that it will then be possible to recover 90% of the light reflected from the cavity, which is collected on a Thorlabs APD130A2/M avalanche photodiode. A motorized half waveplate allows to control the orientation of the linear polarization injected in the injection fiber, which will serve to pump the NIM system. The maximum injected power employed in our experiments is around 10 µW.

On the transmission fiber side, we can directly connect the fiber on a photodiode to collect the signal. However, given the numerical aperture of the fiber and the dimension of our sensor (Thorlabs APD130A/M), it was more efficient to go back in free space, collimate the beam and focus it back on the detector with a 25.4 mm focal length.

The fiber coupling ports are identical to the ones described in section 2.4.2. Here we used aspheric lenses with a focal length of $f = +15$ mm (C260TMD-B) for the spatial mode cleaning fiber, and a focal length of $f = +11$ mm (C220TMD-B) for the reflection and transmission ports.

VISIBLE PROBE LIGHT To provide a readout of the mechanical vibrations of the nanowire, independent from the cavity field state, we added a visible laser in our setup. It will serve to calibrate the nanowire mechanical properties using the standard methods developed in the group, and will be employed to determine the force field exerted by the intracavity field experienced by the nanowire.

We use a He-Ne 633 nm red laser (15 mW), which is co-propagating in the cavity fibers. At that wavelength, the cavity coatings are not efficient anymore so that the probe light can reach the nanowire, and they are sufficiently separated from the employed IR wavelengths to permit an efficient spectral filtering. It is injected in the cavity fibers through the reflection (or the transmission) side by mean of a wavelength division multiplexers (WDM, Thorlabs NR73A1), which provides a transmission larger than 90% and crosstalks smaller than −20 dB. The readout mechanism is similar to the one employed in the cryogenic objectives (section 2.3.1): part of the light is reflected on the fiber cavity output and interferes with the one reflected by the nanowire. The red power employed, typically between 3 and 10 µW, is sufficiently small not to perturb neither the cavity state via residual thermal absorption, nor the mechanical oscillator via optical forces or residual absorption.

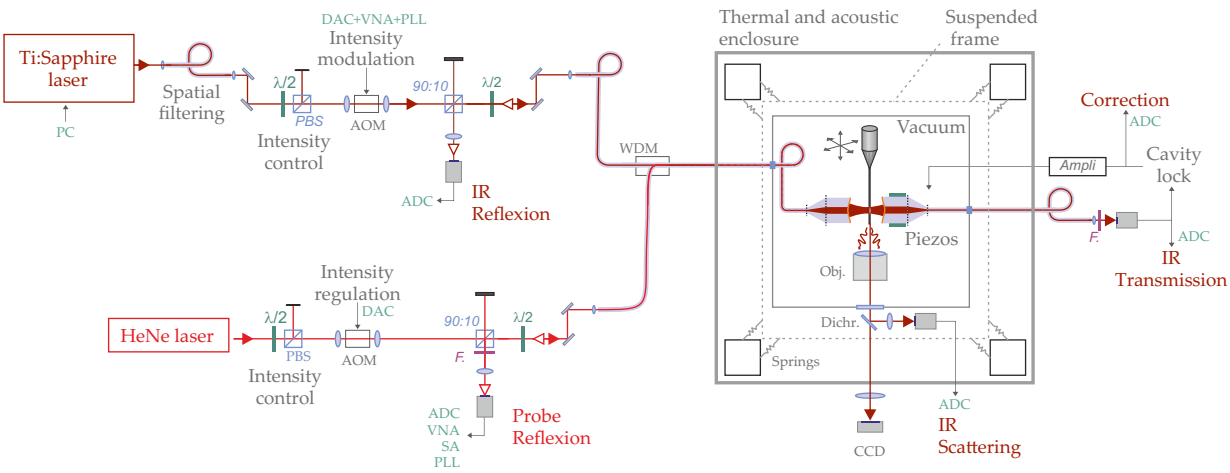

FIGURE 4.18 – Scheme of the optical setup employed in the NIM system.

The optical probe beam is prepared in a similar fashion as for the infrared cavity pump light: its power can be coarsely controlled with a half waveplate and a PBS, and an AOM follows for the fine settings. Before the non-polarizing 90:10 beam splitter cube, use to inject and collect the reflected light, a telescope ($f_1 = 200\,\text{mm}, f_2 = 50\,\text{mm}$) serves to optimize the beam waist and to improve the fiber coupling efficiency. The fiber injection is realized with an aspheric lens with focal length $f = +11.00\,\text{mm}$ (C220TMD-A). The reflected probe light is recorded on a standard avalanche photodiode (Thorlabs APD410A2/M).

SCATTERED LIGHT When inserted in the cavity field, the nanowire scatters the IR light out of the cavity mode. It is collected using a $20\times/0.4$NA microscope objective, added inside the vacuum chamber (see insert of fig. 4.11a), to provide additional measurement channels of both the IR and the red scatter light fields. With a working distance of $\sim 12\,\text{mm}$, it can be easily placed in proximity of the cavity without affecting the alignment process. In addition, it can be used to obtain an enlarged view of the system, critical for operating with cavity lengths smaller than $20\,\mu\text{m}$.

The scatter light is collected with the help of a photodiode (Thorlabs APD110A2/M) outside of the chamber. The latter is mounted on the suspended breadboard, to preserve the optical alignment even in presence of vibrations of the chamber suspension. A filter or a dichroic mirror can be employed in order to determine the recorded wavelength.

VISUALIZATION AND ALIGNMENT Three optical windows have been mounted on the chamber: two on the cavity lateral sides and one the lid for illumination. During the alignment phase, we adopt the following procedure: when initially the two fibers and the nanowire are far apart from each other, we start the alignment looking through the lateral window that gives a direct visual access to the experiment (see fig. 4.19a), using a long working distance zoom lens objective and a CCD camera. This allows us to have a general overview of the ensemble and to realize the first fine positioning steps. Figure 4.19a to d show a typical view of the system for different magnification. Also visible in panel (a) is a silicon wafer inclined at 45° below the fibers, which allows to achieve a visualisation from the bottom side, very helpful for lateral positioning of the nanowire, as well as for the adjustment of the relative angles between the fibers.

When we enter the final alignment phase, the camera is moved to the opposite optical window side and the NIM system observed through the microscope objective (fig. 4.19e): this way, cavities as small as $10\,\mu\text{m}$ can be safely aligned (fig. 4.19f), even if this can require some patience. Particular care must be taken to minimize fast and abrupt movement that increases the possibility for the NW to stick on one of the fibers (and potentially damage the coating).

The illumination causes a temperature increase in the system which leads to slight spatial thermal drifts. The use of diffuse light instead of direct illumination can partially mitigate this effect, but we mainly try to minimize the observation phases and employ minimal optical powers once the setup is aligned and stabilized. All the final alignment steps are thus realized in the dark, and only make use of IR or visible optical signals (transmission/reflection essentially) for refined alignment of the system. Also it is worth mentioning that due to the mechanical vibrations induced by the turbo pump, it is necessary to remove the nanowire out of the cavity during the pumping phase.

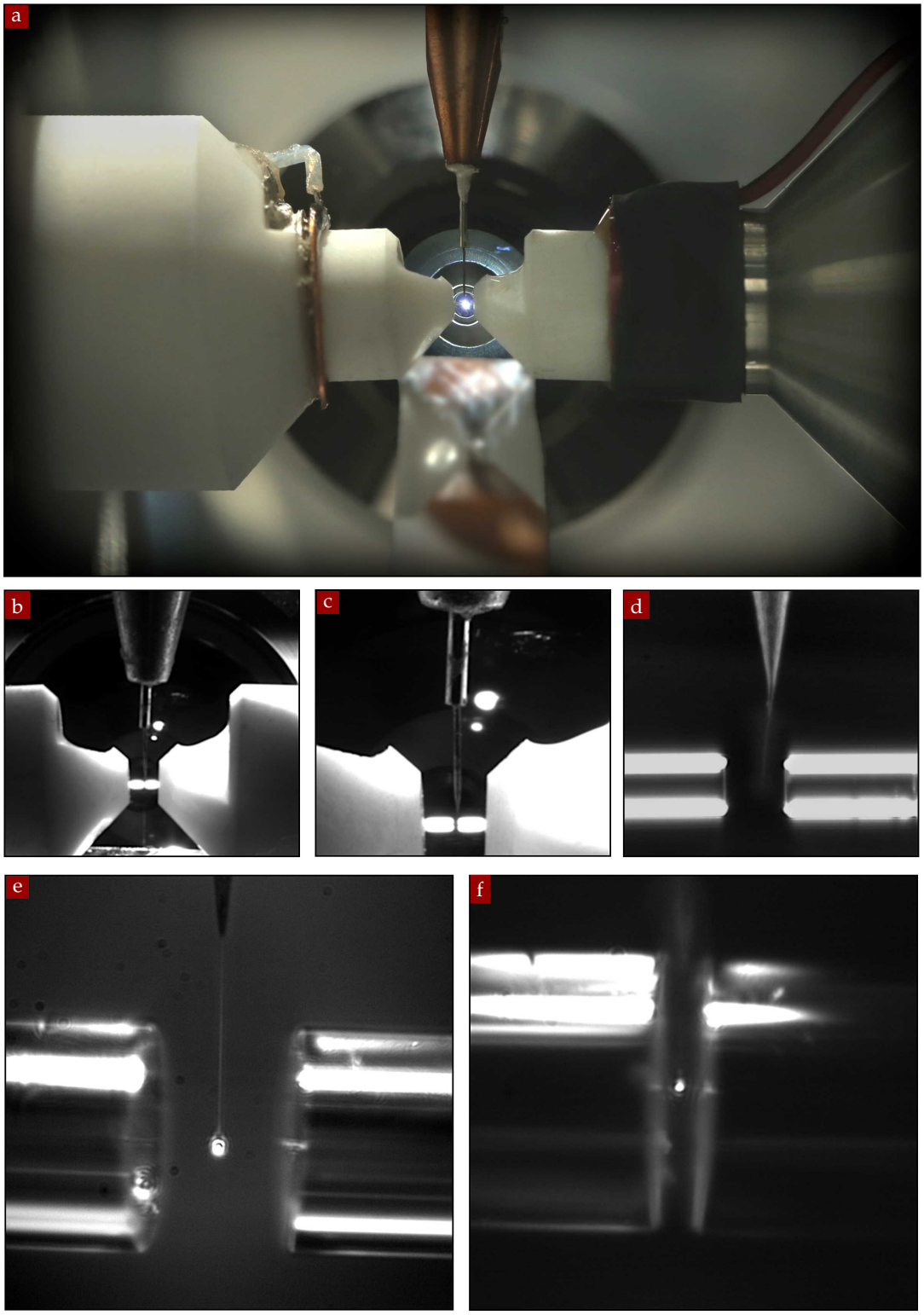

FIGURE 4.19 – Screenshot from the camera used to align the optical cavity and position the NW in the middle of it. The initial coarse alignment is realized from the free optical port of the chamber (a)-(d), where one can also observe the reflection of the NIM system on the inclined silicium mirror which permits a visualization from the bottom. Then one can see the microscope objective in the back, which serves for the final alignment (e),(f). The nanowire is first inserted in a largely opened cavity (200 µm) and centered on the mode using the laterally scattered light (e). The cavity is then progressively closed (f), by continuously optimizing the fiber position. With this technique, it is possible to have the nanowire vibrating in the middle of small mode volumes microcavities. The smallest cavity lengths obtained were around 10 µm.

4.5.8 Experiment control and interface

The experiment requires a precise positioning of the nanowire in the cavity field, a control of the cavity and laser states, as well as recording multiple signals not only from the photodiodes but also measurements obtained from separate devices, such as spectrum or network analyzers or synchronous detection. The experiment is controlled by a similar python interface as the one described in the cryogenic experiment (section 2.4.1), NIL. It has been adapted to this experiment to allow for a faster acquisition speed in order to quickly scan the cavity length. We also had to increase the number of measurement channels in order to simultaneously record the IR reflection, transmission and scatter fields, the reflected and scattered visible channels, as well as the correction of the cavity lock. This amounts to approx. six input channels. In addition, for the force field measurements, it was necessary to record in real time the output of the multiple locked-in detector channels, amounting to up to 8x2 additional signals: dynamical beta measurements, mechanical response at six different frequencies both in amplitude and phase. To do so a module developed for rapid force field measurements (with the help of P. Heringlake) was integrated. The aforementioned interface is depicted in fig. 4.20. The acquisition card is the same *National Instrument PCI-6323e* we previously described, whose output channel are employed in this case to control the cavity slow-piezo as well as the fine-positioning of the nanowire in the optical mode volume.

Besides the core interface, the main experimental signals are continuously recorded on oscilloscopes (Lecroy Wavesurfer or internal scope of FPGA Red Pitaya cards, see section 5.1). For the spectral analysis we make use of the two base-band inputs of an Agilent MXA *N*0920 spectrum analyzer: the integrated VSA software allows for the acquisition of two spectra at the same time, with resolution bandwidths smaller than 1 Hz. A Rhode&Schwarz FSVR spectrum analyzer was also alternatively employed for faster spectrum acquisitions and in particular for the soft-tracking of mechanical peaks.

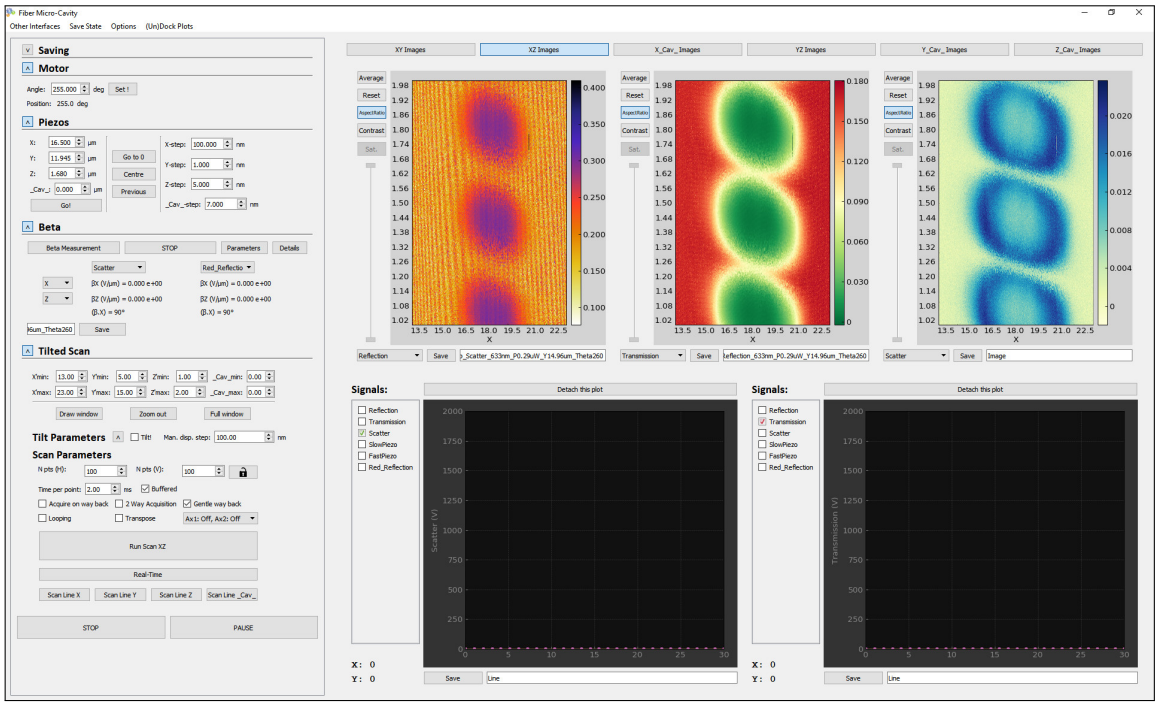

FIGURE 4.20 – Graphical user interface developed to control the NIM system.

4.6 OPTOMECHANICAL COUPLING IN A NIM

We now present the investigation of the optomechanical coupling in a Nanowire-In-the-Middle system. Moving from the behaviour of the bare cavity (without the NW), which constitutes our starting point, we will show and quantify how the cavity resonance is affected by the NW. Scanning our vertical nanowire across both the transverse and the axial planes of the cavity, we will report the observed frequency cavity shifts, how they are affected both by the NWs properties and the light polarization, as well as their dependence on the relative position between the optical and the mechanical system. From our observations we will then deduce the value of the *single photon coupling* g_0 and how it compares to the mechanical frequency. We will conclude showing how, properly tuning the cavity parameters, it is possible to investigate the OM coupling for higher order modes, as well as to observe a cross-coupling among them.

4.6.1 Bare cavity resonances

The properties of the bare cavity are determined by recording the transmission (or the reflection) signals while dithering the cavity length with the slow piezo (maximum span of 1.1 µm). Specifically, we want to evaluate the cavity length and the cavity finesse (and so its decay rate κ.) In particular we will show the dependence of the latter on the wavelength, as this will constitute an important tunable parameter for the following measurement.

Figure 4.21 shows a typical transmission signal obtained when scanning the cavity length over 1 µm, around a base value of 6 µm. Imposing that the distance between two subsequent longitudinal mode equals to $\lambda/2$ permits to calibrate the piezo deformation efficiency (V/m) and to compensate for possible histeretic phenomena.

The overall cavity length depends on the fibers' relative positions. Its proper determination can be realized by simultaneously injecting two different wavelengths in the cavity, intially very close (λ_0), and progressively varying one of the laser wavelength up to the value λ_1 where the cavity is found again to be simultaneously resonant

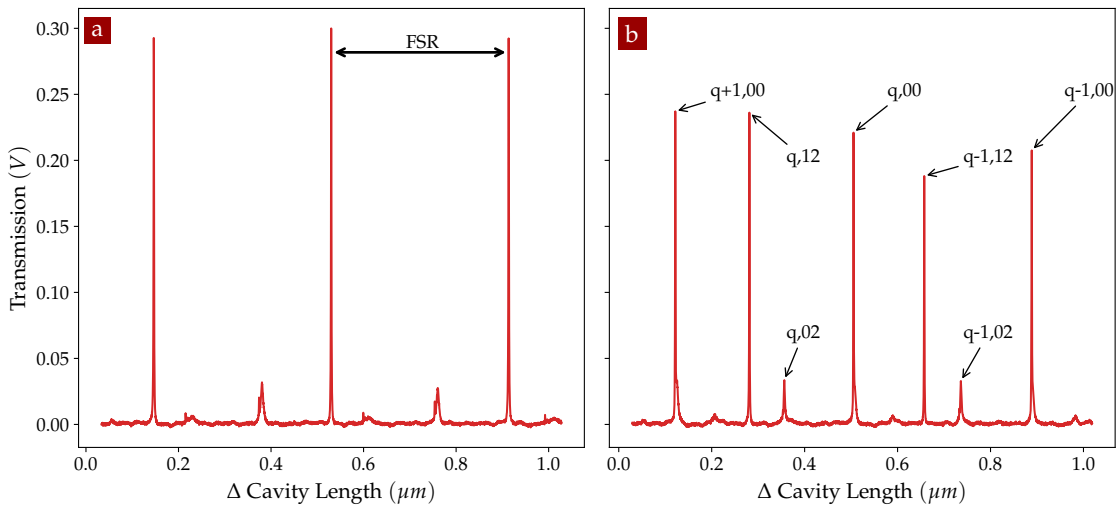

FIGURE 4.21 – Cavity scan over two free-spectral-range, maximising alternatively the fundamental mode TM_{00} or the transversal mode TM_{12}.

for both wavelengths. In that situation, the total cavity length simultaneously verifies: $L = q\frac{\lambda_0}{2} = (q-1)\frac{\lambda_1}{2}$, with $\lambda_1 > \lambda_0$. Solving those equations leads to

$$L = \frac{\lambda_0 \lambda_1}{2(\lambda_1 - \lambda_0)}, \tag{4.6.1}$$

allowing to determine the overall cavity length and the longitudinal order of the pumped resonances (q). In practice, we operate with cavities presenting lengths down to 10 µm, for which the spectral separation is of 30 nm approximately, corresponding to 25 arches of the EM standing wave.

The cavity length can also be estimated using the spacing between the transversal modes. If the fibers are assumed to present the same radii of curvature R, the difference Δ_L in cavity length between two transverse resonances of the same longitudinal family is given by (see section 4.2):

$$\Delta_L = L_{q,00} - L_{q,01} \simeq \frac{\lambda_0}{2\pi} \arccos\sqrt{g_1 g_2} = \frac{\lambda_0}{2\pi} \arccos(1 - L/R). \tag{4.6.2}$$

We can then extract for the cavity length

$$L \simeq R\big(1 - \cos(2\pi\Delta_L/\lambda_0)\big). \tag{4.6.3}$$

Note that by optimizing the alignment of the two fibers in the transverse plane we can choose to maximize either the fundamental mode TM_{00} (fig. 4.21a), or the other transverse mode (fig. 4.21b). The alignment of a certain mode consist of a series of optimisation steps with the servo motors, constantly alternating between the two transverse directions. The

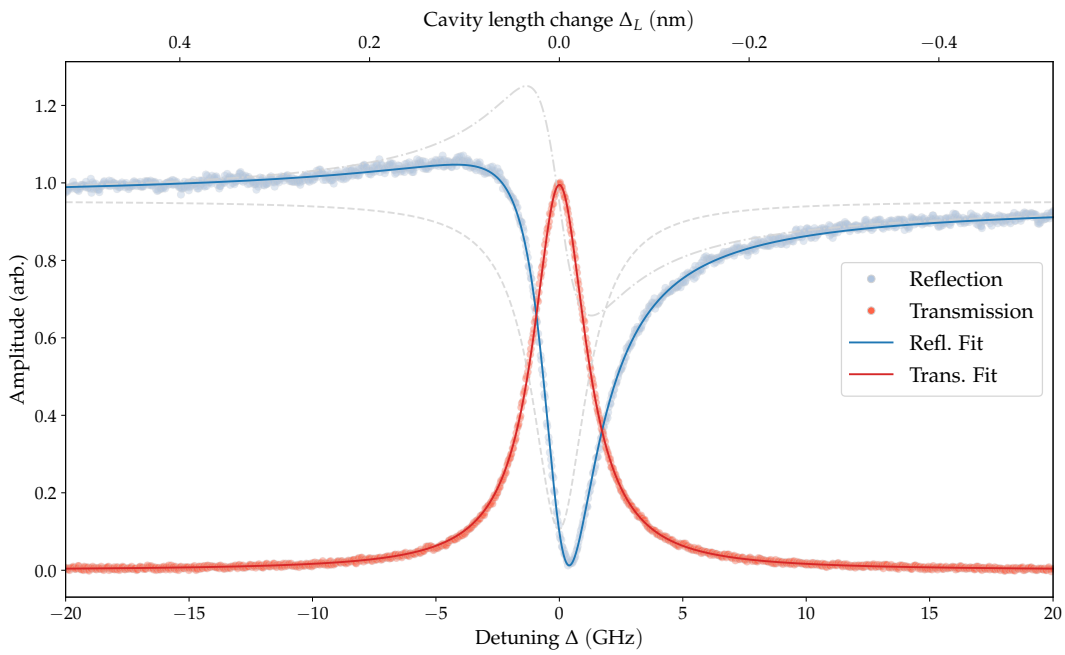

FIGURE 4.22 – Typical reflection and transmission signals of the fiber micro-cavity. The data have been fit with the expression from eq. (4.6.4). The fitted linewidth is of 2.6 GHz which corresponds to a 68 pm cavity length change. The dispersive shape observed on the reflection signal is due to an interference between the cavity reflection field and another signal. Since its shape depends on the alignment conditions, it can also originates from the non perfect mode matching between the cavity and fiber modes.

goal being to simultaneously maximize both the transmission signal and the finesse, it must be noted that a non-ideal alignment between the center of the mirror and the cavity core (see section 4.5.2) implies that the two can attain the maximum value not in the same position. In our case, we have been mainly working in the low-finesse regime (see below), so we almost always decided to maximize the signal intensity. Usually this also corresponds to minimizing the transmitted intensity of all other modes. In the example shown here the estimate distance between the fiber is $L = 6 \pm 1\mu\text{m}$, assuming $R = 29\,\mu\text{m}$. The error is mainly due to the incertitude in the calibration of the slow-piezo.

Figure 4.22 shows a zoom of the reflection and the transmission signals around a cavity resonance for a wavelength of 780 nm, obtained by dithering the cavity length. The horizontal axis corresponds to the relative cavity length change Δ_L, also expressed into the equivalent laser frequency shift (detuning) Δ, which we obtained using $\Delta_L/L = -\Delta/\nu_{\text{cav}} = -\Delta/(c/\lambda_{\text{cav}})$. The latter can be calibrated by adding a frequency modulation on the laser frequency, realized with a fast electro-optic modulator (EOM). For the former instead, given a temporal trace acquired with the oscilloscope, we use the length of the FSR as reference: $\Delta_L/L_{\text{FSR}} = \Delta_t/t_{\text{FSR}}$, where $L_{\text{FSR}} = \lambda_{\text{cav}}/2$, while Δ_t and t_{FSR} are the cavity width and the cavity FSR measured in time (which of course depend on the scan speed of the piezo and are meaningful only as relative quantities).

This measurement can be fitted to extract the value of the cavity decay rate κ. Accordingly to section 4.2.2, we used the following expressions:

$$C_T(\Delta) = \frac{P_T}{P_{\text{in}}} = \mathcal{A}\frac{1}{1+(\frac{2\Delta}{\kappa})^2} \tag{4.6.4a}$$

$$C_R(\Delta) = \frac{P_R}{P_{\text{in}}} = \left| r_F e^{i\psi} - \eta^R_{\text{mm}} \frac{r_A e^{i\varphi} - r_B e^{-i\varphi}}{r_A r_B e^{i\varphi} - e^{-i\varphi}} \right|^2 = \mathcal{B} - \mathcal{C}\left(\frac{1}{1+(\frac{2\Delta}{\kappa})^2} - \mathcal{D}\frac{2\Delta/\kappa}{1+(\frac{2\Delta}{\kappa})^2}\right) \tag{4.6.4b}$$

where Δ is the detuning.

The transmission signal is well fitted using a Lorentzian function, with a linewidth of 2.6 GHz or equivalently a relative cavity length change of 68 pm. The corresponding finesse is of ~ 5600. The transmission efficiency largely depends on the microcavity geometry, and the alignment procedure generally aims at maximizing the peak transmission. In practice, we observe transmissions efficiencies up to $\sim 80\%$ (to be calculated using the V/µW data from the manufacturer). $\mathcal{A} = \eta^T_{\text{MM}}\eta_{\text{imp}}$ is thus a fitting constant whose value depends both on the mode-matching of the cavity mode with the input and the output fiber modes ($\eta^T_{\text{MM}} = \eta^A_{\text{MM}}\eta^B_{\text{MM}}$) and on the impedance matching condition (η_{imp}). Since we operate with identical mirrors on both sides, we normally assume $\eta_{\text{imp}} \sim 1$.

The reflection signals, for the very same reason, present in general a very good contrast, so that at resonance most of the light is transmitted. It also presents a non-symmetric character, whose magnitude largely depends on the cavity alignment. It originates from an interference between the signal reflected from the cavity mode and the light reflected from the first mirror, both being spatially filtered by the fiber mode and the latter being enhanced by a non-perfect mode matching between the cavity and the fiber modes. To adjust the reflected signal, we thus employ the expression of eq. (4.6.4b): Δ is the cavity bandwidth, $\eta^R_{\text{MM}} = \eta^A_{\text{MM}}$ is the mode matching coefficient between the cavity and the first mirror and r_F, ψ describes the parasitic signal amplitude and relative phase. The other constants are then $\mathcal{B} = (\eta^R_{\text{MM}})^2 + r_F^2 - 2\eta^R_{\text{MM}} r_F \cos\psi$, $\mathcal{C} = (\eta^R_{\text{MM}})^2 - 2\eta^R_{\text{MM}} r_F \cos\psi$ and $\mathcal{D} = \frac{2r_F \sin\psi}{\eta^R_{\text{MM}} - 2r_F\cos\psi}$. The consequence of this interference is also to slightly displace

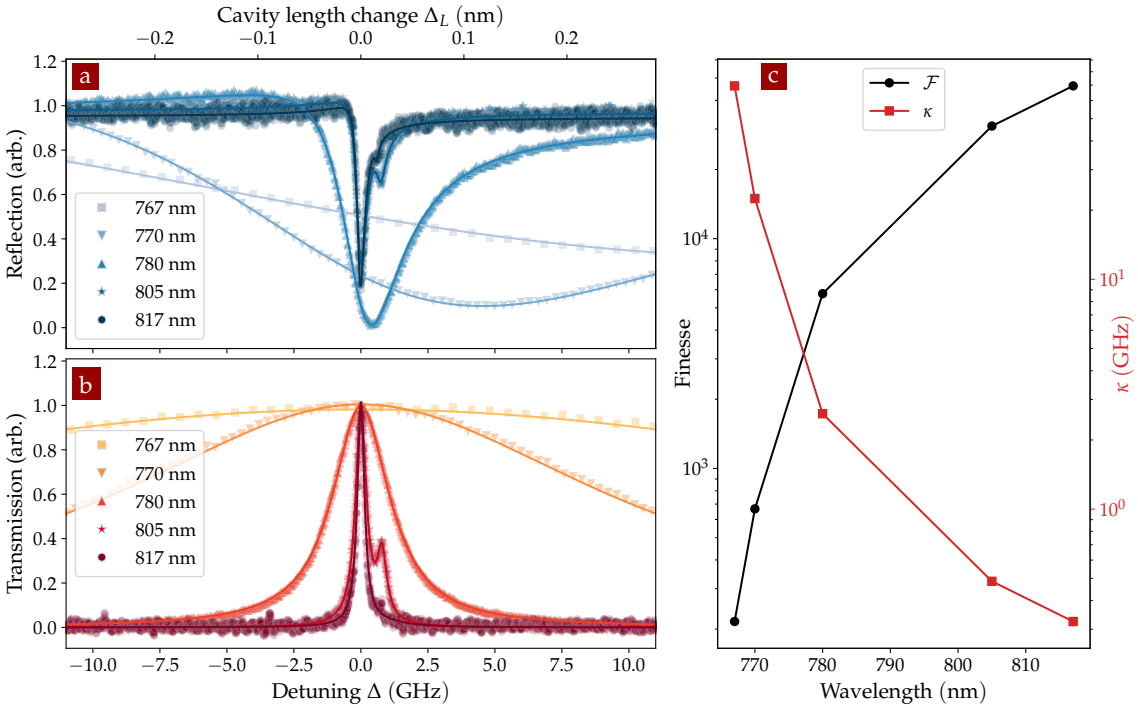

FIGURE 4.23 – Cavity properties as a function of the pump wavelength: (a) reflection, (b) trasmission, (c) finesse and linewidth.

the minimum of the reflection curve. In practice we will always employ the transmission signals to lock the cavity precisely on resonance. For more details on this effect see [79].

The analysis has been repeated varying the wavelength of the pump light, the results begin shown in fig. 4.23. The finesse obtained rapidly varies with the laser wavelength, as expected from the coating specifications (see section 4.5.2).

For cavities with finesse larger than 20000, we can observe the splitting of each mode into two modes. This is a consequence of the slight elliptic shape of the mirrors (approx 10%) and of possible birefringence in the coatings. Both effects leads to the apparition of a polarization dependence in the pumping efficiency, as shown in fig. 4.24. To further investigate those effects, it would be necessary to rotate the fibers to align their principal curvatures orientations. This was too delicate to realize experimentally, but we note that in practice we will only operate with lower finesses, where the polarisation and birefringence effects are not resolved. Instead the nanowire itself will induce a strong birefringence in the system.

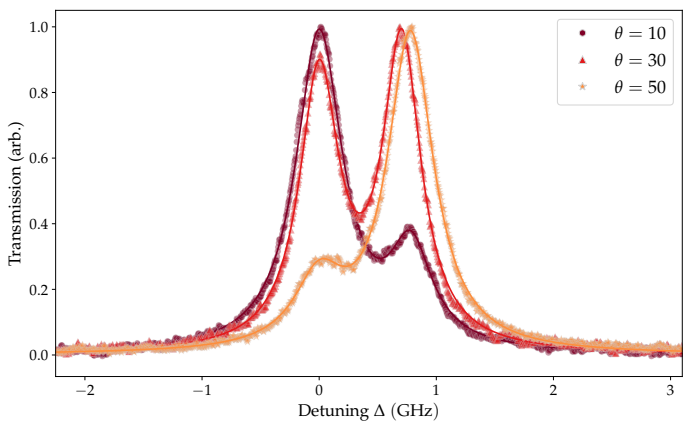

FIGURE 4.24 – Split of the TM_{00} mode due to birefringence effect and its dependence on the light polarization.

4.6.2 Optomechanical interaction

We now investigate how the insertion of a nanowire inside the optical mode affects the cavity properties. To do so, we will move the nanowire extremity in the optical cavity mode while simultaneously dithering the cavity length across an optical resonance. We will analyse the dependence of the frequency shifts on the NW position, as well as its impact on the cavity losses and on the transmission, reflection and scatter signals.

TRANSVERSE X SCAN This measurement principle is schematized in fig. 4.25e: we dither the cavity length while scanning the nanowire transversally with respect to the optical axis. We simultaneously record the transmission signal. The results presented here are obtained with the cavity Cav2 and the nanowire NW2. The cavity is set to a length $L \sim 12\,\mu m$ and is pumped with a 767 nm laser light (which corresponds to a finesse ~ 390 and the cavity length supports approx 30 optical nodes along its optical axis). The piezo dither the cavity length of $\sim 20\,nm$ around its resonant position, while the nanowire is scanned across the optical mode, at an axial Z position corresponding to an antinode of the optical standing wave (see below). The light polarization is orthogonal to the nanowire axis, oriented along the X axis. For small nanowires, this polarisation is the least interacting one. The maps is obtained by scanning rapidly the cavity length (a full vertical line is recorded in fig. 4.25d), while slowly scanning the nanowire laterally. This allows not to suffer from mechanical vibrations which can blur the transmission signals if taken too slowly. In fig. 4.25a we observe that the nanowire shifts the cavity length for which the resonant condition is met by a quantity $\Delta L = -12\,nm$, corresponding to an equivalent optical frequency shift $\Delta\omega_0 = -\omega_0 \Delta L / L = 2\pi \times 400\,GHz$. When we insert

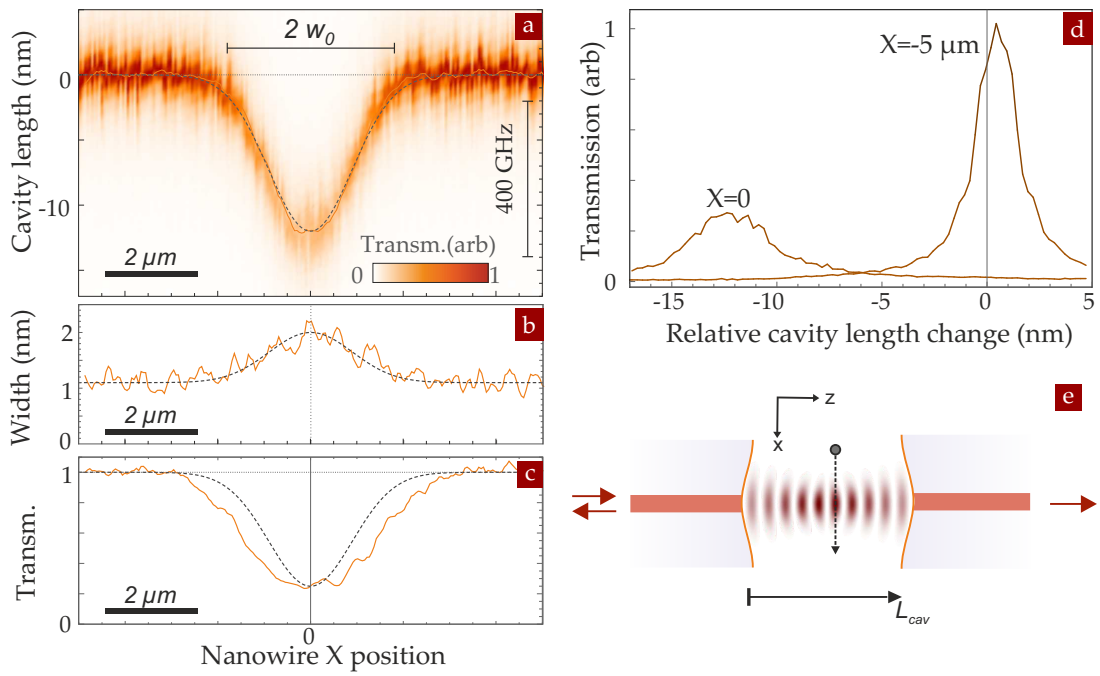

FIGURE 4.25 – Dependence of the optical frequency shift on the NW position in the transverse plane: (a) shift of the cavity length for which the resonant condition is met, monitored through the transmission, when scanning the NW across the optical mode while simultaneously dithering the cavity length. (b) dependence of the cavity linewidth on the NW position on the optical mode. (c) dependence of the intensity of the transmission signal on the NW position on the optical mode. (d) transmission signals for two different position of the NW in the optical mode, fully entered ($x = 0$) and fully out ($x = -5\,\mu m$). (e) scheme of the measurement principle.

the nanowire in the microcavity, this increases the optical path length, leading to a reduction of the cavity length required to maintain the system at resonance with the nanowire. We note that this value is an appreciable fraction of the nanowire diameter (130 nm here), despite the fact that the illuminated area only represents a small fraction of the optical mode transverse dimension (1.8 µm waist). Since the nanowire diameter is much smaller than the optical wavelength and thus the optical waist (1.8 µm), it is possible to explore and resolve the Gaussian shape of the TM_{00} mode.

We can fit each vertical line of the map using eq. (4.6.4a) (see fig. 4.25d), so that we get the resonant length, the linewidth and transmission amplitude for each nanowire position along X. The resonant length presents a scan to scan variability, which is due to the vibrations in the setup, with a rms value of 0.6 nm typically, which is smaller but comparable to the microcavity linewidth. The resulting variations of the resonant cavity length change are reported in fig. 4.25c, and can now be adjusted by a Gaussian function: $\Delta L \exp(-2x^2/w_0^2)$, with a maximum amplide of $\Delta L = -12$ nm and a waist of $w_0 = 1.8$ µm. This value is in good agreement with the expected waist for a cavity length of 12 µm and radii of curvature of 29 µm: $w_0 = \sqrt{\frac{\lambda}{2\pi}}(L(2R-L))^{1/4} = 1.7$ µm.

The modified cavity linewidth (fig. 4.25b) is also well adjusted by a Gaussian function: $\kappa_0 + \Delta\kappa \exp(-2x^2/w_0^2)$ using the same optical waist, a starting value of $\kappa_0 = 32$ GHz and a variation of $\Delta\kappa = 32$ GHz.

The peak transmission level presents a minimum when the nanowire is in the middle of the optical axis, but the reduction observed decreases more rapidly than the Gaussian profile. This observation comes from the fact that the transmission of the nanowire in the middle does not linearly depend on the nanowire induced loss rate, but is also affected by its impact on the optical finesse, which reduces the intracavity power and thus the transmitted one.

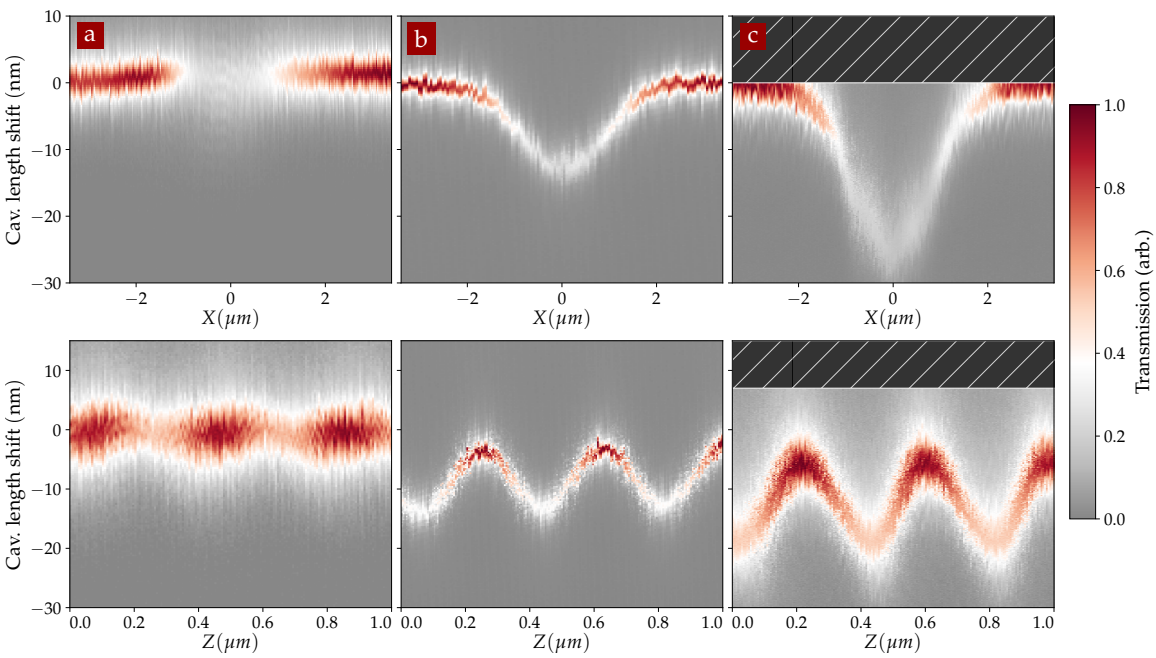

FIGURE 4.26 – Resonance cavity shit in the transverse and axial directions for three different NW diameters: (a) NW1 250 nm ($\lambda = 765$ nm), (b) NW2 130 nm ($\lambda = 767$ nm), (c) NW3 160 nm ($\lambda = 766$ nm).

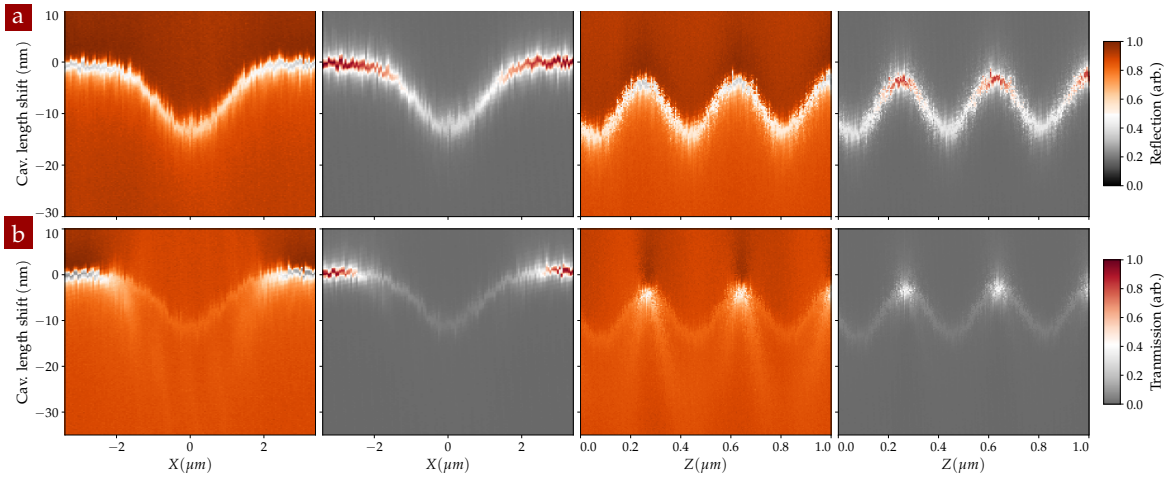

FIGURE 4.27 – Resonant cavity shift in the transverse and axial direction for the orthogonal (a) and parallel (b) polarizations (NW2, $\lambda = 767\,\text{nm}$).

We experimentally tested several NW samples to investigate how their diameter affects the frequency shift we observed. In fig. 4.26 one can appreciate the maximum shifts measured with three NWs with different dimensions (NW1, NW2, NW3). In particular, the highest interaction was observed for diameters around 160 nm, producing a cavity length shift $\Delta L = -25\,\text{nm}$ corresponding to a frequency shift $\Delta\omega_0 = 2\pi \times 800\,\text{GHz}$ for the 12 µm length microcavity employed.

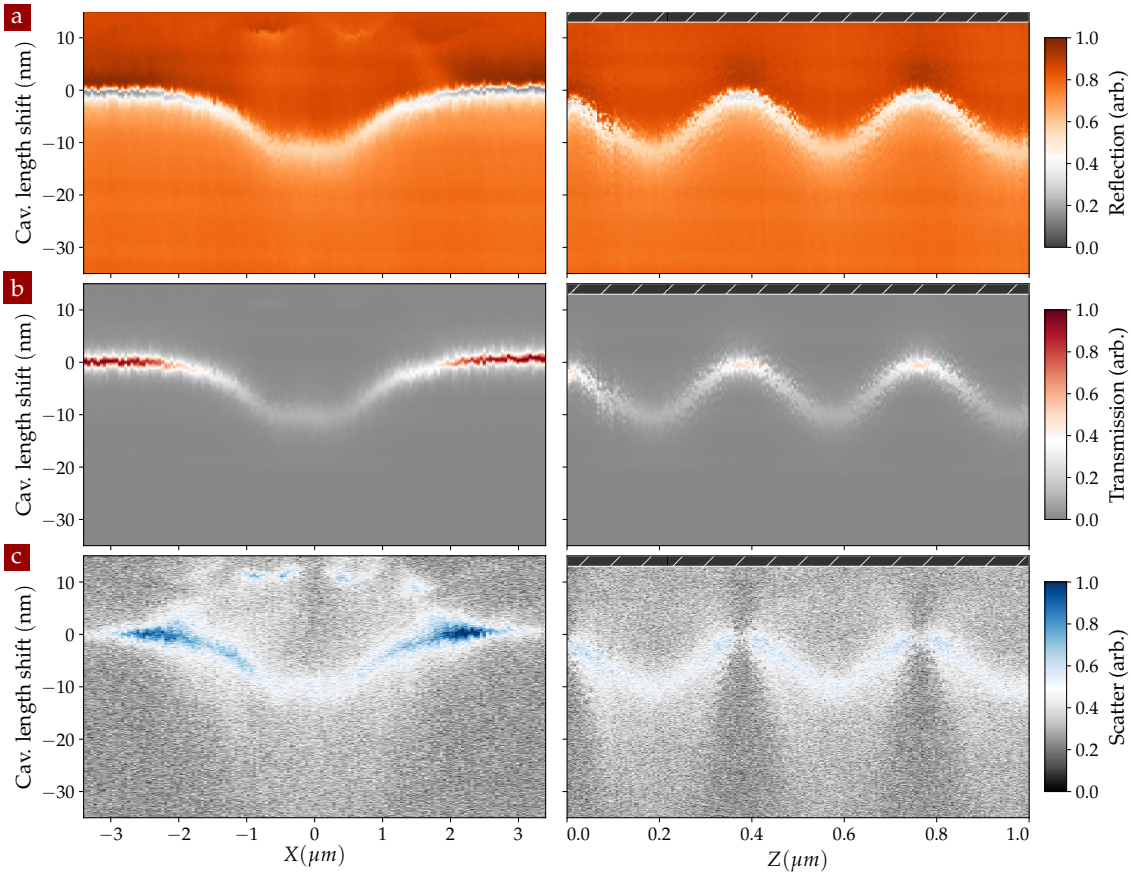

FIGURE 4.28 – Resonant cavity shift in the transverse and axial direction measured through three different channels: (a) reflection, (b) transmission and (c) scatter.

The light polarization is known to have a large impact on the nanowire interaction strength as described in section 3.1.3. For the small-diameter ones employed, the nanowire essentially interacts as a dipole, with a maximum interaction when the light is polarized along its axis. Switching from a perpendicular to a parallel polarization, with respect to the nanowire axis, clearly exhibits a much stronger perturbation of the optical field. As visible in fig. 4.27, the interaction becomes so strong that most of the light is scattered out of the cavity and not enough signal is left behind to be used. Nonetheless, this remains a powerful tool that can be used to tune the interaction strength.

It is important to notice that we normally use the transmission signal for this analysis. Anyway it can be interesting to record simultaneously the reflection and scatter signals (see fig. 4.28). Although the former tends to be more easily altered by the interference effect described in section 4.6.1, it presents the interest of more easily revealing the presence of other transverse modes, which can participate to the cavity-nanowire interaction. The scatter signal is interesting because it provides a signal that is directly proportional to the amount of cavity light scattered out of the cavity mode, it can however be too weak in certain scenarios.

AXIAL SCAN The previous measurements were performed while having the nanowire cross the optical mode through an antinode. Now instead, we place the nanowire at the center of the optical waist and scan it along the cavity axis (see scheme in fig. 4.29e). As in the previous case, we can analyze the parametric frequency shift as a function of the nanowire position (fig. 4.29a), the change in the cavity linewidth (fig. 4.29b) and that of the maximum of the transmission (fig. 4.29c). Well visible is the $\lambda/2$ periodicity

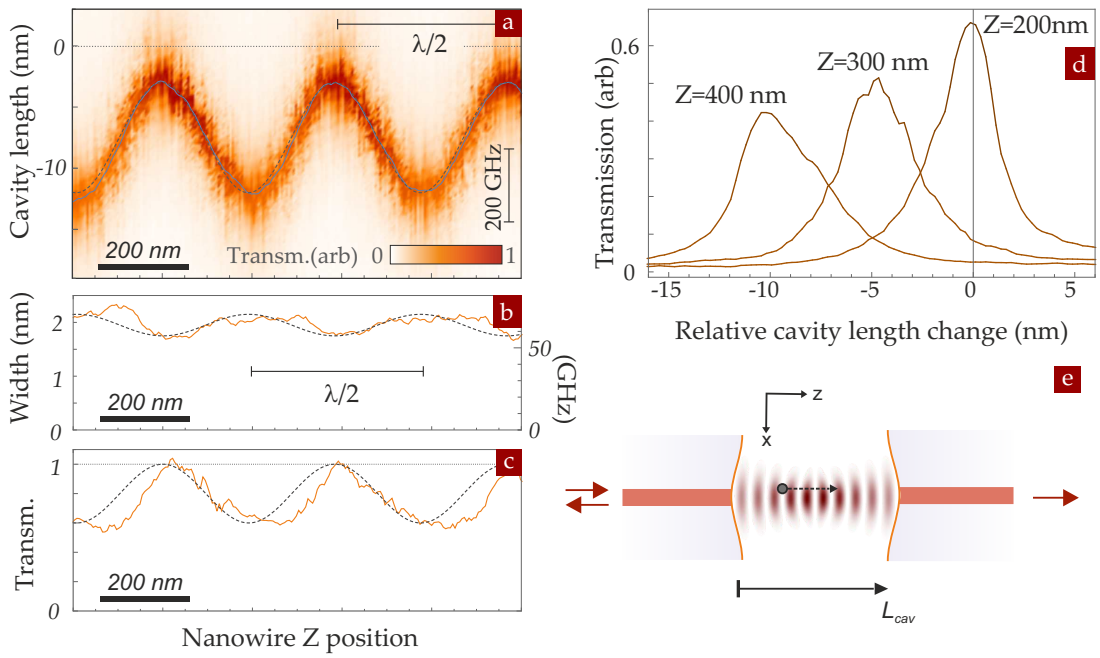

FIGURE 4.29 – Dependence of the optical frequency shift on the NW position in the axial plane: (a) shift of the cavity length for which the resonant condition is met, monitored through the transmission, when scanning the NW along the optical axis while simultaneously dithering the cavity length. (b) dependence of the cavity linewidth on the NW position on the optical mode. (c) dependence of the intensity of the transmission signal on the NW position on the optical mode. (d) transmission signals for three different position of the NW in the optical mode, on a node ($z = 200$ nm), on an antinode ($z = 400$ nm) and in between ($z = 300$ nm). (e) scheme of the measurement principle.

of the standing wave of the cavity mode, as well as the fact that we now obtain the same frequency shift magnitude but over a much smaller distance, indicating a stronger coupling in the Z direction compared to the X one. In the vicinity of a node, the optical mode is not much affected by the presence of the NW, which is reasonable since there is no light to interact with at that position. On the contrary one observes a maximum shift (and minimum intensity) on the antinode (cfr. fig. 4.29d).

Like before, a change in the nanowire diameter or in the light polarization can have a huge impact on the measured signal. Some examples are shown in figs. 4.26 and 4.27.

When reporting the maximum transmission as a function of the nanowire position, one can notice that there is an asymmetry between the positive and negative slopes. As underlined in the model, those branches correspond to a situation where there is more light stored in the left or right sub-cavities. An asymmetry in the effective reflection coefficients of the microcavity mirrors can also be responsible for such an asymmetry.

VERTICAL SCAN In general, we only insert part of the nanowire extremity in the cavity mode volume. Since the insertion point always remains very close to the nanowire extremity, this does not change significantly the lever effect of the force field on the nanowire dynamics. However the interaction strength and the force can be largely tuned by controlling the insertion of the nanowire in the optical waist. This effect can be investigated by fixing the nanowire in the center of the optical waist (in X) and on an antinode (in Z), while scaninng the vertical position of its extremity.

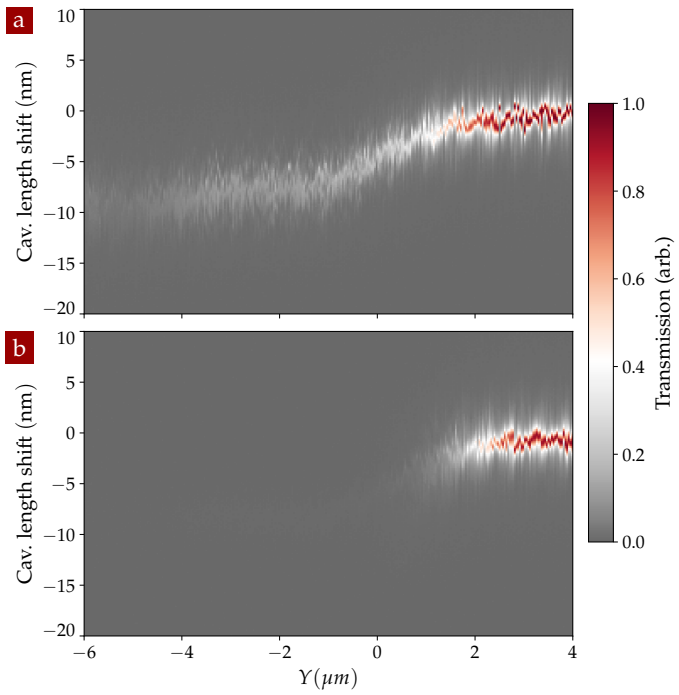

FIGURE 4.30 – Resonant cavity shift in the vertical plane, respectively for (a) orthogonal and (b) parallel polarized pump light.

When the nanowire is progressively inserted in the cavity mode, one observes a progressive decrease of the resonant cavity length, which occurs on typically 22 µm length, in agreement with the optical waist measured through the lateral X scans. Once the nanowire is fully inserted, the parametric shift is evolving less rapidly, the residual shift can sometime be explained by a slight angle between the nanowire plane and the normal to the optical axis. This type of measurements also permits to identify optical cavity modes with a vertical substructure, and possible non-homogeneities in the nanowire diameter, which can result in positions generating a larger optomechanical interaction. As observed in fig. 4.30, the impact of light polarisation is also very visible in those plots for the nanowire employed.

4.6.3 The ultrastrong coupling regime

The above measurements thus allow to investigate how the microcavity resonance frequency $\omega_0(\mathbf{r})$ depends on the nanowire extremity position $\mathbf{r}$. They can be employed to quantify the parametric coupling strength, which corresponds to the derivative of the optical frequency with respect to the displacement of the oscillator. Since the nanowire can identically move along both transverse directions (X and Z), we introduce a vectorial coupling strength $\boldsymbol{G} \equiv \boldsymbol{\nabla}\omega_0|_{\mathbf{r}_0}$, evaluated at the NW rest position $\mathbf{r}_0$. From the above measurements, we can compute the local derivatives, whose maximum values amount to $G_x/2\pi \approx 0.3\,\mathrm{GHz/nm}$ for the transverse X scan and $G_z/2\pi \approx 3\,\mathrm{GHz/nm}$ for the axial scan.

To better appreciate the magnitude of these values, it is useful to compute the single-photon coupling $\mathbf{g}_0 \equiv \mathbf{G}\delta r_{\mathrm{zpf}}$, where we have employed an isotropic zero point fluctuation for the nanowire (assuming a quasi frequency degenerated nanowire) $\delta r_{\mathrm{zpf}} = \sqrt{hbar/(2M\Omega_{\mathrm{m}})}$. For this sample we have $\delta r_{\mathrm{zpf}} \sim 0.47\,\mathrm{pm}$, leading to a maximum single-photon coupling strengths of $g_0^z/2\pi = 1.4\,\mathrm{MHz}$ along the Z axis and $g_0^x/2\pi = 140\,\mathrm{kHz}$ for the other direction. Larger values were measured for the sample NW3, for which we obtain up to $g_0^z/2\pi = 2.6\,\mathrm{MHz}$ (see fig. 4.26c). This values are rather large compared to other optomechical systems, for which values in the order of or close to 1 MHz are normally reached only by cold atoms [145, 31], photonic crystals [39, 66, 116, 174], microresonators [62] and recently some electromechanical systems (Bachtold group, oral communication).

It is very interesting then, to compare the value of the single photon coupling to that of the mechanical frequency. For the two samples analyzed here, we obtain respectively $g_0^z/\Omega_{\mathrm{m}} = 25$ and $g_0^z/\Omega_{\mathrm{m}} = 96$. As we saw in section 1.2.2, this ratio means that we fall largely in the ultrastrong coupling regime. In other terms, the interaction due to a single intracavity photon is strong enough to displace the oscillator by more than its zero-point-fluctuations: $\delta x^{(1)} = g_0/\Omega_{\mathrm{m}}\delta r_{\mathrm{zpf}} > \delta r_{\mathrm{zpf}}$. We will return on this aspect in section 5.3.3, where we will show how combining this results with the ones obtained at low temperature opens the doors to the observation of optomechanical effects at the single photon level.

The above determination of the parametric optomechanical coupling strength allows to estimate the broadening of the cavity linewidth due to thermal noise (cfr. [116]). The cavity linewidth is always very large compared to the mechanical frequencies so we can consider that the electromagnetic field instantaneously follows the perturbation induced by the nanowire motion. The thermal fluctuations of NW2 (see table 4.2) are spreading over a rms value of the order of $\Delta r^{\mathrm{th}} \approx 7\,\mathrm{nm}$ at room temperature, which causes a rms broadening of the cavity linewidth up to a maximum value of $G_z\Delta r^{\mathrm{th}} \approx 2\pi \times 21\,\mathrm{GHz}$ (or equivalently to 0.6 nm rms cavity length change). This magnitude is smaller but comparable to the measured cavity linewidth (see figs. 4.25 and 4.29), but it remains much smaller than the observed parametric frequency shifts.

4.6.4 Coupling to higher-order optical modes

We conclude this chapter by presenting a collection of interaction images obtained with high order modes. Up to now we only focused our attention on the fundamental transverse modes of the optical cavity, TM_{00}. However, during the alignment process we are free to maximize the signal of any other transverse mode, as well as to change the

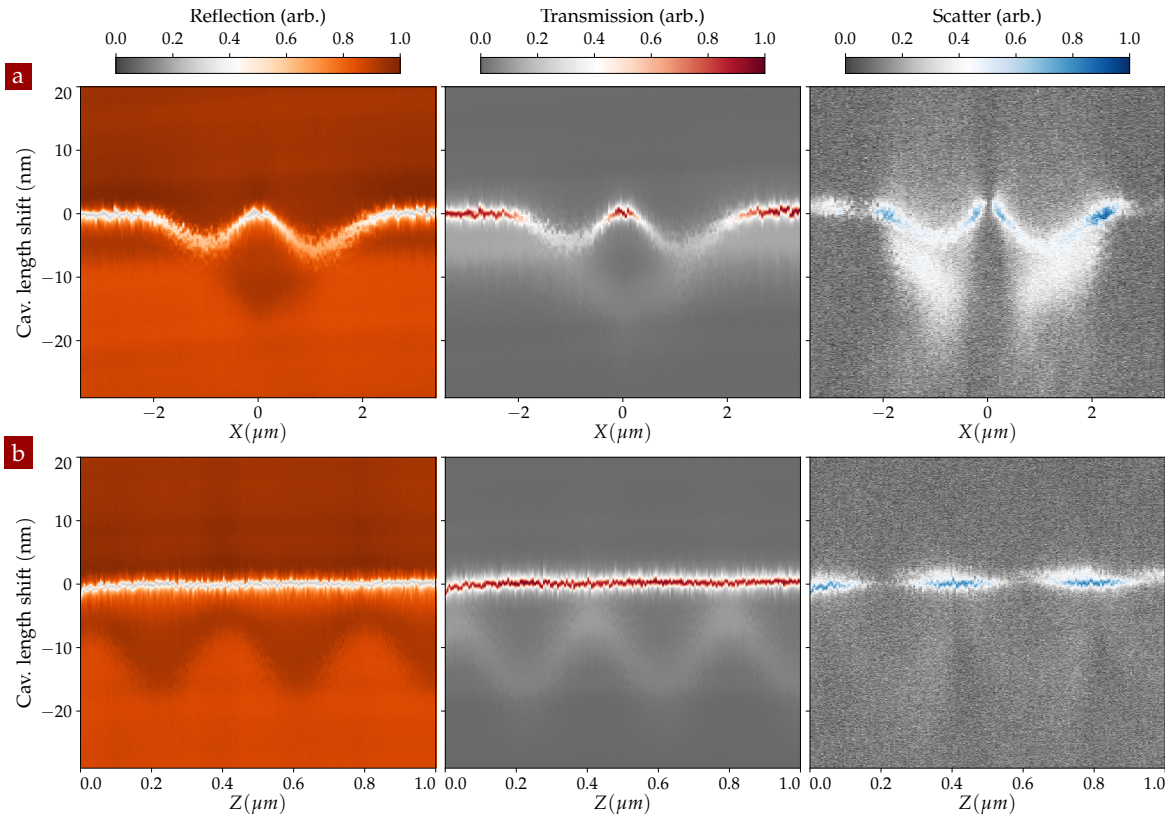

FIGURE 4.31 – Resonant cavity shift of the transverse mode TM_{12}, measured along the transverse (a) and the axial (b) plane. The two lobes can be clearly distinguished along X, while the signal is almost unperturbed along Z. Much less intense but clearly visible is also the frequency shift of the (almost superimposed) fundamental mode TM_{00}. This is also the probable cause of the alternating pattern along Z of the scatter signal.

cavity length in order to change the frequency splitting of the different transverse modes, in order to investigate how the nanowire can cross couple them.

Concerning the first case, we performed the same previous measurements for the TM_{12} mode, as shown in fig. 4.31, where one can identify the characteristic two lateral lobes, and the absence of interaction along the optical axis. Regarding the second situation, we could easily observe complex cross-coupling interaction between two or more transverse modes (see fig. 4.32). We didn't further investigate this aspect in the present work, but it could be interesting to explore quadratic or cubic interaction mechanisms in the future.

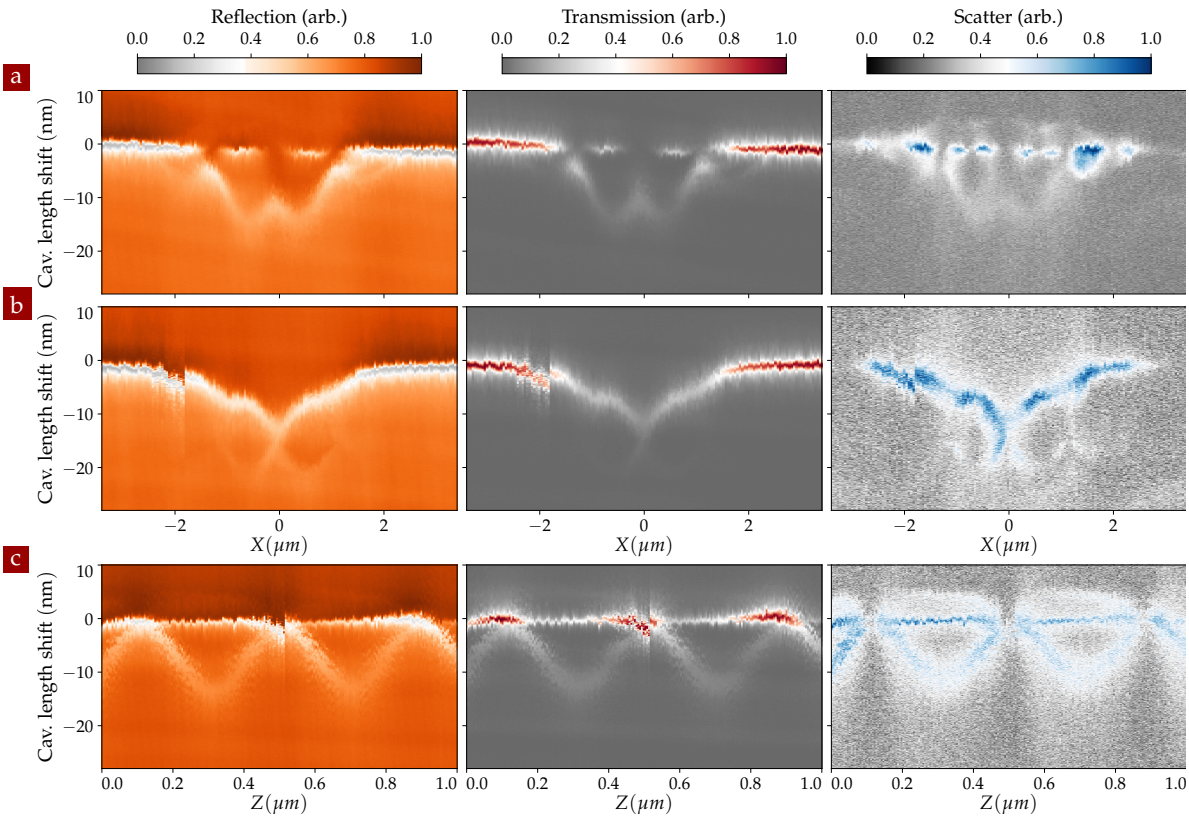

FIGURE 4.32 – Measuring the resonant cavity shift when several transverse modes are pumped at the same time, gives rise to complex cross-coupling interaction, whose structure is extremely dependent on the cavity length (and so to the distance among the mode) as well as to the number of the modes involved. Figure (b) and (c) show a cross-coupling between the fundamental mode TM_{00} and a transverse mode TM_{1x}, while in figure (a) we can also distinguish the presence of a third mode, possibly TM_{2x} or TM_{3x}.

5 OPTICAL MODE IMAGING AND FORCE SENSING IN A NIM SYSTEM

This chapter shows how the nanowire can be used to realize a three dimensional imaging of the optomechanical interaction by measuring its impact on the intracavity field. Furthermore, we also investigate the reverse optomechanical interaction and measure and map the force experienced by the nanowire within the cavity mode. By using a pump-probe technique, a vectorial measurement of the optomechanical interaction is established.

CONTENTS

5.1 Cavity locking **150**
Error signal 150
PID 151
Red-Pitaya FPGA 152
5.2 Intracavity field characterization **153**
5.2.1 Cavity mode imaging 153
5.2.2 Scattered light and cavity losses 154
5.2.3 Correction maps 158
5.2.4 Imaging higher-order optical modes 160
5.3 Nano-optomechanical investigation of the intracavity force **162**
5.3.1 Independent optical readout and nanowires dynamics 162
Thermal noise 163
Response measurement 164
5.3.2 Intracavity force in a NIM 166
1*D* optical axial force 166
Multi-frequency response measurement 166
2*D* force field map 170
5.3.3 Brownian motion 2D map 171

5.1 CAVITY LOCKING

In order to complete the study of the optomechanical interaction in a NIM as a function of the NW position, a locking is needed to maintain the optical cavity at resonance. Using a close-loop feedback mechanism permits to compensate for the environmental noise as well as for the OM induced frequency shift. In practice, the optical frequency shifts observed above can amount to more than 800 GHz, which is far beyond the mode-hop free tuning range of any existing laser (30 GHz for the laser employed in this work). We thus had no choice but locking the cavity length on the laser wavelength, using the two axial piezo elements positioned on the cavity.

ERROR SIGNAL A common technique employed in optical cavity experiments is the Pound-Drever-Hall frequency stabilization [23]. The generation of the error signal, tracking the difference between the cavity and the laser frequency, starts by phase-modulating the light sent to the cavity (for example by mean of an Electro-Optical-Modulator [EOM]) at a frequency ω_{mod}. The resulting incident beam presents a carrier at a frequency ω_{L} plus two sidebands at frequencies $\omega_{\text{L}} \pm \omega_{\text{mod}}$, which serve as phase references to produce the error signal. The latter is obtained by demodulating the reflected signal at the modulation frequency using a mixer and a low pass filter.

We applied this technique at first, when operating in high finesse conditions at wavelengths around 810 - 820 nm. We had to face some technical problems with the fiber EOM employed which were producing an unwanted residual amplitude modulation, which could not be permanently suppressed due to unwanted temperature drifts in the modulator. Another limitation was the presence of the standing wave in the reflection signal, also impacted by the dynamical phase modulation, which was not stable over time, leading to a constant deformation of the error signal.

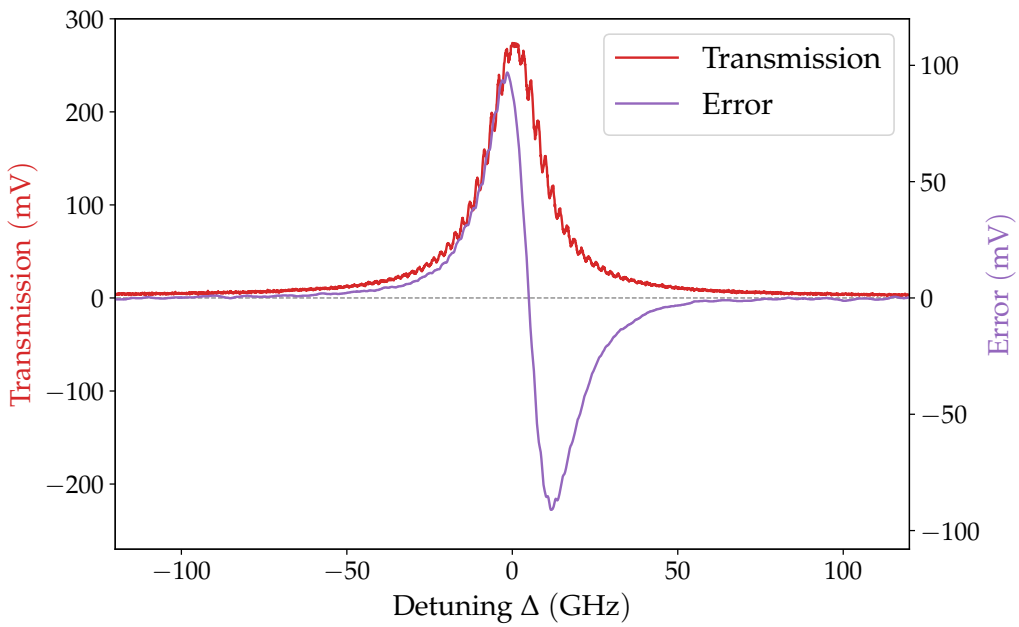

FIGURE 5.1 – Typical experimental error signal that we measure in our system, obtained using the transmission signal and a modulation frequency $\omega_{\text{mod}} = 2\pi \times 253\,\text{kHz}$. The injected power is of 5 µW, the optical finesse of ~ 760. The error signal is produced with a demodulation bandwidth of 20 kHz, which is beyond the mechanical frequencies and thus contains the dynamical perturbations of the cavity state by the oscillator.

Most of the subsequent measurements were realized with a lower finesse, while the transmitted signal was found cleaner due to the absence of the residual standing wave effects seen in reflection. We thus decided to generate our error signal using the transmission channel and to modulate the cavity length instead of the laser frequency using the fast piezo element. This approach has several advantages: the transmission signal is filtered by the cavity and does not have any asymmetry; a low-frequency modulation is easy to generate with the fast-piezo in our setup for frequency up to 1 MHz (all the measures shown in the following were obtained with a modulation frequency of 253 kHz); the slow-piezo used to regulate the cavity length allows for broad correction span (up to 2.5 FSR) and can easily compensate for cavity optical frequency shifts of several hundreds of GHz, which correspond to only tenths of nm in cavity length change (around 10 µm length). Figure 5.1 shows a typical error signal generated in our setup, produced by the RedPitaya card (see below) using a demodulation bandwidth of 20 kHz (we have data using 50 kHz), sufficient to keep track of the mechanically induced cavity perturbations.

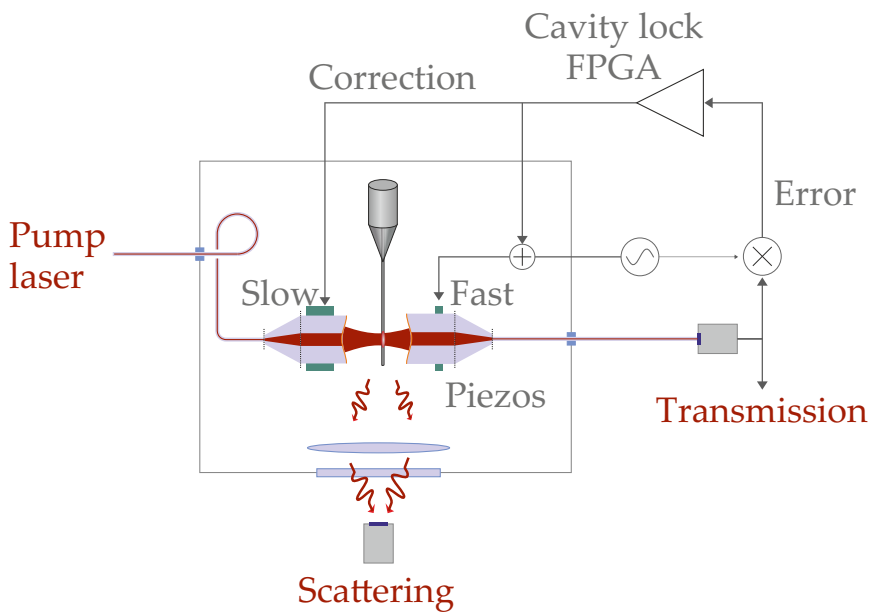

FIGURE 5.2 – Scheme of the cavity locking system.

PID The error signal is then used in a feedback loop to lock the cavity at resonance. It is fed to a proportional-integral-derivative (PID) module which is employed to generate the correction signal sent to the piezos to keep the system at resonance [20]. In our case it was not necessary to make use of the derivative part of the control and we only employed the P and I modules. A first channel was used to control the slow piezo, compensating for noise, thermal drift and frequency shifts in the range DC - 20 Hz. A second loop was used to control the fast piezo and serve to correct acoustic noise in the 20 Hz - 2 kHz range. The 20 Hz frequency was set by a high pass filtering module employed before the PID module, allowing to avoid cross talks in the two loops. Instead the high frequency cutoff was adapted depending on the NW sample used to a frequency significantly lower than Ω_m, in order not to compensate for the optomechanical perturbations induced by the oscillator on the cavity state. This has the additional advantage of keeping the mechanical information encoded in the error signal, resulting in an additional measurement channel.

RED-PITAYA FPGA In our implementation both the error signal and the PIs where made and controlled by means of a Red-Pitaya 14 bits FPGA card and the PyRPL software. The latter is an open-source software developed in the Optomechanics and Quantum Measurement Group at the LKB in Paris, during the PhD of L. Neuhaus, specifically designed for controlling the FPGA board. It offers multiple functionalities such as oscilloscope, network and spectrum analyzers, lock-in amplifier, IQ demodulator, PID etc. Analog input and output can be sampled up to a frequency of 125 MHz with a resolution of 14 bits. The software allows to control the digital-signal-processing modules implemented on the FPGA: this implies not only fast operation, but also the ability to implement multiples and cascaded tasks in a single compact element.

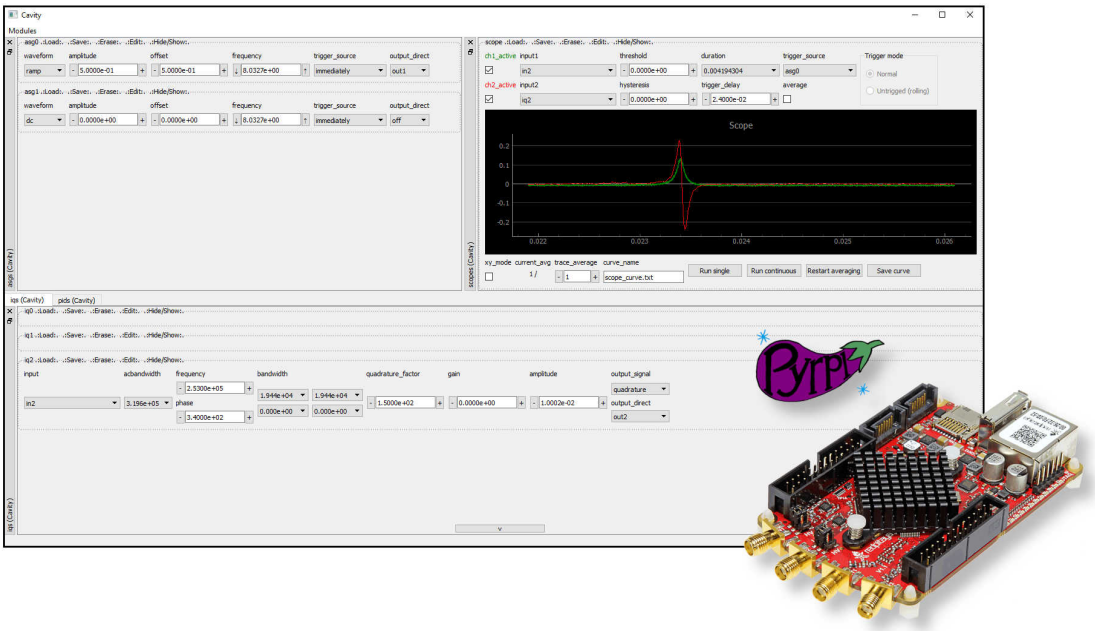

FIGURE 5.3 – Interface of the PyRPL software used to control the Red-Pitaya FPGA card (inset).

In our specific case, we made use of an IQ module (modulation/demodulation module) to drive the fast-piezo at the frequency $\omega_{\text{mod}} = 253\,\text{kHz}$ while demodulating the transmission signal to produce the error signal. This was then internally used by two of the PIDs of the card to generate the correction signal sent back to the two piezos. A slow feedback loop was employed on the slow piezo, with a bandwidth around 20 - 100 Hz, while a faster feedback loop was employed on the fast piezo (in addition to the 253 kHz modulation) operating up to a few kHz. This value remains smaller than the usual mechanical frequencies employed, which ensures that the lock does not perturb the OM signals which can be recorded on the bare error signal. In practice, the correction of the lock is added to the scan voltage produced by the NI card, and recorded on a separate input channel of the card. This permits to record the cavity length changes induced by the nanowire, on top of the intrinsic cavity length fluctuations and drifts. Figure 5.2 shows a scheme of the cavity locking mechanism we employed, while fig. 5.3 present the GUI of the PyRPL software we normally use to apply this control.

5.2 INTRACAVITY FIELD CHARACTERIZATION

Once a stable locking set-point has been achieved, the sub-wavelength sized NW can be exploited to map the intracavity modes structure. To do so, we scan the nanowire position within the optical mode volume and record the different signals to gather information on the dispersive and dissipative coupling strengths. This imaging technique also provides quantitative informations on the cavity mode spatial structures which can hardly be investigated otherwise [21, 127]. If not stated otherwise, all the results which follow have been measured using the cavity Cav2 and the nanowire NW2.

Similarly to the unlocked case, while performing the mapping of an optical mode, we can simultaneously record the transmitted, the reflected and the scattered signals, as well as the correction signal. Combining their information we can more precisely analyse the optical mode and the OM interaction. Of particular interest is the comparison among several maps taken for the nanowire inserted more or less deeply in the cavity mode, that we will discuss in the following. Particular care must then be taken in the analysis of the polarization effects as well as in the cross-coupling with other modes, to properly describe both the dispersive and the dissipative coupling in the different cases.

5.2.1 Cavity mode imaging

Exploring the intracavity field structure can be envisioned through multiple imaging channels: scanning the nanowire in the XZ plane we can reconstruct the transverse (horizontal) section of the mode for a given insertion depth along the Y axis; scanning in the YZ plane (vertical) we can image how the interaction changes at different heights; scanning in the XY plane we obtain a cross-section image of the mode.

Figure 5.4 depicts a typical map obtained in the XZ plane. The nanowire is scanned over a 500×500 grid, spanning over $7 \times 1\,\mu$m, with an acquisition time of 2 ms per point for a total duration of $\sim$ 8 min (1 s per line). The lock is efficient enough to maintain the system at resonance, despite the strong variation observed in the transmission signal (from which the error signal is processed). It is possible to recognize the standing wave structure of the TM_{00} mode with the usual $\lambda/2$ axial periodicity. Similarly to fig. 4.29, we clearly observe that when the nanowire crosses a node the transmission signal is almost unperturbed, while the interaction is maximal (and the transmitted intensity minimal) when it is positioned on an antinode. Note that the two axes use quite different scale factors for better visualisation (the inset at the bottom shows the image with the actual 1 to 1 scale factor). A circle (ellipse) on the right hand side also outlines the dimensions of the nanowire for comparison (sample NW2, diameter 130 nm).

We note that the slight tilt visible in the image is actually very limited and it is enhanced here by the aspect ratio of the image. A similar tilt effect can be observed also in fig. 5.6 and fig. 5.9a. Among the possible explanation we could consider the small astigmatism of the mirrors and consequently that of the optical beam, as well as the Gaussian (instead of circular) shape of the mirrors. However we found that it can be significantly modified by changing the lateral position of the fibers, so that it could be explained mainly by geometrical and alignment reasons.

The axial and lateral cuts of fig. 5.4 permits to observe that the transmission signal does not fully follow the shape of the cavity mode, expected to be laterally Gaussian and axially sinusoidal (compare figs. 4.25 and 4.29). In reality, the nanowire has a larger impact on the transmission channel than expected in a first order expansion. This is due

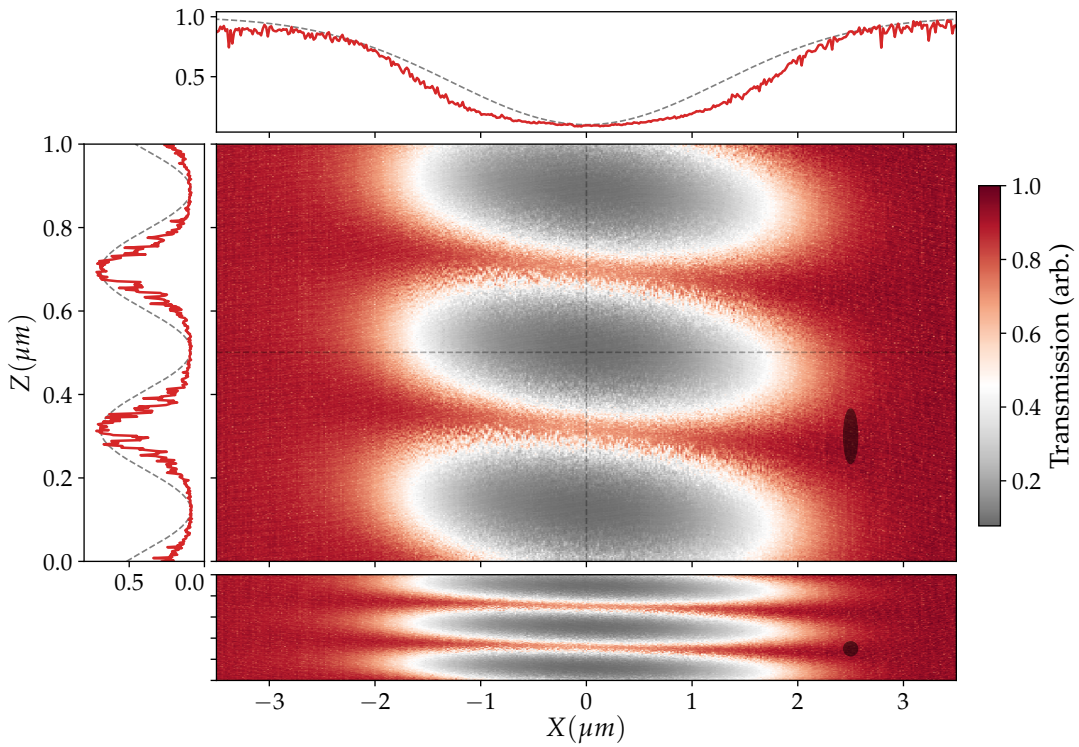

FIGURE 5.4 – Imaging of the fundamental TM_{00} mode in the horizontal XZ plane, by means of the transmission signal. A different scale factor of the two axes allows for a better visualization. The inset at the bottom shows the image with the real scale factor. The black circle on the right hand side illustrates the NW dimensions for comparison. The top and lateral inset present a lateral and an axial cut of the intensity of the transmission signal.

to the fact that the cavity finesse is also affected by it, so that the intracavity build up is also modified. We will come back on this point in the analysis of the scatter maps.

Describing fig. 4.29 we showed that the finite transverse dimension of the NW is responsible for the offset between the oscillating pattern and the actual 0-shift position. For the same reason we can see that scanning the NW around a node still has a small impact on the signal intensity. Nevertheless, we can resolve detail on the map that are smaller than the characteristic size of our probe.

In this kind of maps the remaining noise has multiple origins: first some technical noise caused by the locking mechanism (which makes use of a 253 kHz cavity length modulation) and the external environment (almost absent in the present figure); second the thermal fluctuations of the NW, which can blur the images as we discuss in section 4.6.3; last the OM interaction between the optical and the mechanical system in the proximity of the point of maximum coupling, which can bring the OM system to unstable regime at high optical powers (see below).

5.2.2 Scattered light and cavity losses

We now analyse the scattered light signals, which are recorded on the lateral photodetector after passing through a microscope objective $(20 \times /0.4NA)$. If we assume that the nanowire isotropically scatters the light, this corresponds to $\approx 10\%$ of collection efficiency, which is small but sufficient to detect on a low noise photodetector. Analysing the scattered signal is rather interesting since it plays the role of a local probe of the intracavity field.

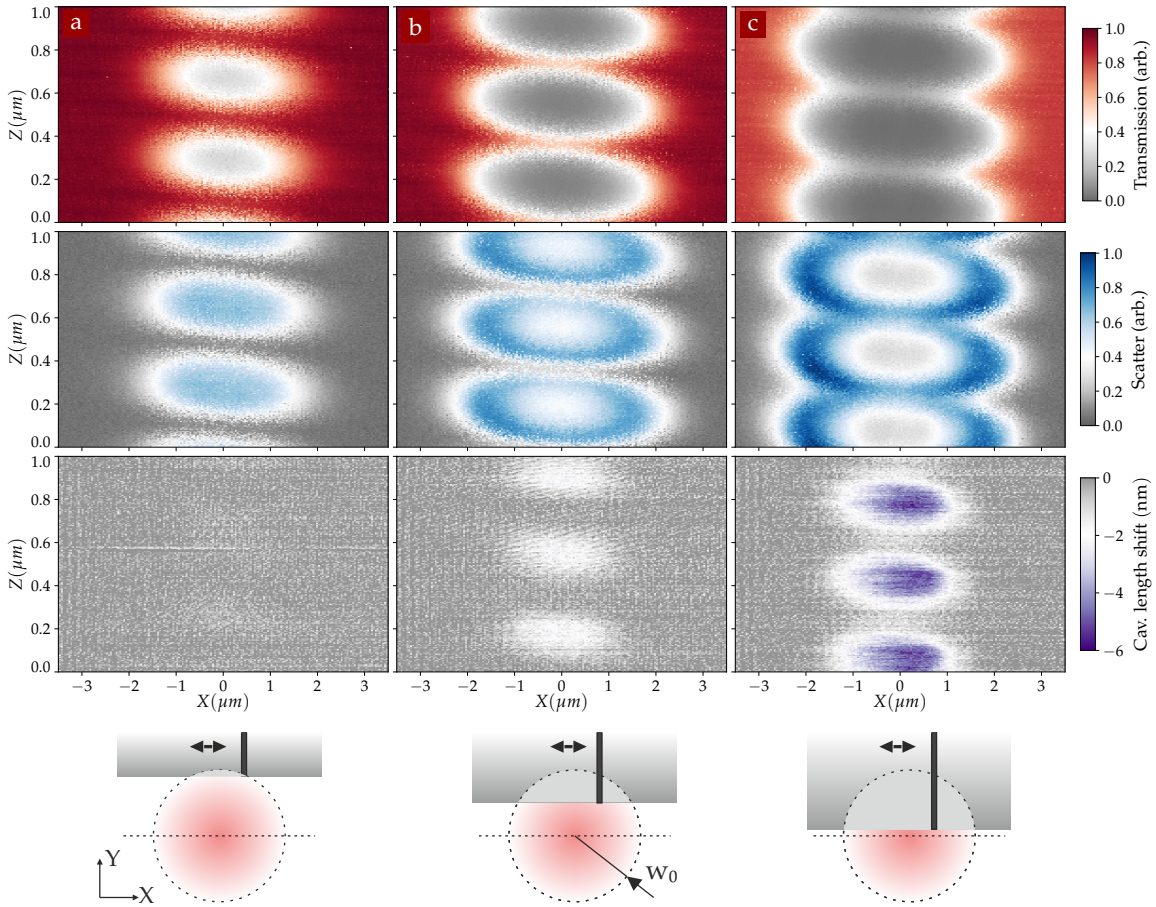

FIGURE 5.5 – Imaging of the fundamental TM_{00} mode in the horizontal XZ plane for three different insertion depth of the NW along the Y axis: (a) slightly, (bv) partially and (c) fully inserted. The measured transmission, scatter and correction signals are compared for each case. The more the NW is inserted, the more the cavity length need to be corrected by the lock, the higher the intensity of the scatter signal. When the losses induced by the NW are higher than the mirrors losses, the ring signature appears in the scatter signal.

Figure 5.5 shows the differences among three different XZ maps, taken for the NW slightly inserted (a), partially inserted (b) and fully inserted (c) in the optical mode.

The evolution of the transmission signal can be qualitatively explained:: the more the NW enters in the optical mode, the more it interacts with the cavity field, increasing the losses and reducing the transmitted field around the antinodes. As far as the correction signal is concerned a larger insertion in the cavity mode corresponds to a larger optical frequency shift, that must be compensated by a larger change in the cavity length by the locking. More surprising is the behaviour of the scatter signal, with the appearance of higher intensity rings around the antinodes.

A simple model to explain this effect consists of a three-mirror ring cavity, as the one described in the insert at page 157. The idea is that inserting the oscillator more and more in the optical mode, the interaction increases and so does the light scattered out of the mode: once the losses due to the NW become comparable to the ones of the mirrors, the overall optical mode is affected and progressively destructed as the induced losses keep increasing; the total amount of light circulating in the cavity is reduced and the same happens to the scattered light. These scatter-rings have also an additional important and practical meaning: as long as the NW stays out of a scatter ring, the cavity finesse remains unchanged at first order, progressively reducing when we move towards the center.

Similar measurements can be performed while scanning the nanowire in the YZ vertical plane, see fig. 5.6. This map is realized by scanning the NW along the optical axis (Z) and progressively inserting it in the optical mode. The intracavity field nodes (antinodes) appear as regions of large (low) transmission. The scattered light map exhibits a transition from a regime where the extremes are located on the antinodes to a regime where they split and are maximum on each side of the antinodes, which correspond to the rings observed in the horizontal plane.

The appearance of this non standard shapes in the scattered light maps can be understood with the following arguments. As long as the additional scatter rate induced by the nanowire remains small compared to the intrinsic cavity loss rate, the nanowire can be viewed as a weak perturbation and the scatter profile reproduces the cavity intensity profile. However, this reasoning is not valid any more when the nanowire induced scatter rate becomes comparable or even exceeds the intrinsic cavity rate: in that situation this affects the overall cavity finesse and thus the build-up of the intracavity field. Since the latter gets reduced, so does the overall scattered rate. This qualitatively explains the apparition of the "rings" in the horizontal maps. As such, this also means that the locations of the rings also delimit the area where the cavity finesse is only weakly affected by the nanowire. In addition, this suggests that we should aim at operating close to the nodes of the intracavity field.

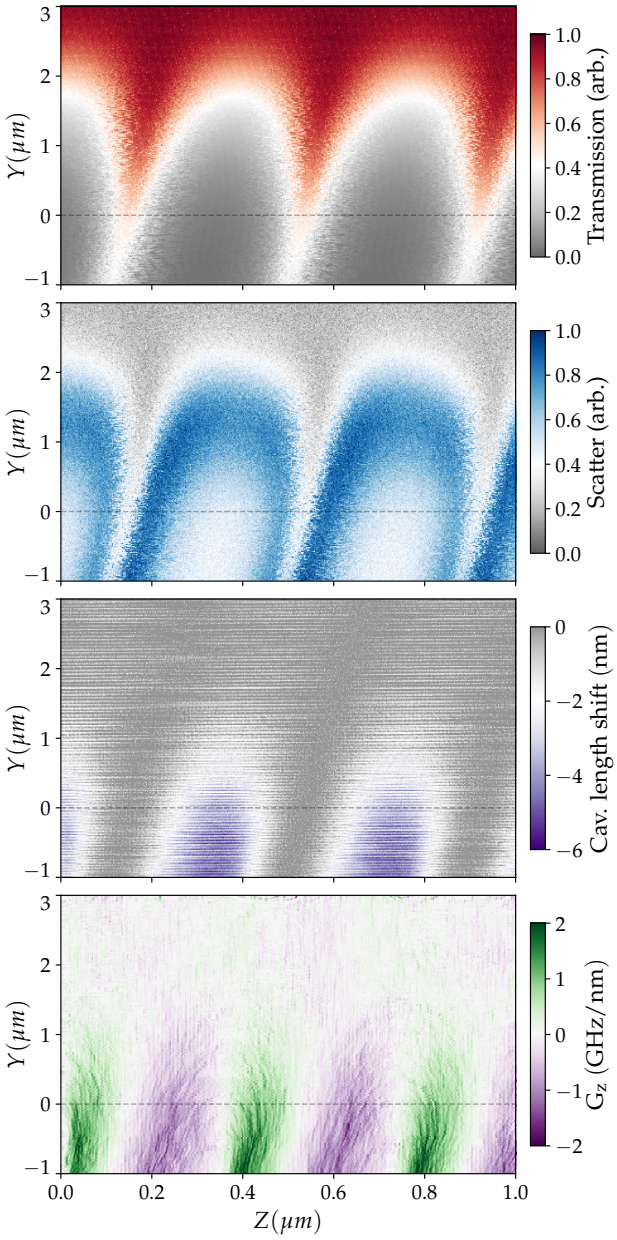

FIGURE 5.6 – Imaging of the fundamental TM_{00} mode in the vertical YZ plane, performed along the optical axis (in X). Transmission, scatter and correction signals are compared, as well as the (calculated) parametric coupling streng G_z.

Those observations can be well understood by numerical simulations as explained above and below, but can be also well formalized by a simpler model based on a 3 port Fabry-Perot ring-cavity (see the insert below).

For consistency, we also verified that the behaviour predicted with the ring-cavity model matched well the prediction of our simulations, the latter being qualitatively in good agreement with our experimental results.

RING CAVITY

A simple system that can be used to model the effect of a scatterer in the middle of a cavity is that of a tree-mirror ring cavity, as the one depicted in the figure. Here the mirror M_S will simulate the scatterer entering the cavity by varying its transmission coefficient T_D between 0 and 1. The mirrors M_A and M_B instead will represent the mirrors of the cavity with fix reflectivity R_A and R_B. $L = L_1 + L_2 + L_3$ is the total length of the cavity. For simplicity, here we will assume that no field enters through the mirror M_S and M_B (but this could be done in order to take into account for example the vacuum fluctuations).

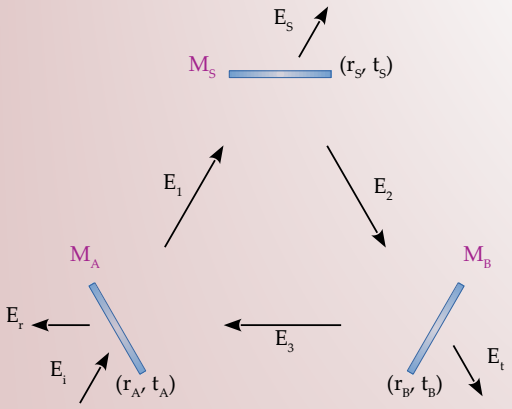

Scheme of a three-mirror ring cavity

It is convenient in this case to use the S scatter matrix formalism to describe the propagation of the field, as introduced in section 4.2.1. Choosing t_i and r_i as the transmission and reflection coefficients of each port and proceeding as before, we can compute the field reflected from the first mirror and the ones transmitted from the other two:

$$E_r = \frac{r_A - r_B r_S e^{ikL}}{1 - r_A r_B r_S e^{ikL}} E_i \qquad E_t = \frac{-t_A t_B r_S e^{ik(L_1/L_2)}}{1 - r_A r_B r_S e^{ikL}} E_i \qquad E_S = \frac{t_A t_S e^{ikL_1}}{1 - r_A r_B r_S e^{ikL}} E_i \, .$$

Defining the intensity coefficient as $R = |E_r/E_i|^2$, $T = |E_t/E_i|^2$ and $S = |E_S/E_i|^2$, we finally obtain:

$$R = \frac{R_A + R_B R_S - 2\sqrt{R_A R_B R_S}\cos(2kL)}{1 + R_A R_B R_S - 2\sqrt{R_A R_B R_S}\cos(2kL)} \qquad T = \frac{T_A T_B R_S}{1 + R_A R_B R_S - 2\sqrt{R_A R_B R_S}\cos(2kL)}$$

$$S = \frac{T_A T_S}{1 + R_A R_B R_S - 2\sqrt{R_A R_B R_S}\cos(2kL)} \, .$$

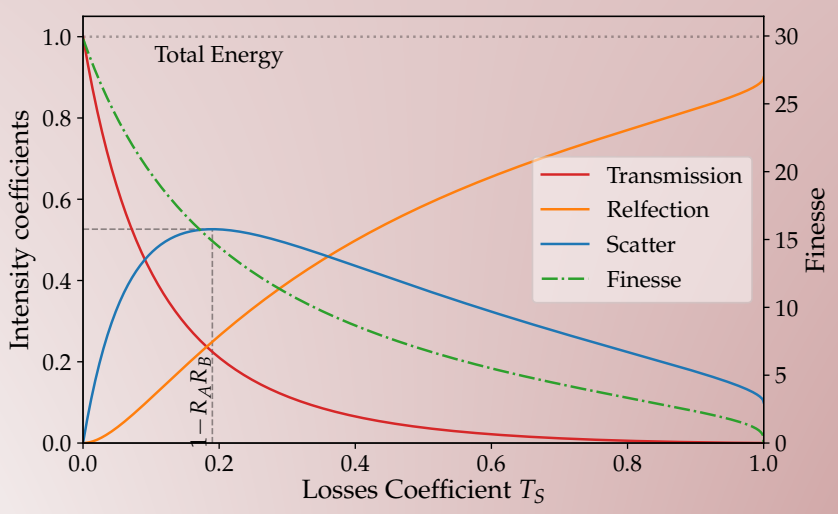

Transmission, reflection and scatter coefficient of a ring cavity at resonance, with $R_A = R_B = 0.9$.

5.2.3 Correction maps

When the cavity is locked at resonance, the parametric shifts can be deduced from the correction signal of the cavity lock, which is also recorded during the imaging sequence. The calibration realized above allows to convert voltages to equivalent cavity length change, using the conversion factor of 110 nm/V.

The slow correction signal contains long term drifts (fig. 5.7a) in the cavity-laser detuning as well as rapid fluctuations which are compensated by the lock, within the lock bandwidth. The extraction of the OM coupling thus requires a bit of signal processing. To do so, we first subtract to the correction map a quadratic surface which is determined outside of the cavity mode, where no OM shifts are expected (see fig. 5.7b). An alternative (or complementary) approach is to take the average value of N point of each line (with N normally being around 5% of the line length), chosen outside of the cavity mode, and subtract this value to the whole line[1].

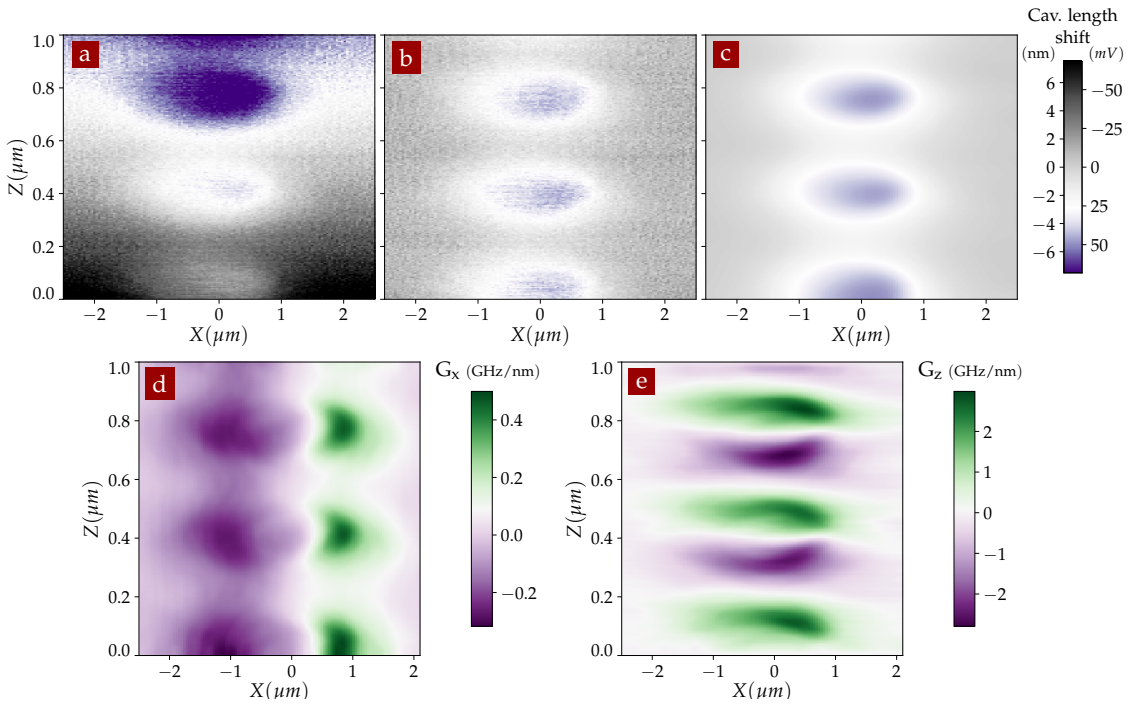

FIGURE 5.7 – Correction signal obtained while imaging the TM_{00} mode whith the NW deeply inserted in the cavity mode. The signal is presented in its raw format (a), after the long-term drift correction (b) and after filtering to compensate for high frequency noise (c). Figure (d) and (e) present the calculated value of the parametric coupling strength G_x and G_z obtained from (c).

To compensate for fast cavity length fluctuations, we can locally smooth the measured data (fig. 5.7c) applying different filtering techniques[2] over the 5 neighbouring points (up to 20, depending on the map grid resolution), which typically correspond to 150×20 nm in size (respectively in X and Z), sufficiently small compared to the size of the measured structures. It would have been more correct to time average the measured signals, but it would have required a longer imaging time, and so it could have suffered from a longer

[1]Note that this method has the advantage of working well even when the fit of the long term drift with a quadratic effect doesn't. On the contrary, it can only be applied if the map has been acquired scanning along X and then moving along Z. In the opposite case the central lines do not have point outside of the cavity mode and this technique could lead to wrong result. It could still work with the assumption that the correction signal is zero close to a node, but this is not always the case.

[2]See for example the gaussian, uniform, median and percentile filter of the Scipy package.

thermal drift. This local averaging thus corresponds to an equivalent 50 ms averaging duration. This is sufficiently long compared to the slow lock loop bandwidth (approx. 100Hz), so that the lock has a sufficient amount of time to reach its stationary value where the cavity shifts are properly compensated.

Once this filtering sequence is performed, we obtained the cavity length change of optomechanical origin: $\Delta_L(\mathbf{r})$. This can be subsequently spatially derived in $2D$ to determine the vectorial parametric coupling strength map (G_x, G_z): $\mathbf{G}(\mathbf{r}) \equiv -\nabla\Delta_L \frac{\omega_{\text{cav}}}{L}$. They are shown in figs. 5.7d and 5.7e (see also fig. 5.6). Those data were obtained using the NW2 and the maximum parametric coupling strength amounts to $G_z^{\max}/2\pi \sim 3\,\text{GHz/nm}$ and $G_x^{\max}/2\pi \sim 0.4\,\text{GHz/nm}$, which is in agreement with the estimations obtained from the cavity scans of section 4.6.3. It is worth noticing that the positions on each side of the nodes on the optical axis, where the cavity finesse remains almost unchanged, are also the ones that feature the larger parametric coupling strength and where the largest optomechanical interaction can be expected.

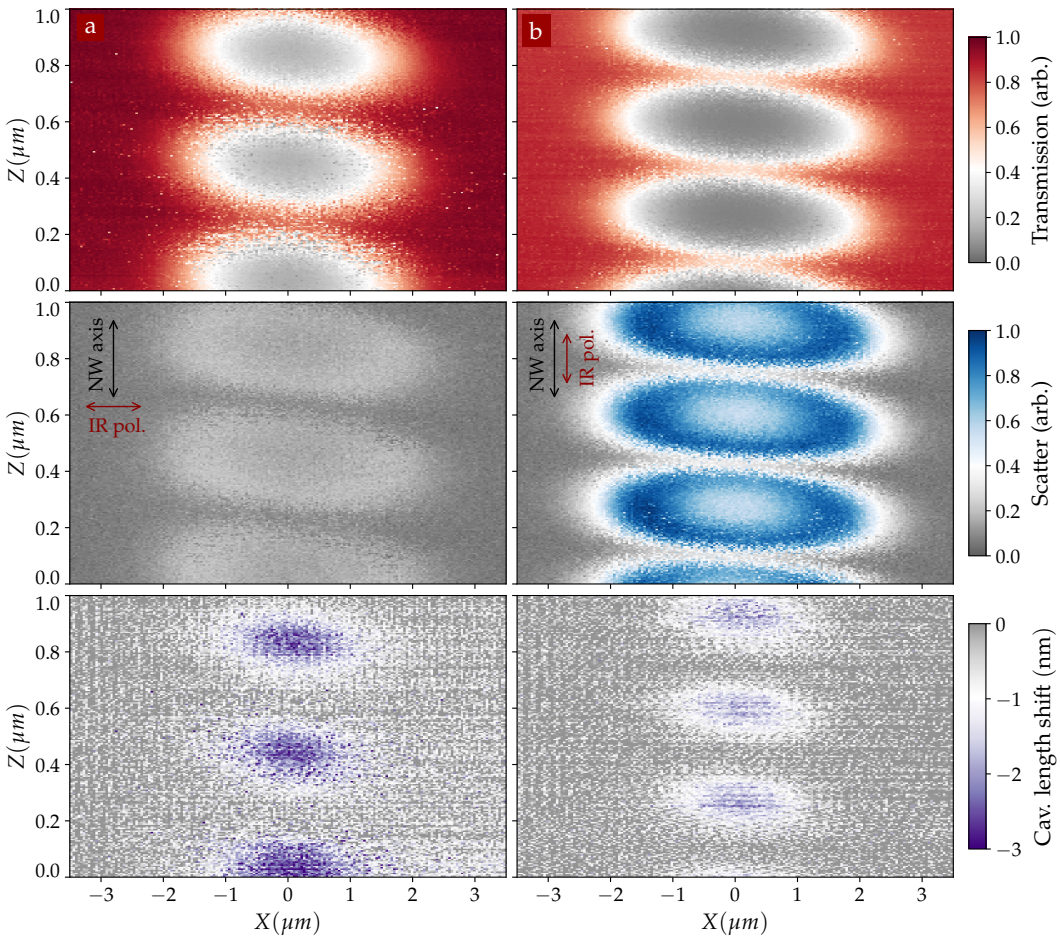

FIGURE 5.8 – Imaging of the TM_{00} mode in the XZ plane for a NW partially inserted in the cavity mode. The injected light is respectively orthogonal (a) and parallel (b) to the NW axis. Note that the two maps were not taken at the same time, which explains the slight displacement along Z of the nodes/antinodes due to thermal drift.

When the cavity is locked at resonance, it is in principle not possible to estimate its finesse out of the transmission or error signals. However the scatter signals can be employed for this purpose, even if a careful analysis of the maps has to be performed since the scatter level is not a monotonous function of the nanowire induced loss rate. The transmission map cross sections indeed show that when the NW is sufficiently inserted

in the cavity so that the added losses are larger than the bare cavity losses, the reduction of the transmission level decreases more rapidly than the Gaussian profile (which instead is preserved when the NW is weakly probing the optical field, compare fig. 4.25 and fig. 5.4).

Finally fig. 5.8 illustrates how these measurements change depending on the polarization of the injected light, respectively orthogonal and parallel to the nanowire axis, for the case of a NW partially inserted in the cavity. Comparing these maps with the ones in fig. 5.5, we can see how a more intense scatter signal not always and not necessarily implies a larger frequency shift. The theoretical developments will permit to get a better understanding of the observed phenomenology.

5.2.4 Imaging higher-order optical modes

The imaging technique described in the previous sections is of course not limited only to the investigation of the nanowire interaction with the fundamental TM_{00} transverse mode, but can be employed to image any kind of longitudinal and transversal mode. To do so, one simply needs to lock the cavity on the optical mode of interest. An example is given in fig. 5.9a, where the transverse mode TM_{12} has been characterized following the same kind of analysis. Noticeably, in addition to the node/antinode structure observed along the optical axis, the transmission, correction and scatter signals are also unperturbed along the optical axis, where the optical field is expected to be zero for this mode.

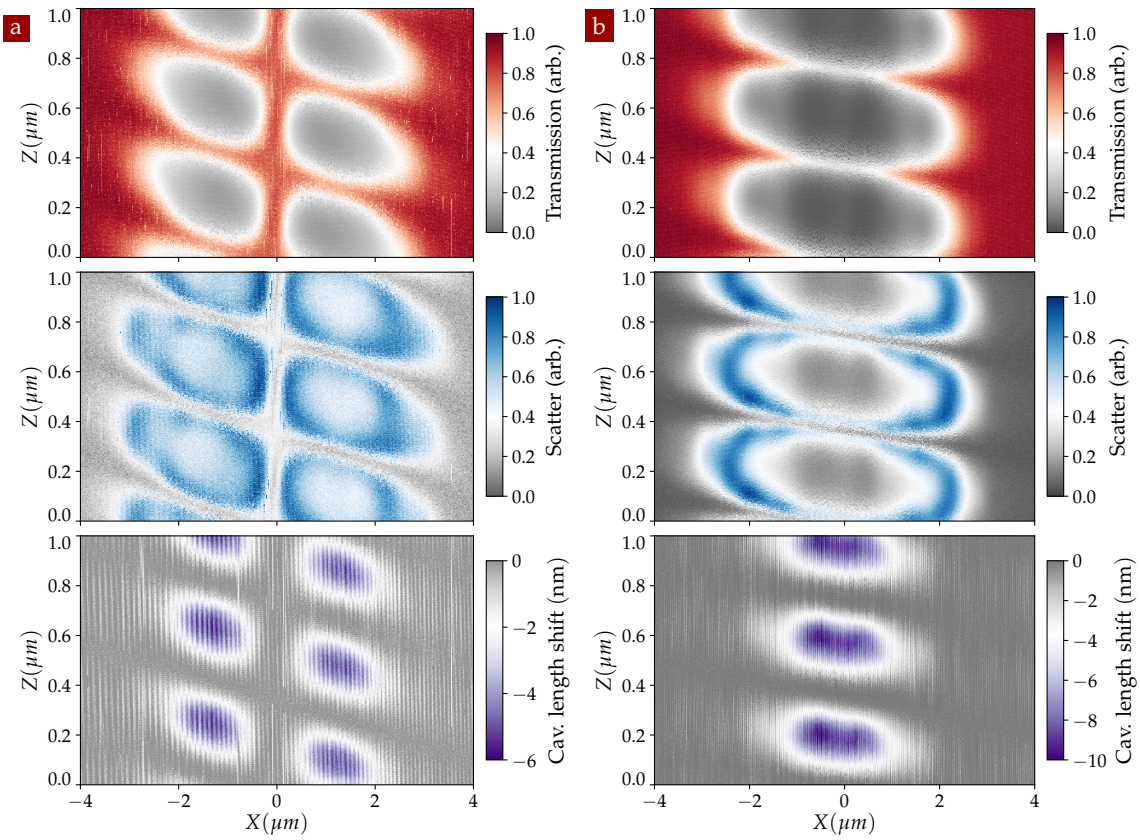

FIGURE 5.9 – (a) Imaging of the TM_{12} mode in the XZ plane for a NW partially inserted in the cavity mode. (b) Imaging of the cross-coupling between the TM_{00} mode and a TM_{3x} mode, performed in the XZ plane and for a NW fully inserted in the cavity mode.

When performing these kind of measurement, we must keep in mind that while the system is maintained at resonance by the locking mechanism, the optical frequencies of the modes are shifted by the nanowire, which can lead to cross couplings between the eigenmodes, as we already showed in section 4.6.4. Depending on the cavity length and on the distance between the transverse optical cavity modes, the NW can be responsible for a cross-coupling between them. As an example, fig. 5.9b shows that despite the system being locked on the fundamental TM_{00} mode, the signature of a transverse TM_{3x} mode is clearly visible and deforms the transmission map structure expected for the fundamental mode. In the following measurements we have tried to avoid those situations, which complicates our investigations and the overall stability of the experiment, essentially by adjusting the cavity length.

It can be also interesting in certain cases to perform other kinds of imaging. For example it is possible to make a map in the XY plane, in order to obtain a cross-section image of a mode at a certain position (fig. 5.10a). In alternative, especially in the case of larger cavities, it can be useful to perform maps over a broader span, to investigate and directly image the variation of the waist dimension inside the cavity, as well as the isophase profile (see fig. 5.10b).

To conclude, we have shown that the imaging technique exposed permits to gain a large set of information on the microcavity properties. Those measurements are based on optical signals or equivalent analysis, based on the investigations of the impact of the nanowire on the microcavity state. We will now investigate the other direction of the OM interaction and analyze how the intracavity field perturbs the nanowire and explore the optical forces in the system.

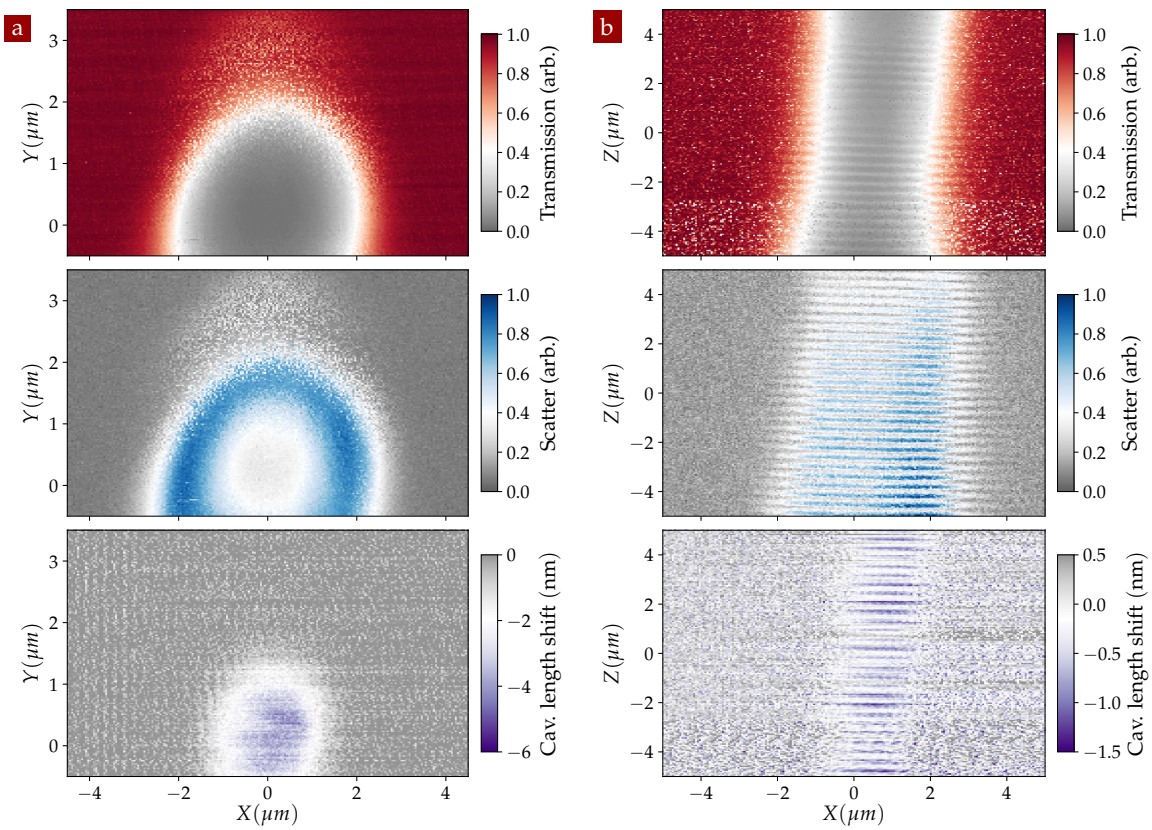

FIGURE 5.10 – (a) Cross-section imaging of the TM_{00} mode in the transversal XY plane. (b) Imaging of the TM_{00} mode in the XZ plane, spanning over a long distance in the Z direction: the variation of the waist dimension as well as the isophase profile can be imaged in this configuration.

5.3 NANO-OPTOMECHANICAL INVESTIGATION OF THE INTRACAVITY FORCE

In the previous sections we have investigated how the oscillator perturbs the intracavity field, which represents one facet of the optomechanical interaction. To fully quantify an optomechanical system it is essential to explore the second facet of the interaction and measure the action of the intracavity light field on the oscillator. This dual characterization is essential, in particular for the "oscillator in the middle" approaches where the nature and excitation level of the optical mode involved in the interaction Hamiltonian (described by the $\hat{a}$, $\hat{a}^\dagger$ operators) strongly depends on the oscillator position (optical mode spatial profile, oscillator induced losses...) and on the pumping conditions.

Here we first determine the mechanical properties of the nanowires using a separate optical readout, independent from the cavity field, we then describe two complementary pump-probe schemes that were employed in order to measure the local intracavity force. We will thus realize a map of the intracavity force field. We will conclude showing how the thermal motion of the NW is affected as a function of its position inside the optical mode.

5.3.1 Independent optical readout and nanowires dynamics

In section 4.5.7 we described the addition of an *HeNe* red laser to the system. This probe laser (few µW at 633 nm, falling outside of the microcavity coating reflection window) is necessary to provide a readout of the mechanical vibrations independent from the cavity field. The probe laser is co-injected with the cavity laser using a WDM, and its reflection is readout on a dedicated photodiode.

Similarly to the behaviour described in section 2.3.1 for the cryogenic objectives, due to the interference between the probe light reflected from the input cavity mirror and the one reflected from the nanowire (and collected back into the fiber), the reflected intensity $P_R(\mathbf{r})$ presents spatial variations that depend on the nanowire position. Figure 5.11a shows the typical interference pattern recorded in absence of the cavity back fiber, while figs. 5.11b to 5.11d compare the (reflected) red signal to the (transmetted) infrared signal when the cavity is aligned (and locked), which permits to visually appreciate the wavelength separation of the two.

When the nanowire oscillates with a vectorial deflection $\delta\mathbf{r}$ around its rest position $\mathbf{r_0}$, it generates a modulated reflected power of $P_R(\mathbf{r_0} + \delta\mathbf{r}(t)) \approx P_R(\mathbf{r_0}) + \delta\mathbf{r}(t) \cdot \boldsymbol{\nabla} P_R|_{\mathbf{r_0}}$. The fluctuations of the photodiode output voltage can be recorded and analysed to obtain a measurement of the nanowire motion $\delta\mathbf{r}$ projected along a measurement vector $\mathbf{e}_\beta$, which is defined as $\mathbf{e}_\beta \equiv \boldsymbol{\nabla} P_R|_{\mathbf{r_0}} / |\boldsymbol{\nabla} P_R|_{\mathbf{r_0}}|$. The latter is determined using a local slope measurement routine, which evaluates the local gradient of the reflected power map. To do so, we record the reflected signal for different positions of the nanowire, placed on a 20 nm grid around the central measurement position. We then compute the local tangent plane to the surface $P_R(\mathbf{r})$, from which we extract the local gradient [86, 56, 232, 233]. As we have extensively described in section 1.2.1, the nanowire dynamics can be written in the Fourier domain as

$$\delta\mathbf{r}[\Omega] = \chi[\Omega] \cdot (\delta\mathbf{F}_{\text{th}} + \mathbf{F}_{\text{opt}}[\Omega]), \tag{5.3.1}$$

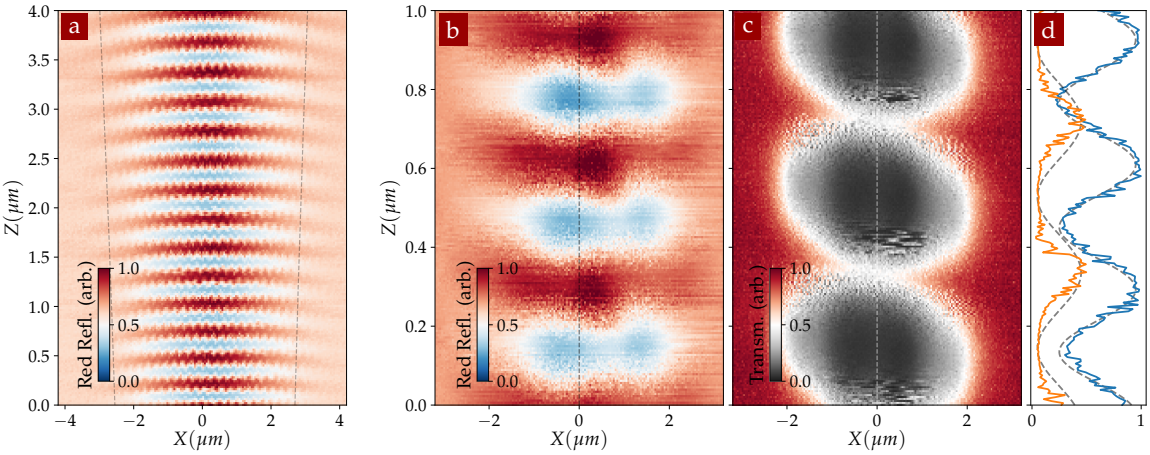

FIGURE 5.11 – Interference patterns of the pump and probe lasers: (a) interference pattern of the red probe laser in absence of the cavity back fiber. Reflected red signal (b) and transmitted infrared signal (c) when the cavity is aligned and locked. (d) interference pattern comparison of the two signals along the optical axis; it is possible to appreciate the wavelength difference between the two.

where χ is the $2D$ mechanical susceptibility. In the $(\mathbf{e}_1, \mathbf{e}_2)$ eigenmode base it reads

$$\chi^{-1}[\Omega] \equiv M_{\text{eff}} \begin{pmatrix} \Omega_1^2 - \Omega^2 - i\Omega\Gamma_{\text{m}} & 0 \\ 0 & \Omega_2^2 - \Omega^2 - i\Omega\Gamma_{\text{m}} \end{pmatrix} . \tag{5.3.2}$$

The projective readout permits to record the nanowire fluctuations along the measurement vector $\mathbf{e}_\beta$: $\delta r_\beta[\Omega] = \mathbf{e}_\beta \cdot \delta\mathbf{r}[\Omega]$.

THERMAL NOISE In absence of optical IR force, when the (red) laser is only used to probe the mechanical vibrations, we can record the thermal noise of the nanowire, driven by the two components of the Langevin force vector $\delta\mathbf{F}_{\text{th}} = (\delta F_1^{\text{th}} \delta F_2^{\text{th}})$ along the two eigenmodes orientations and with $S_i^{\text{th}} \equiv 2M_{\text{eff}}\Gamma_{\text{m}} k_{\text{B}} T$. The thermal noise of the nanowire has also been analyzed in a standard setup using a single focussed laser beam [56, 117], see fig. 5.12a, where a simultaneous measurement of the nanowire thermal noise along two non-collinear measurement vectors is shown. Figure 5.12b presents the spectrum of NW2 measured on the cavity set-up using the red probe measurement channel. These signals have been fitted with the expression

$$S_{\delta\mathbf{r}_\beta}[\Omega] = \sum_{i=1,2} (\mathbf{e}_\beta \cdot \mathbf{e}_i)^2 \frac{2\Gamma_{\text{m}} k_{\text{B}} T}{M_{\text{eff}}\left((\Omega_i^2 - \Omega^2)^2 + \Gamma_{\text{m}}^2 \Omega^2\right)}, \tag{5.3.3}$$

allowing to extract the effective mass M_{eff}, the eigenfrequencies $\Omega_1/2\pi$ and $\Omega_2/2\pi$, the damping rate Γ_{m} and the eigenmode orientations $\mathbf{e_1}$ and $\mathbf{e_2}$ of the two fundamental transverse modes for each sample. The estimated mechanical parameters are reported in table 4.2. Note that when using a single measurement channel, as in the present case, we need to assume that the eigenmodes are orthogonal in order to determine their orientations and effective mass. In practice the measurements exposed in the following section, have been intentionally realized with a nanowire (NW2) presenting a large frequency splitting ($\approx 20\%$), in order to reduce the possible eigenmode rotation caused by the force field shear components; a proper vectorial readout will be implemented in the near future.

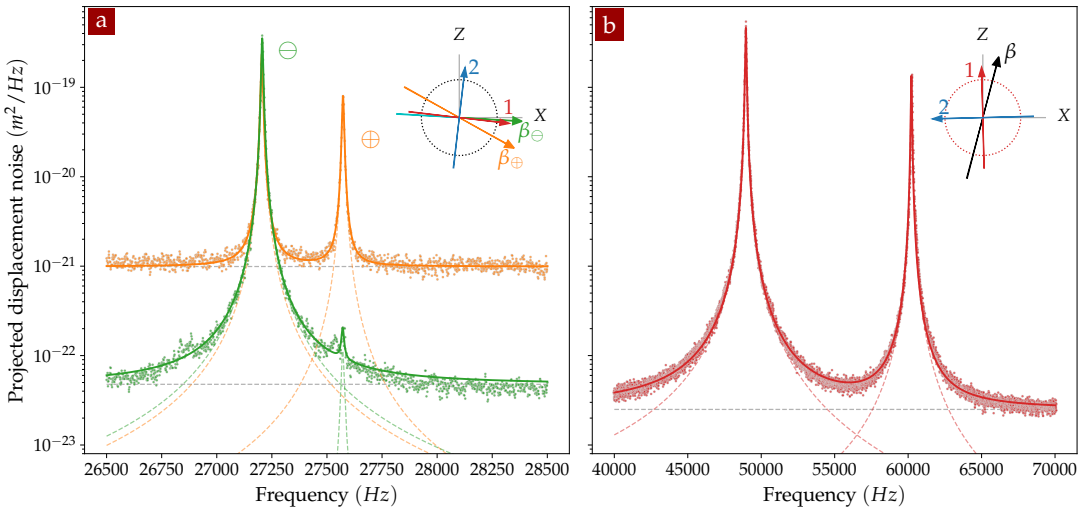

FIGURE 5.12 – Estimation of the mechanical parameters of the cavity samples: (a) measurement of the thermal noise of the sample $NW3$ in a standard setup [233] along two measurement channels; (b) measurement of the thermal noise of the sample $NW2$ using the red probe laser in the setup.

RESPONSE MEASUREMENT In order to evaluate the intracavity force field we implemented a pump-probe scheme [86], realized by modulating the intracavity intensity at frequencies close to the mechanical resonances, while simultaneously recording the driven nanowire trajectories with the red probe laser.

The optical force vector $\mathbf{F}_{\text{opt}}(t)$ is proportional to the IR intracavity field, and thus to the injected IR power P(t). The latter can be modulated, at a frequency $\Omega/2\pi$, with an amplitude δP around a mean value P_0 by means of an acousto-optic modulator (AOM): $P(t) = P_0 + \delta P \cos(\Omega t)$. The optical force will then present a static component (which displaces the nanowire rest position but remains weak (sub 10 nm) and can be neglected) and an oscillating counterpart $\delta\mathbf{F}_{\text{opt}} \cos(\Omega t + \phi)$. For the case of a pure optical force and in the adiabatic cavity limit ($\Omega_{\text{m}} \ll \kappa$) where we operate, the intracavity force instantaneously follows on mechanical time-scales the temporal variations of the input intensity (resulting in $\phi = 0$). In case of thermal-optical forces instead, the establishment of the force may be delayed. Previous analysis [86] have shown that the thermal dephasing is of 90 degrees at room temperature (with a thermal cutoff around 1 kHz for the nanowires employed in that work). As such the Fourier component of the time modulated optical force vector can be generally written in the complex form:

$$\delta\mathbf{F}_{\text{opt}}[\Omega] = \delta F \mathbf{e}_{\mathbf{F}} + i\delta\tilde{F}\mathbf{e}_{\tilde{\mathbf{F}}} \tag{5.3.4}$$

We note that since our response will be realized on a narrow frequency span, it is not necessary to include a possible frequency dependence in $\delta\tilde{F}$. We employed a vectorial network analyser (VNA) to measure the steady state trajectories of the nanowire driven by the optical force and swept the drive frequency across both eigenmodes to determine the orientation of the optical force vector. In order to estimate the overall delays in the VNA measurement (delays in the cables, in the AOM, in the readout channels), we simply removed the IR filter in front of the detector collecting the red probe laser reflection. The WDM indeed (see fig. 4.18) is not perfectly cancelling the IR signal, letting a few percentage of the IR light going through that must be filtered. We can then directly record the magnitude of $\delta r_\beta[\Omega]$ and its dephasing with respect to the intensity modulation. The recorded response data, shown in fig. 5.13a, are well fitted in amplitude and phase by mean of the expression:

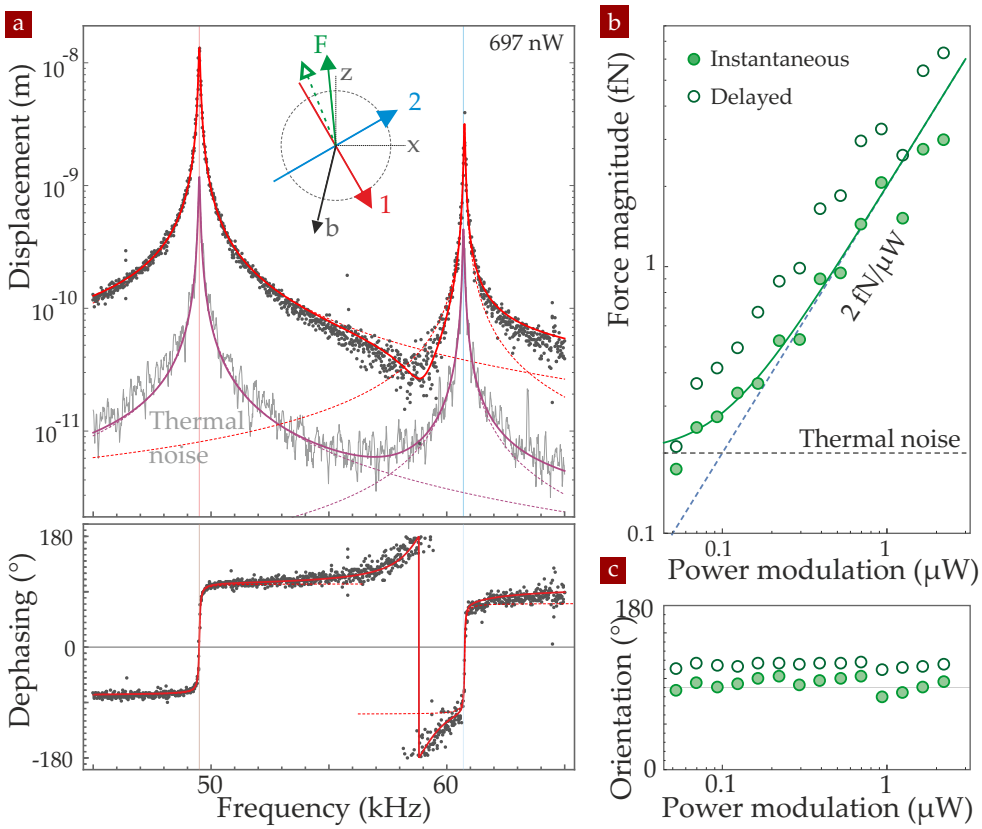

FIGURE 5.13 – Nanomechanical measurement of the intracavity optical force: (a) Thermal noise (gray line) and response measurements (dots) measured with the red probe laser providing a projective measurement of the nanowire vibrations along the $\mathbf{e}_\beta$ axis (inset), for a cavity locked at resonance for a position close to a node. The eigenmodes and the force orientations are also shown. (b,c) Evolution of the magnitude and orientation of the optical force vectors (instantaneous and delayed) for increasing modulation depth ($P_0 = 3\,\mu\text{W}$), illustrating the linearity of the system response.

$$\delta r_\beta[\Omega] = \sum_{i=1,2} \frac{(\mathbf{e}_\beta \cdot \mathbf{e_i})(\delta \mathbf{F}_{\text{opt}} \cdot \mathbf{e_i})}{M_{\text{eff}}(\Omega_i^2 - \Omega^2 - i\Omega\Gamma_{\text{m}})} \,. \tag{5.3.5}$$

Because all the mechanical and the readout parameters are already independently determined, the only fitting parameter is the complex drive vector $\delta\mathbf{F}[\Omega]$, which possesses four degrees of freedom (real and imaginary parts of both spatial components). In practice, employing the expression of eq. (5.3.4) the fitting parameters are the magnitudes $(\delta F, \delta\tilde{F})$ and the orientations $(\mathbf{e_F}, \mathbf{e_{\tilde{F}}})$ of the instantaneous and delayed force components.

Figures 5.13b and 5.13c represent the amplitude and phase of both the instantaneous and delayed force components, for increasing values of the modulation depth δP at a fixed position of the nanowire extremity in the optical mode (slightly before a node, see below). This measurement allows to verify the linearity of the system, with a dependence of $\approx 2\,\text{fN}/\mu\text{W}$ of the optical force on the input optical power, which emerges above the thermal noise for a modulation strength larger than 200 aN (RBW = 30 Hz). This order of magnitude can be compared to the force applied by a laser of power P fully scattered on an object, which amounts to $P/c \approx 3.3\,\text{fN}/\mu\text{W}$. Despite the sub-wavelength size of the nanowire and the relatively large optical waist ($w_0 = 1.8\,\mu\text{m}$), the multi-interaction permitted by the cavity significantly enhances the single-pass interaction. In the following sections we will mainly address the instantaneous optical response, whose spatial gradients can generate mechanical frequency shifts and eigenmode rotations.

5.3.2 Intracavity force in a NIM

The procedure we described in the previous section can be repeated for several positions of the NW inside the cavity mode, in order to fully map the optical force field. Because of technical constraints of the acquisition time, mainly due to the stability of the system, this method is suitable for a $1D$ measurement along one axis, while for a full $2D$ mapping an innovative multi-frequency technique has been employed (see below).

$1D$ OPTICAL AXIAL FORCE The instantaneous component of intracavity force field F_z exerted on the nanowire and its variations along the optical axis are reported in fig. 5.14. This was measured with a fixed modulation depth $\delta P/P_0 \approx 0.70$, for increasing average input powers P_0 ranging from 1 to 5 µW. For the employed sample, higher pumping powers were bringing the OM system into unstable regimes. With a resolution bandwidth of 30 Hz, a span of 20 kHz, 600 points per scan and two to three subsequent averaging, each point of the figure required roughly 1 min to be measured[3] (including the $\mathbf{e}_\beta$ estimation), adding up to around 1 h for the 60 points taken along the 1 µm long line on the axis. The image also shows (fig. 5.14c) the corresponding transmission signals, in order to identify the nodes and antinode locations.

The measured optical force shows a $\lambda/2$ periodicity which reproduces the standing wave nature of the intracavity field; it presents a strong repulsive character in the vicinity of the nodes and on the contrary is found to be weakly attractive towards the antinodes. This phenomenology is well predicted by our theoretical model (see fig. 5.15) and can be qualitative understood with the following argument, which also holds for membrane in middle experiments [197]: regions of positive (resp. negative) dispersive shifts, $G_z > 0$ (resp. < 0), are associated to situations where a larger amount of light is stored in the first (resp. second) sub-cavity, so that the total force is found to be positive (resp. negative). In addition, the $\approx 30\%$ asymmetry observed between the positive and the negative values of the force extrema can be connected to the laser pumping direction (along $\mathbf{e_z}$), but it can also be attributed to an asymmetry between the effective reflection coefficient of the two mirrors.

The intracavity force field $\mathbf{F}(z)$ exerted on the nanowire presents some large spatial variations of $\partial_z F_z \approx 1.5 \times 10^{-7}$ N/m for 5 µW input power in the vicinity of the intracavity nodes. They are playing as an antitrapping force, which opposes against the intrinsic nanowire stiffness, $k = M_{\text{eff}}\Omega_{\text{m}}^2 \approx 10^{-4}$ N/m, and are responsible for a frequency softening at the nodes locations. The measured frequency shifts are shown in fig. 5.14d, and are in good agreement with the ones deduced from the gradient of force measurements using the expression

$$\Delta\Omega_{\text{m}} = -\frac{\partial_z F_z}{2\Omega_{\text{m}} M_{\text{eff}}}, \tag{5.3.6}$$

as discussed in section 1.3. This good agreement validates the force measurement protocol exposed above. Again, this measurements were realized using a largely frequency split nanowire to avoid eigenmode rotations.

MULTI-FREQUENCY RESPONSE MEASUREMENT Applying the previous technique to map the intracavity force field on a $2D$ surface, with an acquisition rate of ≈ 1 min per point, would require several days to register a 60×60 grid of point. Here we present an

[3] A full response measurement requires to stay at least a duration of $1/\Gamma_{\text{m}}$ per frequency point.

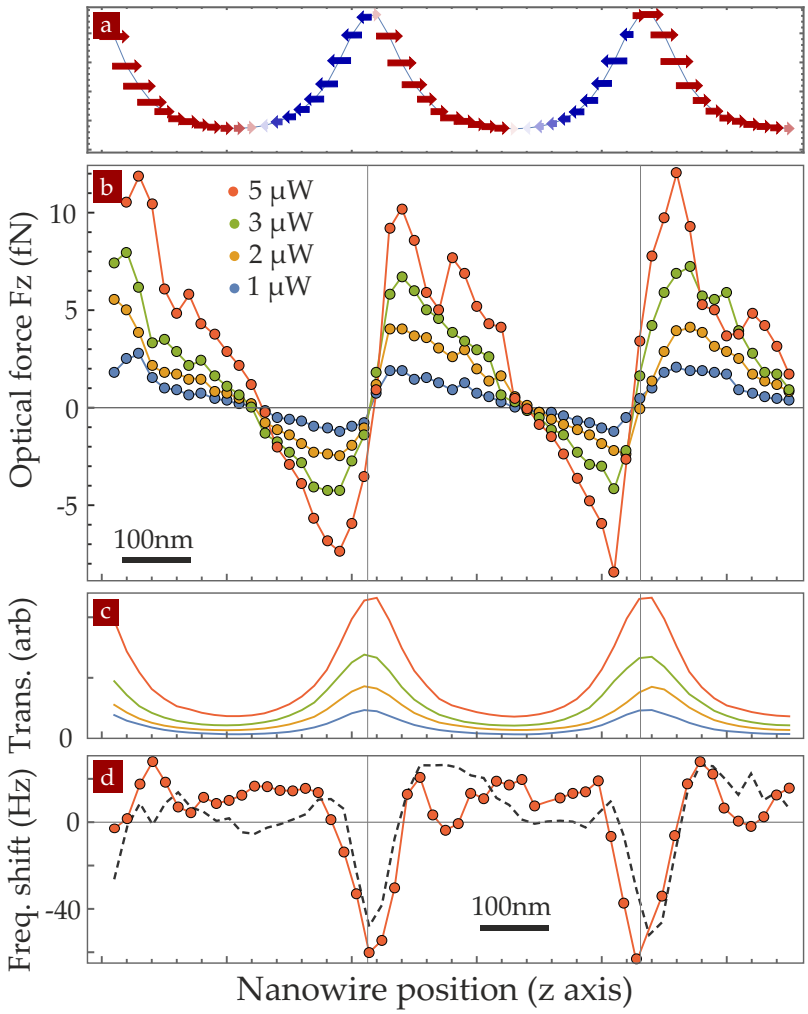

FIGURE 5.14 – Intracavity force along the optical axis: (a,b) Dependence of the instantaneous force F_z with the position along the optical axis for increasing input powers. The nodes of the electromagnetic modes are indicated as dashed lines and correspond to the maxima in the transmissions plots (c). (d) Measured relative frequency shifts (dashed lines) obtained for 5 μW compared to the shifts expected from the measured optical force field gradients (red dots).

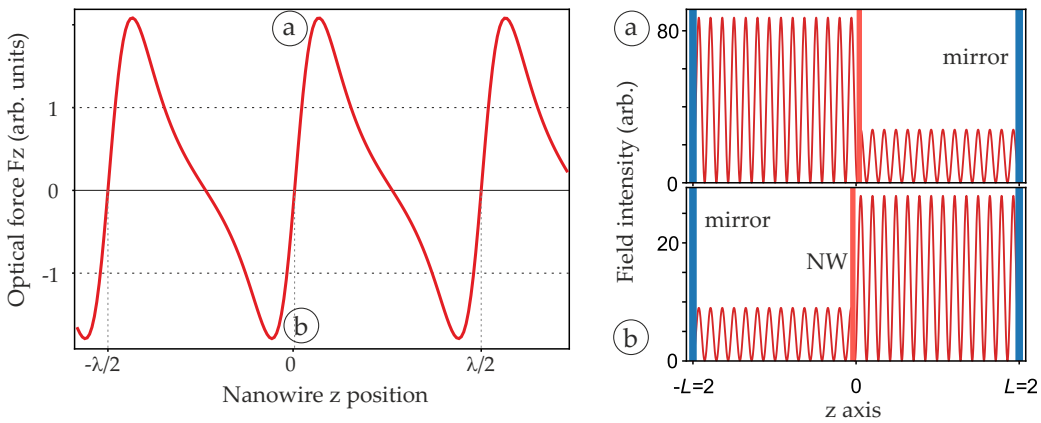

FIGURE 5.15 – Simulations of the optical axial force computed for different nanowire positions along the optical axis. The right panels show the intensity distributions in the system for two positions of the nanowire, on the left and right sides of an optical node of the intracavity field. The left-right distributions of the field intensity in the two sub-cavities permits to understand the repulsive character of the force profile observed in the vicinity of optical nodes.

alternative (and complementary) approach, which allowed us to reduce the measurement duration by a factor of 100.

This technique exploits the large linearity of our apparatus and consists in simultaneously driving the nanowire with several (six in the results shown here) frequencies and demodulating the different driven trajectories at each of those frequencies. In order to simultaneously determine the eigenmode frequencies and damping rates and to compensate for possible variations due to force field gradients or thermal drifts, we choose to employ three tones per mechanical mode, at frequencies $\Omega_i^{0,\pm 1}$, separated by 50 Hz, which is comparable to the eigenmode linewidth. The central frequency Ω_i^0 is maintained close to the mechanical resonance using a soft-tracking routine using a peak detection mode on a fast spectrum analyzer (FSVR).

Those measurements are realized using a multifrequency synchronous detector (Zurich Instrument HF2LI) and permit to reduce the measurement duration to 100 ms per point. Recording the amplitudes and dephasing for each tone permits to determine the quality factors and eigenmodes frequencies, as well as the local complex driving force vector (see fig. 5.16). Probing each NW resonance with three tones permits in particular to evaluate the modifications of its damping rate possibly induced by the delayed force field contributions (see bellow). For example, if the damping rate decreases, thus increasing the mechanical quality factor, the amplitude of the central peak will increase more than the one of the lateral peaks, and simultaneously, the phase difference between the central and lateral peaks will be increased.

The measurement vectors $\mathbf{e}_\beta$ are also determined in real time, using a dynamical mode different to the previous statical one. The nanowire rest position is dynamically modulated in the XZ plane through the piezo stage supporting the nanowire at two different frequencies (80 and 85 Hz), along each axis. We simultaneously demodulate the (red) re-

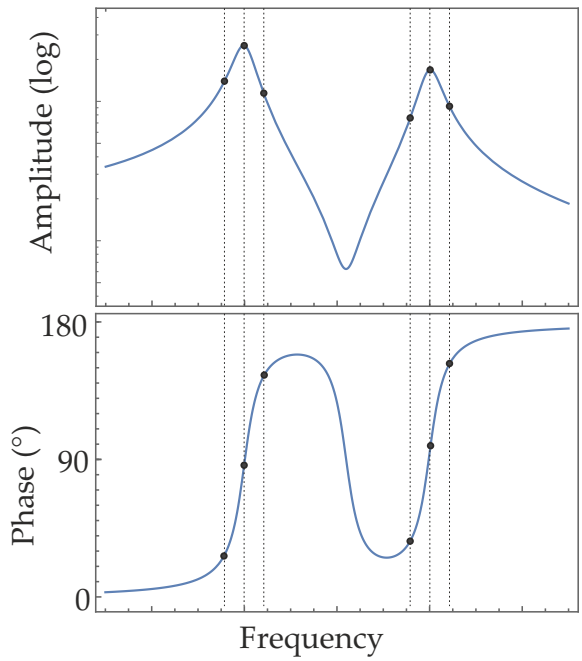

FIGURE 5.16 – The nanowire is simultaneously driven by the intracavity field at six different frequencies, in order to accelerate the measurement time of the local force vector. Three tones are driving each eigenmode, the central tone of which is locked on the eigenmode resonance, while the two sidebands are separated by 50 Hz, which is comparable to the eigenmode linewidth. Recording the amplitudes and dephasing for each tone permits to determine the quality factors and the eigenmodes frequencies, as well as the local complex driving force vector.

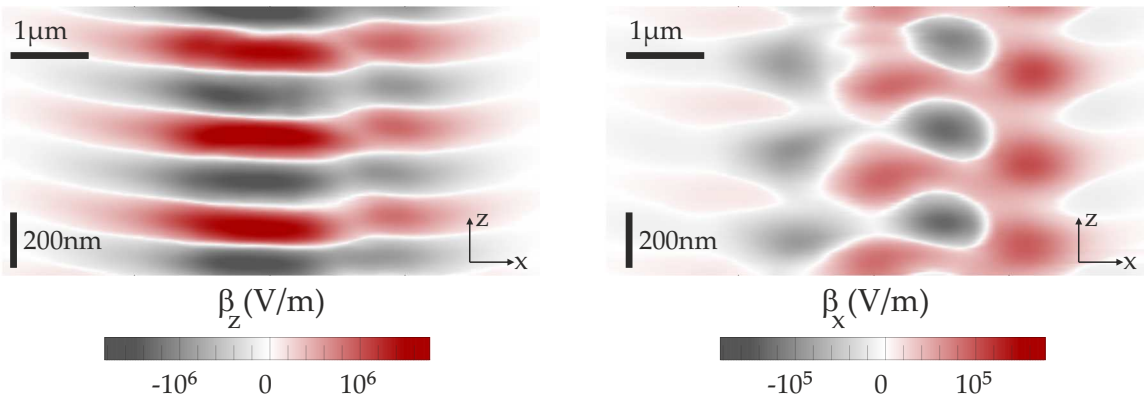

FIGURE 5.17 – XZ maps of the measurement vectors (β_z, β_x) obtained with the spatial interference measured on the red probe laser reflection photodiode signal $P_R(\mathbf{r}_0)$. Measurement vectors defined as $\boldsymbol{\beta} \equiv \boldsymbol{\nabla} P_R$ are measured dynamically, by modulating the piezo stage supporting the nanowire and demodulating the photodiode output signal. Those measurements are acquired simultaneously during the multi-frequency response maps. The z-periodicity observed corresponds to half the probe laser wavelength (633 nm). In most positions, the measurement vectors $\mathbf{e}_\beta = \beta/|\beta|$ are almost aligned with the optical axis $\mathbf{e}_z$.

flected signal at those two driving frequencies. The amplitude and phase of both signals are then used to determine the local slope and orientations of the readout map gradients along the two axes. Figure 5.17 shows a map of the measurement vectors recorded during the multi-freqeuncy XZ map shown in fig. 5.19. The oscillation amplitudes employed here are of a few nanometers and do not significantly affect the force measurement.

It is important to notice that the interference pattern measured in reflection of the red probe laser, that is exploited to readout the nanowire vibrations, presents positions (interference extrema) featuring no spatial gradient, which prevents from correctly measuring the nanowire vibrations. It is important to properly estimate the local measurement vectors, but this may become delicate close to those extrema. In order to compensate for this potential source of errors, we have applied a local barycentric correction to the data: the force measurements are spatially averaged and weighted by the norm of the measurement vector magnitude:

$$F_i^{\text{avg}} = \frac{\sum_{j=i-\Delta,i+\Delta} F_j|\beta_j|}{\sum_{j=i-\Delta,i+\Delta}|\beta_j|}, \tag{5.3.7}$$

where F_i represents the force estimated at position i. We employed a sliding averaging over $2\Delta + 1$ neighbouring points, spreading over 25 nm on the Z axis (Δ is adjusted depending on map grid). Figure 5.18 illustrates this mechanism. The upper curve represents the cavity transmission, which permits to identify nodes and antinodes of the intracavity field; the bottom curve represents the norm of the measurement vector, which exhibits blind positions (marked by gray dashed lines). The central panel shows the force measured before (dots) and after (line) the barycentric correction. We note that due to the large signal to noise ratio observed in our measurement conditions (force signal of 20 dB above the thermal noise and 60 dB above the background for 5 Hz resolution bandwidth), it is always possible to detect the driven force, even very close to the blind positions. The barycentric averaging thus serves to compensate for the errors arising in the evaluation of the measurement vectors close to the blind positions.

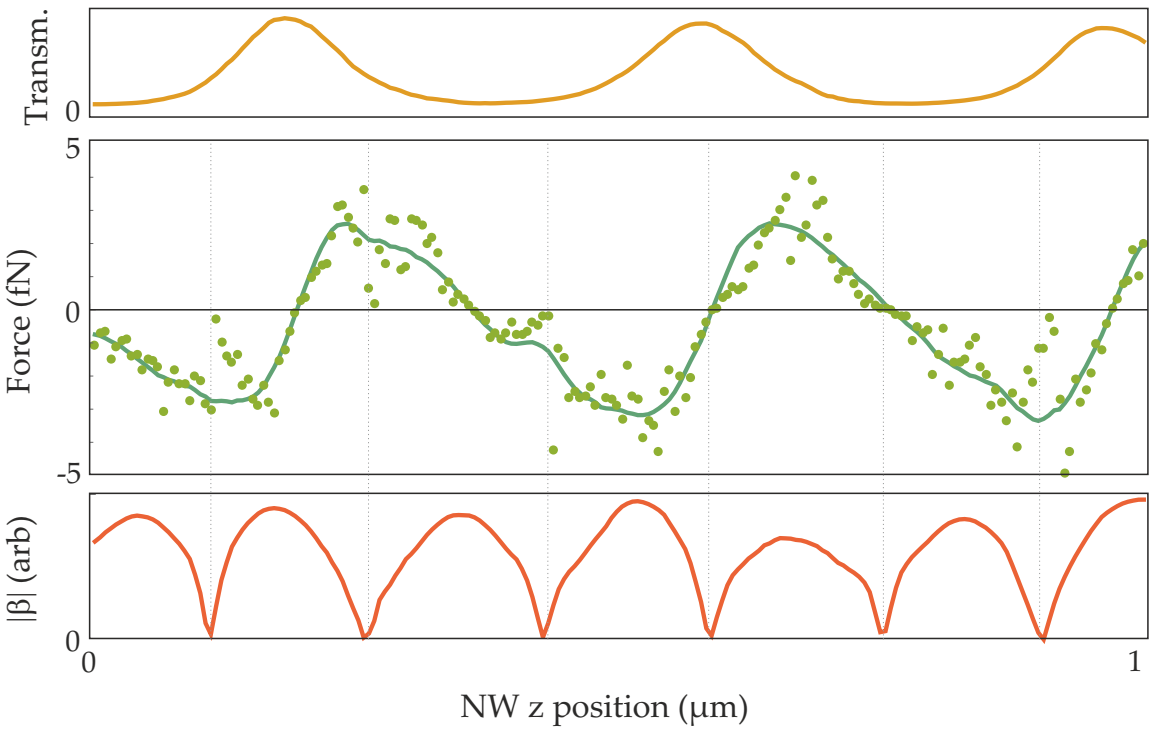

FIGURE 5.18 – Illustration of the local barycentric smoothing employed in the data analysis to compensate for the reduction of readout sensitivity observed in the readout channel at the interference extrema. The cavity transmission is shown on top, while the bottom curve represents the norm of the measurement vector. Blind positions are marked by gray dashed lines. The central panel shows the force measured before (dots) and after (line) the local weighted averaging.

2D FORCE FIELD MAP The results of the application of the multi-frequencies technique, both in the XZ and in YZ plane, are shown in fig. 5.19, where the intracavity force field is superimposed to the transmission map encoded as iso-values to help localizing the $\lambda/2$ periodic structure.

The color code shows the measured optical force projected along the optical axis (Fz), shown as colored arrows in the maps. To realize those measurements it was used a 400×400 grid of pixels, it required slightly more than four hours of acquisition time, and the signal processing routine described previously employed signal averaging up to 10 neighbouring pixels. It is possible to recognize the anti-trapping / trapping structures in the vicinity of the nodes /antinodes, and the vanishing of the optical force when the nanowire is extracted out of the intracavity mode volume, both transversally (X) and vertically (Y). The parametric coupling map (G_z) is derived by calculating the gradient of the cavity lock correction signal map, recorded during the same XZ measurement sequence. Note that the long-term shift of this map, that we normally subtract to obtain the cavity length change, can be used to estimate the stability of the system and compensate for eventual deformation of the resulting map. On each side of the antinodes, it is possible to identify locations of simultaneous large optical backaction and large parametric coupling strength. Those regions are clearly of great interest for future experiments in the ultrastrong coupling regime (see Conclusion and future developments). We also note that operating with a quasi-frequency-degenerated nanowire and a full $2D$ readout scheme will allow future investigations of the possible non-reciprocal (non-conservative [117]) character of the intracavity force field and its impact on the nanowire dynamics. Such non reciprocal couplings are expected to arise on the side of the optical mode.

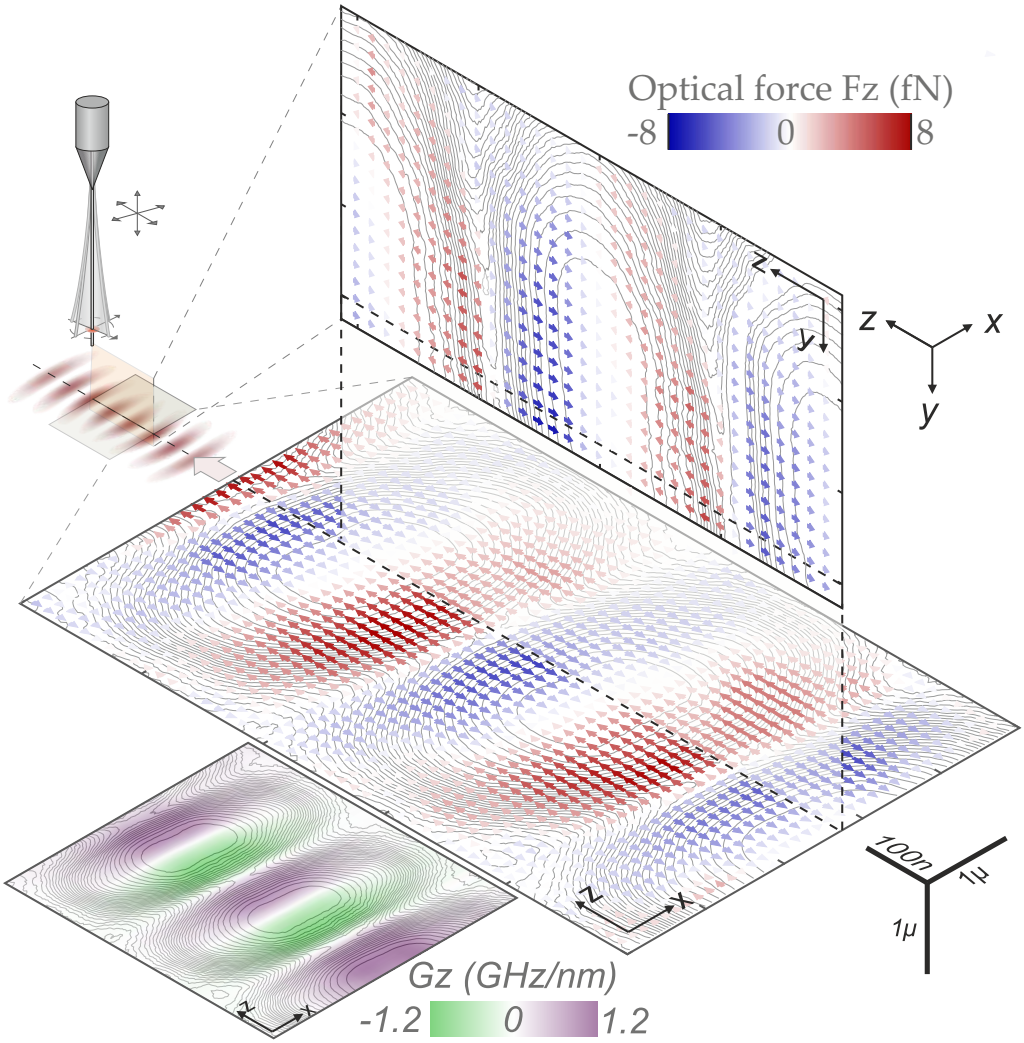

FIGURE 5.19 – Horizontal (XZ) and vertical (YZ) maps of the intracavity force field (anisotropic length scales), measured for an injected power of 3 µW at 767 nm. The pump laser is injected along $\mathbf{e}_z$ and the dashed line represents the optical axis. The color code indicates the force component along the optical axis F_z . Inset: parametric coupling strength G_z derived from the correction of the cavity lock. The transmission iso-values are superimposed as gray lines to help visualize the intracavity field structure.

5.3.3 Brownian motion 2D map

An alternative way to quantify the impact of the intracavity force on the nanowire dynamics is to analyse how scanning the sample across the optical mode affect its Brownian motion. At this stage of the experiment, due to technical reasons, the probe laser was still not in place, thus the measurements have been performed using directly the transmission and the scatter signals. Later we switched to the improved response technique we described in the previous section, therefore we didn't repeat these measurements with the addition of the visible laser, due to the long acquisition time ($\sim$ 5 h for a 30×30 grid) and similar (or fewer) information achievable. However, it is useful to compare these results to the previous ones, in order to gather information about the peculiar areas inside the optical mode where interesting OM effects can be expected, as well as to illustrate some of the challenges and the technical difficulties linked to the readout non-linearities and the environment noise.

The readout principle we illustrate in the previous section can still be applied, although the intensity gradient due to the interference (of the red laser) is now replaced by the pattern of the standing wave of the intracavity field. Nonetheless, as we will show, the large impact on the intensity of the transmitted field caused by the interaction with the nanowire, especially when placed inside of a "scatter ring" (see section 5.2.2), can be a major issue on the reliability of the estimation of the $\mathbf{e}_\beta$ measurement vector. This, together with readout non-linearities which occur when close to a node or an antinode, as well as some mechanical instabilities in certain positions (for higher pump power), can seriously complicate the analysis. This is one of the reason why we decided to move to a pump-probe scheme later on (see previous section). Nonetheless, these measurements are yet a precious source of information to better understand the role of the measurement process and to learn how to distinguish OM physical effect from spurious signature due to a sub-optimal readout, especially when compering results from different signals (red reflection, IR transmission, IR scatter...).

In analogy to the locked-map in the XZ plane we previously showed, the measurement routine proceed as follow: set a certain polarization of the pump light and a certain vertical insertion in the cavity mode, the NW is scanned on a grid across the XZ plane. For each position of the grid, we first evaluate the measurement vector $\mathbf{e}_\beta$ and then record the mechanical spectrum with a spectrum analyser. This for both the transmission and the scatter signals at the same time. A typical grid of 30×30 points, using a resolution bandwidth of 10 Hz and averaging the spectrum between 10 and 100 times, required 3 to 5 hours to be completed, during which the locked must keep the system stable and eventual long-time drifts have to be limited or taken into account because they can result in distorted maps. Note that the estimation of $\mathbf{e}_\beta$ required around 10 s in each point, accounting for 50% to 80% percent of the total acquisition time. At the beginning and at end of the measuring routine a usual imaging of the optical mode is performed, so that later on they can be used as a reference to compare to the result of the analysis and to better evaluate the possible thermal spatial drifts. The imaging of the mode TM_{12} that we will consider in the following is shown in fig. 5.20.

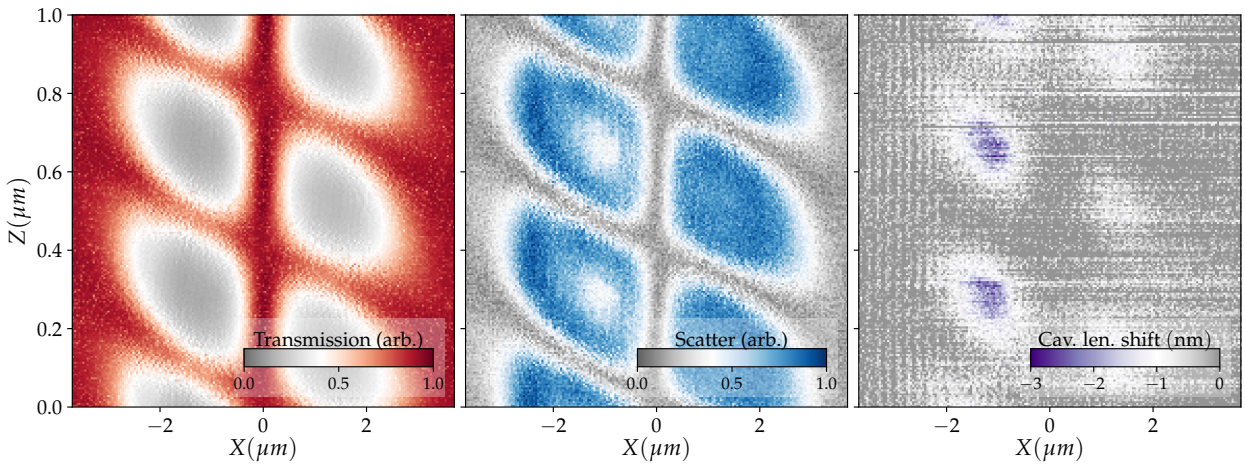

FIGURE 5.20 – Transmission, scatter and correction signals of the TM_{12} mode analyse in this section. The transmission signal shows a node along the optical axis while the scatter signal exhibits the characteristic rings within each lobe of the transverse mode. The asymmetry between the left and the right side of the scatter signal is probably due to a small tilt between the optical mode and the NW axis.

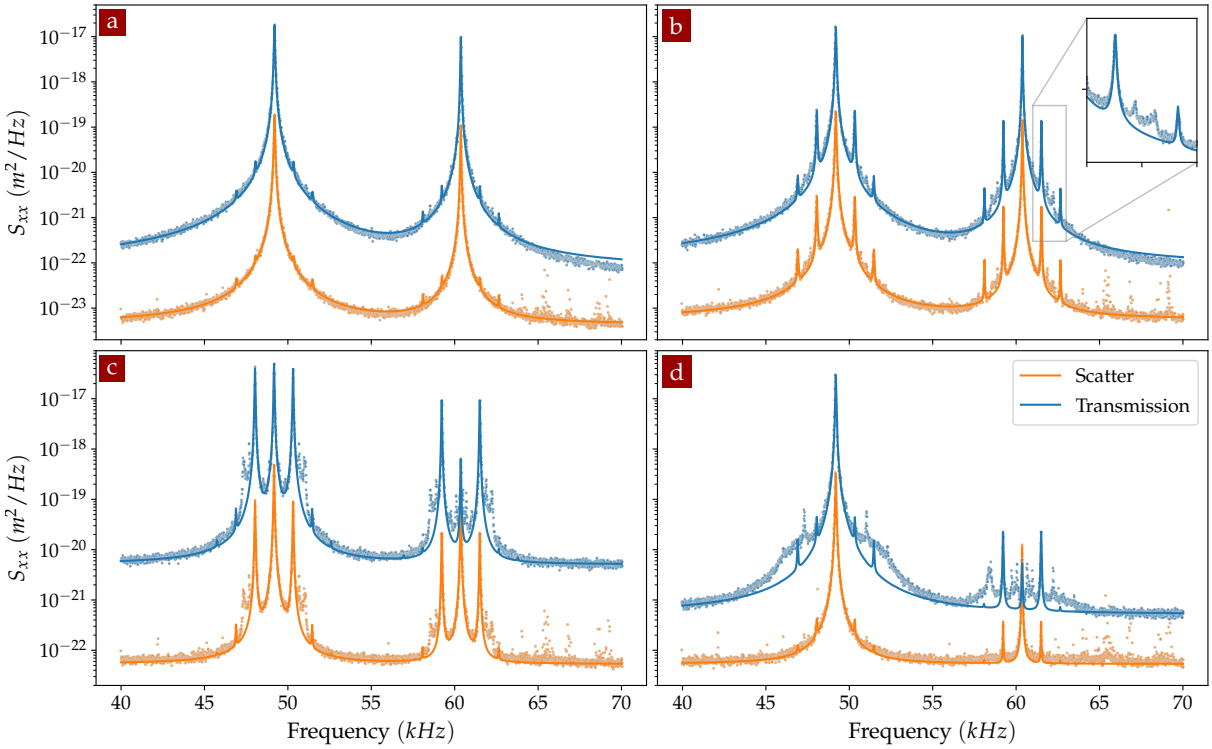

FIGURE 5.21 – Spectra of the transmission and scatter signals for different positions of the NW in the optical mode. In addition to the two main mechanical peaks (a), several sidebands can appear when the readout becomes non-linear (b,c,d).

Spectra of the two signals, for different positions of the NW in the optical mode, are presented in fig. 5.21. As we can immediately observe, compare to fig. 5.12 the recorded signals exhibit a much more complex structure and various additional sidebands around the two main peaks. With the help of simple numerical simulation to replicate this scenario, we can explain most of this phenomenology by means of two general arguments, which allow to discriminate the artefacts of the measurement process from the actual physical effects. When approaching a node or an antinode, the way the NW vibrations modulate the optical signal became increasingly non-linear (see fig. 5.11d), resulting in a modified spectrum: the main effect is the reduction of the peak at frequency Ω_m and the appearance of a peak at twice this frequency. This for both mechanical polarization. Moreover, because we are dealing with two nearby frequencies, it is possible to observe the appearance of additional sidebands spaced in frequency of $\Omega_2 - \Omega_1$. Because in our case this difference is of the order of 10 kHz, these peaks fell outside of the spectral window we measured. To partially explain the complex structure of fig. 5.21, we have to suppose the presence of an additional noisy signal at a frequency of $\sim$ 1 kHz, which could possibly be caused by small residual oscillations of the cavity lock and residual parasitic vibrations of the piezo stage moving the nanowire. These effects, almost absent when the readout behaves linearly (cfr. fig. 5.21a), appears as a set of sidebands of increasing intensity around the two mechanical peaks the more the readout becomes non-linear (fig. 5.21b). Close to a node (or antinode) the odd sidebands become predominant, while the central peaks and the even sidebands progressively disappear (fig. 5.21c). Additional noisy tones (see the inset of fig. 5.21b) as well as some other kind of phase noise would need to be include in a more complete model to fully explain the rich phenomenology we observed (see for example the discrepancy between the data and the fit in fig. 5.21d).

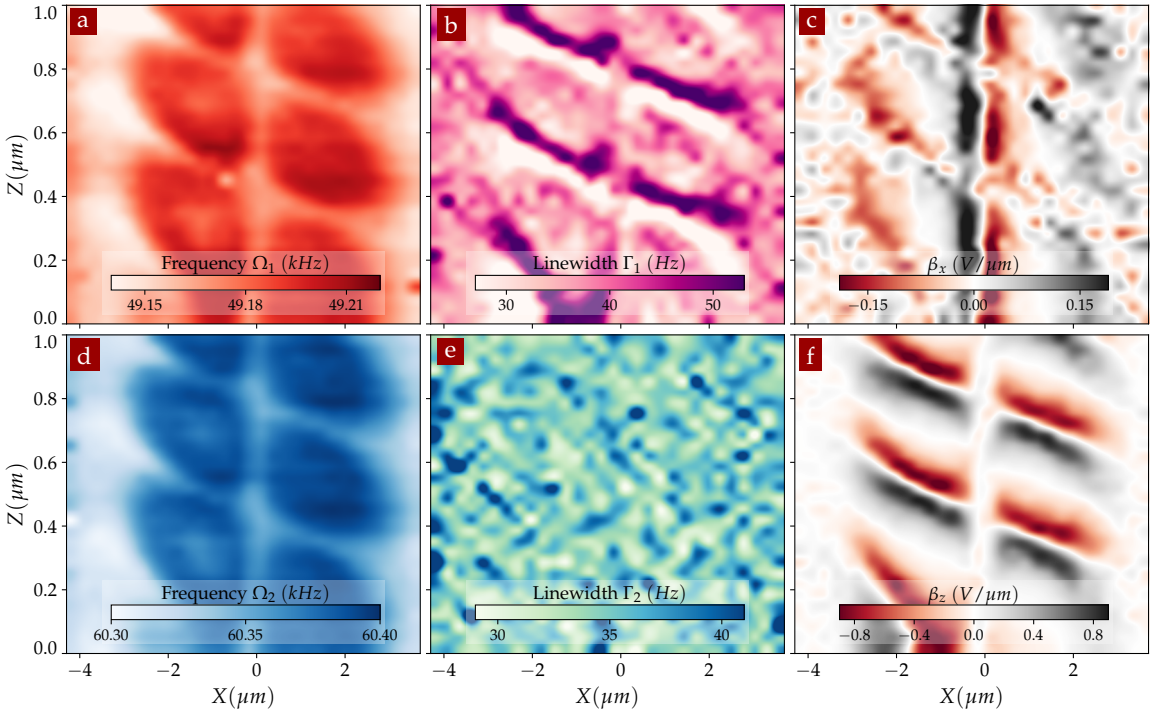

FIGURE 5.22 – $2D$ map of the mechanical properties of the NW measured through the transmission signal, when scanned through the cavity mode TM_{12}. Both mode exhibit a shift in frequency (a,d), while only the linewidth of the low-frequency mode seems to be affected (b,e). The measurement vectors β_x and β_z are also shown (c,f).

However, the presence of those sidebands do not prevent from realizing a decent evaluation of the mechanical frequencies and linewidths of the two mechanical modes in each point. These can then be used to reconstruct a $2D$ map, as shown in fig. 5.22 for the cavity transmission. Note that in most cases the linewidth of the sidebands is equivalent to that of the mechanical peak, allowing for a good estimation of Γ_m even when the central peak disappear. Similar for the mechanical frequency, which always lies in the middle of the two first sidebands.

We can see that both mechanical modes present a shift in frequency up to $\sim$ 80 Hz (figs. 5.22a and 5.22d), which is correlated to the spatial structure of the optical mode. The linewidth of the low-frequency mode also varies with the position within the optical mode (figs. 5.22b and 5.22e), but not the one of the high-frequency mode, traducing that the delayed force field is essentially oriented along the optical axis and thus only affects mode 1.

Similar analysis and results have been achieved using the scatter signal, as illustrate in fig. 5.23, these being more noisy due to the much lower intensity of this measurement channel. Note how the maps of the measurement vectors β_x and β_z (figs. 5.23c and 5.23f) reflect well the ring structure of the scatter signal, in contrast to the previous ones of the transmission.

In a second time, after developing the multi-frequency scheme illustrated in the previous section, the same nanowire was used to map the intracavity force field of this transverse mode, the result is shown in fig. 5.24.

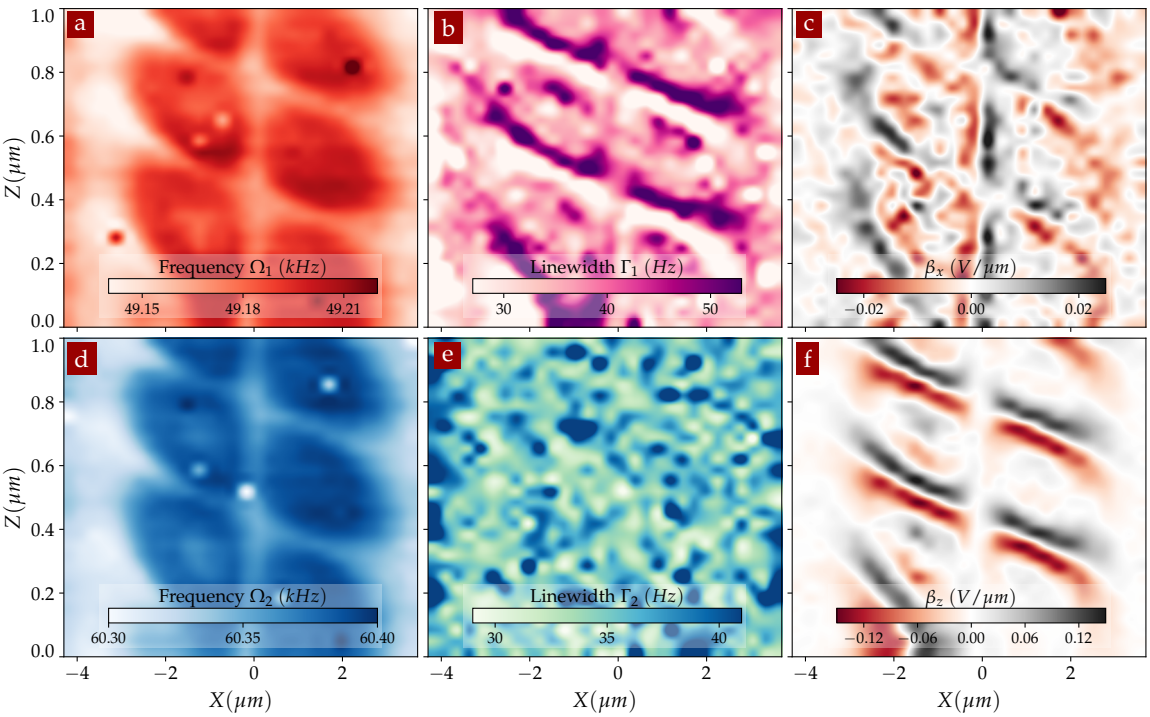

FIGURE 5.23 – $2D$ map of the mechanical properties of the NW measured through the scatter signal, when scanned through the cavity mode TM_{12}. Both mode exhibit a shift in frequency (a,d), while only the linewidth of the low-frequency mode seems to be affected (b,e). The measurement vectors β_x and β_z are also shown (c,f)

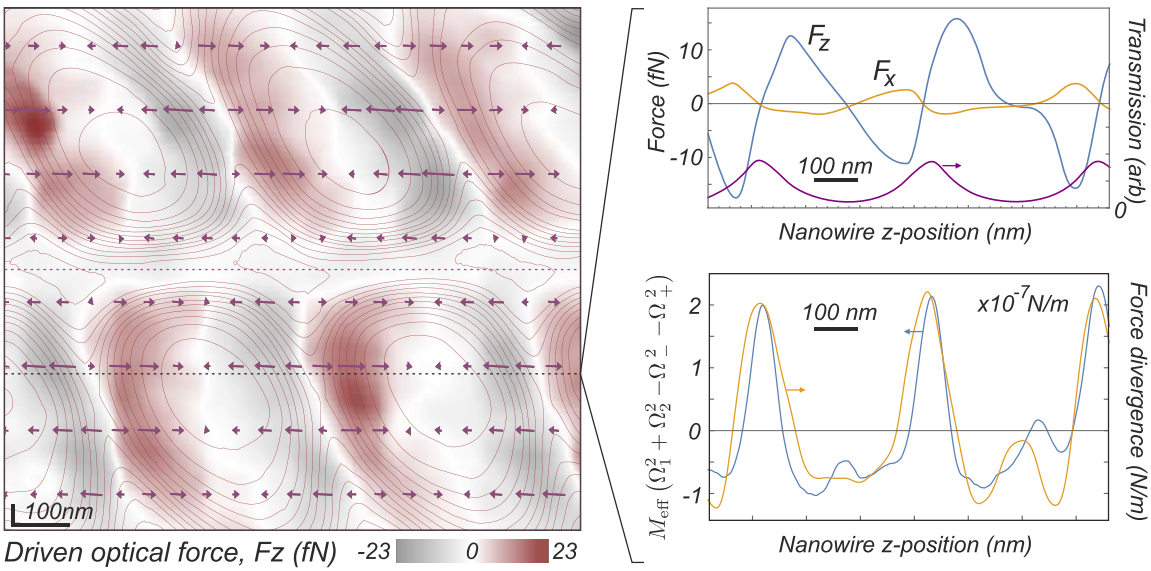

FIGURE 5.24 – Force map measured when locking the cavity on a TM_{12} optical mode. The force field is essentially oriented along the optical axis for this nanowire and cavity dimensions. The phenomenology observed is very similar to the one observed with the same nanowire on the TM_{00} mode.

CONCLUSION AND FUTURE DEVELOPMENTS

In this final section we discuss the future applications and developments following the exposed work and the results achieved. Several questions have emerged for both experiments and will constitute the focus of future investigations, together with the exciting possibility of combining both apparatus to achieve novel regime in cavity nano-optomechanics.

NANOWIRES AT DILUTION TEMPERATURE

Probing the Brownian motion of a nanomechanical resonator at dilution temperature was a challenging task, which required to overcome multiple difficulties, both scientific and technical. In this work we described in great detail the realization of the optical apparatus capable of working reliably from room to dilution temperatures. A new optical readout technique, making use of APD detectors working in the photon-counting regime, has allowed to demonstrate the thermalisation of the sensor at the base temperature of the cryostat, and to achieve new record force sensitivities for a scanning force probe system.

Making use of a SIONLUDI dilution fridge, we investigated the mechanical and thermal properties of ultralong silicon-carbide nanowires. The cryogenic system has been carefully designed and realized in order to isolate the experiment from all possible external noise sources, both mechanical and electrical. The optical head has been suspended above the cold plate of the cryostat in order to filter the residual noise coming from the helium mixture circulating in the dilution unit.

We have shown that it is possible to probe the Brownian motion of a nanomechanical force sensor thermalised at a temperature of 32 mK, comparable with the temperature of the sample holder at 27 mK. New record force sensitivity for a scanning force probe were also demonstrated, down to $\sim 40\,\mathrm{zN}/\sqrt{\mathrm{Hz}}$ at 20 mK. New force field sensing techniques based on coherently driven trajectories have been proven to work at those low temperatures, opening the door to the actual use of SiC nanowires as ultrasensitive $2D$ force field sensors at dilution temperature.

PERSPECTIVES AND APPLICATIONS After having demonstrated that it is possible to perform optical measurements on our ultrasentive force sensor at dilution temperature, several fundamental question still need to be answered, while at same time several application can start to be put into place.

On a fundamental level, the thermal properties and the heat propagation mechanisms inside the nanowires at low temperature still need to be fully understood and explained. To approach this problem it is necessary to pursue multiple strategies: first it is mandatory to test several other samples to increase the statistics and corroborate our observations, while at the same time investigating the impact of different geometries (lengths, diameters) and the role of crystal defects and surface condition. We showed that all the samples studied up to this moment present an oxide crust: we expect that removing this layer can have a substantial impact both on the mechanical and on the thermal properties of the resonator. Finally we will implement a two laser pump-probe scheme, where the intensity of a pump green laser is modulated in order to induce a thermal wave propagating within the nanowire, while a red probe laser will be used to investigate how it propagates inside the material. This kind of measurement has already been used in the group to investigate the properties of silicon carbide nanowires at room temperature [232]; several tests have already been performed on the cryogenic setup at 300 K (see fig. 5.25) and should readily be transposed down to low temperatures.

During our investigations, we faced several other phenomena which still need a proper explanation. *NW*1 in particular exhibited a peculiar systematic shift or jump in frequency when scanning the power of the probe laser, as can be seen in fig. 5.26. The striking fact

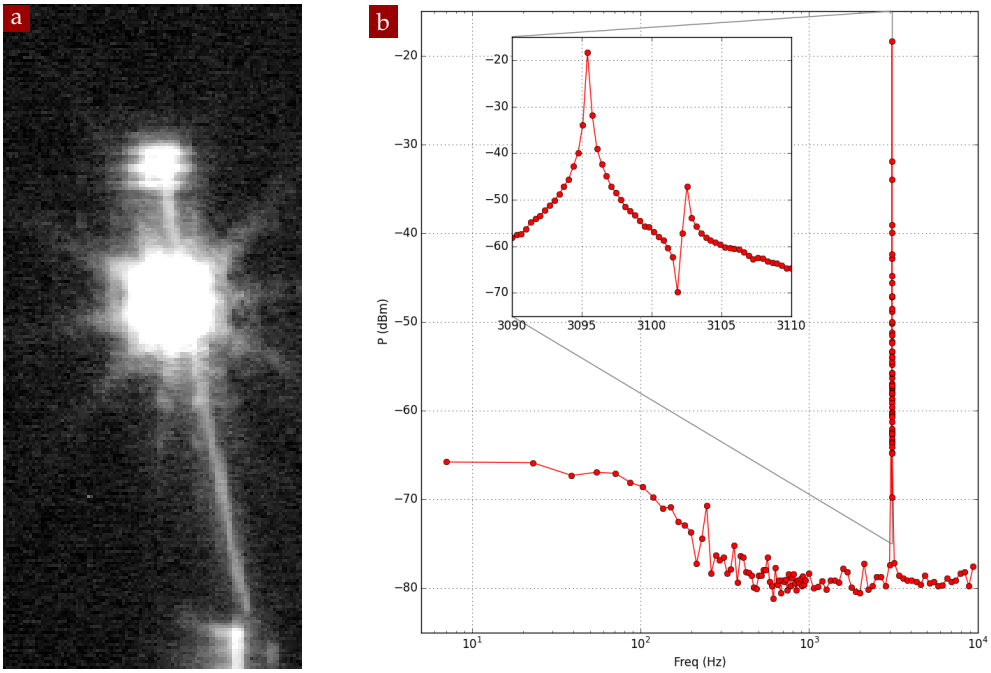

FIGURE 5.25 – Pump-probe measurements used to coherently drive the nanowire into coherent motion and to investigate the thermal properties of SiC nanowires (here at 300 K): (a) zoomed image of the nanowire *NW*1 where the pump green laser (top) and the red probe laser (bottom) are both visible. (b) mechanical and photothermal response of the system to an optical excitation produced by an intensity modulated green pump laser, whose frequency modulation is swept from a few Hertz up to 10 kHz. The low pass thermal response (70 Hz cutoff) observed at low frequencies permits to determine the heat diffusion coefficient in the nanowire. Similar measurements realized at different positions along the nanowire will allow to further investigate the heat conduction mechanism at dilution temperatures.

about this measurement is its magnitude and its reproducibility: compared to the frequency inversion due to amorphous contribution described in section 3.2.4, that tend to be of a few tens of mHz, here we observed a frequency shift larger than 1 Hz. Unfortunately at the time the noise temperature of the nanowire was affected by internal cryostat vibrations and could not be properly calibrated (around 400 mK at low powers). However, from our subsequent investigations, we can affirm that this kind of drive does not affect the mechanical properties of the resonator and that the frequency remains a good marker of its temperature. This effect was observed on one single sample and it is premature to promote any conclusion; nonetheless, the results reported in the figure refer to several sets of data, some of which were recorded more than one month apart, making this shift robust and well reproducible.

In order to further evaluate the frequency properties of this resonator, it will be interesting to measure the Allan variance of our nanowires, in particular to establish their frequency stability compared to other systems, which is an important requirement in many precision applications. Our preliminary measurements indicate an exceptional stability of the system.

Concerning the optical components, a new generation of cryogenic objectives is under development and will be based on aspherical lenses with a higher numerical aperture of 0.83, while trying to partially compensate their chromatic aberrations using a triple set of lenses. To enhance the nanowire reflectivity and thus the measurement efficiency, it could also be possible to engineer the NWs surface with a photonic-crystal-like structure, which could also be designed to reduce its absorption by localising the light out of the material

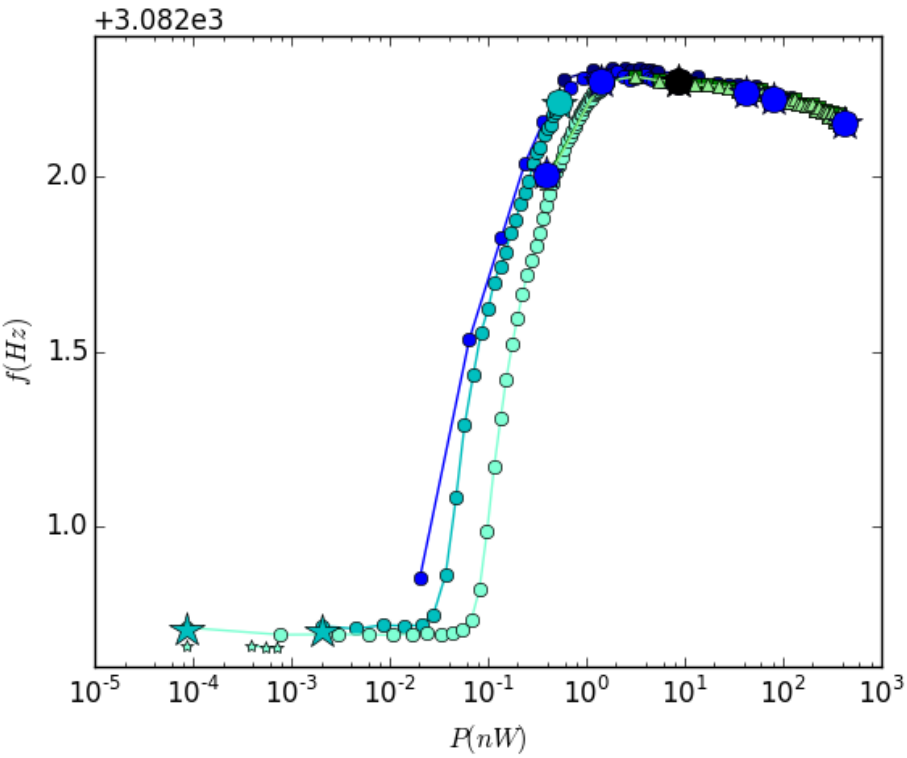

FIGURE 5.26 – Unexplained frequency signature: *NW*1 exhibited an unexpected jump in frequency when scanning the injected power. The frequency difference is of the order of a few Hertz, roughly two orders of magnitude bigger than the frequency shift induced by TLS effects. This measurements have been repeated several times over a period of more than one month: they result consistent and well reproducible, but they haven't been observed on others samples.

(see fig. 5.27a). The optical apparatus developed and the low-power techniques can also be employed to study other kinds of systems. As an example, we were able to measure the mechanical properties of silicon-nitride nanowires from the group of E. Collin and A. Fefferman at Institut Néel (such as the one shown in fig. 5.27b), but also doubly clamped ultralong (600 µm) nanowires microfabricated by B. Fernandez and S. Dufresnes from Nanofab out of high stress silicon-nitride membrane. This kind of resonators are usually probed using electrical methods and, given the use of superconductive material on the contact, are hardly employed at temperatures above 10 K. An optical probe instead allows to investigate them from room to dilution temperature and to have an alternative measurements method to compare with the electromechanical ones.

Finally, the next step consists in employing our ultrasensitive nano-resonators to map a force real field at dilution temperature and in particular to exploit their extraordinary sensitivity to investigate novel kinds of physics. To do so, we need to approach their vibrating extremity above a sample of interest, which requires a second XYZ scanner stage in the experiment, which we envision to mount on the transmission tower. Among the possible experiments and applications that can be imagined, we can think of scanning our nanowire above a single-electron-transistor (SET) island and try to detect the displacement induced by the presence of one single electron. The nanowires can also be functionalised by attaching a magnetic nanoparticle at their extremity and using it to investigate magnetic structures such as vortices, in particular in superconductors, or skyrmions. Alternatively, they can be coupled to a NV-center or to a quantum dot to realize an hybrid quantum mechanical system, taking advantage of the ultralow temperatures to study phenomena that otherwise can be masked or limited by the thermal noise at room temperature.

Several other related project are also ongoing, among which the attempt to try to optically detect carbon nanotubes and graphene membranes as well as the development of a Raman spectroscopy experiment at dilution temperature through the work of L. Marty, N. Bendiab, C. Felix and L. Del'Rey.

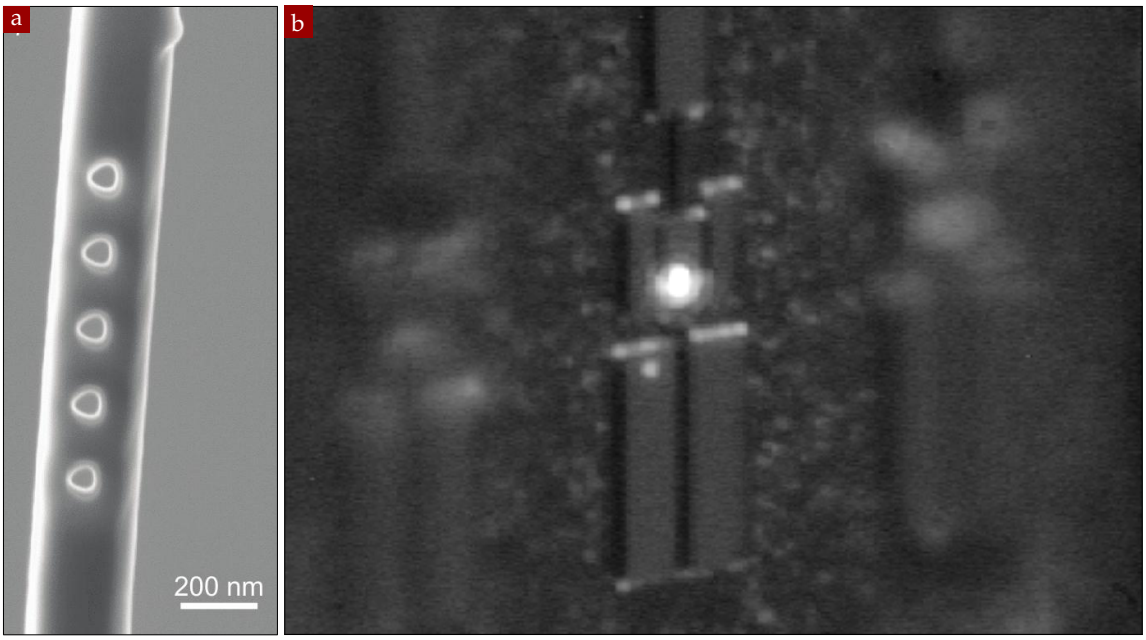

FIGURE 5.27 – (a) Hole in a SiC nanowire made with a FIB (J.F. Motte, Néel Institute). This could allow to realize photonic crystal on the tip of a NW to increase its reflectivity. (b) laser beam focus on the structure that support a SiN nanowire (E. Collin, Néel Institute).

NIM AT ROOM TEMPERATURE

By decoupling the mechanical and the optical degrees of freedom, it was possible to reduce the size of the first while preserving a high-quality optical cavity for the second. In this work we showed that by employing silicon-carbide nanowires inserted in a fiber micro-cavity it was possible to enter the unexplored ultra-strong coupling regime of cavity optomechanics, where one single photon should displace the oscillator by more than its zero-point-fluctuations, requiring $g_0 \gg \Omega_m$.

The realization of a versatile experiment together with the choice of a nanowire-in-the-middle (NIM) configuration, has allowed the demonstration of an optomechanical system which exhibits an (ultra-)strong interaction between the light and the mechanics. Being able to tune multiple parameters of the system, from the cavity length to the laser wavelength, from the NW diameter to the cavity resonant mode, we optimized our system to achieve the largest single-photon-coupling. Working with a typical cavity length of $\sim 10\,\mu m$, NWs diameter between 100 and 200 nm and wavelength around 770 nm, we demonstrated coupling strength up to $g_0^z/2\pi = 2.6\,\text{MHz} \approx 100 \times \Omega_m/2\pi$, which means that we largely enter the ultra-strong coupling regime.

We realized a dual characterization of the optomechanical coupling: using nanowire mediated scanning probe measurement of the cavity field, we were able to image the intracavity field in space and to map the optomechanical interaction as a function of the NW position inside the optical mode, while at the same time we realized a vectorial map of the force exerted on the nanowire by the intracavity light field. We investigated the impact of the light polarization on the OM interaction and how it can affect the magnitude of both the parametric frequency shifts and the light scattering. We realized similar measurements not only on the fundamental TM_{00} cavity mode, but also for higher order transverse optical modes of the cavity. In particular, the nanowire can be used to couple several modes at the same time, opening the doors to multimodes optomechanics, both on the optical and mechanical sides, which will constitute an interesting direction for future investigation.

PERSPECTIVES The simple model we described in section 4.4, based on the interaction between a Gaussian beam and a squared nanowire, can qualitatively explain most of our experimental observations and has been a practical tool to reduce the large parameters space we have access to. However it is not a quantitative model and a more refined one is needed to correctly account for the light diffusion in the system.

A significantly more advanced model is currently under investigation, both analytically (thanks to the work of A. Reigue in our group) and numerically in collaboration with G. Bachelier. Among other things, it takes into account the internal optical resonances hosted in a large refractive index and sub-wavelength sized object [238] (Mie resonances, see section 3.1.3). It describes the interaction between an infinite cylinder and the fundamental mode of a Fabry-Pérot cavity with curved mirrors and has permitted to optimize our system to reach large coupling strength while preserving the cavity quality. Some preliminary results are shown in fig. 5.28 where the expected transmission, scatter and reflection channels are shown for both polarisations of the pump field. This type of analysis in the model allows to investigate and compare how the maximum frequency shift varies as a function of the NW diameter and of the light polarization: the results, presented in fig. 5.29 are really useful when choosing a new sample and has proven to be accurate when compared to the NWs examined up to this moment.

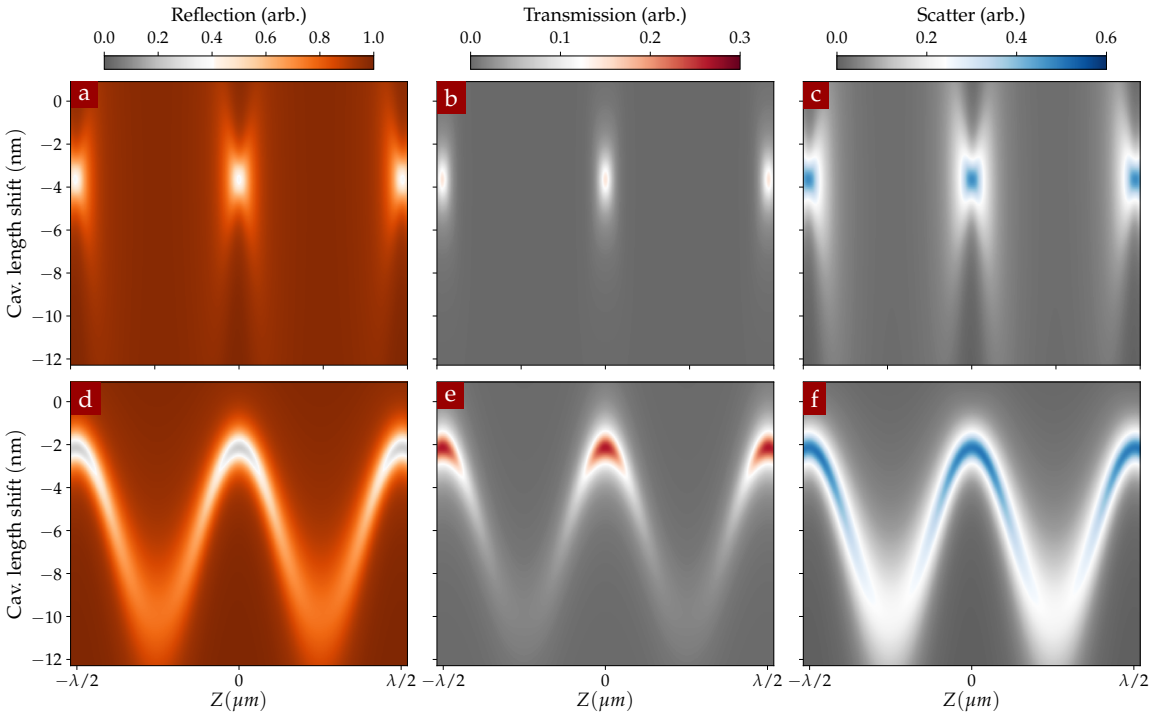

FIGURE 5.28 – Analytical simulation of the resonance frequency shift when moving the NW along the optical (Z) axis, taking into account the internal optical (Mie) resonances of the nanowires. The results for the reflected, transmitted and scattered signal, for both the parallel (a, b, c) and perpendicular polarization (d, e, f), are shown. The simulations have been realized for a cavity of length $L = 12.44\,\mu m$, mirrors with radius of curvature $\mathcal{R} = 28\,\mu m$ and reflectivity $R_A = R_B = 0.994$, wavelength $\lambda = 770\,nm$ and a nanowire with diameter $D = 130\,nm$.

The simulation are also used to compute the optical force exerted on the nanowire and to predict possible regions where the optical forces are non-conservative. Experimentally, a full $2D$ vectorial readout of the mechanical trajectories will shortly be implemented, allowing for a more robust measurement of the transverse force along the X direction, which is necessary to access the rotational character of the force field.

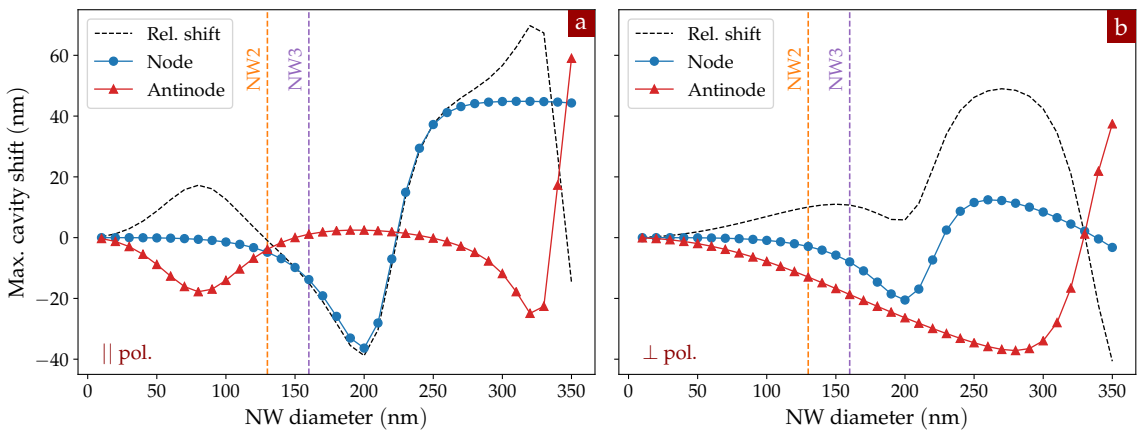

FIGURE 5.29 – Simulation of the maximum frequency shift that can be expected in a NIM system as a function of the NW diameter, both for the parallel (a) and perpendicular (b) polarisation. The simulations have been realized for a cavity of length $L = 12.1\,\mu m$, mirrors with radius of curvature $\mathcal{R} = 28\,\mu m$ and reflectivity $R_A = R_B = 0.994$, wavelength $\lambda = 770\,nm$.

All the force sensing results presented in this work have been obtained while locking the cavity at resonance and for moderate powers. In the near future it will be interesting to study the dynamical back action in the system, and in particular using feedback techniques in $2D$. The anticipated rotational character of the intracavity force field, coupled to the cavity physics should be interesting to investigate. Furthermore, operating with longer cavities and slightly shorter nanowires, should permit to have the mechanical resonance and the cavity linewidth becoming comparable, which opens a rather interesting regime when combining cavity optomechanical back action and rotational optomechanical coupling profiles. The retarded forces arising from light absorption will be studied in further detail and, taking advantage of the strong interaction and of the bad-cavity limits, it will be interesting to implement cooling protocols in this regime, with the novelty of having a quasi frequency degenerated dual oscillator [70, 84, 211, 172]. The realization of a similar experiment with a slightly asymmetric cavity has been suggested to be a good candidate for the realization of quantum-limited measurements in the bad-cavity limit [192].

NIM AT ULTRA-LOW TEMPERATURE

The most important outcomes of this work are the promising results which can be expected when combining the ultra-strong interaction of a NIM approach with a nanowire thermalised at 20 mK.

We stated in our introduction that the single-photon regime of cavity optomechanics is a long-standing goal of the field. In the resolved side-band regime this would allow the realization of the single-photon-blockade and of the quantum entanglement of macroscopic mechanical systems, as well as the implementation of several quantum protocols of non-linear optomechanics. In the adiabatic cavity limit, the system becomes extremely interesting as an advanced platform for quantum optics objectives.

Operating with ultrasentive kHz nanowires, such as the ones we employed at dilution temperature, should permit to reach single photon coupling strength up to ~ 7 MHz (due to their larger zero-point-fluctuations), while the low temperature operation should allow to reduce the spreading of their thermal fluctuations $\Delta\mathbf{r}^{\text{th}}$ down to ~ 500 times their zero-point-fluctuations, when thermalised at 20 mK. If we estimate the static displacement induced by one single photon, we would now reach $\delta x^{(1)} \approx 8000 x_{\text{zpf}} =\approx 15\Delta x^{\text{th}}$: this displacement should be largely detectable on top of the nanowire thermal noise. Such

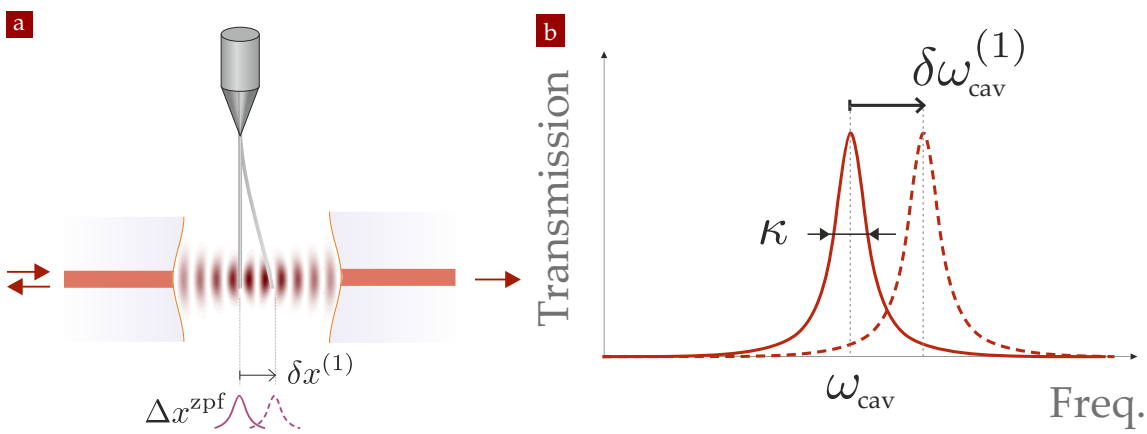

FIGURE 5.30 – (a) single-photon recoil. (b) single-photon bistability.

a static displacement $\delta x^{(1)}$ could then be independently measured with a second non-resonant laser, opening the road towards QND measurements at ultra low optical fluxes. Finally, this static displacement $\delta x^{(1)}$ should in turn generate a corresponding parametric shift of the cavity resonance due to one single intracavity photon, $\delta\omega_0^{(1)} = g_0 \delta x^{(1)}/x_{\mathrm{zpf}}$. If the latter becomes larger than the cavity linewidth κ, the system would then present a static optomechanical bistability at the single intracavity photon level, thus exhibiting a Kerr non-linearity for ultralow pumping powers. This regime is reached when the single photon parametric cooperativity becomes larger than unity $\mathcal{C}^{(1)} \equiv g_0^2/\Omega_{\mathrm{m}}\kappa > 1$: in our case we should be able to achieve $\mathcal{C}^{(1)} \approx 10$ even for a modest cavity linewidth (6 GHz).

Those considerations are thus a strong incentive for the realization of a Nanowire-In-the-Middle experiment at dilution temperature, which would allow to explore with a macroscopic oscillator the regime of single-photon optomechanics, where mean-field theories are not pertinent anymore.

BIBLIOGRAPHY

ARTICLES

1. "A gravitational wave observatory operating beyond the quantum shot-noise limit". *Nature Physics* **7,** 962–965 (Dec. 2011). (Cit. on p. 4)
2. Abbott, B. *et al.* "Observation of a kilogram-scale oscillator near its quantum ground state". *New Journal of Physics* **11,** 073032 (July 2009). (Cit. on p. 5)
3. Abelès, F. "La théorie générale des couches minces". *J. Phys. Radium* **11,** 307–309 (1950). (Cit. on p. 104)
4. Akcay, C., Parrein, P. & Rolland, J. P. "Estimation of longitudinal resolution in optical coherence imaging". *Applied Optics* **41,** 5256 (Sept. 1, 2002). (Cit. on p. 47)
5. Albrecht, R., Bommer, A., Deutsch, C., Reichel, J. & Becher, C. "Coupling of a Single Nitrogen-Vacancy Center in Diamond to a Fiber-Based Microcavity". *Physical Review Letters* **110,** 243602 (June 12, 2013). (Cit. on p. 103)
6. Albrecht, R. *et al.* "Narrow-band single photon emission at room temperature based on a single nitrogen-vacancy center coupled to an all-fiber-cavity". *Applied Physics Letters* **105,** 073113 (Aug. 18, 2014). (Cit. on p. 103)
7. Albrecht, T. R., Grütter, P., Horne, D. & Rugar, D. "Frequency modulation detection using high-Q cantilevers for enhanced force microscope sensitivity". *Journal of Applied Physics* **69,** 668–673 (Jan. 15, 1991). (Cit. on p. 71)
8. Allen, J. F. & Misener, A. D. "Flow Phenomena in Liquid Helium II". *Nature* **142,** 643–644 (Oct. 1938). (Cit. on p. 31)
9. Alles, H. *et al.* "Cooled video camera for optical investigations below 1 mK". *Review of Scientific Instruments* **65,** 1784–1785 (May 1, 1994). (Cit. on p. 43)
10. Anderson, M. H., Ensher, J. R., Matthews, M. R., Wieman, C. E. & Cornell, E. A. "Observation of Bose-Einstein Condensation in a Dilute Atomic Vapor". *Science* **269,** 198–201 (1995). (Cit. on p. 4)
11. Anderson, P. w., Halperin, B. I. & Varma, c. M. "Anomalous low-temperature thermal properties of glasses and spin glasses". *The Philosophical Magazine: A Journal of Theoretical Experimental and Applied Physics* **25,** 1–9 (Jan. 1, 1972). (Cit. on p. 85)
12. Andreani, L. C., Panzarini, G. & Gérard, J.-M. "Strong-coupling regime for quantum boxes in pillar microcavities: Theory". *Physical Review B* **60,** 13276–13279 (Nov. 15, 1999).(Cit. on p. 108)
13. Anetsberger, G. *et al.* "Near-field cavity optomechanics with nanomechanical oscillators". *Nature Physics* **5,** 909–914 (Dec. 2009). (Cit. on pp. 26, 71 and 102)
14. Anetsberger, G. *et al.* "Measuring nanomechanical motion with an imprecision below the standard quantum limit". *Physical Review A* **82,** 061804 (Dec. 29, 2010). (Cit. on p. 4)
15. Arcizet, O., Cohadon, P.-F., Briant, T., Pinard, M. & Heidmann, A. "Radiation-pressure cooling and optomechanical instability of a micromirror". *Nature* **444,** 71–74 (Nov. 2006). (Cit. on pp. 5 and 43)
16. Arcizet, O. *et al.* "A single nitrogen-vacancy defect coupled to a nanomechanical oscillator". *Nature Physics* **7,** 879–883 (Nov. 2011). (Cit. on pp. 5, 17 and 64)
17. Ashkin, A. "Trapping of Atoms by Resonance Radiation Pressure". *Physical Review Letters* **40,** 729–732 (Mar. 20, 1978). (Cit. on p. 4)

18. Aspelmeyer, M., Kippenberg, T. J. & Marquardt, F. "Cavity optomechanics". *Reviews of Modern Physics* **86,** 1391–1452 (Dec. 30, 2014). (Cit. on pp. 4, 6, 11 and 14)

19. Bechelany, M., Brioude, A., Cornu, D., Ferro, G. & Miele, P. "A Raman Spectroscopy Study of Individual SiC Nanowires". *Advanced Functional Materials* **17,** 939–943 (2007).(Cit. on pp. 20, 64 and 65)

20. Bechhoefer, J. "Feedback for physicists: A tutorial essay on control". *Reviews of Modern Physics* **77,** 783–836 (Aug. 31, 2005). (Cit. on p. 151)

21. Benedikter, J. *et al.* "Transverse-mode coupling and diffraction loss in tunable Fabry–Pérot microcavities". *New Journal of Physics* **17,** 053051 (May 2015). (Cit. on p. 153)

22. Berman, R., Foster, E. L., Ziman, J. M. & Simon, F. E. "Thermal conduction in artificial sapphire crystals at low temperatures I. Nearly perfect crystals". *Proceedings of the Royal Society of London. Series A. Mathematical and Physical Sciences* **231,** 130–144 (July 19, 1955). (Cit. on p. 88)

23. Black, E. D. "An introduction to Pound–Drever–Hall laser frequency stabilization". *American Journal of Physics* **69,** 79–87 (Dec. 15, 2000). (Cit. on p. 150)

24. Bleszynski-Jayich, A. C., Shanks, W. E. & Harris, J. G. E. "Noise thermometry and electron thermometry of a sample-on-cantilever system below 1Kelvin". *Applied Physics Letters* **92,** 013123 (Jan. 7, 2008). (Cit. on pp. 26 and 94)

25. Bon, J. *et al.* "Cryogenic optomechanic cavity in low mechanical loss material". *Journal of Applied Physics* **124,** 073104 (Aug. 17, 2018). (Cit. on p. 43)

26. Bose, S., Jacobs, K. & Knight, P. L. "Preparation of nonclassical states in cavities with a moving mirror". *Physical Review A* **56,** 4175–4186 (Nov. 1, 1997). (Cit. on p. 5)

27. Braakman, F. R. & Poggio, M. "Force sensing with nanowire cantilevers". *Nanotechnology* **30,** 332001 (May 2019). (Cit. on p. 25)

28. Braginsky, V. B. & Manukin, A. B. "Ponderomotive effects of electromagnetic radiation". *Soviet Physics Jetp* **25,** 653–655 (Oct. 1967). (Cit. on pp. 4 and 5)

29. Braginsky, V. B., Manukin, A. B. & Tikhonov, M. Y. "Investigation of Dissipative Ponderomotive Effects of Electromagnetic Radiation". *Soviet Physics Jetp* **31,** 829–830 (Nov. 1970). (Cit. on pp. 4 and 5)

30. Braginsky, V. B., Vorontsov, Y. I. & Thorne, K. S. "Quantum Nondemolition Measurements". *Science* **209,** 547–557 (Aug. 1, 1980). (Cit. on p. 4)

31. Brennecke, F., Ritter, S., Donner, T. & Esslinger, T. "Cavity Optomechanics with a Bose-Einstein Condensate". *Science* **322,** 235–238 (Oct. 10, 2008). (Cit. on pp. 4, 14 and 145)

32. Brooks, D. W. C. *et al.* "Non-classical light generated by quantum-noise-driven cavity optomechanics". *Nature* **488,** 476–480 (Aug. 2012). (Cit. on p. 4)

33. Callen, H. B. & Welton, T. A. "Irreversibility and Generalized Noise". *Physical Review* **83,** 34–40 (July 1, 1951). (Not cited)

34. Casabone, B. *et al.* "Cavity-enhanced spectroscopy of a few-ion ensemble in Eu3$\mathplus$:Y2O3". *New Journal of Physics* **20,** 095006 (Sept. 2018). (Cit. on p. 103)

35. Casimir, H. B. G. "Note on the conduction of heat in crystals". *Physica* **5,** 495–500 (June 1, 1938). (Cit. on p. 88)

36. Caves, C. M. "Quantum-Mechanical Radiation-Pressure Fluctuations in an Interferometer". *Physical Review Letters* **45,** 75–79 (July 14, 1980). (Cit. on p. 4)

37. Caves, C. M. "Quantum-mechanical noise in an interferometer". *Physical Review D* **23,** 1693–1708 (Apr. 15, 1981). (Cit. on p. 4)

38. Caves, C. M., Thorne, K. S., Drever, R. W. P., Sandberg, V. D. & Zimmermann, M. "On the measurement of a weak classical force coupled to a quantum-mechanical oscillator. I. Issues of principle". *Reviews of Modern Physics* **52,** 341–392 (Apr. 1, 1980). (Cit. on p. 4)

39. Chan, J. *et al.* "Laser cooling of a nanomechanical oscillator into its quantum ground state". *Nature* **478,** 89–92 (Oct. 2011). (Cit. on pp. 4, 5, 102 and 145)

40. Chaste, J. *et al.* "A nanomechanical mass sensor with yoctogram resolution". *Nature Nanotechnology* **7,** 301–304 (May 2012). (Cit. on pp. 4 and 26)

41. Chen, Y. "Macroscopic quantum mechanics: theory and experimental concepts of optomechanics". *Journal of Physics B: Atomic, Molecular and Optical Physics* **46,** 104001 (2013). (Cit. on p. 4)

42. Childress, L. *et al.* "Cavity optomechanics in a levitated helium drop". *Physical Review A* **96,** 063842 (Dec. 29, 2017). (Cit. on p. 4)

43. Cimalla, V., Pezoldt, J. & Ambacher, O. "Group III nitride and SiC based MEMS and NEMS: materials properties, technology and applications". *Journal of Physics D: Applied Physics* **40,** 6386–6434 (Oct. 2007). (Cit. on p. 64)

44. Classen, J., Burkert, T., Enss, C. & Hunklinger, S. "Anomalous Frequency Dependence of the Internal Friction of Vitreous Silica". *Physical Review Letters* **84,** 2176–2179 (Mar. 6, 2000). (Cit. on p. 85)

45. Classen, J., Enss, C., Bechinger, C., Weiss, G. & Hunklinger, S. "Low frequency acoustic and dielectric measurements on glasses". *Annalen der Physik* **506,** 315–335 (1994). (Cit. on p. 84)

46. Clerk, A. A., Devoret, M. H., Girvin, S. M., Marquardt, F. & Schoelkopf, R. J. "Introduction to quantum noise, measurement, and amplification". *Reviews of Modern Physics* **82,** 1155–1208 (Apr. 15, 2010). (Cit. on pp. 4, 6 and 8)

47. Clerk, A. A. "Optomechanics and quantum measurement". *Les Houches 2015 Summer School on Optomechanics,* 56 (2015). (Cit. on p. 6)

48. Cohadon, P. F., Heidmann, A. & Pinard, M. "Cooling of a Mirror by Radiation Pressure". *Physical Review Letters* **83,** 3174–3177 (Oct. 18, 1999). (Cit. on p. 5)

49. Colombe, Y. *et al.* "Strong atom–field coupling for Bose–Einstein condensates in an optical cavity on a chip". *Nature* **450,** 272–276 (Nov. 2007). (Cit. on p. 103)

50. Cousins, D. J. *et al.* "An Advanced Dilution Refrigerator Designed for the New Lancaster Microkelvin Facility". *Journal of Low Temperature Physics* **114,** 547–570 (Mar. 1, 1999).(Cit. on p. 32)

51. Danilishin, S. L. & Khalili, F. Y. "Quantum Measurement Theory in Gravitational-Wave Detectors". *Living Reviews in Relativity* **15,** 5 (Apr. 26, 2012). (Cit. on pp. 4 and 6)

52. Davis, K. B. *et al.* "Bose-Einstein Condensation in a Gas of Sodium Atoms". *Physical Review Letters* **75,** 3969–3973 (Nov. 27, 1995). (Cit. on p. 4)

53. De Liberato, S., Lambert, N. & Nori, F. "Quantum noise in photothermal cooling". *Physical Review A* **83,** 033809 (Mar. 8, 2011). (Cit. on p. 103)

54. De Bonis, S. L. *et al.* "Ultrasensitive Displacement Noise Measurement of Carbon Nanotube Mechanical Resonators". *Nano Letters* **18,** 5324–5328 (Aug. 8, 2018). (Cit. on pp. 26 and 94)

55. De Lépinay, L. M., Pigeau, B., Besga, B., Fogliano, F. & Arcizet, O. "Thermal noise squeezing generated by circulating optical forces". *In preparation* (2019). (Cit. on p. xx)

56. De Lépinay, L. M. *et al.* "A universal and ultrasensitive vectorial nanomechanical sensor for imaging 2D force fields". *Nature nanotechnology* **12,** 156 (2017).(Cit. on pp. 17, 18, 56, 57, 61, 64, 162 and 163)

57. De Waele, A. T. A. M. "Basic Operation of Cryocoolers and Related Thermal Machines". *Journal of Low Temperature Physics* **164,** 179 (June 10, 2011). (Cit. on p. 30)

58. De Wit, M. *et al.* "Vibration isolation with high thermal conductance for a cryogen-free dilution refrigerator". arXiv: 1810.06847 (Oct. 16, 2018). (Cit. on p. 40)

59. Degen, C. L., Poggio, M., Mamin, H. J., Rettner, C. T. & Rugar, D. "Nanoscale magnetic resonance imaging". *Proceedings of the National Academy of Sciences* **106,** 1313–1317 (Feb. 3, 2009). (Cit. on pp. 26 and 94)

60. Den Haan, A. M. J. *et al.* "Atomic resolution scanning tunneling microscopy in a cryogen free dilution refrigerator at 15 mK". *Review of Scientific Instruments* **85,** 035112 (Mar. 1, 2014). (Cit. on p. 40)

61. Des Cloizeaux, D. "Linear Response, Generalized Susceptibility and Dispersion Theory". *Theory of condensed matter. Lectures presented at an international course* (1968). (Not cited)

62. Ding, L. *et al.* "Wavelength-sized GaAs optomechanical resonators with gigahertz frequency". *Applied Physics Letters* **98,** 113108 (Mar. 14, 2011). (Cit. on p. 145)

63. Dorsel, A., McCullen, J. D., Meystre, P., Vignes, E. & Walther, H. "Optical Bistability and Mirror Confinement Induced by Radiation Pressure". *Physical Review Letters* **51,** 1550–1553 (Oct. 24, 1983). (Cit. on p. 5)

64. Dubrovskii, G. B., Lepneva, A. A. & Radovanova, E. I. "Optical absorption associated with superlattice in silicon carbide crystals". *physica status solidi (b)* **57,** 423–431 (1973). (Cit. on p. 66)

65. Edelstein, W. A., Hough, J., Pugh, J. R. & Martin, W. "Limits to the measurement of displacement in an interferometric gravitational radiation detector". *Journal of Physics E: Scientific Instruments* **11,** 710–712 (July 1978). (Not cited)

66. Eichenfield, M., Camacho, R., Chan, J., Vahala, K. J. & Painter, O. "A picogram- and nanometre-scale photonic-crystal optomechanical cavity". *Nature* **459,** 550–555 (May 2009). (Cit. on p. 145)

67. Eichenfield, M., Chan, J., Safavi-Naeini, A. H., Vahala, K. J. & Painter, O. "Modeling dispersive coupling and losses of localized optical and mechanical modes in optomechanical crystals". *Optics Express* **17,** 20078–20098 (Oct. 26, 2009). (Cit. on p. 5)

68. Ekinci, K. L., Yang, Y. T. & Roukes, M. L. "Ultimate limits to inertial mass sensing based upon nanoelectromechanical systems". *Journal of Applied Physics* **95,** 2682–2689 (Feb. 19, 2004). (Cit. on p. 71)

69. Elouard, C., Besga, B. & Auffèves, A. "Probing the State of a Mechanical Oscillator with an Ultrastrongly Coupled Quantum Emitter". *Physical Review Letters* **122,** 013602 (Jan. 9, 2019). (Not cited)

70. Elste, F., Girvin, S. M. & Clerk, A. A. "Quantum Noise Interference and Backaction Cooling in Cavity Nanomechanics". *Physical Review Letters* **102,** 207209 (May 22, 2009).(Cit. on pp. 103 and 183)

71. Etaki, S. *et al.* "Motion detection of a micromechanical resonator embedded in a d.c. SQUID". *Nature Physics* **4,** 785–788 (Oct. 2008). (Cit. on p. 26)

72. Fabre, C. *et al.* "Quantum-noise reduction using a cavity with a movable mirror". *Physical Review A* **49,** 1337–1343 (Feb. 1, 1994). (Cit. on p. 5)

73. Favero, I. & Karrai, K. "Cavity cooling of a nanomechanical resonator by light scattering". *New Journal of Physics* **10,** 095006 (Sept. 2008). (Cit. on p. 103)

74. Favero, I. *et al.* "Fluctuating nanomechanical system in a high finesse optical microcavity". *Optics Express* **17,** 12813–12820 (July 20, 2009). (Cit. on pp. 5, 102 and 103)

75. Fefferman, A. D., Pohl, R. O., Zehnder, A. T. & Parpia, J. M. "Acoustic Properties of Amorphous Silica between 1 and 500 mK". *Physical Review Letters* **100,** 195501 (May 13, 2008). (Cit. on pp. 84 and 85)

76. Flowers-Jacobs, N. E. *et al.* "Fiber-cavity-based optomechanical device". *Applied Physics Letters* **101,** 221109 (Nov. 26, 2012). (Cit. on p. 103)

77. Flubacher, P., Leadbetter, A. J. & Morrison, J. A. "The heat capacity of pure silicon and germanium and properties of their vibrational frequency spectra". *The Philosophical Magazine: A Journal of Theoretical Experimental and Applied Physics* **4,** 273–294 (Mar. 1, 1959).(Cit. on p. 65)

78. Frossati, G. "Obtaining ultralow temperatures by dilution of 3He into 4He". *Journal de Physique Colloques* **39,** C6–1578–C6–1589 (C6 1978). (Cit. on p. 32)

79. Gallego, J. *et al.* "High-finesse fiber Fabry–Perot cavities: stabilization and mode matching analysis". *Applied Physics B* **122,** 47 (Mar. 10, 2016). (Cit. on p. 139)

80. Ganzhorn, M., Klyatskaya, S., Ruben, M. & Wernsdorfer, W. "Strong spin–phonon coupling between a single-molecule magnet and a carbon nanotube nanoelectromechanical system". *Nature Nanotechnology* **8,** 165–169 (Mar. 2013). (Cit. on p. 26)

81. Garcia, S., Maxein, D., Hohmann, L., Reichel, J. & Long, R. "Fiber-pigtailed optical tweezer for single-atom trapping and single-photon generation". *Applied Physics Letters* **103,** 114103 (Sept. 9, 2013). (Cit. on p. 103)

82. Gavartin, E., Verlot, P. & Kippenberg, T. J. "A hybrid on-chip optomechanical transducer for ultrasensitive force measurements". *Nature Nanotechnology* **7,** 509–514 (Aug. 2012).(Cit. on pp. 26 and 94)

83. Geitner, M., Aguilar Sandoval, F., Bertin, E. & Bellon, L. "Low thermal fluctuations in a system heated out of equilibrium". *Physical Review E* **95,** 032138 (Mar. 27, 2017).(Cit. on p. 85)

84. Genes, C., Ritsch, H. & Vitali, D. "Micromechanical oscillator ground-state cooling via resonant intracavity optical gain or absorption". *Physical Review A* **80,** 061803 (Dec. 7, 2009). (Cit. on pp. 103 and 183)

85. Gigan, S. *et al.* "Self-cooling of a micromirror by radiation pressure". *Nature* **444,** 67–70 (Nov. 2006). (Cit. on p. 5)

86. Gloppe, A. *et al.* "Bidimensional nano-optomechanics and topological backaction in a non-conservative radiation force field". *Nature Nanotechnology* **9,** 920–926 (Nov. 2014).(Cit. on pp. 17, 18, 25, 56, 57, 61, 162 and

87. Gozzini, A., Maccarrone, F., Mango, F., Longo, I. & Barbarino, S. "Light-pressure bistability at microwave frequencies". *JOSA B* **2,** 1841–1845 (Nov. 1, 1985). (Cit. on p. 5)

88. Guzmán Cervantes, F., Kumanchik, L., Pratt, J. & Taylor, J. M. "High sensitivity optomechanical reference accelerometer over 10 kHz". *Applied Physics Letters* **104,** 221111 (June 2, 2014). (Cit. on p. 4)

89. Hauer, B. D., Doolin, C., Beach, K. S. D. & Davis, J. P. "A general procedure for thermomechanical calibration of nano/micro-mechanical resonators". *Annals of Physics* **339,** 181–207 (Dec. 1, 2013). (Cit. on pp. 66 and 72)

90. Heidmann, A., Hadjar, Y. & Pinard, M. "Quantum nondemolition measurement by optomechanical coupling". *Applied Physics B* **64,** 173–180 (Jan. 1, 1997). (Cit. on p. 5)

91. Heisenberg, W. "Über den anschaulichen Inhalt der quantentheoretischen Kinematik und Mechanik". *Zeitschrift für Physik* **43,** 172–198 (Mar. 1, 1927). (Cit. on p. 6)

92. Heron, J. S., Fournier, T., Mingo, N. & Bourgeois, O. "Mesoscopic Size Effects on the Thermal Conductance of Silicon Nanowire". *Nano Letters* **9,** 1861–1865 (May 13, 2009). (Cit. on pp. 88 and 89)

93. Higginbotham, A. P. *et al.* "Harnessing electro-optic correlations in an efficient mechanical converter". *Nature Physics* **14,** 1038–1042 (Oct. 2018). (Cit. on p. 102)

94. Hood, C. J., Kimble, H. J. & Ye, J. "Characterization of high-finesse mirrors: Loss, phase shifts, and mode structure in an optical cavity". *Physical Review A* **64,** 033804 (Aug. 13, 2001). (Cit. on p. 109)

95. Hunger, D., Deutsch, C., Barbour, R. J., Warburton, R. J. & Reichel, J. "Laser micro-fabrication of concave, low-roughness features in silica". *AIP Advances* **2,** 012119 (Jan. 13, 2012).(Cit. on p. 125)

96. Hunger, D. *et al.* "A fiber Fabry–Perot cavity with high finesse". *New Journal of Physics* **12,** 065038 (2010). (Cit. on pp. 103, 107, 109, 124 and 125)

97. Jacobs, K., Tombesi, P., Collett, M. J. & Walls, D. F. "Quantum-nondemolition measurement of photon number using radiation pressure". *Physical Review A* **49,** 1961–1966 (Mar. 1, 1994). (Cit. on p. 5)

98. Janssen, P. J. C. *Académie des sciences. Comptes rendus hebdomadaires des séances de l'Académie des sciences* **67,** 494 (1868). (Cit. on p. 31)

99. Jayich, A. M. *et al.* "Dispersive optomechanics: a membrane inside a cavity". *New Journal of Physics* **10,** 095008 (Sept. 2008). (Cit. on p. 102)

100. Jensen, K., Kim, K. & Zettl, A. "An atomic-resolution nanomechanical mass sensor". *Nature Nanotechnology* **3,** 533–537 (Sept. 2008). (Cit. on p. 71)

101. Joyce, W. B. & DeLoach, B. C. "Alignment of Gaussian beams". *Applied Optics* **23,** 4187–4196 (Dec. 1, 1984). (Cit. on p. 109)

102. Kamerlingh Onnes, H. "The liquefaction of helium". *Proceedings of the royal netherlands academy of arts and science* **11,** 168–185 (1908). (Cit. on p. 31)

103. Kapitza, P. "Viscosity of Liquid Helium below the λ-Point". *Nature* **141,** 74 (Jan. 1938). (Cit. on p. 31)

104. Kaupp, H. *et al.* "Purcell-Enhanced Single-Photon Emission from Nitrogen-Vacancy Centers Coupled to a Tunable Microcavity". *Physical Review Applied* **6,** 054010 (Nov. 22, 2016). (Cit. on p. 103)

105. Knight, P. L. *et al.* "Magnetic microchip traps and single–atom detection". *Philosophical Transactions of the Royal Society of London. Series A: Mathematical, Physical and Engineering Sciences* **361,** 1375–1389 (July 15, 2003). (Cit. on pp. 103 and 107)

106. Kogelnik, H. & Li, T. "Laser Beams and Resonators". *Applied Optics* **5,** 1550–1567 (Oct. 1, 1966). (Cit. on pp. 104 and 107)

107. Krause, A. G., Winger, M., Blasius, T. D., Lin, Q. & Painter, O. "A high-resolution microchip optomechanical accelerometer". *Nature Photonics* **6,** 768–772 (Nov. 2012). (Cit. on p. 4)

108. Kubo, R. "The fluctuation-dissipation theorem". *Reports on Progress in Physics* **29,** 255 (1966). (Cit. on p. 8)

109. Kuhn, A. G. *et al.* "Free-space cavity optomechanics in a cryogenic environment". *Applied Physics Letters* **104,** 044102 (Jan. 27, 2014). (Cit. on p. 43)

110. LaHaye, M. D., Buu, O., Camarota, B. & Schwab, K. C. "Approaching the Quantum Limit of a Nanomechanical Resonator". *Science* **304,** 74–77 (Apr. 2, 2004). (Cit. on p. 26)

111. LaHaye, M. D., Suh, J., Echternach, P. M., Schwab, K. C. & Roukes, M. L. "Nanomechanical measurements of a superconducting qubit". *Nature* **459,** 960–964 (June 2009). (Cit. on p. 26)

112. Lassagne, B., Tarakanov, Y., Kinaret, J., Garcia-Sanchez, D. & Bachtold, A. "Coupling Mechanics to Charge Transport in Carbon Nanotube Mechanical Resonators". *Science* **325,** 1107–1110 (Aug. 28, 2009). (Cit. on p. 26)

113. Law, C. K. "Interaction between a moving mirror and radiation pressure: A Hamiltonian formulation". *Physical Review A* **51,** 2537–2541 (Mar. 1, 1995). (Cit. on p. 12)

114. Lecocq, F., Clark, J. B., Simmonds, R. W., Aumentado, J. & Teufel, J. D. "Quantum Nondemolition Measurement of a Nonclassical State of a Massive Object". *Physical Review X* **5,** 041037 (Dec. 7, 2015). (Cit. on p. 4)

115. Lee, C. *et al.* "Vibration isolation system for cryogenic phonon-scintillation calorimeters". *Journal of Instrumentation* **12,** C02057 (2017). (Cit. on p. 40)

116. Leijssen, R., La Gala, G. R., Freisem, L., Muhonen, J. T. & Verhagen, E. "Nonlinear cavity optomechanics with nanomechanical thermal fluctuations". *Nature Communications* **8,** ncomms16024 (July 7, 2017). (Cit. on pp. 4, 102 and 145)

117. Lépinay, L. M. d., Pigeau, B., Besga, B. & Arcizet, O. "Eigenmode orthogonality breaking and anomalous dynamics in multimode nano-optomechanical systems under non-reciprocal coupling". *Nature Communications* **9,** 1401 (Apr. 11, 2018). (Cit. on pp. 18, 25, 64, 163 and 170)

118. Li, D. *et al.* "Thermal conductivity of individual silicon nanowires". *Applied Physics Letters* **83,** 2934–2936 (Sept. 30, 2003). (Cit. on p. 88)

119. Liao, J.-Q., Huang, J.-F., Tian, L., Kuang, L.-M. & Sun, C.-P. "Generalized Ultrastrong Optomechanics". arXiv: 1802.09254 (Feb. 26, 2018). (Cit. on p. 14)

120. Liao, J.-Q., Wu, Q.-Q. & Nori, F. "Entangling two macroscopic mechanical mirrors in a two-cavity optomechanical system". *Physical Review A* **89,** 014302 (Jan. 10, 2014). (Cit. on p. 103)

121. Lifshitz, R. & Roukes, M. L. "Thermoelastic damping in micro- and nanomechanical systems". *Physical Review B* **61,** 5600–5609 (Feb. 15, 2000). (Cit. on p. 85)

122. LIGO Scientific Collaboration and Virgo Collaboration *et al.* "Observation of Gravitational Waves from a Binary Black Hole Merger". *Physical Review Letters* **116,** 061102 (Feb. 11, 2016). (Cit. on pp. 4 and 5)

123. Lin, G. J., Ho, J. C. & Dandekar, D. P. "Low-temperature heat capacities of silicon carbide". *Journal of Applied Physics* **61,** 5198–5198 (June 1, 1987). (Cit. on p. 65)

124. Lockyer, J. N. *Académie des sciences. Comptes rendus hebdomadaires des séances de l'Académie des sciences* **67,** 836 (1868). (Cit. on p. 31)

125. London, H., Clarke, G. R. & Mendoza, E. "Osmotic Pressure of He^3 in Liquid He^4, with Proposals for a Refrigerator to Work below 1° K". *Physical Review* **128,** 1992–2005 (Dec. 1, 1962). (Cit. on p. 32)

126. Macrí, V., Garziano, L., Ridolfo, A., Di Stefano, O. & Savasta, S. "Deterministic synthesis of mechanical NOON states in ultrastrong optomechanics". *Physical Review A* **94,** 013817 (July 8, 2016). (Cit. on p. 103)

127. Mader, M., Reichel, J., Hänsch, T. W. & Hunger, D. "A scanning cavity microscope". *Nature Communications* **6,** 7249 (June 24, 2015). (Cit. on p. 153)

128. Mamin, H. J. & Rugar, D. "Sub-attonewton force detection at millikelvin temperatures". *Applied Physics Letters* **79,** 3358–3360 (Nov. 8, 2001). (Cit. on pp. 26 and 94)

129. Mancini, S., Man'ko, V. I. & Tombesi, P. "Ponderomotive control of quantum macroscopic coherence". *Physical Review A* **55,** 3042–3050 (Apr. 1, 1997). (Cit. on p. 5)

130. Mancini, S. & Tombesi, P. "Quantum noise reduction by radiation pressure". *Physical Review A* **49,** 4055–4065 (May 1, 1994). (Cit. on p. 5)

131. Mancini, S., Vitali, D. & Tombesi, P. "Optomechanical Cooling of a Macroscopic Oscillator by Homodyne Feedback". *Physical Review Letters* **80,** 688–691 (Jan. 26, 1998). (Cit. on p. 5)

132. Marinković, I. *et al.* "Optomechanical Bell Test". *Physical Review Letters* **121,** 220404 (Nov. 29, 2018). (Cit. on p. 4)

133. Mason, D., Chen, J., Rossi, M., Tsaturyan, Y. & Schliesser, A. "Continuous force and displacement measurement below the standard quantum limit". *Nature Physics* **15,** 745–749 (Aug. 2019). (Cit. on p. 4)

134. McCullen, J. D., Meystre, P. & Wright, E. M. "Mirror confinement and control through radiation pressure". *Optics Letters* **9,** 193–195 (June 1, 1984). (Cit. on p. 102)

135. Meenehan, S. M. *et al.* "Thermalization properties at mK temperatures of a nanoscale optomechanical resonator with acoustic-bandgap shield". arXiv: 1403.3703 (Mar. 14, 2014). (Cit. on pp. 26 and 94)

136. Metcalfe, M. "Applications of cavity optomechanics". *Applied Physics Reviews* **1,** 031105 (Sept. 1, 2014). (Cit. on p. 4)

137. Metzger, C. H. & Karrai, K. "Cavity cooling of a microlever". *Nature* **432,** 1002–1005 (Dec. 2004). (Cit. on p. 5)

138. Meystre, P., Wright, E. M., McCullen, J. D. & Vignes, E. "Theory of radiation-pressure-driven interferometers". *JOSA B* **2,** 1830–1840 (Nov. 1, 1985). (Cit. on pp. 5 and 102)

139. Meystre, P. "A short walk through quantum optomechanics". *Annalen der Physik* **525,** 215–233 (Mar. 1, 2013). (Cit. on p. 4)

140. Monsel, J., Fellous-Asiani, M., Huard, B. & Auffèves, A. "A coherent quantum engine based on bath and battery engineering". arXiv: 1907.00812 (July 1, 2019). (Not cited)

141. Morelli, D. T., Heremans, J. P., Beetz, C. P., Yoo, W. S. & Matsunami, H. "Phonon-electron scattering in single crystal silicon carbide". *Applied Physics Letters* **63,** 3143–3145 (Dec. 6, 1993). (Cit. on p. 65)

142. Moser, J., Eichler, A., Güttinger, J., Dykman, M. I. & Bachtold, A. "Nanotube mechanical resonators with quality factors of up to 5 million". *Nature Nanotechnology* **9,** 1007–1011 (Dec. 2014). (Cit. on p. 4)

143. Moser, J. *et al.* "Ultrasensitive force detection with a nanotube mechanical resonator". *Nature Nanotechnology* **8,** 493–496 (July 2013). (Cit. on pp. 26 and 94)

144. Müller, K.-P. & Haarer, D. "Spectral diffusion of optical transitions in doped polymer glasses below 1 K". *Physical Review Letters* **66,** 2344–2347 (May 6, 1991). (Cit. on p. 43)

145. Murch, K. W., Moore, K. L., Gupta, S. & Stamper-Kurn, D. M. "Observation of quantum-measurement backaction with an ultracold atomic gas". *Nature Physics* **4,** 561–564 (July 2008). (Cit. on pp. 4, 14 and 145)

146. Niguès, A., Siria, A. & Verlot, P. "Dynamical backaction cooling with free electrons". *Nature Communications* **6,** 1–7 (Sept. 18, 2015). (Cit. on p. 26)

147. Nishiguchi, N., Ando, Y. & Wybourne, M. N. "Acoustic phonon modes of rectangular quantum wires". *Journal of Physics: Condensed Matter* **9,** 5751–5764 (July 1997). (Cit. on p. 89)

148. Oliphant, M. L. E., Kinsey, B. B. & Rutherford, E. "The transmutation of lithium by protons and by ions of the heavy isotope of hydrogen". *Proc. R. Soc. Lond. A* **141,** 722–733 (Sept. 1, 1933). (Cit. on p. 32)

149. Park, Y.-S. & Wang, H. "Resolved-sideband and cryogenic cooling of an optomechanical resonator". *Nature Physics* **5,** 489–493 (July 2009). (Cit. on p. 5)

150. Pelliccione, M., Sciambi, A., Bartel, J., Keller, A. J. & Goldhaber-Gordon, D. "Design of a scanning gate microscope for mesoscopic electron systems in a cryogen-free dilution refrigerator". *Review of Scientific Instruments* **84,** 033703 (Mar. 1, 2013). (Cit. on p. 40)

151. Perisanu, S. *et al.* "Mechanical properties of SiC nanowires determined by scanning electron and field emission microscopies". *Physical Review B* **77,** 165434 (Apr. 30, 2008). (Cit. on p. 17)

152. Peterson, G. A. *et al.* "Ultrastrong parametric coupling between a superconducting cavity and a mechanical resonator". arXiv: 1906.11353 (June 26, 2019). (Cit. on p. 4)

153. Peterson, R. W. *et al.* "Laser Cooling of a Micromechanical Membrane to the Quantum Backaction Limit". *Physical Review Letters* **116,** 063601 (Feb. 8, 2016). (Cit. on p. 43)

154. Petrak, B., Konthasinghe, K., Perez, S. & Muller, A. "Feedback-controlled laser fabrication of micromirror substrates". *Review of Scientific Instruments* **82,** 123112 (Dec. 1, 2011). (Cit. on p. 125)

155. Phillips, W. A. "Tunneling states in amorphous solids". *Journal of Low Temperature Physics* **7,** 351–360 (May 1, 1972). (Cit. on p. 85)

156. Pigeau, B. *et al.* "Observation of a phononic Mollow triplet in a multimode hybrid spin-nanomechanical system". *Nature Communications* **6,** 8603 (Oct. 19, 2015).(Cit. on pp. 17 and 64)

157. Pinard, M., Fabre, C. & Heidmann, A. "Quantum-nondemolition measurement of light by a piezoelectric crystal". *Physical Review A* **51,** 2443–2449 (Mar. 1, 1995). (Cit. on p. 5)

158. Pinard, M., Hadjar, Y. & Heidmann, A. "Effective mass in quantum effects of radiation pressure". *The European Physical Journal D - Atomic, Molecular, Optical and Plasma Physics* **7,** 107–116 (Aug. 1, 1999). (Cit. on pp. 71 and 72)

159. Pinard, M. *et al.* "Entangling movable mirrors in a double-cavity system". *EPL (Europhysics Letters)* **72,** 747 (Nov. 3, 2005). (Cit. on p. 43)

160. Pirkkalainen, J.-M., Damskägg, E., Brandt, M., Massel, F. & Sillanpää, M. A. "Squeezing of Quantum Noise of Motion in a Micromechanical Resonator". *Physical Review Letters* **115,** 243601 (Dec. 7, 2015). (Cit. on p. 4)

161. Poggio, M. *et al.* "An off-board quantum point contact as a sensitive detector of cantilever motion". *Nature Physics* **4,** 635–638 (Aug. 2008). (Cit. on p. 26)

162. Pohl, R. O., Liu, X. & Thompson, E. "Low-temperature thermal conductivity and acoustic attenuation in amorphous solids". *Reviews of Modern Physics* **74,** 991–1013 (Oct. 30, 2002). (Cit. on p. 85)

163. Pollack, G. L. "Kapitza Resistance". *Reviews of Modern Physics* **41,** 48–81 (Jan. 1, 1969). (Cit. on p. 30)

164. Purdy, T. P., Peterson, R. W. & Regal, C. A. "Observation of Radiation Pressure Shot Noise on a Macroscopic Object". *Science* **339,** 801–804 (Feb. 15, 2013). (Cit. on p. 43)

165. Purdy, T. P., Peterson, R. W., Yu, P.-L. & Regal, C. A. "Cavity optomechanics with Si3N4membranes at cryogenic temperatures". *New Journal of Physics* **14,** 115021 (Nov. 2012). (Cit. on p. 43)

166. Purdy, T. P., Yu, P.-L., Peterson, R. W., Kampel, N. S. & Regal, C. A. "Strong Optomechanical Squeezing of Light". *Physical Review X* **3,** 031012 (Sept. 3, 2013). (Cit. on p. 4)

167. Rabl, P. "Photon Blockade Effect in Optomechanical Systems". *Physical Review Letters* **107,** 063601 (Aug. 3, 2011). (Cit. on p. 14)

168. Ramsay, W. "Terrestrial Helium (?)" *Nature* **51,** 512 (Mar. 28, 1895). (Cit. on p. 31)

169. Ramsay, W. "Terrestrial Helium (?)" *Nature* **52,** 7–8 (May 2, 1895). (Cit. on p. 31)

170. Regal, C. A., Teufel, J. D. & Lehnert, K. W. "Measuring nanomechanical motion with a microwave cavity interferometer". *Nature Physics* **4,** 555–560 (July 2008). (Cit. on pp. 5 and 26)

171. Rego, L. G. C. & Kirczenow, G. "Quantized Thermal Conductance of Dielectric Quantum Wires". *Physical Review Letters* **81,** 232–235 (July 6, 1998). (Cit. on p. 89)

172. Restrepo, J., Gabelli, J., Ciuti, C. & Favero, I. "Classical and quantum theory of photothermal cavity cooling of a mechanical oscillator". *Comptes Rendus Physique. Nano- and micro-optomechanical systems* **12,** 860–870 (Dec. 1, 2011). (Cit. on pp. 103 and 183)

173. Reynaud, S. "Introduction à la réduction du bruit quantique". *Annales de Physique* **15,** 63–162 (1990). (Cit. on p. 6)

174. Riedinger, R. *et al.* "Remote quantum entanglement between two micromechanical oscillators". *Nature* **556,** 473 (Apr. 2018). (Cit. on p. 145)

175. Rohr, S. *et al.* "Synchronizing the Dynamics of a Single Nitrogen Vacancy Spin Qubit on a Parametrically Coupled Radio-Frequency Field through Microwave Dressing". *Physical Review Letters* **112,** 010502 (Jan. 7, 2014). (Cit. on p. 17)

176. Rolley, E., Chevalier, E., Guthmann, C. & Balibar, S. "Stepped surfaces of hcp helium-4 crystals". *Physical Review Letters* **72,** 872–875 (Feb. 7, 1994). (Cit. on p. 43)

177. Rugar, D., Budakian, R., Mamin, H. J. & Chui, B. W. "Single spin detection by magnetic resonance force microscopy". *Nature* **430,** 329–332 (July 2004). (Cit. on pp. 5 and 26)

178. Safavi-Naeini, A. H. *et al.* "Squeezed light from a silicon micromechanical resonator". *Nature* **500,** 185–189 (Aug. 2013). (Cit. on pp. 4 and 102)

179. Safavi-Naeini, A. H. *et al.* "Two-Dimensional Phononic-Photonic Band Gap Optomechanical Crystal Cavity". *Physical Review Letters* **112,** 153603 (Apr. 14, 2014). (Cit. on p. 5)

180. Sage, E. *et al.* "Single-particle mass spectrometry with arrays of frequency-addressed nanomechanical resonators". *Nature Communications* **9,** 1–8 (Aug. 16, 2018). (Cit. on p. 4)

181. Satzinger, K. J. *et al.* "Quantum control of surface acoustic-wave phonons". *Nature* **563,** 661–665 (Nov. 2018). (Cit. on pp. 4 and 5)

182. Schliesser, A., Del'Haye, P., Nooshi, N., Vahala, K. J. & Kippenberg, T. J. "Radiation Pressure Cooling of a Micromechanical Oscillator Using Dynamical Backaction". *Physical Review Letters* **97,** 243905 (Dec. 14, 2006). (Cit. on p. 5)

183. Schwab, K., Henriksen, E. A., Worlock, J. M. & Roukes, M. L. "Measurement of the quantum of thermal conductance". *Nature* **404,** 974–977 (Apr. 2000). (Cit. on p. 89)

184. Schwab, K., Arlett, J. L., Worlock, J. M. & Roukes, M. L. "Thermal conductance through discrete quantum channels". *Physica E: Low-dimensional Systems and Nanostructures. Proceedings of the Eleventh International Winterschool on New Developments in Solid State Physics, "New Frontiers in Low-Dimensional Physics"* **9,** 60–68 (Jan. 1, 2001). (Cit. on p. 89)

185. Schwarz, C. *et al.* "Deviation from the Normal Mode Expansion in a Coupled Graphene-Nanomechanical System". *Physical Review Applied* **6,** 064021 (Dec. 29, 2016). (Cit. on p. 92)

186. Scurlock, R. G. "A matter of degrees: A brief history of cryogenics". *Cryogenics* **30,** 483–500 (June 1, 1990). (Cit. on p. 32)

187. Siria, A. & Niguès, A. "Electron beam detection of a Nanotube Scanning Force Microscope". *Scientific Reports* **7,** 1–6 (Sept. 14, 2017). (Cit. on p. 26)

188. Srinivasan, K., Miao, H., Rakher, M. T., Davanço, M. & Aksyuk, V. "Optomechanical Transduction of an Integrated Silicon Cantilever Probe Using a Microdisk Resonator". *Nano Letters* **11,** 791–797 (Feb. 9, 2011). (Cit. on p. 71)

189. Steiner, M., Meyer, H. M., Reichel, J. & Köhl, M. "Photon Emission and Absorption of a Single Ion Coupled to an Optical-Fiber Cavity". *Physical Review Letters* **113,** 263003 (Dec. 29, 2014). (Cit. on p. 103)

190. Steiner, M., Meyer, H. M., Deutsch, C., Reichel, J. & Köhl, M. "Single Ion Coupled to an Optical Fiber Cavity". *Physical Review Letters* **110,** 043003 (Jan. 25, 2013). (Cit. on p. 103)

191. Steinmetz, T. *et al.* "Stable fiber-based Fabry-Pérot cavity". *Applied Physics Letters* **89,** 111110 (Sept. 11, 2006). (Cit. on pp. 103 and 107)

192. Tagantsev, A. K. & Fedorov, S. A. "Quantum-Limited Measurements Using an Optical Cavity with Modulated Intrinsic Loss". *Physical Review Letters* **123,** 043602 (July 23, 2019). (Cit. on p. 183)

193. Tao, Y., Eichler, A., Holzherr, T. & Degen, C. L. "Ultrasensitive mechanical detection of magnetic moment using a commercial disk drive write head". *Nature Communications* **7,** 1–8 (Sept. 20, 2016). (Cit. on pp. 26 and 94)

194. Teufel, J. D., Donner, T., Castellanos-Beltran, M. A., Harlow, J. W. & Lehnert, K. W. "Nanomechanical motion measured with an imprecision below that at the standard quantum limit". *Nature Nanotechnology* **4,** 820–823 (Dec. 2009). (Cit. on p. 4)

195. Teufel, J. D. *et al.* "Circuit cavity electromechanics in the strong-coupling regime". *Nature* **471,** 204–208 (Mar. 2011). (Cit. on p. 5)

196. Teufel, J. D. *et al.* "Sideband cooling of micromechanical motion to the quantum ground state". *Nature* **475,** 359–363 (July 2011). (Cit. on p. 4)

197. Thompson, J. D. *et al.* "Strong dispersive coupling of a high-finesse cavity to a micromechanical membrane". *Nature* **452,** 72–75 (Mar. 2008). (Cit. on pp. 5, 102 and 166)

198. Tielbürger, D., Merz, R., Ehrenfels, R. & Hunklinger, S. "Thermally activated relaxation processes in vitreous silica: An investigation by Brillouin scattering at high pressures". *Physical Review B* **45,** 2750–2760 (Feb. 1, 1992). (Cit. on p. 84)

199. Treutlein, P. *et al.* "Quantum information processing in optical lattices and magnetic microtraps". *Fortschritte der Physik* **54,** 702–718 (2006). (Cit. on p. 103)

200. Usenko, O., Vinante, A., Wijts, G. & Oosterkamp, T. H. "A superconducting quantum interference device based read-out of a subattonewton force sensor operating at millikelvin temperatures". *Applied Physics Letters* **98,** 133105 (Mar. 28, 2011). (Cit. on pp. 26 and 94)

201. Verhagen, E., Deléglise, S., Weis, S., Schliesser, A. & Kippenberg, T. J. "Quantum-coherent coupling of a mechanical oscillator to an optical cavity mode". *Nature* **482,** 63–67 (Feb. 2012). (Cit. on p. 5)

202. Vermeulen, G. A. & Frossati, G. "Powerful dilution refrigerator for use in the study of polarized liquid 3He and nuclear cooling". *Cryogenics* **27,** 139–147 (Mar. 1, 1987). (Cit. on p. 32)

203. Volz, J., Gehr, R., Dubois, G., Estève, J. & Reichel, J. "Measurement of the internal state of a single atom without energy exchange". *Nature* **475,** 210–213 (July 2011). (Cit. on p. 103)

204. Wagner, R., Ras, P. J., Remeijer, P., Steel, S. C. & Frossati, G. "Observation of ^{3}He crystallization down to 1 mK using a cooled CCD camera". *Journal of Low Temperature Physics* **95,** 715–728 (June 1, 1994). (Cit. on p. 43)

205. Wang, M. C. & Uhlenbeck, G. E. "On the Theory of the Brownian Motion II". *Reviews of Modern Physics* **17,** 323–342 (Apr. 1, 1945). (Not cited)

206. Weber, P., Güttinger, J., Noury, A., Vergara-Cruz, J. & Bachtold, A. "Force sensitivity of multilayer graphene optomechanical devices". *Nature Communications* **7,** 1–8 (Aug. 9, 2016). (Cit. on p. 26)

207. Weiss, T., Bruder, C. & Nunnenkamp, A. "Strong-coupling effects in dissipatively coupled optomechanical systems". *New Journal of Physics* **15,** 045017 (Apr. 2013). (Cit. on p. 103)

208. Weiss, T. & Nunnenkamp, A. "Quantum limit of laser cooling in dispersively and dissipatively coupled optomechanical systems". *Physical Review A* **88,** 023850 (Aug. 27, 2013). (Cit. on p. 103)

209. Wiederhecker, G. S., Chen, L., Gondarenko, A. & Lipson, M. "Controlling photonic structures using optical forces". *Nature* **462,** 633–636 (Dec. 2009). (Cit. on p. 5)

210. Wollman, E. E. *et al.* "Quantum squeezing of motion in a mechanical resonator". *Science* **349,** 952–955 (Aug. 28, 2015). (Cit. on p. 4)

211. Xuereb, A., Schnabel, R. & Hammerer, K. "Dissipative Optomechanics in a Michelson-Sagnac Interferometer". *Physical Review Letters* **107,** 213604 (Nov. 16, 2011).(Cit. on pp. 103 and 183)

212. Yanay, Y., Sankey, J. C. & Clerk, A. A. "Quantum backaction and noise interference in asymmetric two-cavity optomechanical systems". *Physical Review A* **93,** 063809 (June 8, 2016). (Cit. on p. 103)

213. Yang, Y. T., Callegari, C., Feng, X. L., Ekinci, K. L. & Roukes, M. L. "Zeptogram-Scale Nanomechanical Mass Sensing". *Nano Letters* **6,** 583–586 (Apr. 1, 2006). (Cit. on p. 4)

214. Yeo, I. *et al.* "Strain-mediated coupling in a quantum dot–mechanical oscillator hybrid system". *Nature Nanotechnology* **9,** 106–110 (Feb. 2014). (Cit. on p. 5)

215. Zeller, R. C. & Pohl, R. O. "Thermal Conductivity and Specific Heat of Noncrystalline Solids". *Physical Review B* **4,** 2029–2041 (Sept. 15, 1971). (Cit. on p. 85)

PROCEEDINGS

216. Classen, J., Burkert, T., Enss, C. & Hunklinger, S. "Beyond the tunneling model—Elastic properties of vitreous silica at low temperatures". in *Advances in Solid State Physics 40* (ed Kramer, B.) (Springer Berlin Heidelberg, 2000), 279–291. (Cit. on p. 85)

217. Das, P., de Ouboter, R. B. & Taconis, K. W. "A Realization of a London-Clarke-Mendoza Type Refrigerator". in *Low Temperature Physics LT9* (eds Daunt, J. G., Edwards, D. O., Milford, F. J. & Yaqub, M.) (Springer US, 1965), 1253–1255. (Cit. on p. 32)

218. London, H. in *Proceedings of the International Conference on Low Temperature Physics* (Clarendon Press Laboratory, Oxford, 1951), 157. (Cit. on p. 32)

219. Morelli, D., Heremans, J., Beetz, C. & Woo, W. S. "Carrier concentration dependence of the thermal conductivity of silicon carbide". in . Silicon carbide and related materials: proceedings of the fifth conference, 1 -3 November 1993, Washington, DC, USA (ed Spencer, M. G.) **137** (Institute of Physics, Bristol [u.a.], 1994), 313–315. (Cit. on p. 65)

220. Stapfner, S. *et al.* "Cavity nano-optomechanics: a nanomechanical system in a high finesse optical cavity". in *Quantum Optics* Quantum Optics. **7727** (International Society for Optics and Photonics, June 4, 2010), 772706. (Cit. on pp. 102 and 103)

COLLECTION

221. *Cavity optomechanics: nano- and micromechanical resonators interacting with light* (eds Aspelmeyer, M., Kippenberg, T. J. & Marquardt, F.) OCLC: 899597161 (Springer, Berlin, 2014). 357 pp. (Cit. on pp. 4 and 14)

222. Choyke, W. J. "Optical properties of polytypes of SiC: interband absorption, and luminescence of nitrogen-exciton complexes". in *Silicon Carbide–1968* (eds Henisch, H. K. & Roy, R.) S141–S152 (Pergamon, Jan. 1, 1969). (Cit. on p. 66)

223. Järrendahl, K. & Davis, R. F. "Materials Properties and Characterization of SiC". in *Semiconductors and Semimetals* (ed Soo Park, Y.) 1–20 (Elsevier, Jan. 1, 1998). (Cit. on p. 64)

224. *Quantum Optics, Experimental Gravity, and Measurement Theory* (eds Meystre, P. & Scully, M. O.) (Springer US, 1983). (Cit. on p. 4)

225. Reynaud, S., Heidmann, A., Giacobino, E. & Fabre, C. "Quantum Fluctuations in Optical Systems". in *Progress in Optics* (ed Wolf, E.) 1–85 (Elsevier, Jan. 1, 1992). (Cit. on p. 6)

226. Round, H. J. "A Note on Carborundum". in *Electrical world* in collab. with Engineering - University of Toronto, 309 ([New York McGraw-Hill Pub. Co., etc.], 1907). (Cit. on p. 64)

227. *Length-Scale Dependent Phonon Interactions* (eds Shindé, S. L. & Srivastava, G. P.) (Springer-Verlag, New York, 2014). (Cit. on p. 88)

THESES

228. Bechelany, M. "Nouveau procede de croissance de nanofils a base SiC et de nanotubes de BN, etude des proprietes physiques d'un nanofil individuel a base de SiC". PhD thesis (Dec. 8, 2006). (Cit. on pp. 20 and 65)

229. Besga, B. "Micro-cavité Fabry Perot fibrée : une nouvelle approche pour l'étude des polaritons dans des hétérostructures semi-conductrices". PhD thesis (Université Pierre et Marie Curie - Paris VI, June 6, 2013). (Cit. on pp. 107, 109 and 125)

230. Bourgeois, O. "Thermique et thermodynamique des nanosystèmes". thesis (Université Joseph-Fourier - Grenoble I, Oct. 9, 2008). (Cit. on pp. 86, 88 and 89)

231. Deutsch, C. "High Finesse Fibre Fabry-Perot Resonators - Production, Characterization, and Applications". PhD thesis (LMU München, Oct. 23, 2008). (Cit. on pp. 107 and 125)

232. Gloppe, A. "Nano-optomécanique au coeur d'un faisceau laser focalisé : cartographie du champ de force optique et action en retour bidimensionnelle". PhD thesis (Université de Grenoble, Dec. 19, 2014). (Cit. on pp. xix, 17, 64, 65, 66, 92, 162 and 178)

233. Lépinay, L. M. d. "Habillage mécanique d'un nanofil par un champ de force : de la mesure vectorielle ultrasensible aux systèmes quantiques hybrides". PhD thesis (Université Grenoble Alpes, June 30, 2017). (Cit. on pp. xix, 18, 20, 65, 66, 74, 75, 76, 92, 162 and 164)

234. Rohr, S. "Hybrid spin-nanomechanical systems in parametric interaction". thesis (Grenoble, Dec. 15, 2014). (Cit. on pp. xix and 17)

235. Schwarz, C. "Optomechanical, vibrational and thermal properties of suspended graphene membranes". PhD thesis (Université Grenoble Alpes, Jan. 15, 2016). (Cit. on p. 92)

236. Tavakoli-Ghinani, A. "Phonon transport in the quantum regime". PhD thesis (Université Grenoble Alpes, Dec. 14, 2017). (Cit. on p. 89)

237. Thiele, S. "Read-out and coherent manipulation of an isolated nuclear spin using a single molecule magnet spin transistor". PhD thesis (Université de Grenoble, Jan. 24, 2014). (Not cited)

BOOKS

238. Bohren, C. F. & Huffman, D. R. *Absorption and Scattering of Light by Small Particles* Google-Books-ID: ib3EMXXIRXUC (John Wiley & Sons, Sept. 26, 2008).(Cit. on pp. 17, 74, 75 and 181)

239. Born, M. *et al.* *Principles of Optics* 7th (Oct. 1999). (Cit. on p. 104)

240. Bowen, W. P. & Milburn, G. J. *Quantum Optomechanics* (CRC Press, Nov. 18, 2015).(Cit. on pp. 4 and 14)

241. Braginsky, V. B., Braginsky, V. B. & Khalili, F. Y. *Quantum Measurement* (Cambridge University Press, May 25, 1995). (Cit. on pp. 4, 6 and 14)

242. Bringhurst, R. *The Elements of Typographic Style* (Hartley & Marks, Point Roberts, Washington, USA, 2002). (Cit. on p. v)

243. Cleland, A. N. *Foundations of Nanomechanics: From Solid-State Theory to Device Applications* (Springer-Verlag, Berlin Heidelberg, 2003). (Cit. on pp. 66 and 85)

244. Enss, C. & Hunklinger, S. *Low-Temperature Physics* (Springer Science & Business Media, Dec. 5, 2005). (Cit. on pp. 30, 65, 84 and 85)

245. Fabre, C., Sandoghdar, V., Treps, N. & Cugliandolo, L. F. *Quantum Optics and Nanophotonics* (Oxford University Press, May 18, 2017). (Cit. on p. 6)

246. Flynn, T. *Cryogenic Engineering, Revised and Expanded* (CRC Press, Nov. 30, 2004).(Cit. on pp. 32 and 44)

247. Harris, G. L. *Properties of Silicon Carbide* Google-Books-ID: Yy_B8GzxNlgC (IET, 1995).(Cit. on pp. 64, 66 and 86)

248. Hecht, E. *Optics, Global Edition* 5th ed. (Pearson Education Limited, Dec. 15, 2016).(Cit. on p. 104)

249. Jackson, J. D. *Classical Electrodynamics* 3rd ed. (Wiley, 2007). (Cit. on p. 115)

250. Jacobs, K. *Quantum Measurement Theory and its Applications* (Cambridge University Press, Aug. 14, 2014). (Cit. on pp. 4 and 6)

251. Levinshtein, M. E., Rumyantsev, S. L. & Shur, M. S. *Properties of Advanced Semiconductor Materials: GaN, AIN, InN, BN, SiC, SiGe* (John Wiley & Sons, Feb. 21, 2001).(Cit. on pp. 64 and 65)

252. Metcalf, H. J., Straten, P. v. d. & Straten, P. v. d. *Laser Cooling and Trapping* (Springer-Verlag, New York, 1999). (Cit. on p. 4)

253. Nowick, A. S. *Anelastic Relaxation In Crystalline Solids* (Elsevier, Dec. 2, 2012). (Cit. on p. 85)

254. Pitaevskii, L. & Stringari, S. *Bose-Einstein Condensation and Superfluidity* (Oxford University Press, Jan. 1, 2016). (Cit. on p. 29)

255. Pobell, F. *Matter and Methods at Low Temperatures* (Springer Science & Business Media, Feb. 15, 2007). (Cit. on pp. 27, 28, 30, 31, 32 and 44)

256. Rao, S. S. *Vibration of Continuous Systems* (John Wiley & Sons, Feb. 9, 2007). (Cit. on p. 66)

257. Reynaud, S., Giacobino, E., Zinn-Justin, J. & Fourier, U. J. *Fluctuations Quantiques: Les Houches, Session LXIII, 27 Juin-28 Juillet 1995* (Elsevier, 1997). (Cit. on p. 6)

258. Schmid, S., Villanueva, L. G. & Roukes, M. L. *Fundamentals of Nanomechanical Resonators* (Springer, June 21, 2016). (Cit. on pp. 66 and 72)

259. Sciver, S. W. V. *Helium Cryogenics* (Springer Science & Business Media, Feb. 10, 2012). (Cit. on p. 30)

260. Shur, M., Rumyantsev, S. L. & Levinshte?n, M. E. *SiC Materials and Devices* Google-Books-ID: WdRoDQAAQBAJ (World Scientific, 2006). (Cit. on p. 64)

261. Siegman, A. *Lasers* (University Science Books, 1986). (Cit. on pp. 104 and 107)

262. Ventura, G. & Risegari, L. *The Art of Cryogenics: Low-Temperature Experimental Techniques* (Elsevier, July 7, 2010). (Cit. on pp. 30 and 32)

263. Wiseman, H. M. & Milburn, G. J. *Quantum Measurement and Control* (Cambridge University Press, Nov. 12, 2009). (Cit. on pp. 4 and 6)

264. Yeh, P. *Optical Waves in Layered Media* (Wiley, Mar. 3, 2005). (Cit. on p. 104)

265. Ziman, J. M. *Electrons and Phonons: The Theory of Transport Phenomena in Solids* (Oxford University Press, Feb. 1, 2001). (Cit. on p. 88)

MANUALS

266. Miede, A. *A Classic Thesis style* (2018). (Cit. on p. v)

267. Pantieri, L. *LaTeXpedia* in Italian (2018), 317. (Cit. on p. v)

268. Pantieri, L. & Gordini, T. *L'arte di scrivere con LaTeX* in Italian (2018). (Not cited)

OTHERS

269. Navarrete-Benlloch, C. "A primer on quantum optics and open systems". Lecture notes. July 2017. (Cit. on p. 6)

ABSTRACT

In recent years nano-optomechanical systems have proven to be a powerful resource to detect ultra-weak forces, thus providing new insights on fundamental interactions. In this work we extend the experimental range of ultrasensitive force measurements based on optically readout vibrations of suspended silicon carbide nanowires to novel experimental regimes: first through operations at dilution temperatures, second in the ultrastrong coupling regime of cavity nano-optomechanics.

Operating those force sensors at dilution temperatures permits to reduce their thermal noise and further benefit from an increased mechanical coherence. However this requires eliminating the sources of unwanted vibrations, such as electrical or mechanical noises, and operating at ultralow optical powers to avoid unwanted laser heating. We expose the experimental developments that lead us to observe a nanowire featuring a noise temperature measured at the 32 mK level, while exploiting novel optical readout schemes operating in the photon counting regime, where less than a photon is detected per mechanical period. We discuss their mechanical and thermal properties at low temperatures and report on enhanced force sensitivities of a few tens of $\mathrm{zN}/\sqrt{\mathrm{Hz}}$, which are sufficient in principle to detect the electron-electron Coulomb interaction over distances larger than 100 µm.

In the second part of the manuscript, we describe a novel cavity nano-optomechanical experiment at room temperature that consists in inserting the vibrating extremity of a suspended nanowire with sub-wavelength sized diameter, in a high finesse fiber micro-cavity. The combination of its small mode volume, of the extreme force sensitivity of the nanowires and of the large optomechanical interaction strength demonstrated makes the system very interesting for further explorations of the field of cavity nano-optomechanics. In particular we demonstrate that one can reach the so-called ultrastrong coupling regime, where one single intracavity photon can displace the oscillator by more than its zero point fluctuations. This is achieved when the single photon coupling strength g_0 exceeds the mechanical frequency Ω_m. After having described the experimental platform, we investigate how the nanowire perturbs the intracavity field by mapping the cavity properties as a function of the nanowire position within the standing wave. This permits to quantify and spatially map the optomechanical interaction strength, which acquires a vectorial character. Furthermore we explored the interaction in the reversed direction by mapping the intracavity optical force field experienced by the nanowire and compared our results with dedicated numerical simulations.

Implementing this nanowire in the middle optomechanical scheme at low temperatures will permit, by significantly reducing the nanowire thermal noise, to explore the regime of single photon cavity nano-optomechanics. In this regime, particularly interesting for fundamental quantum optics, one single intracavity photon should render the cavity statically bistable and mean field descriptions should not be relevant anymore.

RÉSUMÉ

Les progrès récents réalisés dans le domaine des systèmes nano-optomécaniques ont démontré leur potentiel pour détecter des forces extrêmement faibles et ouvrir de nouveaux champs d'étude en physique. Ce travail de thèse vise à étendre le champ d'application des mesures de force ultrasensibles basées sur la lecture optique des vibrations de nanofils suspendus à de nouveaux domaines : d'abord à très basse température, en démontrant la possibilité de les exploiter dans un cryostat à dilution, ensuite dans le domaine de la nano-optomécanique en cavité où leur extrême sensibilité permet d'atteindre le régime de couplage ultra-fort.

Leur mise en œuvre dans un cryostat à dilution permet en effet de réduire leur bruit thermique tout en bénéficiant d'une augmentation de leur cohérence mécanique mais nécessite de réduire drastiquement les sources de bruits externes, d'origine électrique ou mécanique, tout en opérant à des puissances optiques extrêmement faibles afin de limiter le chauffage par absorption. Nous présentons les développements réalisés, qui nous ont permis d'observer un nanofil présentant une température de bruit de 32 mK grâce à des techniques de mesures fonctionnant en régime de comptage de photon, lorsque moins d'un photon est détecté par période mécanique. Nous étudions les propriétés mécaniques et thermique de ces sondes de force à très basses températures, qui ont permis d'atteindre une sensibilité record pour une sonde locale, de l'ordre de quelques dizaines de $\mathrm{zN}/\sqrt{\mathrm{Hz}}$, ce qui est en principe suffisante pour détecteur l'interaction électron-électron à une distance de plus de 100 µm.

Dans la seconde partie du manuscrit, on décrit une nouvelle expérience de nano-optomécanique en cavité fonctionnant à température ambiante. Elle consiste à insérer l'extrémité vibrante d'un nanofil suspendu dans une micro-cavité fibrée de grande finesse. La combinaison de son volume de mode très réduit, de la très grande sensibilité en force des nanofils et de l'interaction optomécanique gigantesque obtenue rend cette approche extrêmement intéressante pour la nano-optomécanique en cavité. En effet, on démontre qu'il est possible d'atteindre le régime de couplage ultrafort, dans lequel un seul photon intra-cavité est capable de déplacer le nano-résonateur de plus que ses fluctuations de point zéro. Ceci nécessite d'avoir une constante de couplage par photon g_0 dépassant la fréquence mécanique du nanofil Ω_m. Après avoir décrit l'expérience, on étudie comment le nanofil permet d'imager le champ lumineux intra-cavité en cartographiant ses propriétés optiques en fonction de la position du nanofil de diamètre sub-longueur d'onde dans l'onde stationnaire. Cela permet de quantifier et de cartographier l'intensité et l'orientation de l'interaction optomécanique qui acquiert alors un caractère vectoriel. De plus nous avons étudié l'interaction en sens inverse, en cartographiant le champ de force intra-cavité ressenti par le nanofil en fonction de sa position dans le mode de cavité et comparé nos résultats à des simulations numériques.

La mise en œuvre de cette approche optomécanique dite du «nanofil au milieu» à très basse température devrait permettre de réduire suffisamment le bruit thermique des nanofils pour explorer l'optomécanique en cavité au photon unique. Dans ce régime, un seul photon intra-cavité est capable de rendre le système bistable statiquement, ce qui ouvre la voie à des développements nouveaux en optique quantique, ne serait que parce que les théories de champ moyen ne sont alors plus pertinentes.